

ISSN 0392-6672

International Journal of Speleology

Official Journal of the Union Internationale de Spéléologie

Volume 44 (1) - January 2015

International Journal of Speleology

Scholarcommons.usf.edu/ijis/

Volume 44(1), January 2015

Original papers

Silvia Frisia

Microstratigraphic logging of calcite fabrics in speleothems as tool for palaeoclimate studies 1-16

**Martin Finné, Malin Kylander, Meighan Boyd, Hanna S. Sundqvist,
and Ludvig Löwemark**

Can XRF scanning of speleothems be used as a non-destructive method to identify paleoflood events in caves?..... 17-23

Ivo Silvestre, José I. Rodrigues, Mauro Figueiredo, and Cristina Veiga-Pires

High-resolution digital 3D models of Algar do Penico Chamber: limitations, challenges, and potential 25-35

**Gerhard C. Du Preez, Paolo Forti, Gerhard Jacobs, Anine Jordaan,
and Louwrens Tiedt**

Hairy Stalagmites, a new biogenic root speleothem from Botswana 37-47

Jiri Kamas, Jiri Bruthans, Helena Vysoka, and Miroslav Kovařík

Range of horizontal transport and residence time of nitrate in a mature karst vadose zone..... 49-59

Heros A.S. Lobo, Paulo Cesar Boggiani, and José A.J. Perinotto

Speleoclimate dynamics in Santana Cave (PETAR, São Paulo State, Brazil): general characterization and implications for tourist management..... 61-73

William Sallun Filho, Bruna Medeiros Cordeiro, and Ivo Karmann

Structural and hydrological controls on the development of a river cave in marble (Tapagem Cave - southeastern Brazil) 75-90

Detlev K. Richter, Adrian Immenhauser, Rolf D. Neuser, and Augusto Mangini

Radiaxial-fibrous and fascicular-optic Mg-calcitic cave cements: a characterization using electron backscattered diffraction (EBSD) 91-98

Gregory S. Springer, Holly A. Poston, Ben Hardt, and Harold D. Rowe

Groundwater lowering and stream incision rates in the Central Appalachian Mountains of West Virginia, USA..... 99-105

Book Reviews

Leslie A. Melim

Kirkland D.W. 2014. Role of hydrogen sulfide in the formation of cave and karst phenomena in the Guadalupe Mountains and western Delaware Basin, New Mexico and Texas. National Cave and Karst Research Institute Special Paper 2. 77 pp., ISBN 978-0-9910009-1-3, \$ 25.00 I



Available online at scholarcommons.usf.edu/ijis

International Journal of Speleology

Official Journal of Union Internationale de Spéléologie



Microstratigraphic logging of calcite fabrics in speleothems as tool for palaeoclimate studies

Silvia Frisia^{1*}

¹Earth Sciences, SELS, The University of Newcastle, Callaghan, NSW Australia

Abstract: The systematic documentation of calcite fabrics in stalagmites and flowstones provides robustness to palaeoclimate interpretation based on geochemical proxies, but it has been neglected because it is difficult to transform crystal morphologies into numerical values, and construct fabric time series. Here, general criteria that allow for coding fabrics of calcite composing stalagmites and flowstones is provided. Being based on known models of fabric development, the coding ascribes sequential numbers to each fabric, which reflect climate-related parameters, such as changes in drip rate variability, bio-mediation or diagenetic modifications. Acronyms are proposed for Columnar types, Dendritic, Micrite, Microsparite and Mosaic fabrics, whose use could then render possible comparison of calcite fabrics in stalagmites and flowstones from diverse latitudinal and altitudinal settings. The climatic and environmental significance of similarities in the geochemical signals and trends analysed in coeval stalagmites and flowstones (or differences in the signals and trends) will be more robust when compared with fabric time series. This is particularly true where, such as in the Holocene, changes in geochemical values may be subtle, yet fabrics may show changes related to variations in supersaturation, drip rate or input of detrital particles or organic compounds. The proposed microstratigraphic logging allows recognition of changes in stable isotope ratio or trace element values that can be ascribed to hydrology and diagenesis, with considerable improvement of reconstructions based on the chemical proxies of stalagmites and flowstones composed of calcite.

Keywords: speleothems; fabrics; calcite; aragonite; diagenesis; microstratigraphy
Received 22 June 2014; Revised 29 October 2014; Accepted 3 November 2014

Citation: Frisia S., 2015. Microstratigraphic logging of calcite fabrics in speleothems as tool for palaeoclimate studies. *International Journal of Speleology*, 44 (1), 1-16, Tampa FL (USA), ISSN 0392-6672 <http://dx.doi.org/10.5038/1827-806X.44.1.1>

INTRODUCTION

Documentation of speleothem fabrics is fundamental for a robust interpretation of speleothem time series where stable isotopes and trace elements are used as proxy (Fairchild & Baker, 2012). Fabrics provide valuable information on post-depositional phenomena (diagenesis), such as phase transformations (aragonite to calcite), aggrading neomorphism (Frisia, 1996), dissolution and re-precipitation processes, which may alter the original geochemical signal. Petrographic observations should not be confined to the sole identification of diagenesis, particularly when U-series dating is problematic (Ortega et al., 2005; Hoffmann et al., 2009; Lachniet et al., 2012). For example, by observing changes in columnar calcite types, high-frequency variability of $\delta^{13}\text{C}$ values in stalagmites could be explained as related to changes in drip rate and degassing (Boch et al., 2011).

A comprehensive classification of fabrics which accounts for growth mechanisms and relates

morphologies to hydrology and drip-water properties (chemistry, presence of organic compounds, particulate etc.) was compiled by Frisia & Borsato (2010). Yet, there has been little advance in the use of fabrics as a complement to palaeo-proxy datasets since Frisia et al. (2000). Although it has been demonstrated that speleothem fabrics record hydrology, bio-influenced and post-depositional processes that influence the way geochemical proxy data are captured by cave minerals (Fairchild & Baker, 2012) their use is limited by the absence of a system that allows to construct a fabric time series comparable with geochemical time series.

Here, a speleothem microstratigraphic log is proposed as a logic system of creating fabric time series. The log is based on the hierarchical coding of fabrics typical of stalagmites and flowstones and builds upon accepted models for their development. The microstratigraphic log relies on the attribution of a progressive number to fabrics as observed by Plane Polarized (PPL) and Cross Polarized Light (XPL) at the optical microscope, which reflects a hierarchic system

*Silvia.Frisia@newcastle.edu.au

that gives the lowest numbers to fabrics developed under conditions of constant drip of waters at low supersaturation with respect to calcite and low Mg/Ca ratio and/or negligible presence of impurities, and the highest to post-depositional (diagenetic) fabrics. The coded fabrics are thus plotted against age model, thus allowing comparison with geochemical time series. The microstratigraphic log is an inexpensive tool that requires a microscope and thin sections and some practice. It is recommended to use more sophisticated techniques, such as electron backscattered diffraction and TEM techniques need to be used (Fairchild & Baker, 2012) only when there is the need to know processes of crystal nucleation and growth processes and/or complex phase transformation.

The documentation of fabrics in a petrographic log was pioneered in a speleothem-based European Holocene palaeoclimate reconstruction (McDermott et al., 1999). The log highlighted for the first time that certain fabrics, such as a scaffold-like dendritic fabric, coincided with systematic shifts to ^{13}C -enriched calcite. More recently, Luetscher et al. (2011) used microstratigraphic logs to reconstruct glacier mass balance fluctuations in the Swiss Alps. Belli et al. (2013) compared microstratigraphic logs, growth rates and stable isotope time series of two speleothems from the same cave in NE Italy to recognize how “site-specific” processes drove stable isotope ratios variations which allowed for the distinction of the hydrologic vs. hydroclimatic component to the isotope signal.

The coding of fabrics in the construction of the microstratigraphic log must be conceptually connected to parameters related to climate, which influence speleothem crystal growth. Only in such conceptual framework, the log becomes useful to provide robustness to the geochemical data or test the overall accuracy of the speleothem record. It becomes, thus, apparent that the most critical issue in its development is the appropriate coding of fabrics, which are significant for the type of speleothem-based study that is being conducted. Given that fabrics are recognized and defined by microscopy observation, coding is a somehow a subjective evaluation. It is, therefore, proposed here that coding shall be rooted on a general knowledge of how fabric relate to their environment of formation. Critically, there are uncertainties in recognizing the origin of fabrics whose development can be primary or the result of post depositional (diagenetic) processes. The study of speleothem diagenesis is still in its infancy, therefore, examples are here provided for fabrics that are accepted as being the result of diagenesis. It is then proposed that some fabrics, such as mosaic calcite and microsparite, are unequivocally of diagenetic origin. The basis of the hierarchy for coding fabrics as proposed here is provided in the following section.

MODELS OF FABRIC DEVELOPMENT: BASELINE FOR CODING

The logic underneath ranking stalagmite and flowstones calcite fabrics as proposed in Table 1 is based on our current understanding of the parameters

that result in their development. Fabrics develop under certain environmental parameters, most important fluid flow and presence of impurities, which influence a certain spatial arrangement of crystals with a dominant form (or a few dominant forms). Calcite shows a large variety of morphologies, but known speleothem fabrics can be grouped in a few broad categories: columnar types, dendritic, micrite, microsparite and mosaic calcite (cf. Frisia & Borsato, 2010). The proposed order, from the columnar types to mosaic calcite, is a plausible hierarchic system that takes into consideration changes in drip rate (flow), progressive increase in calcite saturation index (where known) and Mg/Ca ratio and, finally, diagenetic transformation.

Columnar Fabrics

Columnar compact and open

Columnar calcite proper (C in Table 1) consists of crystals with the c axis commonly at 90 to 60° to the substrate, unit extinction, length fast, with a length to width ratio < 6:1 (Frisia et al., 2000). The acute and equant rhombohedra are the predominant individual crystal forms (Dickson, 1993). Columnar fabrics are characterized by competitive growth, or geometric selection, whereby crystals compete growing away from an interface. Crystals whose greatest growth vector is perpendicular to the substrate will be favoured, those with greatest growth vector orientated in different directions will be outcompeted. Above the interface, thus, small crystals with “random” growth directions are observed, as testimony of a nucleation episode (Fig. 1C). A crystal fabric with preferred orientation than develop in the “maturation stage” (Dickson, 1993) and the elongation can be with the slow (length slow) or the fast (length fast) optic ray parallel to crystal length. Commonly, columnar fabric consists of length-fast crystals, and Transmission Electron Microscope diffraction patterns have shown that the cleavage rhombohedron (10.4) is a common form (Frisia et al., 2000). Thus, both the cleavage and the acute rhombohedron (40.1) potentially create aggregates of crystals with straight to serrated boundaries with the elongation parallel to the fast optic ray and perpendicular to the substrate (cf. Dickson, 1993). Geometric selection should occur when growth of a stalagmite or flowstone is interrupted by an interface that requires re-nucleation.

When the crystals form a compact aggregate, with welded crystal boundaries, where inter-crystalline porosity is not discernible at the optical microscope, the fabric is columnar compact (C in Table 1). When intercrystalline boundaries are marked by the presence of linear inclusions, or pores, then the fabric is columnar open (Co in Table 1 and Fig. 1 A-B).

The established general model for the development of compact (complete coalescence of crystallite) and open (incomplete coalescence) columnar calcite was established by Kendall & Broughton (1978), whereby the first type forms from a thin film of fluid, under relatively slow drip rate and enhanced degassing conditions (enhanced cave ventilation) and the latter forms from a thicker film of fluid, under higher drip

rate and less efficient degassing. Frisia & Borsato (2010) observed that, in temperate climate settings, C fabric forms under relatively constant discharge, low (up to 0.35) calcite supersaturation state (SI_{cc}), low Mg concentration in the dripwater (Mg/Ca ratio < 0.3) and negligible

presence of particulate and/or organic colloids. Boch et al. (2011) illustrated that lamina couplets of compact and open columnar calcite in stalagmites from Katerloch cave in Austria developed from drip waters characterized by low Mg/Ca ratio (mean 0.01). The complete

Table 1. Calcite Fabrics, types and acronyms, code numbers and acronym of special features, which may provide additional information.

Fabrics	Type	Acronym	Progression in coding	Acronym for additional features
Columnar	Compact	C	1	C_{rt} ; C_{ff}
Columnar	Open	Co	2	Co_{rt} ; Co_{ff}
Columnar	Elongated	Ce	3	
Columnar	With lateral overgrowths	Ce_{lo}	4	
Columnar "spherulitic type growth"	Fascicular Optic	Cfo	5	
	Radiaxial fibrous	Crf	5.5	
Columnar	Microcrystalline	Cm	6	
Dendritic		D	7	D_o (Dendritic open)
Micrite		M	8	Hm = hiatus with micrite layer
Diagenetic	Microsparite	Ms	9	
Diagenetic	Mimetic replacement of aragonite fabrics by microsparite	Ms_{mra}	10	
Diagenetic (?)	Mosaic calcite	Mc	11	
Diagenetic	Mosaic calcite with visible aragonite needle relicts	Mc_{an}	12	

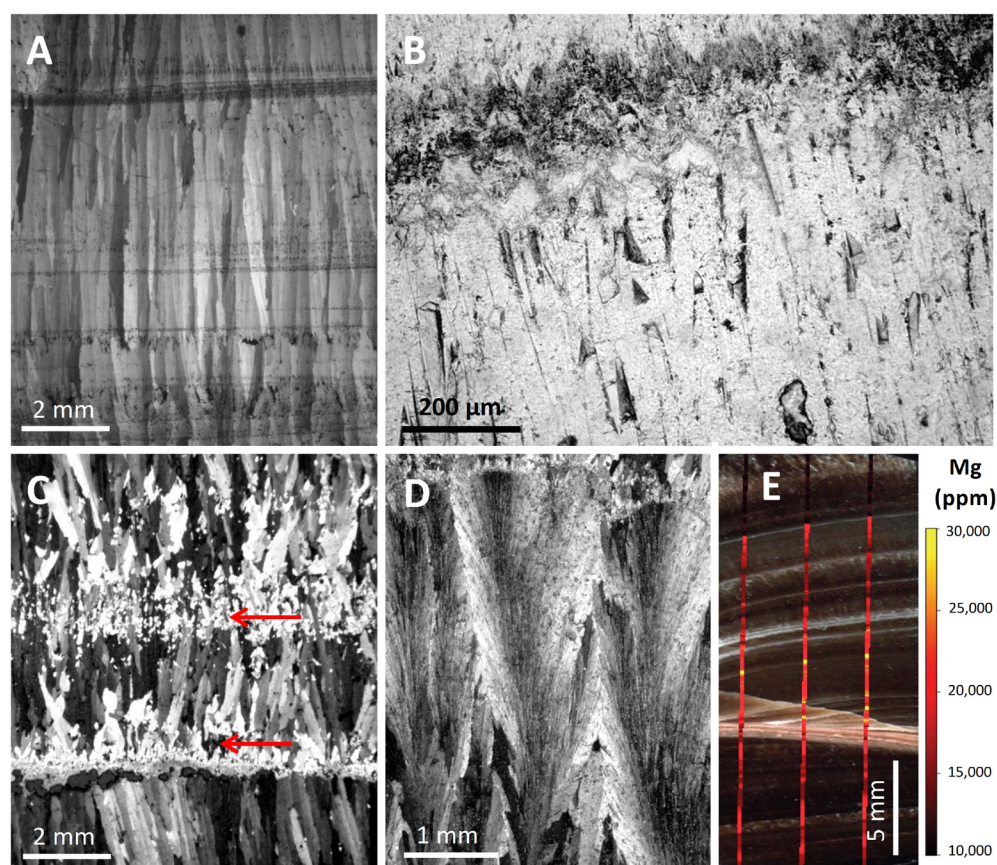


Fig. 1. Columnar Types. A) Elongated columnar, XPL, stalagmite from Liang Luar Cave, Flores Indonesia; B) Protruding crystal terminations in a stalagmitic flowstone, PPL, from Cave 370 in the Nullarbor, Australia; C) Columnar fabric showing lateral overgrowths marked by red arrows, XPL, Conturines Cave, N Italy. Note that the lateral overgrowths are not the same as randomly oriented crystals that, after nucleation, do not survive for the law of geometric selection. The lateral overgrowth "stem" from the stepped faces of a columnar individual, which survived thanks to geometric selection. D) Fascicular Optic Calcite (FOC), XPL, from a stalagmitic flowstone collected in Cave 370 Nullarbor, Australia. E) Map showing average Mg concentrations in FOC calcites in the same sample illustrated in D. Average Mg concentration in FOC is ca. 20,000 ppm. The FOC nucleated on a micrite/microsparite layer with Mg concentration up to 30,000 ppm.

coalescence of "crystallites" in the Katerloch stalagmites was attained under low drip rates, high rate of degassing and water pH of ca 8.4, and a low HCO_3^-/CO_3^{2-} ratio, which favoured horizontal linear growth rate. By contrast, the open columnar type resulted from incomplete coalescence of "crystallites" in laminae produced by high drip rates, low rate of degassing, pH from 7.4 to 8 and, consequently, high HCO_3^-/CO_3^{2-} ratios, which promoted vertical linear growth rates. More positive C isotope ratios values in the compact columnar laminae then should reflect enhanced degassing, typical of low drip rates combined with intense cave ventilation (Boch et al., 2011).

Within the open and compact columnar calcite fabrics, it is common to observe growth surfaces characterized by well-developed rhombohedra terminations, and/or flat terminations. Rhombohedra terminations are more common in the open columnar type. Flat terminations have been observed in association with dark, organic-rich laminae

(Frisia et al., 2000 and Frisia et al., 2005), which suggests the possibility that organic matter oxidation may promote localized dissolution resulting in the overall “flat” appearance of the crystal tips (cf. Frisia, 1996). The different types of crystal terminations, thus, encapsulate environmental significance and their distinction in a microstratigraphic log can be useful information. A subscript to describe morphology of crystal terminations is suggested in Table 1: C_{rt} , Co_{rt} or C_{lf} where *rt* stands for protruding rhombohedra terminations (cf. Fig. 1B) and *lf* for laminae, flat.

Because columnar compact and columnar open columnar fabrics result from growth processes that imply a combination of low/high drip rate and high/low degassing, the C isotope ratios in the two types may be more/less modified by kinetics. Given the common, low Mg/Ca ratio range measured to date in their parent waters (0 to 0.3), trace element variability may likely reflect impurities trapped within intercrystalline spaces in the open type. The distinction between C (compact) and Co (open columnar) thus becomes important, as it provides useful information to distinguish a climatic from a local hydrological signal (Belli et al., 2013).

Elongated Columnar type

Elongated columnar (Ce) is composed of crystals with a length to width ratio of 6:1, most commonly 2 up to 60 mm long, and 0.2 up to 5 mm wide. These figures can be, in certain cases, exceeded, particularly where stalagmites do not show visible interfaces and re-nucleation phenomena. According to Dickson (1993), the elongated columnar fabric is the result of the preferential growth of the acute rhombohedron (40.4). Gonzalez et al. (1992) observed that development of acute rhombohedra in speleothems from Indiana, Kentucky, New Mexico and Puerto Rico resulted from the combination of supersaturation state, Mg/Ca ratio in the parent water and flow. Elongated arrays of crystals required fluid flow over the surface of the speleothem, a Mg/Ca ratio in the parent fluid ranging from 0.85 up to 2.8 and SI_{cc} ranging from 0.1 to 0.4. Frisia et al (2000) reported that elongated columnar fabric in speleothems from temperate settings in Europe developed under constant drips, SI_{cc} ranging from 0.1 to 0.35 and Mg/Ca ratio higher than 0.3.

Gonzalez et al. (1992) further proposed that elongated columnar fabrics develop from relatively fast flow that accelerates crystal growth perpendicular to the substrate and high nucleation rate (Gonzalez et al., 1992). This interpretation was then contrasted by Kendall (1993), who demonstrated that the formation of elongated columnar fabrics neither imply fast flow, nor high nucleation rates. Thus, it seems plausible to hypothesize that elongated columnar type forms from constant drip (water flowing at the speleothem surface as inferred by Gonzalez et al., 1992), similar SI_{cc} but higher Mg/Ca ratios (>0.3) than for columnar compact and open.

Elongated columnar calcite fabric is common in flowstones developed from parent waters whose catchment intersected dolomitic or Mg-rich rocks. Turgeon & Lundberg (2001) observed elongated

columnar type in flowstones from a cave in the Klamath Mountains (Oregon, USA) where the host rocks consist of marble, argillite and basalt. The elongated columnar fabric they described is characterized by large, acute crystal terminations, exceeding 750 μm , which have been interpreted as indicative of high flow in interglacial periods (Turgeon & Lundberg, 2001). The protruding terminations should favour a relatively turbulent flow, which would prompt degassing, increase the precipitation rate and promote incomplete coalescence of crystals and development of linear inclusions. Flat terminations, or rhombohedra terminations <200 μm then, should be interpreted as documenting low flow (Turgeon & Lundberg, 2001).

Elongated crystals may show lateral overgrowths (Ce_{lo} in Table 1), in particular when micrite-rich layers are present in flowstones (cf. Frisia, 1996) (Fig. 1C). The formation of this type of elongated columnar calcite has not yet been fully explained. A plausible model of formation would be growth under relatively fast flow, similarly to the open columnar calcite, where intercrystalline spaces are occluded by organic colloidal particles that subsequently become the nucleation sites for micrite (cf. Freydet & Verrecchia, 1999). Freydet & Verrecchia (1999) also documented diagenetic replacement of micrite by elongated calcite crystals with overgrowths in freshwater stromatolites. When “clots” of micrite are observed in sinters (flowstones) consisting of elongated columnar fabric with lateral overgrowths, thus, diagenesis may have occurred. Thus, the interpretation of elongated columnar calcite with lateral overgrowths and relicts of micrite clots may imply diagenesis in flowstone layers, which were once porous and rich in organic particulate. This interpretative model does not disagree with the mechanism of formation of elongated columnar calcite proposed by Kendall (1993), although, it may imply post-depositional changes (Frisia, 1996). In such case, it is expected that some chemical properties were re-set and caution should be taken when interpreting stable isotope ratio values variability (or lack of it) recorded in flowstones consisting of Ce_{lo} associated with relict micrite.

Spherulitic type growth in columnar fabrics: Fascicular Optic, Radial.

These fabrics consist of columnar polycrystals (length to width ratio > 6:1, commonly > 10:1) characterized by undulatory extinction due to the systematic variations of the orientation of the c-axes with respect to the substrate of “fibre-like” individuals that compose each polycrystal. If the c-axes of the crystal units that compose the polycrystal diverge from the centre outward, these are similar to the Fascicular Optic Fibrous Calcite (FOFC) described in Kendall (1985), (Fig. 1D). This fabric can then be labelled Columnar Fascicular Optic (Cfo) and its overall appearance is that of a sector of a spherulite, or a fan, consisting of bundles of elongated crystals bending outward. If the polycrystals possess a pattern of converging fast vibration directions, that is undulatory extinction converge away from the

substrate, then they are similar to radial calcite (Kendall & Tucker, 1973; Kendall and Broughton, 1978; Kendall, 1985). Fabrics consisting of polycrystals showing brush extinction converging away from substrate when the rotating table is turned clockwise should then be labelled Columnar radial fibrous (Cr_f). Both C_{fo} and Cr_f columnar types are characterized by curved cleavage, with upper concave curvature in the case of Cr_f and downward concave curvature in the case of C_{fo}. The extinction characteristics of Radial calcite and Fascicular optic calcite are thoroughly described and illustrated for polycrystals in Neuser & Richter (2007).

These two fabrics are here grouped together because they form through a mechanism typical of spherulitic growth (cf. Sunagawa, 2005). This implies splitting of a crystal into a number of units with slightly diverging lattice orientation. When split growth is systematic, it is manifested as an “extinction brush”, or sweeping (undulatory) extinction on a polarizing microscope. Kendall (1993) proposed that the generation of fascicular optic and radial calcites was related to crystal splitting caused either by high supersaturation or by the presence of ions (or colloids) that poisoned crystal surfaces. The formation of polycrystalline aggregates with spherulitic-type growth has been documented through experimental settings that used organic compounds and Magnesium (Mg) as additives. Magnesium typically affected crystal morphologies by altering the calcite nucleation sites and eventually caused crystal splitting (Meldrum & Hide, 2001).

In stalagmites from St. Michaels Cave in Gibraltar, low-Mg calcite polycrystals with sweeping, fascicular optic type extinction, formed under low drip rates (0.04 to 0.06 litres/day), from parent water with Mg/Ca ratio > 1.5 and SI_{cc} of 0.5 (Mattey et al., 2010). Radial Fibrous Calcites were documented in speleothems sampled in caves cut in dolomitic rocks (Neuser & Richter, 2007), which confirms an important role for Mg in driving the formation of spherulitic-type fabrics. The occurrence of C_{fo} and Cr_f seem to be typical in stalagmites and flowstones whose calcite Mg content is high (cf. Folk & Assereto, 1976), but still within the range of Low-Mg calcite, typically from >10,000 to <30,000 ppm (this study, Fig. 1E). Yet, the boundary conditions that shift the system from one that favours the development of elongated low-Mg calcites, to one that favours that of spherulitic-type fabrics (and finally the precipitation of aragonite) depend on a series of variables factors, including: temperature, the SI_{cc} and Mg/Ca ratio, the carbonate ion concentration and the presence of organic compounds in the parent waters (Meldrum & Hide, 2001). Because all these factors interfere with each other, it becomes difficult to set precise Mg/Ca ratio and SI_{cc} values for cave waters at which the transition from elongated to fascicular optic or radial fabric occur. It is reasonable, however, to infer that Mg/Ca ratio of the parent water needs to exceed 0.35.

In terms of environmental and/or climate significance, an increase in Mg concentration in speleothems is commonly related to dry periods, when drip rate is low, transport of colloid from the soil

should be reduced, Mg, Sr, Ba concentration should increase and δ¹⁸O values of the drips should become more positive (Orland et al., 2014). It is reasonable to assume, then, that C_{fo} or Cr_f are indicative of Prior Calcite Precipitation (PCP) and/or prolonged water-rock interaction (WRI) in dolomitized aquifers during dry episodes. The observation that C_{fo} is common in flowstones from caves cut in dolomite, however, also suggests that flow may influence crystal splitting, as already inferred by Gonzalez et al. (1992). For spherulitic growth, in fact, it is necessary that the growth front receives a continuous supply of “building material” from the solution, in order for the “platelets” originating from a nucleus to keep growing in the fastest direction (Sand et al., 2011). Thus, it is here proposed that the presence of C_{fo} in a speleothem implies an increase in Mg concentration in the parent water and laminar flow. In the case of the stalagmitic flowstone from a Nullarbor cave illustrated in Fig. 1D and E, the highest concentration of magnesium, up to 30,000ppm, is recorded in micrite layers capping the C_{fo} fabric and marking surfaces above which re-nucleation and geometric selection occurred. Hence, it is likely that the C_{fo} fabrics formed only when the speleothem surface was continuously wetted by the regular flow of a thin film of fluid. Under conditions of strong cave breathing in the Nullarbor caves PCP increased the Mg/Ca ratio in the parent waters (Wong et al., 2011). When fluid was not regularly flowing at the surface, than micrite rich in magnesium, rather than C_{fo}, developed.

Overall, the presence of C_{fo} and/or Cr_f indicates that speleothems formed under conditions of at least constant flow, and suggest that cave breathing or ventilation may result in kinetic modifications of the geochemical signals encoded in the two fabrics. From the available literature data, and this study, it is reasonable to assume that the columnar fabrics with spherulitic type growth most likely develop from dripwaters with Mg/Ca ≥ ~0.4 and ≤ ~3 and SI_{cc} ≥ ~0.3 and ≤ ~0.5, that is, higher than those required for the development of elongated, compact or open columnar fabrics.

Columnar Microcrystalline type

The columnar microcrystalline type (C_m in Table 1) has been observed in stalagmites, not in flowstones and distinguished as a distinct type of columnar fabric in specimens from Italian Alpine settings. The C_m fabric is characterized by polycrystals with length to width ratio < 6:1, highly irregular intercrystalline boundaries, uniform extinction, punctuated by inter- and intra-crystalline microporosity (Frisia et al., 2000). The C_m is typical in speleothems showing laminae rich in organic colloidal particles (Fig. 2 A, B) (cf. Frisia et al., 2000). The notable difference with the typical columnar fabric is in the highly irregular crystal boundaries, which developed because of the presence of foreign particles that favoured the formation of crystal defects (see the examples illustrated in Fig. 7.18c in Fairchild & Baker, 2012) visible at the Transmission Electron Microscope (TEM). At the TEM, C_m polycrystals are clearly defect-ridden, with dislocations, lamellae and subgrain boundaries

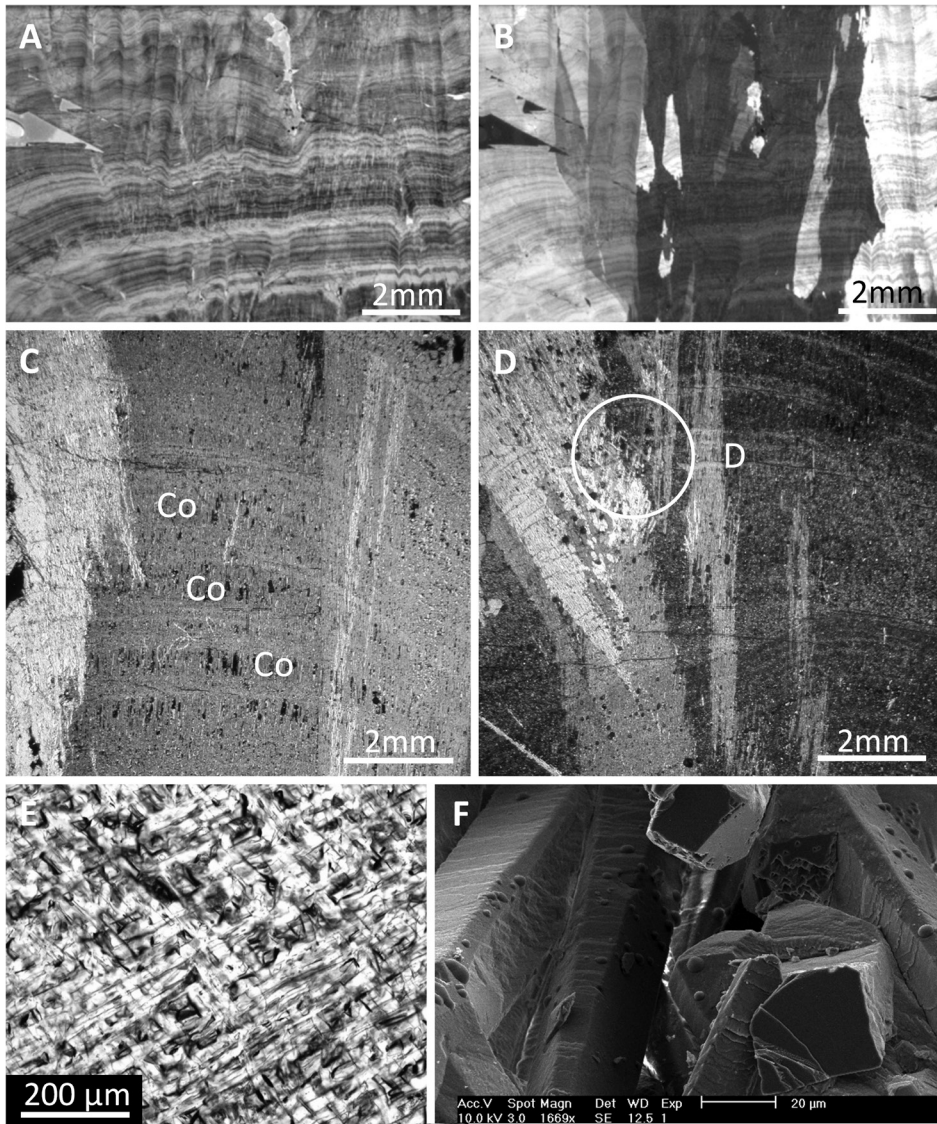


Fig. 2. Microcrystalline, dendritic and associated fabrics. Note how subtle changes in the arrangement of crystals distinguish open columnar, where the single composite crystals are mostly elongated along the c axis, from dendritic, where crystals branch in a scaffold-like texture. A) and B) Microcrystalline fabric at XPL, in a stalagmite from Grotta di Ernesto (N Italy) showing irregular boundaries, porosity, and domains of uniform extinction with irregular boundaries. These domains consist of polycrystalline aggregate. C) and D) Co fabrics at XPL in a stalagmite from Grotta di Carburangeli (S Italy) characterized by strong seasonal contrast in drip rate. In C) the composing crystals are $> 50 \mu\text{m}$ long and single crystals, thus the fabric is not microcrystalline. Crystals do not branch, thus the fabric is not dendritic. D) shows incipient branching crystals with interfingering boundaries. The branching fabric inside the circle can be considered dendritic, because the composing crystals form an angle and show diverse extinction patterns. Nevertheless, the distinction is very subtle and, for the sake of simplicity, the overall fabric can still be classified Co. E) Real dendritic fabric, with scaffold-like morphology clearly visible in PPL in a stalagmite from Tham Doun May, Laos. F) The SEM image of the same specimen highlights the presence of semi-spheres attached to the calcite crystal surfaces, which consist of amorphous SiO_2 , a likely a by-product of microbial metabolism. This observation suggests both hydrologic instability and presence of microbial populations at the stalagmite surfaces as possible necessary component in a genetic model for the development of dendritic fabric.

(Frisia et al., 2000). This results in high intracrystalline microporosity that distinguishes Cm from the Co type, which is characterized by intercrystalline porosity. When comparing Cm and Co in thin section (Fig. 2A-C), the open columnar type shows relatively large, linear pores between each crystals, whereas the microcrystalline type has serrated boundaries, and because of the composite nature of each individual with uniform extinction, some of the “crystallites” of adjacent polycrystals cross-cut each-other, creating areas where the extinction is different from that of cross-cut individual. The presence of intracrystalline

porosity and impurity-rich layers results in the opaque and milky appearance of Cm type in the polished hand specimen with visible “flame-like” polycrystals. Co type is also opaque and milky at the naked eye, but shows regular arrangement of parallel columnar crystals, similar to an open palisade.

The distinction between Co and Cm is useful when logging the microstratigraphy of a speleothem. Although they both form from parent fluid at low supersaturation with respect to calcite (SI_{cc} 0.1 to 0.35, Frisia et al., 2000) and variable drip rate, Cm formation implies input through the feeding system of organic colloids and particulate “in excess” when compared to the conditions of formation of Co. The “foreign” particles form a regular layer at the growing surface when the combination of low degassing and high drip rate results in an undersaturated (or barely at saturation) state for the film of fluid wetting the speleothem. Colloidal particles are most probably adsorbed at defect sites on the rugged surface of calcite crystals, and subsequently incorporated in the speleothem, possibly between single “crystallites” composing any of the polycrystal (see Fig. 5F in Frisia et al., 2000). The adsorption of foreign particles or organic molecules triggers development of crystal defects (Cölfen, 2003) typical of the Cm fabric.

In stalagmites from Alpine settings, the combination of low supersaturation, low degassing and increase in flushing of colloidal particles occurs in autumn, when soil efficiency diminishes because plants become dormant (Frisia et al.,

2005). It is, thus, reasonable to hypothesize that the development of Cm is typical in stalagmites from temperate regions characterized by marked seasonal contrast in temperature, vegetation activity and autumnal rainfall. Its development requires also seasonal changes in cave ventilation, with a less efficient exchange between cave and atmospheric air occurring when the inflow of colloidal particle from the soil is greater. To date, available information about the vegetation cover suggests that Cm forms in Alpine caves developed below mixed conifers and deciduous forest (Frisia et al., 2000).

Dendritic Fabric

The Dendritic (D in Table 1) fabric is composed of branching polycrystals, with each branch consisting of stacked (10.4) rhombohedra. Under the optical microscope, two branches form an angle of ca. 90°, and are inclined of ca. 45° relative to the substrate. This V-shaped aspect of the fabric, which is particularly visible in cross polarized light, distinguishes D from Co, and its overall appearance resembles a scaffold, or warp and waft in a woven cloth, defining rounded to elongated pervasive porosity, rather than series of linear pores as in Co (Fig. 2D). The well-defined, rod-like crystal boundaries, branching into the adjacent crystal and the high intercrystalline, rather than intracrystalline, porosity distinguishes D from Cm. In the hand specimen, D fabric is characterized by milky, opaque appearance due to high intercrystalline porosity, related to the voids between the “warp and waft” which may then be sites where particles, impurities or fluid inclusions are trapped. Figures 2E and F illustrate dendritic fabric characterizing a stalagmite from cave Tam Doun May, in Laos. The dendritic fabric did not develop in all the stalagmites from the cave, but only in those with relatively fast drip, where a portion of the dripwater infiltrated within the speleothems, rather than flowing at their surfaces. Scanning Electron Microscopy observations show that the fabric is indeed very porous, where voids are defined by the arrangements of rods in a scaffold-like structure. The flanks of each rod are characterized by macrosteps that accommodate hemispheric particles. The hemispheres entirely consist of Si, most probably an amorphous phase, and it is reasonable to assume that they are indicative of bio-influenced precipitation (Frisia et al., 2012). Preliminary culture data on swabs taken at the tip of stalagmites in Tam Doun May cave reveal the presence of diverse microbial species, some derived from the soil zone, but others endemic (Evans, pers. comm., 2014). This supports growing evidence for bio-influenced calcium carbonate precipitation in caves (Banks et al., 2010) and suggests that some speleothem fabrics, such as D, may be the result of bio-influenced mineralization. McDermott et al. (1999) documented for the first time the dendritic fabric in stalagmites from Crag Cave, and reported that the layers consisting of D fabric were characterized by more positive $\delta^{13}\text{C}$ values relative to C fabric layers in the same specimen. This phenomenon was attributed to more enhanced CO_2 degassing during D fabric formation. Subsequently, Frisia et al. (2000) documented that the development of D fabrics required variable discharge, and a slightly higher SI_{cc} (up to 0.4) than the C fabrics formed in the same Alpine regional settings. The Tam Doun May D fabric reported in the present study suggests that bio-influenced precipitation should be included in its model of development in addition to degassing and hydrological instability. If microbial influence in carbonate precipitation plays the most important role in the formation of the scaffold-like structure typical of D fabric, then it becomes possible that a stalagmite consisting (or having layer) of D-fabric should not be discarded on the assumption that degassing influences the C isotope ratio. More specifically, if the D fabric is

still porous in a sample, that is, if there has not been syndepositional occlusion of the pores by cementation, than the fabric may preserve geochemical signals that record rainfall and soil efficiency at the time of formation. To test the accuracy of D fabric in recording climate and environmental signal, it is recommended to run a few stable isotope ratio analyses in sectors of the stalagmites to be used for palaeoclimate reconstructions that are characterized by more and less porous D fabrics, and compare the results with C fabrics from the same sample (if present). If the C isotope ratios of D have more negative values than in the compact C, one could infer that kinetic processes did not modify the signal in D. In palaeoclimate studies, the best strategy of sampling when speleothems show D fabric is to compare geochemical time series in two coeval specimens from the same cave with diverse stalagmite morphologies.

Micrite fabric

By micrite fabric (M in Table 1) it is here intended a fabric consisting of crystals whose max dimension is 2 μm , which commonly appears dark in PPL (Fig. 3A) and dark brown in XPL (Fig. 3B). Micrite is one of the most intriguing speleothem fabrics, because the precipitation of micrite in experimental studies commonly requires an exceptionally high number of pre-existing nuclei, high supersaturation and/or the presence of organic compounds (Morse et al., 2003). In seawater, which has a calcite saturation index that greatly exceeds that of cave waters, abiotic formation of micrite appears to require nucleation on “old” sediment and is clearly favoured by organic molecules (Kaźmierczak et al., 1996; Morse et al., 2003). In continental environments, mechanisms of micrite formation in laminar calcretes and tufas implies a biotic intervention, such as precipitation mediated by cyanobacteria (Kaźmierczak et al., 1996; Alonso-Zarza & Wright, 2010). Micrite fabric has been observed associated with bio-influenced calcite moonmilk fibres and in calcareous tufa (Borsato et al., 2000; Frisia & Borsato, 2010). Similarly, micrite fabrics characterizes stromatolite-like structures in speleothems from the Swiss Alps grown under a glacier, where these structures mark periods of glacier retreat, highlighting that micrite is a palaeoglaciological proxy (Luetscher et al., 2011). Stromatolite-like micrite layers were observed in Holocene stalagmites from a mid altitude cave in the Dolomites and in Pliocene stalagmitic flowstones from the Nullarbor, where they coincide with reduction or cessation of the common abiotic speleothem growth processes (Frisia & Borsato, 2010; Frisia et al., 2012). Epifluorescence (UV) observations support the hypothesis that micrite fabric in stromatolitic-like structures is related to organic compounds and, most likely, to microbial laminae (Fig. 3C-D). Studies on Ca-homeostasis of cave bacteria suggest that cave microbes influence the formation of micrite (Banks et al., 2010). Thus, it appears plausible that the presence of micrite fabric is indicative of bio-influenced processes, which has important implications for palaeoclimate studies as micrite layers may be associated with shifts to more

positive values in the C isotope ratios (cf. Kaźmierczak et al., 1996). In the Nullarbor sample illustrated in Fig. 1E, for example, the $\delta^{13}\text{C}$ values shift from -10.5‰ in Cfo to -4.0‰ in stromatolitic-like micrite (M) layers. This phenomenon was interpreted as a possible result of microbial colonization of the speleothem surface during a relatively dry period (Frisia et al., 2012).

Micrite may be also a “destructive” fabric (Cañaveras et al., 2001). Etching, biomechanical “micritization”, and condensation-corrosion may all create micrite

(Cañaveras et al., 2001). Micrite associated with aragonite relicts has been considered a “destructive” fabric, formed through condensation-corrosion (Martín-García et al., 2009; Martín-Pérez et al., 2012). However, aragonite needles in many speleothems are replaced by microsparite ($> 2 \mu\text{m} < 30 \mu\text{m}$), rather than by micrite (Folk & Assereto, 1976; Frisia et al., 2002). Furthermore, in Antro del Corchia cave speleothems, micrite associated with aragonite forms layered “clots” that are not converted to microsparite (Fig. 3E).

Because of the high surface to volume ratio of micrite, one would expect that the small crystals were converted to a microsparite mosaic when aragonite rays were transformed into low-Mg calcite, as observed by Folk & Assereto (1976). It is, therefore, unclear whether micrite fabric is a diagenetic product of condensation-corrosion or a primary fabric. Most probably, micrite associated with stromatolite-like structures is a primary fabric, whereas micrite associated with aragonite can be diagenetic or not. To date, a general model for the genesis of micrite in stalagmites and flowstones does not exist because all occurrences of micrite reported in the literature pertain to fossil specimens. From the analogy with stromatolitic-structures and experimental data, it is plausible to infer that micrite development in speleothems consisting of calcite is favoured by bio-mediation in a regime of relatively low discharge (Frisia et al., 2012).

The diagenetic fabrics: Microsparite and Mosaic calcite

Microsparite (Ms in Table 1) consists of crystals $>2 \mu\text{m}$ and $< 30 \mu\text{m}$ in diameter arranged in a mosaic of anhedral to sub-euhedral crystals. Its origin is still uncertain, but a model for the genesis of microsparite needs to be proposed to assist in the logics behind the construction of a petrographic and microstratigraphic log that bears palaeoclimate significance. Microsparite is inferred to be the product of aggrading neomorphism of micrite (Folk, 1965; Folk & Assereto, 1976). The process of neomorphism implies the *in-situ* transformations of a mineral in itself (replacement of calcite by calcite) or by a polymorph (replacement of aragonite by calcite) (Armenteros,

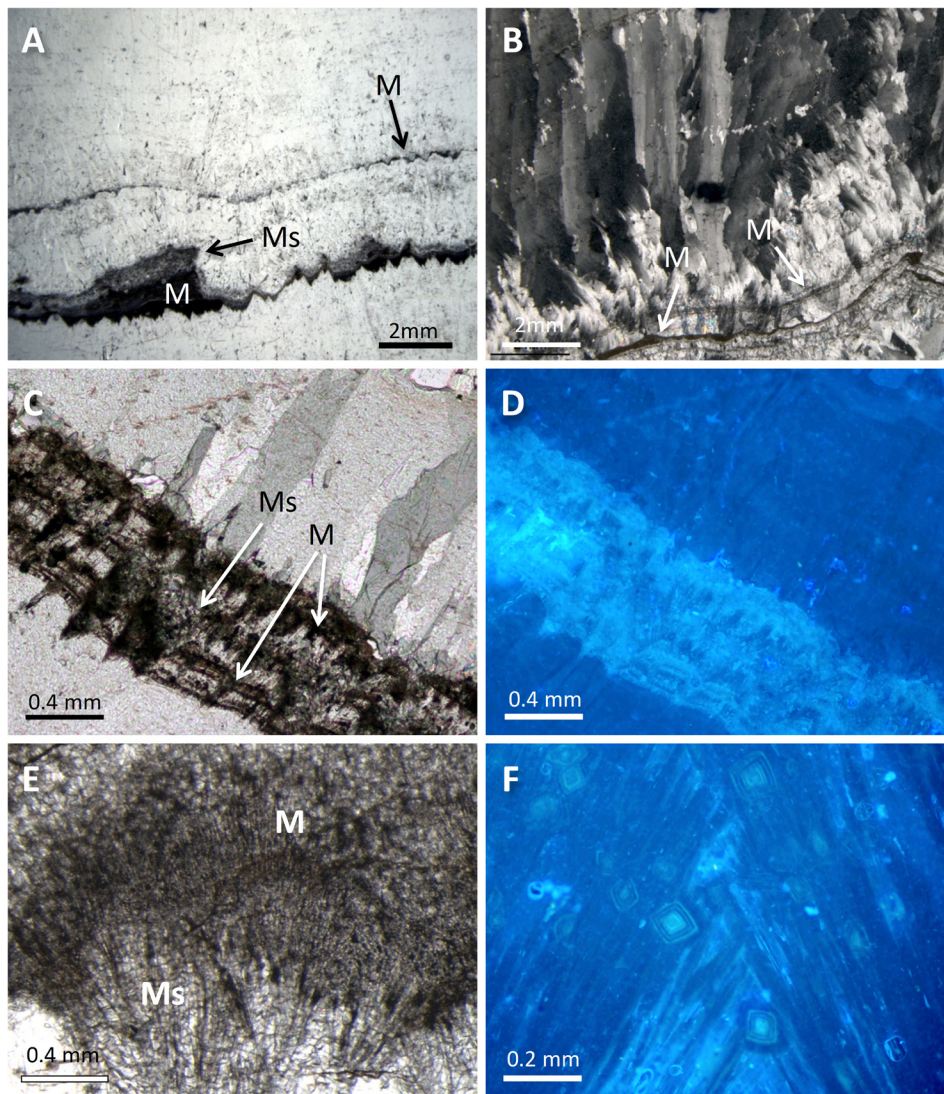


Fig. 3. Micrite and microsparite. A) and B): flowstone from Cave Grotta di Conturines, N Italy. A) Micrite (M) in PPL marking protruding both rhombohedra and flat crystal terminations of columnar fabric. The black arrow shows a thin micrite layer coating crystals with flat terminations, indicative of a very thin film of fluid wetting speleothem top. Ms, microsparite (Ms) aggrades micrite and, most probably, transforms in coarser columnar calcite via diagenesis (ripening). B) Thin micrite layer (white, thin arrow) aggrading into microsparite. Above the microsparite, and partially incorporating it, is an example of columnar calcite with extreme splitting, which induces a “feathery” appearance (the “coconut meat calcite” of Folk & Assereto, 1976) to the crystals when viewed, as in this photo, in XPL. The “feathery” calcite has a relatively high content of Mg, similar to that of the FOC illustrated in Fig. 1D. C and D: Micrite, “stromatolite-like” layer capping columnar crystals in a stalagmite from Cogola di Giizzera, N Italy. C) is viewed in PPL and D) in UV epifluorescence. The micrite layers exhibit fluorescence, which indicates that the fabric incorporates organic compounds. By contrast, microsparite (Ms) and columnar crystals between the micrite layers, do not show fluorescence. The micrite forming stromatolite-like coatings (see Fig. 13 in Frisia and Borsato, 2010) has been interpreted as associated to bio-influenced precipitation (see text for details. E) Micrite associated with aragonite transformation. The aragonite needles are being replaced by a mosaic of microsparite, but micrite has not been aggraded into microsparite. Photo taken in PPL, in a stalagmite from Antro del Corchia Cave, Italy. F) Epifluorescence image of microsparite rhombs grown on aragonite rays in a subaqueous speleothem from Tommy Graham Cave, Nullarbor, Australia. The microsparite rhombs have a fluorescent core and growth bands. This suggests that organic compounds may influence microsparite growth. The microsparite may then act as the trigger for the replacement of aragonite.

2010). Neomorphism is believed to take place through dissolution of the “precursor” on one side of a film of fluid and precipitation of the neomorphic phase on the other side of the film. The replacement of micrite by low Mg-calcite microsparite is most probably a process of aggrading neomorphism (Frisia, 1996). This is driven by the instability of very small crystals with high surface to volume ratio. But in order to occur at the low temperatures under which speleothems commonly form, the crystal size must be very small, which is the case of micrite (cf. Fairchild et al., 1994). Aggradation would occur when a flow of saturated solutions enters in contact with micrite (Fairchild et al., 1994), thus, the replacement of micrite by microsparite should imply a partial (or complete) opening of the system.

Microsparite is commonly observed in association with micrite in stromatolite-like layers within stalagmites (Fig. 3C, D) and in dark, organic-rich laminae (Frisia, 1996). In these cases, organic matter oxidation may have promoted sin-depositional dissolution-re-precipitation, with little consequence on the preservation of original geochemical signals, including the mobilization of U. The Microsparite fabric is also typical as a replacement phase in aragonite needles (Fig. 3E), in the form of mosaics of calcite crystals that mimic single aragonite crystals morphologies (Frisia et al., 2002). In speleothems, the process of neomorphism with replacement of a precursor by calcite microsparite may be favoured when discharge resumes after a dry period, where either aragonite or micrite had previously formed.

The process of microsparitization may also be influenced by the presence of inorganic or organic additives, which may control both the morphology of the precipitates and polymorphism (Sand et al., 2011; Rodriguez-Navarro & Benning, 2013). In speleothem-forming environments, the presence of organic compound and microbes is bound to be ubiquitous, and speleothem formation may not be dictated by sole inorganic processes (cf. De Choudens-Sánchez & González, 2009). For example, in some phreatic speleothems from the Nullarbor, calcite microsparite crystals growing on aragonite needles show at their nuclei UV fluorescence, which also marks growth stages of the rhombohedra (Fig. 3F). It is, thus, reasonable to infer that the development of microsparite is facilitated by the presence of organic compounds. It is plausible to infer that a bio-influenced mechanism favour the mimetic replacement of

speleothem aragonite fabrics into microsparite (cf. Frisia et al., 2002). In summary, it is here proposed that occurrence of microsparite fabric in speleothems is indicative of diagenetic processes and it is suggested to consider Ms as a diagenetic fabric.

The Mosaic fabric (M in Table 1) consists of euhedral to sub-euhedral low-Mg calcite crystals > 30 µm and < 1 cm in diameter, commonly showing triple junctions (angle between faces of three adjacent crystals = 120°). Each crystal in the Ms fabric typically includes ghosts of dark, needles, which are a distinguishing characteristic of calcite replacing aragonite (Frisia et al., 2002; Fairchild & Baker, 2012). The occurrence of Ms fabric has been, to date, mostly related to speleothem aragonite transformed into calcite (Fig. 4 A-C). Mosaic calcite, however, has been reported also as the product of dissolution and reprecipitation of former low-Mg calcite (cf. Fairchild & Baker, 2012). It is unclear, as yet, if mosaic calcite is the final product of neomorphism in a micrite → microsparite → sparite series in continental carbonates (Armenteros, 2010) or a product of dissolution of columnar calcite and re-precipitation of mosaic calcite driven by influx of undersaturated waters causing dissolution of a pre-existing fabric, and reprecipitation of sub-euhedral crystals. The latter case would be expected, as an example, when glacial meltwaters invaded cave systems during deglaciations.

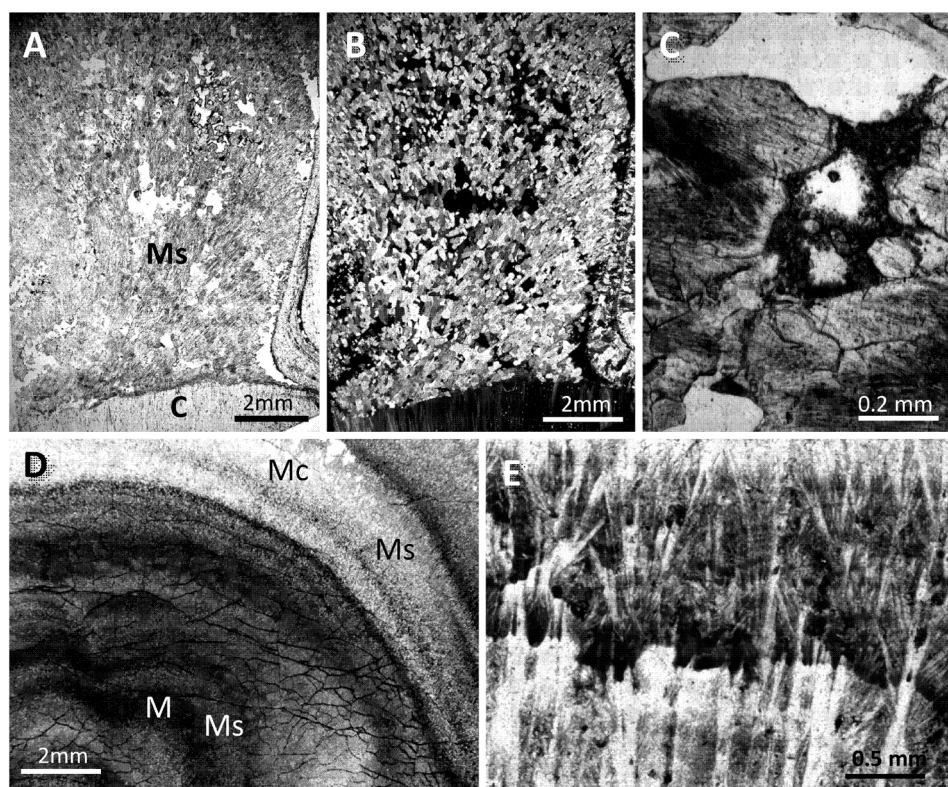


Fig. 4. Diagenetic fabrics and Aragonite. A) Mosaic fabric. General appearance of mosaic calcite (Mc) replacing aragonite. Photo taken in PPL, stalagmite from Liang Luar cave, Flores, Indonesia; B) The same as A but seen at XPL; C) Relic aragonite clearly visible within the subeuhedral to euhedral mosaic of calcite spar, same speleothem as in A and B; D) Micrite (M) associated with aragonite needles in a stalagmite from Antro del Corchia, Italy. Note the dark appearance in PPL of the micrite, due to its fine grained size. Microsparite (Ms) appears lighter, has crystals larger than micrite and replaces aragonite needles, but there is no clear replacement of micrite. The mosaic calcite (Mc) almost completely blurs the original aragonite fabric.; E) Elongated columnar calcite capped by acicular fabric radiating from a micrite layer. The needle-like crystals entirely consist of calcite, although their terminations may appear commonly square. There is no indication that the calcite needles replaced aragonite needles in the form of relic aragonite. Rather, it seems as if the crystals grew constrained by impurity-rich micrite. Flowstone from Grotta di Collalto, Italy, PPL.

Given that most speleothems formed at relatively low temperature, and that microsparite is more stable than micrite, it seems plausible that sparite mosaic is not the product of ripening of microspar (cf. Fairchild et al., 1994). Then, mosaic fabric consisting of sparite, without evidences of former aragonite needles within any euhedral or sub-euhedral individual, should be considered a diagenetic product of dissolution and re-precipitation of any of the primary calcite fabrics, most probably of the most porous, such as dendritic or microcrystalline or columnar open.

Aragonite transformation into Calcite as documented by the diagenetic fabrics

Microsparite and Mosaic calcite are considered, in the present study, diagenetic fabrics, which, in most cases, document aragonite to calcite transformation. Diagenetic mosaic calcite destroys the original aragonite fabrics, be it rays or needles (see Figs. 4C, D), and the preservation of metastable polymorphs “ghosts” (Fig. 4C) depends on the flow (cf. Armenteros, 2010), whereby “diagenetic” fluids may (or may not) be in contact with a “metastable” phase depending on the original porosity. The unequivocal presence of relict aragonite must be identified by X-Ray diffraction (XRD) with a diffractometer or by Electron Backscattered diffraction on a polished section. Quantification of the percentage of relict aragonite within the calcite is recommended to correctly interpret the chemical data.

In some cases, the transformation process preserves, at least partially, the fabric of the precursor aragonite. It is common to observe “transformed” aragonite speleothems characterized by an arrangement of mosaics of calcite crystals outlining columnar aragonite crystals with quadratic terminations (see Kendall & Broughton, 1978). Columnar aragonite crystals are pseudo-hexagonal individuals formed by twinning, and commonly radiate from the substrate forming Rays (Folk & Assereto, 1976; Frisia et al., 2002; Frisia & Borsato, 2010). Replacement has been observed to occur preferentially at crystal defects (Frisia & Wenk, 1985), such as twin planes, and, in this case, transformation results in the partial preservation of the aragonite speleothem fabric (Fig. 4A). Aragonite in speleothems commonly shows acicular or elongated crystals (Railsback et al., 1997; Railsback et al., 2011; Wassenburg et al., 2012), and these morphologies may still be visible after transformation into calcite as illustrated in Fig. 4C and D.

Mimetic replacement is a possible candidate to explain occurrence of highly elongated columnar calcite crystals, very similar to acicular aragonite crystals, as the product of transformation. The case illustrated in Fig. 4E is that of an ancient flowstone, whose age is ca. 120,000 years (unpublished data, analyses performed by John Hellstrom), which formed in Collalto Cave in NE Italy cut in dolomite rock. The age implies the possibility that the flowstone underwent dissolution and re-precipitation when the cave was invaded by glacial meltwater during the deglaciation. Because the host rock is dolomite, it is reasonable to assume that the flowstone may have originally consisted of aragonite. However, petrographic observations

of crystal tips show most common rhombohedra termination, rather than square terminations. In addition, the highly elongated columnar crystals and “needles” consist of single individuals, not of a mosaic of calcite microsparite as would be expected as a product of mimetic transformation. Finally, the crystals do not show any clear evidence, such as micro-inclusions, of the presence of aragonite. Therefore, the fabric illustrated in Fig. 4E is most probably primary, not diagenetic, or should be considered primary in the microstratigraphic log.

It is here suggested to consider the presence of aragonite relicts in speleothem calcite “mimicking” aragonite as the unequivocal evidence for diagenetic transformation. Relicts of former primary or secondary aragonite are less frequent when aragonite is replaced by columnar calcite rather than by mosaic calcite (Perrin et al., 2014), yet relicts of aragonite still attest to the diagenetic origin of columnar calcite encasing them. Samples similar to that illustrated in Fig. 4E consist exclusively of calcite as documented by XRD analyses, whereby an aragonite precursor should not be hypothesized on the basis of morphologic similarity.

To summarize, the presence of acicular fabric or of very elongated columnar individuals is not, by itself, indicative of aragonite transformation. Not even the presence of square terminations is unequivocal. Thus, if in doubt, XRD analyses and Transmission Electron Microscopy observations remain the best options to investigate diagenetic transformations in speleothem fabrics (Frisia et al., 2002; Wassenburg et al., 2012).

CODES AND MICROSTRATIGRAPHIC LOGGING

The microstratigraphic log is constructed by ascribing a progressive code, which is the same as a progressive number, to fabrics observed in thin section, in PPL and XPL, at the optical microscope. For each fabric, an acronym, or symbol, is provided in Table 1 as well as the hierarchic code. The construction of the microstratigraphic log in the basis for the fabric time series, and relies on a logic progression in the coding, from fabrics which are related to the most stable hydrological conditions to those which formed through diagenetic processes. Fabric recognition and coding is a subjective operation, because it relies on a human operator, but, if based on accepted models for fabric development as proposed in Section 2, it has the potential to become a common tool shared by speleothem-based palaeoclimate researchers.

The coding of fabrics proposed here to produce follows that already used by McDermott et al. (1999) and ascribes the lowest numbers to primary fabrics whose accepted model of formation implies relatively constant drips (hydrologic stability), and parent waters characterized by relatively low supersaturation state with respect to calcite and with low concentration of inorganic and/or organic “additives” to the solution. These are the columnar proper (C) and Columnar open (Co) fabrics (Table 1). The highest numbers should then be ascribed to the diagenetic fabrics, such as microsparite (Ms) and mosaic calcite (Mc), because

these indicate opening of the system and re-setting of the original climate signals. The assignment of a code between “end members” then takes into account the whole spectrum of hydrological instability, changes in supersaturation state, input of impurities and bio-influenced precipitation that may be recorded in speleothems through the development of different fabrics. Obviously, if only one fabric constitutes the whole speleothem, then the microstratigraphic logging may have little significance. But when at least two primary fabrics are present, logging is useful, as it may highlight changes in degassing or drip-rate worth mentioning for the correct interpretation of the paleodata (cf. Boch et al., 2011).

The very first step to construct a microstratigraphic log is to obtain a continuous sequence of fabrics. This can be done by cutting the top and bottom of each section at an angle as shown in Fig. 5. Thus, the top of the lower section overlaps with the bottom of the upper section even if there is a minimum loss of material due to sawing. Thin sections should be 30 μm thick, polished and uncoated to allow for successive analyses in epifluorescence, or backscattered electron microscopy, or by LA-ICP-MS. Transmitted light microscopy observations should be carried out at a research microscope with high quality optics, equipped with: a rotating table, an x-y moving stage with micrometer steps, at least 3 objectives (2x, 10x, 40x), analyser and polarizer lenses, a condenser and a camera attached to a PC. If the x-y stage is not available, it is recommended to mark on a clear image of the whole sample (for example a scan at high resolution) specific bounding surfaces (“markers”). Alternatively, one could mark directly on the thin sections increments of 1 or 5 mm from top to bottom (Fig. 5). The operator should bear in mind that it is essential to keep precise track of distances from the top where changes in fabric occur.

To build the microstratigraphic log in a electronic spreadsheet one column is labelled the “distance from top” and a second column “fabric code”, following the progression in coding given in Table 1. It is recommended to perform a first rapid check of the fabrics present in the thin sections before starting the actual microstratigraphic logging. In this first screening, the fabrics are recognized and organized hierarchically in a legend, where each code is assigned to its fabric acronym (Table 1). Then, sequential cells in the “distance from top” column report the spatial increments in mm where a specific fabric is observed,

and the cells in the “fabric code” column report the code ascribed to the fabric.

In Fig. 6 a large thin section is illustrated with its microstratigraphic log overlain to show the correspondence between codes and actual fabrics. From Fig. 6 it becomes evident that coding is a subjective operation, because each observer may privilege one fabric over another where subtle differences are present. Yet, in the thin section shown in Fig. 6, the most important information is the occurrence of compact, open and elongated columnar calcite, and of micrite layers. According to the models of development for each of these fabrics, the stalagmite portion logged in Fig. 6 suggests changes in hydrology through time from constant (compact) to variable (open), with periods when particulate and foreign ions are transported by dripwater to the surface of the speleothem (elongated). The presence of micrite indicates that the system experienced periods of reduced flow, when microbial films could have colonized the speleothem surface. Critically, the fabrics in the speleothem illustrated in Fig. 6 have been found to record rainfall amount variability, and support the $\delta^{18}\text{O}$ interpretation in terms of monsoon intensity changes in the Holocene (Griffiths et al., 2009).

The selection of the spatial resolution of the microstratigraphic log should be optimized for the research question. The highest resolution used to date in a microstratigraphic log was 20 to 50 μm , which was the resolution required to reconstruct hydrological variability in the Younger Dryas from a speleothem portion characterized by very slow growth rate (cf. Belli et al., 2013).

The progression in the coding system proposed in Fig. 6, follows the models of fabric development discussed in section 2 and summarized in Table 1, where 12 calcite fabrics are listed with their respective acronyms. Table 1 also supplies in the “Notes” column, acronyms that supplement the general information encoded in the number.

In any single speleothem, commonly only a few fabrics (three or four) are present. Thus, once the codes are replaced by the acronym for each fabric, the microstratigraphic log will appear as a relatively simple curve that shifts from the fabrics to the left hand side (lower code numbers), which identify relatively “regular” flow of water at low supersaturation and transporting few impurities, to fabrics on the right hand side of the graph, which mark dry events and/or diagenetic processes (higher values).

In the example shown in Fig. 7, there are four columnar calcite types present, and the order is: C, Co, Ce and Cfo. This progressive order follows the criteria provided in section 1, where the lowest code of C indicates development of the stalagmite from waters at low supersaturation state for calcite and little Mg or organic molecules

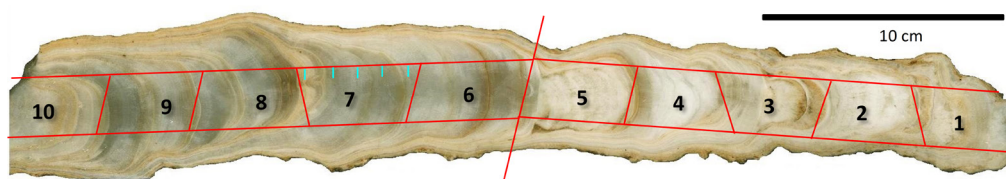


Fig. 5. Suggested sampling strategy to obtain a continuous thin section microstratigraphic sequence. Each section is labelled progressively from the top. A scanned picture of the whole specimen with the outline of the thin section sequence is handy at the microscope to keep constant track of the stratigraphy. It is recommended to mark major features, such as hiatuses, and mark also the thin section outlines each cm. Thus, even if the stage of the microscope is not equipped with an x-y microstage system, it is possible to keep track of the distance from top for each passage of fabric observed in thin sections.

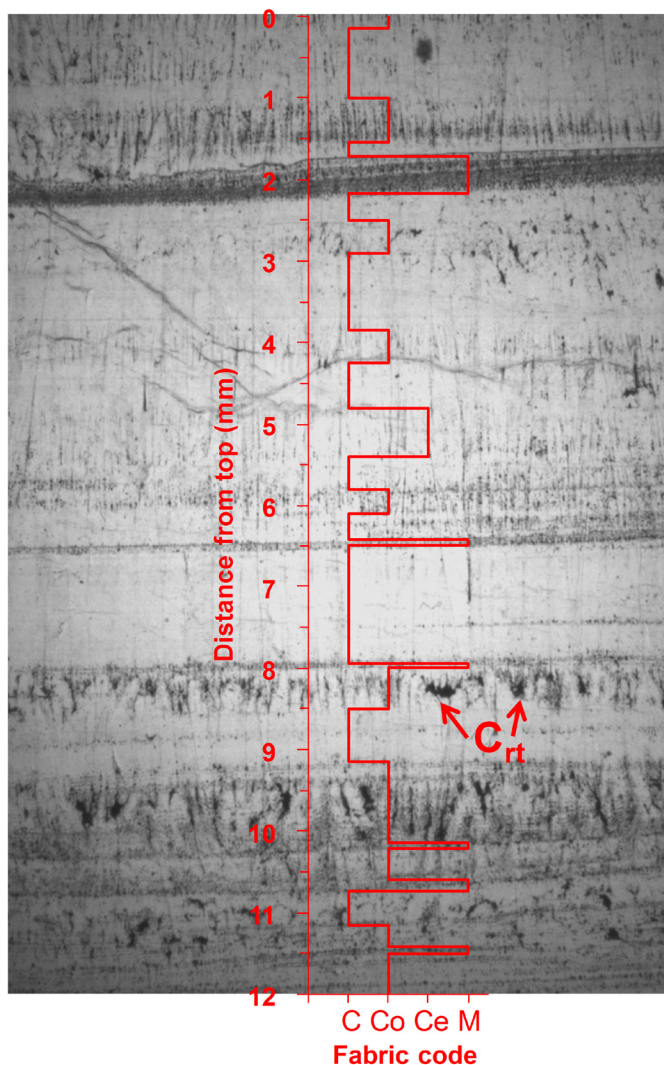


Fig. 6. Microstratigraphic log of a thin section from a stalagmite predominantly consisting of columnar, columnar open and columnar elongated fabrics. A thick micrite layer occurs at 2mm from top. Thinner micrite layers are outlined in the log. Columnar fabric showing rhombohedra terminations is also highlighted by the acronym Crt, but not reported as different fabric in the log (see text for details).

as “additives”, and the highest code for Cfo indicates higher supersaturation and most likely the relatively highest Mg/Ca ratio reached by the feeding drip waters throughout the formation of the specimen. There are other two fabrics, micrite and microsparite, which suggest, respectively, a prolonged period of dryness and aggrading neomorphism. The association of micrite and microsparite in the same layers testifies to the ripening of micrite when its conditions of formation changed, possibly through the recovery of flow. The rationale for constructing the microstratigraphic log of the sample is hierarchizing the fabrics according to the progression provided in Table 1. Then, in the “Fabric code” column of the spreadsheet, depths from top when fabric changes occur are reported. For example: from 0 to 1 mm from top the fabric code is 1, or C, from 1 to 2 mm from top the code is 8 (or M), from 2 to 3 mm from top the code is 9 (or Ms), from 3 to 4 mm from top the code is 8 (M), from 4 to 5 mm from top the code is 1 (or C), ... from 9 to 13 mm the code is 1 (or C) and so on and so forth. Once all the sequence of fabrics from top to bottom has been rendered in numerical form through the codes, and the log constructed, the

numbers are replaced by the fabric acronyms. It is, therefore, important to use the acronyms provided in Table 1 for the speleothem calcite fabrics, so that researchers can compare fabric datasets that use a common reference.

The issue of a common “reference” for transforming fabric changes in a curve becomes critical when fabrics are plotted against geochemical curves. In Fig. 7 it is clear that the shift of C isotope ratio values at ca. 25 cm from top occurs at a layer characterized by M, and the most positive C isotope ratio values in the series pertain to M and Ms. For example, if different speleothem records from the same region show coeval M layers associated with similar shifts to more positive $\delta^{13}\text{C}$ values, then it would be reasonable to infer that the occurrence of M reflects a regional history of hydrological stress when stalagmite tops became almost dry. The sole coeval shift to more positive $\delta^{13}\text{C}$ values without support of the microstratigraphic log would be more equivocal, as the shift could be ascribed to different processes, such as more intense degassing, a change in vegetation or prior calcite precipitation (cf. Fairchild & Baker, 2012).

If hiatuses are present, because they identify depositional gaps, it is here suggested not to code them. Rather, features characterizing the hiatus can be provided as notes or a red line mark a fabric boundary believed to be a hiatus.

BENEFITS OF THE FABRIC LOG IN SPELEOTHEM RESEARCH

The construction of microstratigraphic log of fabrics in speleothems allows for the recognition of changes through time (vertical dimension) of depositional models (or environments of deposition). Changes in the succession of fabrics are here given a simple, graphic form, which allows direct comparison with the series of geochemical data (Fig. 7). In the conceptual framework proposed here, the hierarchy of fabrics is operated through criteria of: a) progressive “hydrological stress”; b) progressive increase in supersaturation state of the dripwater; c) progressive increase in Mg and impurities; d) diagenesis. (Fig. 7)

In the microstratigraphic log a shift to highest fabric codes from bottom to top, then, suggests that a regime of relatively constant drip rate, although with some variability (Co) was punctuated by periods of lower discharge, when dripwaters were characterized by higher Mg concentration (Cfo), up to a point when the supersaturation of the water was very high, or a microbial coating formed (M). The development of Ce following C or Co, according to the proposed model of development, signifies that the supersaturation state and the Mg/Ca ratio of the parent water changes, but not necessarily the drip rate, which should have been relatively constant.

In Fig. 8, the coded fabrics are plotted against their relative stable isotope values to produce the *IsoFab* plot (Isotopes + Fabrics). All columnar fabric types seem to have similar $\delta^{13}\text{C}$ and $\delta^{18}\text{O}$ values, which are more negative with respect to the $\delta^{13}\text{C}$ and $\delta^{18}\text{O}$ of micrite and microsparite. The good correlation

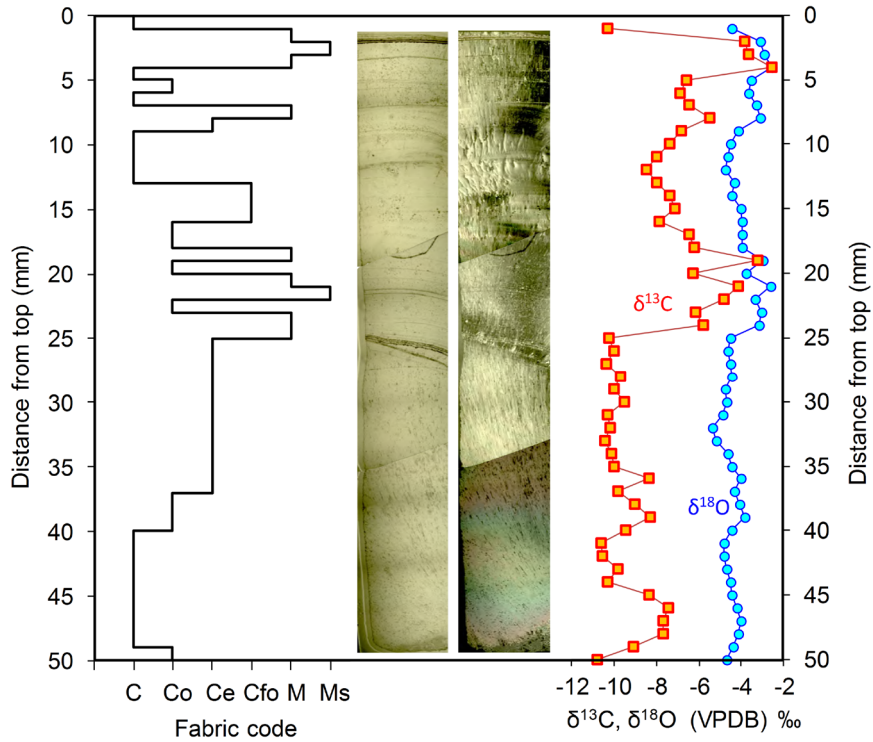


Fig. 7. Microstratigraphic log (left) of the stalagmitic flowstone from Cave 370 in the Nullarbor illustrated in Fig. 1D and E. The log was constructed measuring fabric changes in the sequence of three thin sections shown in the middle (PPL and XPL). To the right, C and O stable isotope ratios profiles are also shown. The microstratigraphic log indicates that layers consisting of micrite (M) and microsparite (Ms) are characterized more positive $\delta^{13}\text{C}$ values. These layers have a stromatolite-like appearance (see text for details) and have been ascribed to relatively dry periods, which would explain the more positive C isotope ratio values. The methods of coding allows for an easy correlation between speleothem fabrics and chemical properties as shown in Fig. 8.

($r^2 = 0.97$) in the inset of Fig. 8, shows that there is progressive kinetic modification from columnar elongated, columnar open, columnar compact, fascicular optic, micrite and, finally, microsparite. The observed correlation is quite intriguing, as it highlights that Ce has the most negative $\delta^{13}\text{C}$ and $\delta^{18}\text{O}$ values.

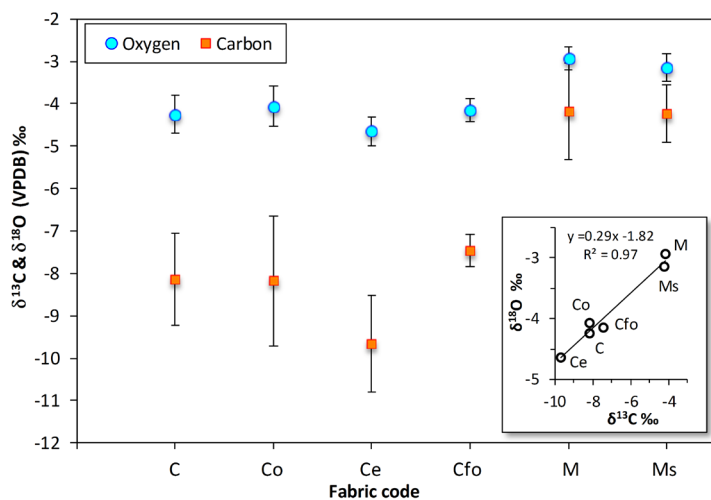


Fig. 8. The *IsoFab* plot compares fabrics (here the fabrics coded in Fig. 7 are reported) and their corresponding mean stable isotope ratios values (plotted with their standard deviation). The correlation plot in the inset shows that columnar fabrics (C, Ce, Cfo, Co) have similar $\delta^{13}\text{C}$ and $\delta^{18}\text{O}$ signatures, with Ce characterized by the most depleted values. Micrite (M) and microsparite (Ms) are enriched in both ^{13}C and ^{18}O . The regression line shows that there is progressive kinetic modification of the isotope signals from columnar calcite to microsparite, possibly due to combined degassing and evaporation.

The content of Mg of Ce calcite in the specimen is up to 20,000 ppm (see Fig. 1E), thus, in the analysed specimen, the high concentration of Mg has no (or little) kinetic effect on stable isotope fractionation. The $\delta^{13}\text{C}$ and $\delta^{18}\text{O}$ values more negative than in C and Co suggest that the drip rate may have been higher during the deposition of the elongated crystals, which opens questions about the provenance of Mg (associated with particulate in addition to incorporation in the lattice) and the significance of the $\delta^{13}\text{C}$ values. The Cainozoic rock hosting the aquifer that fed the speleothem illustrated in Fig. 7 has $\delta^{13}\text{C}$ values as negative as ca. -12‰ (Miller et al., 2012), which hints at the possibility that Ce recorded wetter periods characterized by the efficient (rapid?) dissolution of Mg-rich clasts in the host rock (Frisia et al., 2012).

In synthesis, hierarchizing fabrics, microstratigraphic logging and the construction of a *IsoFab* plot provide information about potential disequilibrium precipitation, with all the implications for stable isotope fractionation and/or trace element partitioning. For example, the *IsoFab* plot for the sample illustrated in Fig. 7 highlighted that C and Co fabrics may be affected by some degassing and evaporation relative to Ce, which modified the C and O isotope ratios.

There is, thus, the potential to use the *IsoFab* plot in conjunction with a correlation between coded fabrics and stable isotope ratio values to act as test for “equilibrium” incorporation similar

to the Hendy test (Hendy, 1971), with the difference that the test proposed here operates on “bulk” fabrics, rather than on the co-variance (or lack of it) of $\delta^{13}\text{C}$ and $\delta^{18}\text{O}$ values along single growth layers.

In addition, the *IsoFab* plot undoubtedly provides an immediate visualization of those changes in stable isotope ratio values that may be related to diagenetic changes, and in particular aggradation, with considerable improvement in palaeoclimate reconstruction from geochemical proxies.

In conclusion, it is here demonstrated that the construction of speleothem microstratigraphic log and of the combined Isotope-Fabric cross correlation diagram (*IsoFab* plot) are indeed necessary tools to provide robustness to the interpretation of the geochemical data. In Appendix 1 a schematic representation of each fabric, name, acronym, code, characteristics and significance are provided to facilitate both the construction of the microstratigraphic log, and the interpretation of fabrics in terms of environment.

ACKNOWLEDGEMENTS

The Author wishes to thank B. Railsback, for his constructive criticism and review, and the suggestion to produce a summary figure to be “hung on petrographers’ wall”. Russell Drysdale and Petra Bajo provided access to thin sections from Antro del Corchia. Russell provided the Tommy Graham and the Liang Luar thin sections, as well as help with mass spectrometry results.

Nullarbor samples were studied within the framework of ARC Discovery Project DP0985214. Bence Paul performed the Mg map of the Nullarbor speleothem from cave 370 with much appreciated precision and skill. Rebeca Martín-García put together the micrographs for Fig. 8. Thanks to Giovanni Gattolin who introduced me to the fascinating issue of the genesis of clotted peloidal micrite and to microbialite fabrics. Kathleen Johnson agreed to show the samples from Tham Doun May, and allowed me to use the SEM micrograph in Fig. 2D.

Christoph Spötl and the project “Speläotheme der Conturines Höle: Ein potentiell einmaliges Paläoumwelt-Archiv in den Dolomiten” are acknowledged for access to speleothems from Conturines cave.

Last, but not least, my profound thank goes to Andrea Borsato, who always supports me, through light and darkness. He also helped with editing the figures.

REFERENCES

Alonso-Zarza A.M. & Wright V., 2010 - *Calcretes*. *Developments in Sedimentology*, **61**: 225-267. [http://dx.doi.org/10.1016/S0070-4571\(09\)06105-6](http://dx.doi.org/10.1016/S0070-4571(09)06105-6)

Armenteros I., 2010 - *Diagenesis of carbonates in continental settings*. *Developments in Sedimentology*, **62**: 61-151. [http://dx.doi.org/10.1016/S0070-4571\(09\)06202-5](http://dx.doi.org/10.1016/S0070-4571(09)06202-5)

Banks E.D., Taylor N.M., Gulley J., Lubbers B.R., Giarrizzo J.G., Bullen H.A., Hoehler T.M. & Barton H.A., 2010 - *Bacterial calcium carbonate precipitation in cave environments: a function of calcium homeostasis*. *Geomicrobiology Journal*, **27**: 444-454 <http://dx.doi.org/10.1080/01490450903485136>

Belli R., Frisia S., Borsato A., Drysdale R., Hellstrom J., Zhao J.X. & Spötl C., 2013 - *Regional climate variability and ecosystem responses to the last deglaciation in the northern hemisphere from stable isotope data and calcite fabrics in two northern Adriatic stalagmites*. *Quaternary Science Reviews*, **72**: 146-158. <http://dx.doi.org/10.1016/j.quascirev.2013.04.014>

Boch R., Spötl C. & Frisia S., 2011 - *Origin and palaeoenvironmental significance of lamination in stalagmites from Katerloch Cave, Austria*. *Sedimentology*, **58**: 508-531. <http://dx.doi.org/10.1111/j.1365-3091.2010.01173.x>

Borsato A., Frisia S., Jones B. & van der Borg K., 2000 - *Calcite moonmilk: crystal morphology and environment of formation in caves in the Italian Alps*. *Journal of Sedimentary Research*, **70**: 1179-1190.

Cañaveras J., Sanchez-Moral S., Soler V. & Saiz-Jimenez C., 2001 - *Microorganisms and microbially induced fabrics in cave walls*. *Geomicrobiological Journal*, **18**.

Cölfen H., 2003 - *Precipitation of carbonates: recent progress in controlled production of complex shapes*. *Current Opinion in Colloid & Interface Science*, **8**: 23-31. [http://dx.doi.org/10.1016/S1359-0294\(03\)00012-8](http://dx.doi.org/10.1016/S1359-0294(03)00012-8)

De Choudens-Sánchez V. & González L.A., 2009 - *Calcite and aragonite precipitation under controlled instantaneous supersaturation: elucidating the role of CaCO_3 saturation state and Mg/Ca ratio on calcium carbonate polymorphism*. *Journal of Sedimentary Research*, **79**: 363-376. <http://dx.doi.org/10.2110/jsr.2009.043>

Fairchild I.J. & Baker A., 2012 - *Speleothem science: from process to past environments*. John Wiley & Sons. Oxford, UK. <http://dx.doi.org/10.1002/9781444361094>

Fairchild I., Bradby L. & Spiro B., 1994 - *Reactive carbonate in glacial systems: a preliminary synthesis of its creation, dissolution and reincarnation*. *International Geological Correlation Project*, **260**: 176-191.

Folk R.L., 1965 - *Some aspects of recrystallization in ancient limestones*. *Society of Economic Paleontologists and Mineralogists, Special Publications*, **13**: 14-48.

Folk R.L. & Assereto R., 1976 - *Comparative fabrics of length-slow and length-fast calcite and calcitized aragonite in a Holocene speleothem, Carlsbad Caverns, New Mexico*. *Journal of Sedimentary Research*, **46**: 486-496. <http://dx.doi.org/10.1306/212F6FCD-2B24-11D7-8648000102C1865D>

Freytet P. & Verrecchia E., 1999 - *Calcitic radial palisadic fabric in freshwater stromatolites: diagenetic and recrystallized feature or physicochemical sinter crust?* *Sedimentary Geology*, **126**: 97-102. [http://dx.doi.org/10.1016/S0037-0738\(99\)00034-2](http://dx.doi.org/10.1016/S0037-0738(99)00034-2)

Frisia S., 1996 - *Petrographic evidences of diagenesis in speleothems: some examples*. *Speleochronos*, **7**: 21-30.

Frisia S. & Borsato A., 2010 - *Chapter 6 Karst*. *Developments in Sedimentology*: **61**: 269-318. [http://dx.doi.org/10.1016/S0070-4571\(09\)06106-8](http://dx.doi.org/10.1016/S0070-4571(09)06106-8)

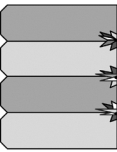
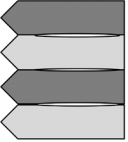
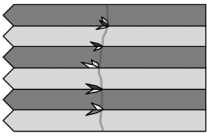
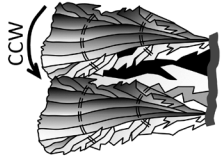
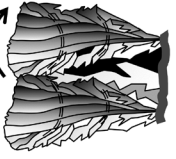

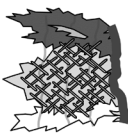
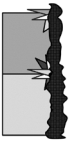

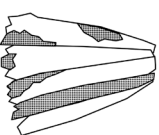


Frisia S. & Wenk H.-R., 1985 - *Replacement of aragonite by calcite in sediments from the San Cassiano Formation (Italy)*. *Journal of Sedimentary Petrology*, **55**: 159-170.

Frisia S., Borsato A., Drysdale R., Paul B., Greig A. & Cotte M., 2012 - *A re-evaluation of the palaeoclimatic significance of Phosphorus variability in speleothems revealed by high-resolution synchrotron micro XRF mapping*. *Climate of the Past*, **8**: 2039-2051.

Frisia S., Borsato A., Fairchild I.J. & McDermott F., 2000 - *Calcite fabrics, growth mechanisms, and environments of formation in speleothems from the Italian Alps and Southwestern Ireland*. *Journal of Sedimentary Research*, **70**: 1183-1196.

- Frisia S., Borsato A., Fairchild I.J., McDermott F. & Selmo E.M., 2002 - *Aragonite-calcite relationships in speleothems (Grotte De Clamouse, France): environment, fabrics, and carbonate geochemistry*. *Journal of Sedimentary Research*, **72**: 687-699.
<http://dx.doi.org/10.1306/020702720687>
- Gonzalez L.A., Carpenter S.J. & Lohmann K.C., 1992 - *Inorganic calcite morphology: roles of fluid chemistry and fluid flow*. *Journal of Sedimentary Petrology*, **62**: 382-399.
- Griffiths M.L., Drysdale R.N., Gagan M.K., Zhao J.-x., Ayliffe L.K., Hellstrom J.C., Hantoro W.S., Frisia S., Feng Y.-x., Cartwright I., St. Pierre E., Fischer M.J. & Suwargadi B.W., 2009 - *Increasing Australian-Indonesian monsoon rainfall linked to early Holocene sea-level rise*. *Nature Geoscience*, **2** (9): 636-639.
<http://dx.doi.org/10.1038/ngeo605>
- Hendy C.H., 1971 - *The isotopic geochemistry of speleothems-I. The calculation of the effects of different modes of formation on the isotopic composition of speleothems and their applicability as palaeoclimatic indicators*. *Geochimica et Cosmochimica Acta*, **35**: 801-824.
[http://dx.doi.org/10.1016/0016-7037\(71\)90127-X](http://dx.doi.org/10.1016/0016-7037(71)90127-X)
- Hoffmann D.L., Spötl C. & Mangini A., 2009 - *Micromill and in situ laser ablation sampling techniques for high spatial resolution MC-ICPMS U-Th dating of carbonates*. *Chemical Geology*, **259**: 253-261.
<http://dx.doi.org/10.1016/j.chemgeo.2008.11.015>
- Kaźmierczak J., Coleman M.L., Gruszczynski M. & Kempe S., 1996 - *Cyanobacterial key to the genesis of micritic and peloidal limestones in ancient seas*. *Acta Palaeontologica Polonica*, **41**: 319-338.
- Kendall A.C., 1993 - *Columnar calcite in speleothems. Discussion*. *Journal of Sedimentary Research*, **63**: 550-553.
<http://dx.doi.org/10.1306/D4267B54-2B26-11D7-8648000102C1865D>
- Kendall A.C. & Broughton P.L., 1978 - *Origin of fabrics in speleothems composed of columnar calcite crystals*. *Journal of Sedimentary Research*, **48**: 519-538.
<http://dx.doi.org/10.1306/212F74C3-2B24-11D7-8648000102C1865D>
- Lachniet M.S., Bernal J.P., Asmerom Y. & Polyak V., 2012 - *Uranium loss and aragonite-calcite age discordance in a calcitized aragonite stalagmite*. *Quaternary Geochronology*, **14**: 26-37.
<http://dx.doi.org/10.1016/j.quageo.2012.08.003>
- Luetscher M., Hoffmann D.L., Frisia S. & Spötl C., 2011 - *Holocene glacier history from alpine speleothems, Milchbach cave, Switzerland*. *Earth and Planetary Science Letters*, **302**: 95-106.
<http://dx.doi.org/10.1016/j.epsl.2010.11.042>
- Martin-García R., Alonso-Zarza A.M. & Martín-Pérez A., 2009 - *Loss of primary texture and geochemical signatures in speleothems due to diagenesis: Evidences from Castañar Cave, Spain*. *Sedimentary Geology*, **221**: 141-149.
<http://dx.doi.org/10.1016/j.sedgeo.2009.09.007>
- Martin-Pérez A., Martín-García R. & Alonso-Zarza A.M., 2012 - *Diagenesis of a drapery speleothem from Castañar Cave: from dissolution to dolomitization*. *International Journal of Speleology*, **41**: 251-266.
<http://dx.doi.org/10.5038/1827-806X.41.2.11>
- McDermott F., Frisia S., Huang Y., Longinelli A., Spiro B., Heaton T.H.E., Hawkesworth C.J., Borsato A., Keppens E., Fairchild I.J., Van der Borg K., Verheyden S. & Selmo E., 1999 - *Holocene climate variability in Europe: Evidence from $\delta^{18}\text{O}$, textural and extension-rate variations in three speleothems*. *Quaternary Science Reviews*, **18**: 1021-1038.
[http://dx.doi.org/10.1016/S0277-3791\(98\)00107-3](http://dx.doi.org/10.1016/S0277-3791(98)00107-3)
- Miller C.R., James N.P. & Bone Y., 2012 - *Prolonged carbonate diagenesis under an evolving late cenozoic climate; Nullarbor Plain, southern Australia*. *Sedimentary Geology*, 261-262: 33-49.
<http://dx.doi.org/10.1016/j.sedgeo.2012.03.002>
- Morse J.W., Gledhill D.K. & Millero F.J., 2003 - *CaCO₃ precipitation kinetics in waters from the great Bahama bank: Implications for the relationship between bank hydrochemistry and whittings*. *Geochimica et Cosmochimica Acta*, **67**: 2819-2826.
[http://dx.doi.org/10.1016/S0016-7037\(03\)00103-0](http://dx.doi.org/10.1016/S0016-7037(03)00103-0)
- Neuser R.D. & Richter D.K., 2007 - *Non-marine radiaxial fibrous calcites—examples of speleothems proved by electron backscatter diffraction*. *Sedimentary Geology*, **194**: 149-154.
<http://dx.doi.org/10.1016/j.sedgeo.2006.05.015>
- Orland I.J., Burstyn Y., Bar-Matthews M., Kozdon R., Ayalon A., Matthews A. & Valley J.W., 2014 - *Seasonal climate signals (1990–2008) in a modern Soreq Cave stalagmite as revealed by high-resolution geochemical analysis*. *Chemical Geology*, **363**: 322-333.
<http://dx.doi.org/10.1016/j.chemgeo.2013.11.011>
- Ortega R., Maire R., Devès G. & Quinif Y., 2005 - *High-resolution mapping of uranium and other trace elements in recrystallized aragonite-calcite speleothems from caves in the Pyrenees (France): Implication for U-series dating*. *Earth and Planetary Science Letters*, **237**: 911-923.
<http://dx.doi.org/10.1016/j.epsl.2005.06.045>
- Railsback L.B., Liang F., Vidal Romani J.R., Grandal-d'Anglade A., Vaqueiro Rodriguez M., Santos Fidalgo L., Fernandez Mosquera D., Cheng H. & Edwards R.L., 2011 - *Petrographic and isotopic evidence for Holocene long-term climate change and shorter-term environmental shifts from a stalagmite from the Serra do Courel of northwestern Spain, and implications for climatic history across Europe and the Mediterranean*. *Palaeogeography, Palaeoclimatology, Palaeoecology*, **305**: 172-184.
<http://dx.doi.org/10.1016/j.palaeo.2011.02.030>
- Railsback L.B., Sheen S.-W., Rafter M.A., Brook G.A. & Keloes C., 1997 - *Diagenetic replacement of aragonite by aragonite in speleothems: criteria for its recognition from Botswana and Madagascar*. *Speleochronos*, **8**: 3-11.
- Rodriguez-Navarro C. & Benning L.G., 2013 - *Control of crystal nucleation and growth by additives*. *Elements*, **9**: 203-209.
- Sand K.K., Rodriguez-Blanco J.D., Makovicky E., Benning L. & Stipp S.L.S., 2011 - *Crystallization of CaCO₃ in water-alcohol mixtures: spherulitic growth, polymorph stabilization, and morphology change*. *Crystal Growth & Design*, **12**: 842-853.
<http://dx.doi.org/10.1021/cg2012342>
- Sunagawa I., 2005 - *Crystals: growth, morphology, & perfection*. Cambridge University Press.
<http://dx.doi.org/10.1017/CBO9780511610349>
- Turgeon S. & Lundberg J., 2001 - *Chronology of discontinuities and petrology of speleothems as paleoclimatic indicators of the Klamath Mountains, Southwest Oregon, USA*. *Carbonates and Evaporites*, **16**: 153-167.
- Wassenburg J.A., Immenhauser A., Richter D.K., Jochum K.P., Fietzke J., Deininger M., Goos M., Scholz D. & Sabaoui A., 2012 - *Climate and cave control on Pleistocene/Holocene calcite-to-aragonite transitions in speleothems from Morocco: Elemental and isotopic evidence*. *Geochimica et Cosmochimica Acta*, **92**: 23-47.
<http://dx.doi.org/10.1016/j.gca.2012.06.002>

Appendix 1

Type	Symbol (code)	Characteristics	Environment of formation
Columnar	C (1)	 /w ratio <6:1; competitive growth at interfaces; straight to serrated boundaries; uniform extinction; common "flat" terminations or protruding rhombohedra terminations (~ 2µm high)	Relatively slow and constant drip, Slcc <0.35; Mg/Ca <0.3; pH up to 8.4; low impurity content
Columnar open	Co (2)	 /w ratio <6:1; competitive growth at interfaces; incomplete coalescence of crystals; high intercrystalline porosity, commonly linear; uniform extinction.	Drip rate > than in C; Slcc up to 0.35; Mg/Ca <0.3; pH 7.5 up to 8.
Columnar elongated	Ce (3)	 /w ratio > 6:1; competitive growth at interfaces; preferential growth of acute rhombohedron; incomplete coalescence of crystals; protruding terminations common; uniform extinction. May show lateral overgrowths, in particular in the presence of impurity-rich layers.	Drip rate constant; Slcc 0.1 to 0.4; Mg/Ca >0.3. Ce ₀ : relatively fast flow; presence of particulate. Diagenesis?
Ce with lateral overgrowth	Ce ₀ (4)	 /w ratio > 6:1; undulatory extinction diverge away from substrate when rotating table is turned CCW; split crystal growth (spherulitic type); downward concave curvature.	
Columnar fascicular optic	Cfo (5)	 /w ratio > 6:1; undulatory extinction converge away from substrate when rotating table turned CW; split crystal growth; upward concave curvature.	Low drip rate or laminar flow, Slcc 0.5; Mg/Ca > 1.5; typical in stalagmites & flowstones formed in caves cut in dolomite
Columnar radialial	Crf (5.5)	 Polycrystals /w < 6:1; irregular intercrystalline boundaries; uniform extinction with "patches" due to cross-cutting by adjacent crystals; high intracrystalline microporosity; typical of laminated speleothems.	Variable drip rate (seasonal); Slcc up to 0.35; Mg/Ca < 0.3; drip/flow carrying colloidal particles.
Columnar micro-crystalline	Cm (6)	 Branching polycrystals; scaffold-like appearance "warp and waft"; irregular intercrystalline boundaries; high intercrystalline porosity.	Variable drip rate; Slcc up to 0.4. Mg/Ca possibly similar to Cm; strong degassing; presence of particulate/ foreign ions. Bio-influenced precipitation
Dendritic	D (7)	 Crystals < 2µm; stromatolitic-like structure; clotted structure. Common geometric selection above micrite layers.	Bio-influenced. Low flow/dry. Condensation/corrosion?
Micrite	M (8)	 /w ratio ~ 1:1; crystal size > 2µm < 30µm; commonly associated with micrite. Fabric-destructive replacement.	Diagenesis. Aggrading neomorphism (micrite to microsparite)
Microsparite	Ms (9)	 /w ratio ~ 1:1; crystal size > 2µm < 30µm; retention of aragonite fabric.	Diagenesis. Mimetic replacement
Replacive microsparite	Ms _{rra} (10)	 /w ratio ~ 1:1; crystal size > 30µm. Fabric destructive.	Diagenesis. If replacing calcite, no relicts of a former unstable phase are visible.
Mosaic calcite	Mc (11)	 /w ratio ~ 1:1; Crystal size > 30µm; Fabric destructive; preserves relicts of aragonite, commonly needles.	Diagenesis. Commonly related to the transformation of speleothem aragonite into calcite

Appendix 1. Summary of calcite speleothem fabrics, their symbols, codes, characteristics and known environmental parameters underpinning their development.



Available online at scholarcommons.usf.edu/ijis

International Journal of Speleology

Official Journal of Union Internationale de Spéléologie



Can XRF scanning of speleothems be used as a non-destructive method to identify paleoflood events in caves?

Martin Finné^{1,2,3*}, Malin Kylander^{3,4}, Meighan Boyd^{1,2,3}, Hanna S. Sundqvist^{1,3}, and Ludvig Löwemark⁵

¹Department of Physical Geography and Quaternary Geology, Stockholm University, 106 91 Stockholm, Sweden

²Navarino Environmental Observatory (NEO), Messina, Greece

³Bolin Centre for Climate Research, Stockholm University

⁴Department of Geological Sciences, Stockholm University, 106 91 Stockholm, Sweden

⁵Department of Geosciences, National Taiwan University, 106 Taipei, Taiwan

Abstract: We have developed a novel, quick and non-destructive method for tracing flood events in caves through the analysis of a stalagmite thick section with an XRF core scanner. The analyzed stalagmite has multiple horizons of fine sediments from past flood events intercalated with areas of cleaner calcite. Flood events detected from the elemental XRF core scanning data show good agreement with the position of flood horizons identified in petrographic thin sections. The geochemical composition of the individual flood layers shows that in certain cases the clay horizons had a distinct geochemical fingerprint suggesting that it may be possible to distinguish individual flood layers based on their geochemistry. This presents the possibility for using flood events as marker horizons to chronologically tie different speleothems in a cave to each other.

Keywords: stalagmite; floods; XRF core scanning; elemental data; Southern Greece

Received 20 May 2014; Revised 26 August 2014; Accepted 28 August 2014

Citation: Finné M., Kylander M., Boyd M., Sundqvist H.S. and Löwemark L., 2014. Can XRF scanning of speleothems be used as a non-destructive method to identify paleoflood events in caves? *International Journal of Speleology*, 44 (1), 17-23. Tampa, FL (USA) ISSN 0392-6672 <http://dx.doi.org/10.5038/1827-806X.44.1.2>

INTRODUCTION

Caves have been, or are, an integral part of the hydrological system in karstic areas. Relict cave systems (abandoned by flowing water) often act as sediment traps, with silts and clays transported in suspension being the most common allogenic deposits (Ford & Willams, 1989). Fine sediments carried into a cave by water mostly accumulate on cave floors. In the Mediterranean realm the allogenic input of e.g. reworked soils is a common phenomenon in karst caves (Lewin & Woodward, 2009). Water entering a relict cave can often be related to flooding, especially in areas where high recharge events occur and the position of the cave is close to the modern water table (Palmer, 1991; Dorale et al., 2005). Traces of cave floods in the form of detrital layers have been recorded in speleothems in a number of caves. For instance, Borsato et al. (2003) found thin veils of silt and clay intercalated with the carbonates of a speleothem found in northern Italy. The usefulness of detrital layers in speleothems as recorders of flooding history has been shown by Dorale et al. (2005) and Dasgupta et al. (2010) by analyzing speleothems from

two North American caves, prompting us to further investigate this field using new methods.

Over the past decade X-ray fluorescence (XRF) core scanning has been increasingly utilized in paleoclimate studies. XRF core scanning has the advantage in that it can provide high-resolution (sub-millimeter) elemental data, as well as radiographic and optical images. This XRF technique requires a minimum of sample preparation - only a flat surface is demanded - and the analysis itself is fast and non-destructive. This method has provided a wealth of data for both marine (e.g., Riethdorf et al., 2013) and lake sediment (e.g., Kylander et al., 2011) sequences. While the analysis of sediment cores is well established, further applications remain to be developed. In theory, all elements with atomic numbers between Al and U can be measured as long as the material has a flat surface. In practice however there are issues that can arise if the matrix is too crystalline, causing diffraction peaks, or if the matrix is dominated by a single element (Croudace et al., 2006). This is the case with speleothems where Ca concentrations overwhelm the signal causing sum peaks in the produced spectra. This makes it difficult

to observe changes in the calcite matrix itself. There are however, some examples of successful applications of XRF scanning to speleothems. These include both micro-XRF analyzes and XRF core scanning to detect variations in trace elements in the calcite matrix (Frisia et al., 2005; Borsato et al., 2007; Dandurand et al., 2011; Cui et al., 2012; Wu et al., 2012). In the case of speleothems that have archived flood layers, the high Ca concentrations of the matrix become an advantage as the contrasting non-calcite signal becomes very easy to locate.

In this paper we investigate whether XRF core scanning can detect layers containing fine sediment particles in a thick section of a stalagmite and thus can be used as a quick, non-destructive method, in the sense that only a cut surface is needed, to detect flooding events in speleothems. We also analyze the geochemical properties of the individual clay horizons to assess the potential for extracting information from these layers.

MATERIAL AND METHODS

Setting and sample description

Kapsia Cave (N37°37', E22°22') is located on the western perimeter of the Mantinea plain in central Peloponnese, southern Greece (Fig. 1). The natural entrance to the cave is located at roughly the same level as the plain floor approximately 20 m SSW of one of the five sinkholes draining the plain (Higgins & Higgins, 1996, see Fig. 1). When surface water inputs exceed the draining capacity of these sinkholes, the Mantinea plain, or parts of the plain, will experience flooding. The sinkholes are typically blocked every 2-3 years, at least for the period 1950-1991, and sometimes water levels are sufficient to flood the cave (Liakopoulos, pers. comm.; Merdenisianos, 2005). The latest major flood affecting the plain and the cave was recorded in 2001 (Rousiotis, pers. comm.). The cave floor is covered by fine, clayey, sediments carried into the cave from the adjacent plain by floodwater. In Kapsia Cave a clear high-water flood mark can be seen on the walls throughout the cave, in areas above this mark clayey sediments are not present indicating that they are mainly transported by water.

Stalagmite GK0901 was collected in 2009. The height of the stalagmite was c. 270 mm and it was conically shaped. Its position at a level similar to the natural entrance increases the likelihood of capturing flooding events in the selected sample (Fig. 1). A one centimeter thick central slab was cut parallel to the growth axis of the stalagmite. Along the growth axis powder for stable isotope analysis (not performed) and U-Th dating was extracted, resulting in cavities.

Clay samples were collected from the floor at three different positions in proximity to the collected stalagmite. Clay samples were dried at room temperature and ground to a fine powder. One clay sample was treated with HCl in order to remove carbonates to investigate the potential effect of precipitated calcite on or in the clay after it was deposited on the cave floor.

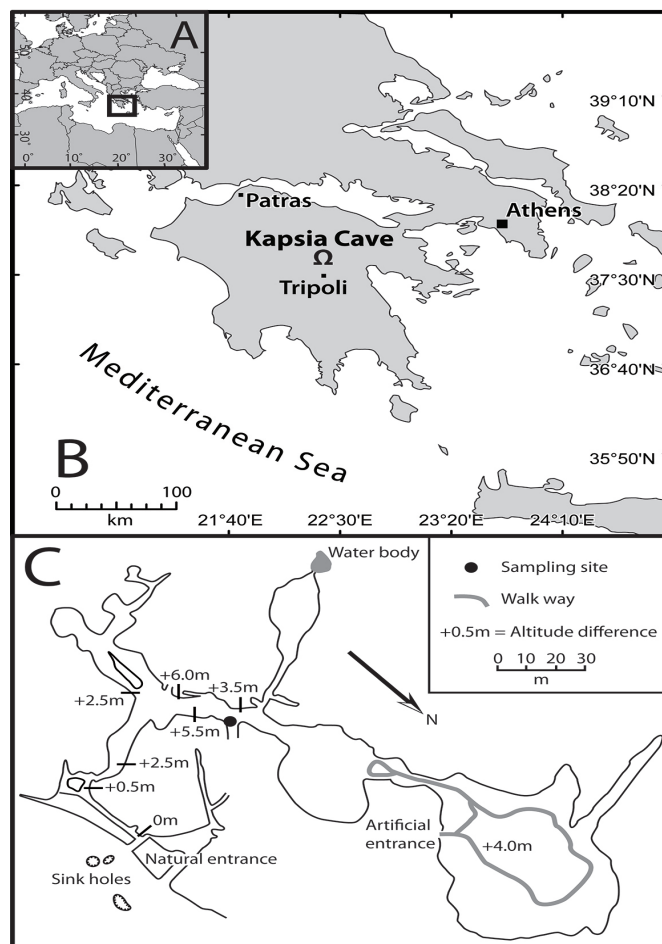


Fig. 1. A. Map A, overview map; B. Map B, location of Kapsia Cave on the Peloponnese; C. Map C, layout of Kapsia Cave. Altitudinal differences in the map are after Merdenisianos (2005). Note that the sampling location is lower than indicated by the nearest altitudinal value as it was collected in an almost vertical tunnel. The sampling location is at a relatively low position in the cave.

U-Th dating

Six samples for U-Th dating were milled at different levels in the stalagmite (Fig. 2). However, low levels of U (<0.378 ppm) and high levels of detrital thorium, as indicated by very low ($^{230}\text{Th}/^{232}\text{Th}$) (<6.90), meant that no reliable U-Th results could be retrieved.

XRF scanning

The polished thick section was scanned using an ITRAX XRF core scanner from Cox Analytical Systems (Gothenburg, Sweden) located at the Department of Geological Sciences, Stockholm University, along the non-uniform central growth axis. A Mo tube set at 30 kV and 30 mA was used and the scanning was made at a step size of 200 μm and an exposure time of 40 s. The scanning produces a digital optical RBG image, a digital radiographic image, and a $\mu\text{-XRF}$ elemental profile. Three separate scans with some overlap were performed in order to produce an accurate trace element profile of the full central growth axis, which has shifted over time (Fig. 2). The three separate sections were pieced together into one series for the whole stalagmite using XRF elemental data for Fe and Ti in the overlapping areas.

Dried clay samples were loaded into open plastic containers, placed on a custom built tray and scanned with the same settings as described above.

Thin sections

Eight petrographic thin sections were produced from the facing side of the scanned surface (Fig. 2). The petrographic thin sections were analyzed for clay horizons under Nikon

Optiphot 2-Pol under x25 and x100 magnification in both plane-polarized light and crossed polarized light. Additionally the thin sections were scanned in 1200 dpi resolution and inspected for clay horizons.

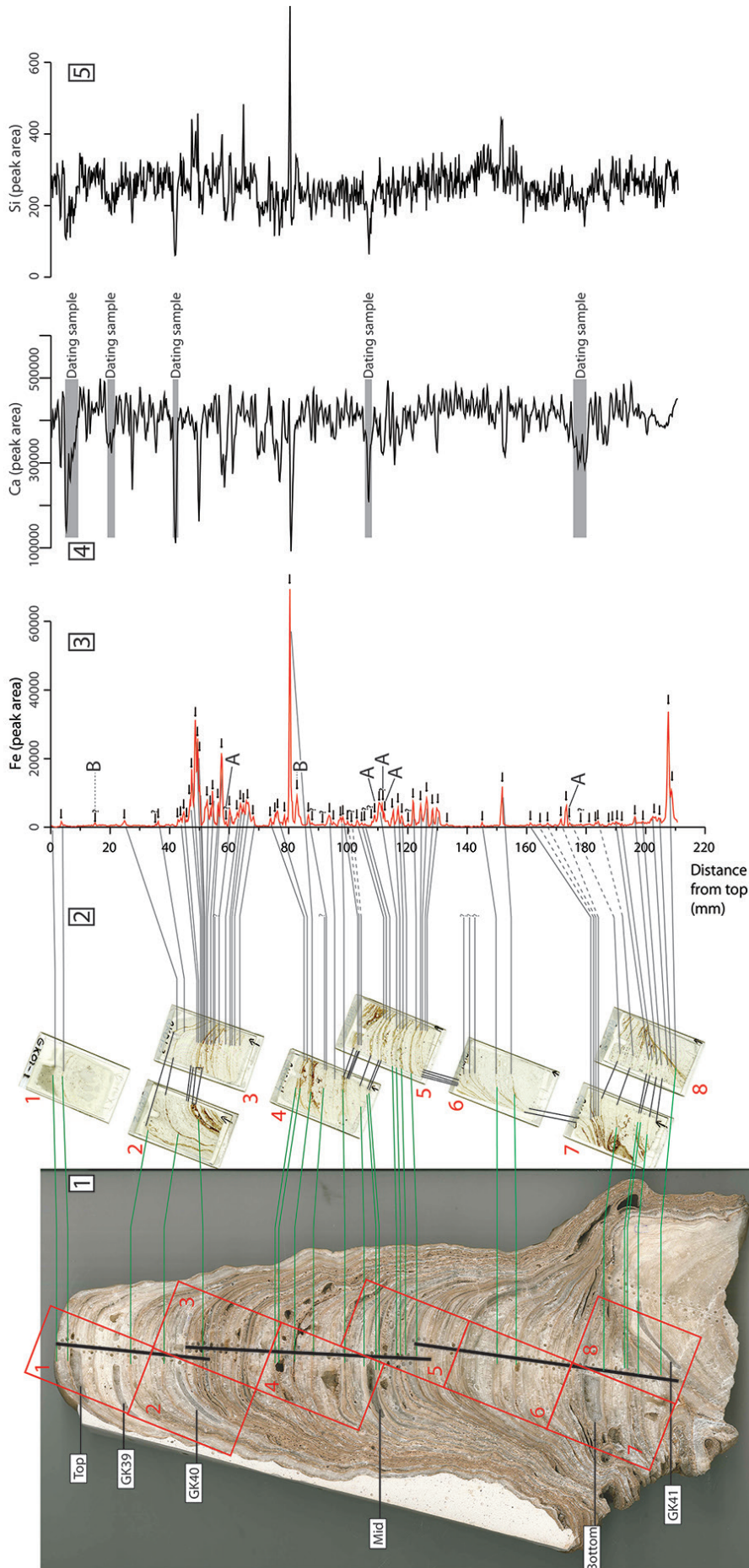


Fig. 2. From left. 1) Photo of thick section of stalagmite (GK0901) with white boxes marking the positions of dating samples, black bars represent approximate position of scanning sections and red squares indicate the position of thin sections (1-8); 2) Thin sections (1-8); 3) Thin sections (1-8); 4) Thin sections (1-8); 5) Thin sections (1-8); 6) Thin sections (1-8); 7) Thin sections (1-8); 8) Thin sections (1-8). Green lines show clay horizons identified in stalagmite and thin section and black lines show interpretation of clay horizons in relation to Fe count from XRF analysis. Black arrows indicate peak areas. Peaks marked with A are examples of peaks interpreted to be overlaying larger peaks, see text for details. Peaks marked with B are recorded in the Fe-signal as peaks but with no flood level identified in the thin sections ("peak no flood"); 4) Ca count from XRF analysis, areas corresponding to dating samples are highlighted by grey bars; 5) Si count from XRF analysis.

RESULTS AND DISCUSSION

Analytical quality

X-ray fluorescence from speleothems gives a strong signal due to their dense nature in comparison to e.g. the lake and marine sediments normally analyzed in the XRF core scanner. The main challenge with analyzing a calcite matrix using XRF core scanning is the generation of Ca sum peaks in the spectra and adjusting the peak fitting during processing to account for this (Brouwer, 2006). Sum peaks are generated when two photons arrive at the detector at the same time and are counted as a single photon. In the case of Ca which has a K_{α} line at 3.69 keV and K_{β} line at 4.01 keV, the sum peaks are generated at 7.38 ($K_{\alpha}+K_{\alpha}$), 7.70 ($K_{\alpha}+K_{\beta}$) and 8.02 ($K_{\beta}+K_{\beta}$) (Fig. 3). Extra lines must be added during peak fitting to account for these sum peaks. The goodness of fit between measured spectra and theoretical spectra during processing is assessed by the mean standard error (MSE). Peak fitting during processing was made in the upper part of the sample which has relatively pure calcite. Therefore the profile of MSE versus depth for the Kapsia speleothem shows the lowest values (i.e. the best fit) in the most pure calcite sections. Increased MSEs are often observed where there is a drop in the counts per second; these decreases are a product of the grooves and gaps produced by the presence of the flood layers (for details see discussion about *washing effect* below) and cavities from sampling. Despite the analytical challenges associated with this type of sample, good counting statistics were acquired for multiple elements including Si, K, Ti, Ca, Fe, Sr, and Zr.

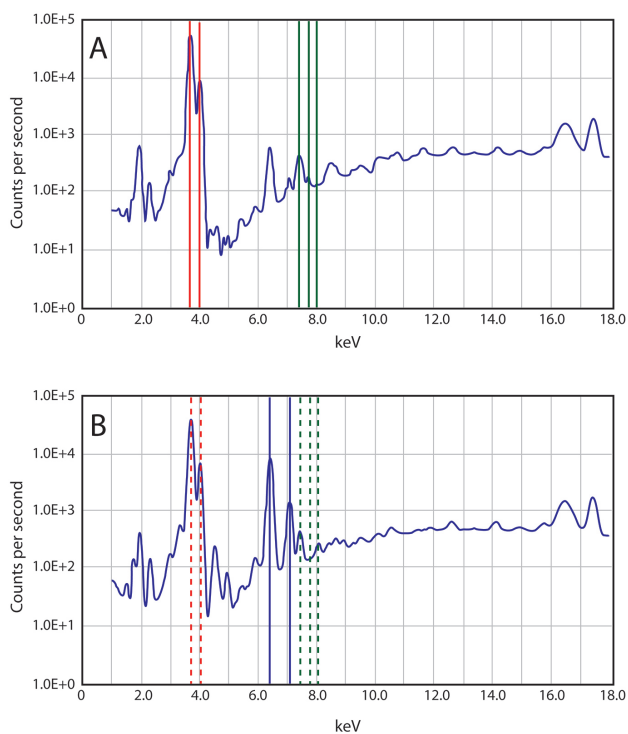


Fig. 3. A. Smoothed XRF spectra from pure calcite showing Ca peaks (indicated by red bars) and Ca sum (green bars) peaks, generated by two photons arriving at the detector simultaneously. Ca lines are located at 3.69 keV (K_{α}) and 4.01 keV (K_{β}) while the Ca sum peaks are found at 7.38 keV ($K_{\alpha}+K_{\alpha}$), 7.70 keV ($K_{\alpha}+K_{\beta}$) and 8.02 keV ($K_{\beta}+K_{\beta}$); B. Smoothed XRF spectra from clay layer showing Fe peaks at 6.39 and 6.40 keV (K_{α}) and 7.06 keV (K_{β}) (blue bars). The two K_{α} are read as one by the detector type used. The Ca signal from the matrix is still detectable indicated by dashed red and green bars (same as in A).

Flood horizons as revealed by XRF scanning and petrographic thin sections

The polished thick section of the stalagmite shows alternating intervals of clean white calcite and thin horizons containing brown sediments (Fig. 2). The sediment horizons are roughly the same color as the clay found on the cave floor. From this fact, together with the knowledge that floods have occurred and drawing on previous research from other caves (Dorale et al., 2005; Dasgupta et al., 2010), we infer that these clayey horizons derive from past floods. Since the stalagmite contains multiple flood horizons of varying thickness it is a highly suitable sample to investigate how well the XRF core scanner can identify flood events and to analyze and compare geochemical properties of individual layers.

The alignment of the three separate scan paths was straightforward as the multiple flood horizons yielded distinct elemental patterns. However, in cases where a scanned specimen does not contain as many flood horizons as the sample studied here, the alignment of separate scans might prove more difficult. This could be overcome by adding artificial marker horizons in the form of e.g. a thin metal wire producing a distinctive signal at two or more levels in the tracks that are to be aligned.

XRF elemental data from the stalagmite thick section show large variability in a number of elements e.g. Fe, Si, Ti, and Ca (Fig. 2). The results from the three cave clay samples show elevated peak area values for e.g. Fe, K, Si, Ti, and Zr compared to the calcite matrix (Fe and Si shown in Fig. 4). Visually clean areas of the stalagmite consisting of mainly white opaque and/or translucent darker calcite show small peak area values of elements associated with clays. In areas where clay horizons are present elevated peak areas of clay elements are recorded while reduced Ca peak areas occur (Fig. 2). Calcium peak areas also decrease in sections where dating samples have been extracted and in places where the XRF beam has passed over cavities in the calcite matrix.

By comparing elemental data from the thick section and the cave clay samples we suggest that Fe and Si are suitable elements to identify flood events in the stalagmite. Both elements are present in lower amounts in the calcite matrix and higher amounts in the clay samples (Fig. 4). We chose to focus on fluctuations in Fe counts from the XRF core scanner as a proxy for flood events because Fe has a strong signal-to-concentration ratio, making it detectable even in small amounts.

From the Fe-signal we identify 3 different peak types: major, medium and minor peaks, based on differences in the strength of the elemental signal (i.e. the magnitude of the peak), along with a base line value representing the calcite matrix. We use the center of each elemental increase, i.e. the highest values in that increase, to define the peak types (Table I).

The Fe peak area versus depth profile shows 81 peaks of variable size along the stalagmite growth axis (Fig. 2). The analysis of the petrographic thin sections revealed 62 clay horizons of variable thicknesses in the Kapsia Cave stalagmite (Fig. 2). There is a good

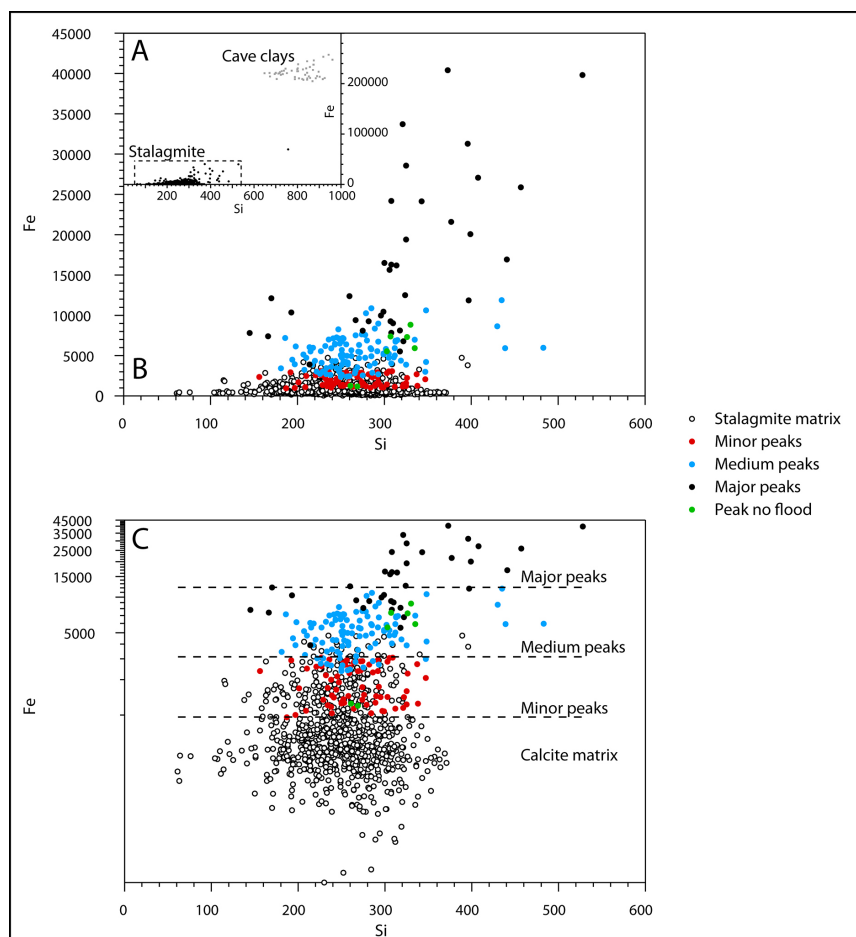


Fig. 4. A. Biplots (Fe vs Si) of stalagmite clays together with stalagmite values (both clayey layers and matrix) showing the difference in the signal between cave clay samples and the stalagmite. The dashed box indicates the area of zoom in B and C; B. Biplots (Fe vs Si) of stalagmite clays and calcite matrix. Revealing a clustering that closely follows the different peak types (major, medium and minor peaks) presented in Table 1. All values in peak areas; C. Biplots (Fe vs Si) of stalagmite clays and calcite matrix same as in B but on a logarithmic y-axis highlighting how close the clustering follows the different identified peak types (major, medium and minor peaks). Intervals, marked by horizontal black bars, follow values in Table 1. It can also be seen that calcite matrix values are distinctly different from the clayey horizons. All values in peak areas.

Table 1. Peak area values defining the different peak types and the speleothem matrix. All values reported in peak areas. *In some instances higher counts on either the increasing or the decreasing side of a peak have been considered to belong to the matrix.

Type	Interval	Average
Major peaks	≥ 12000	17817
Medium peaks	$\geq 3100 < 12000$	5252
Small peaks	$\geq 959 < 3100$	1915
Matrix	$< 959^*$	894

agreement between the position of flood horizons identified in the thin sections and the elemental Fe data with 59 of 81 Fe peaks ascribed to a flood horizon identified in the thin sections.

Discrepancies between the thin section and XRF core scanning methods can be explained by three factors. Firstly, considering the mismatch between total Fe peaks ($n=81$) and Fe peaks ascribed to a flood horizon ($n=59$), we note that several of the Fe peaks (17 of the deviating 22) signaling flood events are actually smaller peaks overlaying a larger peak (as shown for example at those depths marked with A in Fig. 2). These most

likely correspond to a single clay horizon identified in the thin sections or to a generally clayey area. We attribute this to a *washing effect* which sees the loss of clay particles and the creation of a micro-undulating surface, especially in thicker clay layers. The washing effect is related to loss of clay material while cutting the sample using a diamond saw cooled and lubricated by water. The XRF-core scanner integrated a signal across a less cohesive material causing more scattered secondary X-rays to be emitted. The remaining 5 peaks (of the deviating 22) that have not been ascribed to a flood horizon are barely separable from the base line Fe values.

Secondly, there are two instances where there is a Fe-signal peak but no flood level identified in the thin sections (referred to as “peak no flood”), in the interval 82.4 to 83.2 mm from the top and in the interval 14.8 to 15.0 mm from the top (Fig. 2, marked with B). In the former case there are multiple clay horizons in close proximity to the Fe peak, making it difficult to exactly match this peak to a certain flood level. In the latter case it is difficult to find a satisfactory explanation.

Thirdly, the three “missing” clay horizons, i.e. the ones identified in the thin sections but not found in the Fe peak area profile (62-59), are visible in the thin sections around 140 mm from the top but have no counterpart in the XRF elemental signal. There is also one clay layer close to the stalagmite top (at ca. 0.05 cm depth), which is not seen as

a discrete peak in the Fe-signal but rather as a slight increase in Fe peak area. From the thin section analysis it is not evident that these horizons are unusually faint or thin compared to other recorded flood layers. The inability of the core scanner to identify these layers may be related to the geometry of the X-ray beam vs. the not perfectly horizontal clay horizons in the stalagmite. A *bleeding effect* results if the X-ray beam hits a calcite/clay boundary at an angle and therefore records the signal of both layers. Because the width of the detection footprint is about 8 mm wide and 0.2 mm thick, any oblique layers may be “smeared” and almost disappear from the record if they are thin enough.

Geochemical composition of individual clay horizons

In order to investigate the geochemical properties of the individual clay horizons, elemental biplots of Fe vs. Si, two elements with stronger peak areas in both the cave and stalagmite clays, were produced. The biplots reveal a pattern of clusters that to a large extent mirror the previously established peak types (major, medium, minor and “peak no flood”) and matrix values (Fig. 4). There is still a substantial

discrepancy between the geochemical composition of the cave and stalagmite clays. The difference in the strength of the signal between the cave clay samples and stalagmite clays, presumably consisting of the same material, can be attributed to the *washing effect*, or the *bleeding effect*, (both outlined above), or the fact that clay layers in the speleothems most likely are intermixed with calcite crystals creating a different signal. The pure clay samples are also different in terms

We also investigated if the geochemical composition of the flood horizons has been affected by post depositional processes by comparing individual peaks downward along the growth axis, i.e. increasing age (Fig. 5). From this analysis it is not possible to detect any post depositional alteration of the clay layers.

CONCLUSIONS/ RECOMMENDATIONS

XRF scanning can be used to detect banding which is assumed to be related to floods in speleothems if these contain elements that are distinct from the carbonate matrix. XRF scanning of clay samples from the cave gave a good indication of which elements may be used as tracers for floods although more work is needed concerning the discrepancies in geochemical characteristics between cave clays and clay layers in the stalagmite. The results from this study show that petrographic thin sections may not be necessary to identify flood events recorded by speleothems. However, the XRF elemental data are highly sensitive to changes in geochemical composition over very short distances sometimes yielding multiple peaks for one flood horizon as seen in the thin section. Similarly, in areas with many flood horizons in close proximity there may be problems separating discrete peaks from a generally detrital (clay) affected matrix. In both cases petrographic thin sections may be needed to increase the precision in the analysis. Nevertheless, the number of thin sections that are needed will be reduced considerably. Geochemical biplots can be useful tools in defining discrete peaks and give valuable information about changes in the depositional history of the stalagmite. The distinct geochemical composition of the clay horizons presents a potential to use certain levels as marker horizons in defining discrete peaks and offer the possibility to chronologically tie different speleothems in a cave together.

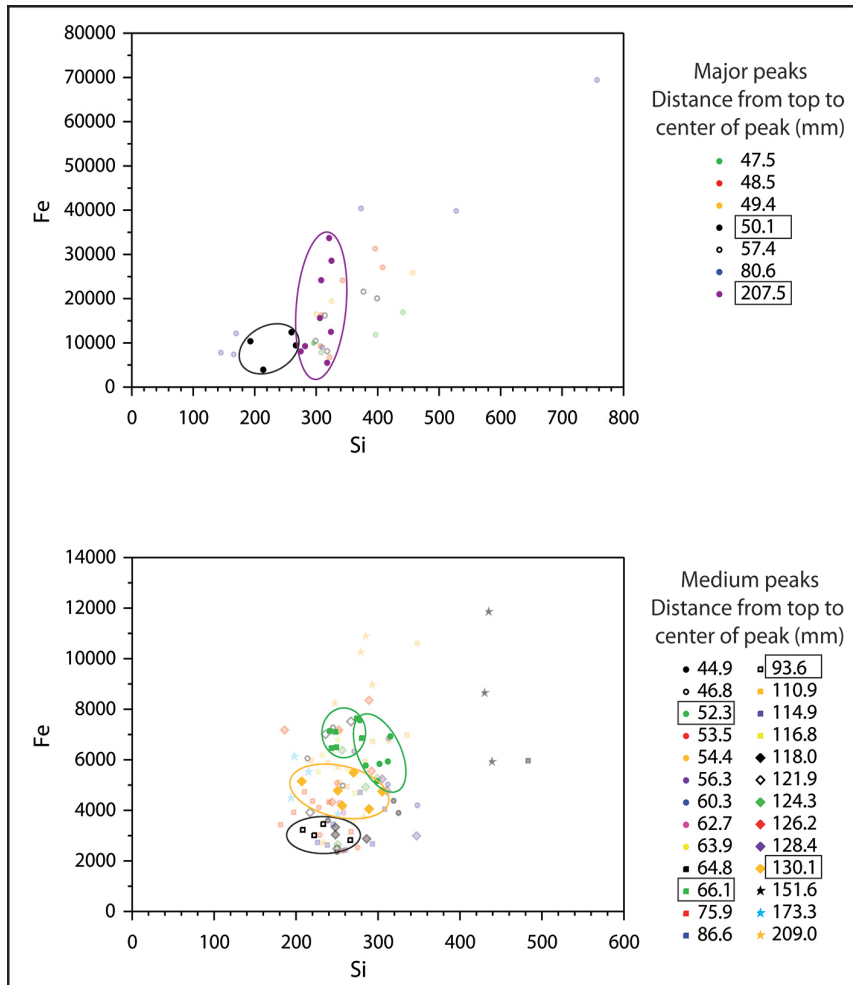


Fig. 5. Individual biplots of individual flood horizons for major peaks (upper plot) and medium peaks (lower plot). Numbers in legends refer to the distance from the top of the center point of the peak. Clustering is evident for some of the individual flood horizons indicating a distinct geochemical signal for instance for peaks at: 50.1 and 207.5 mm in upper plot and at: 52.3, 66.1, 93.6, and 130.1 mm in the lower plot - all enclosed by boxes.

of homogeneity compared to the speleothem. Variations in sedimentation of different fractions of the suspended sediments on the stalagmite compared to the cave floor could also have an effect on the signal.

A closer inspection of the geochemistry of the individual clay horizons in the biplots reveals a distinct geochemical pattern of the separate layers (Fig. 5). This suggests that it is possible to distinguish individual flood layers based on their geochemistry. This presents a possibility for using a geochemically distinct individual flood layer as a *marker horizon* for multiple speleothems from a cave creating a way to chronologically tie them together, much in a similar way as tephra layers may be utilized for sediments (e.g. Lowe, 2011; Kylander et al., 2012). This possibility calls for further investigation of speleothems from the same cave.

Miryam Bar-Matthews is acknowledged for processing the U-Th samples. Dan Zetterberg (Department of Geological Sciences) helped with cutting the stalagmite for thin section preparation. Grigoris Rousiotis provided information on recent floods. Ilias Liakopoulos also organized information from several people in Kapsia Village about historical floods of the cave. We thank Grégory Dandurand and three anonymous reviewers as well as Editor Dr. Bogdan P. Onac for input and comments that improved the manuscript.

REFERENCES

- Borsato A., Frisia S., Fairchild I.J., Somogyi A. & Susini J., 2007 - *Trace element distribution in annual stalagmite laminae mapped by micrometer-resolution X-ray fluorescence: Implications for incorporation of environmentally significant species*. *Geochimica et Cosmochimica Acta*, **71**: 1494-1512.
<http://dx.doi.org/10.1016/j.gca.2006.12.016>
- Borsato A., Quinif Y., Bini A. & Dublyansky Y., 2003 - *Open-system alpine speleothems: implications for U-series dating and paleoclimate reconstructions*. *Studi Trentini di Scienze Naturali, Acta Geologica*, **80**: 71-83.
- Brouwer N.P., 2006 - *Theory of XRF- Getting Acquainted with the Principles*, 2nd ed., PANalytical B.V., Almelo, 71 p.
- Croudace I.W., Rindby A. & Rothwell R.G., 2006 - *ITRAX: description and evaluation of a new multi-function X-ray core scanner*. In: Rothwell R.G. (ed.), *New techniques in sediment core analysis*. *Geological Society Special Publication 267*. London. Geological Society of London: 51-63.
<http://dx.doi.org/10.1144/GSL.SP.2006.267.01.04>
- Cui Y.F., Wang Y.J., Cheng H., Zhao K. & Kong X.G., 2012 - *Isotopic and lithologic variations of one precisely-dated stalagmite across the Medieval/LIA period from Heilong Cave, central China*. *Climate of the Past*, **8**: 1541-1550.
<http://dx.doi.org/10.5194/cp-8-1541-2012>
- Dandurand G., Maire R., Ortega R., Devès G., Lans B., Morel L., Perroux A.-S., Vanara N., Bruxelles L., Jaillet S., Billy I., Martinez P., Ghaleb B. & Valla F., 2011 - *X-ray fluorescence microchemical analysis and autoradiography applied to cave deposits: Speleothems, detrital rhythmites, ice and prehistoric paintings [Analyses microchimiques par fluorescence X et autoradiographie appliquées aux dépôts de grotte : Spéléothèmes, rythmites détritiques, glace et peintures rupestres]*. *Geomorphologie: Relief, Processus, Environnement*, **4**: 407-426.
- Dasgupta S., Saar M.O., Edwards R.L., Shen C.-C., Cheng H. & Alexander E.C., 2010 - *Three thousand years of extreme rainfall events recorded in stalagmites from Spring Valley Caverns, Minnesota*. *Earth and Planetary Science Letters*, **300**: 46-54.
<http://dx.doi.org/10.1016/j.epsl.2010.09.032>
- Dorale J.A., Lepley S.W. & Edwards R.L., 2005 - *The ultimate flood recorder: flood deposited sediments preserved in stalagmites*. *Geophysical Research Abstracts*, **7**: 09901.
- Finné M., Bar-Matthews M., Holmgren K., Sundqvist H. S., Liakopoulos I. & Zhang Q., 2014 - *Speleothem evidence for late Holocene climate variability and floods in Southern Greece*. *Quaternary Research*, **81**: 213-227.
<http://dx.doi.org/10.1016/j.yqres.2013.12.009>
- Ford D.C. & Williams P.W., 1989. *Karst Geomorphology and Hydrology*. Unwin Hyman, London: 601 p.
- Frisia S., Borsato A., Fairchild I.J. & Susini J., 2005 - *Variations in atmospheric sulphate recorded in stalagmites by synchrotron micro-XRF and XANES analyses*. *Earth and Planetary Science Letters*, **235**: 729-740.
- Higgins M.D. & Higgins R.A., 1996 - *A geological companion to Greece and the Aegean*. Duckworth, London, 240 p.
- Kylander M.E., Ampel L., Wohlfarth B. & Veres D., 2011 - *High-resolution X-ray fluorescence core scanning analysis of Les Echets (France) sedimentary sequence: New insights from chemical proxies*. *Journal of Quaternary Science*, **26**: 109-117.
<http://dx.doi.org/10.1002/jqs.1438>
- Kylander M.E., Lind E.M., Wastegård S. & Löwemark L., 2012 - *Recommendations for using XRF core scanning as a tool in tephrochronology*. *Holocene*, **22**: 371-375.
<http://dx.doi.org/10.1177/0959683611423688>
- Lewin J. & Woodward J.C., 2009 - *Karst geomorphology and environmental change*. In: Woodward J.C. (ed), *The physical geography of the Mediterranean*. Oxford: Oxford University Press: 287-317.
- Lowe D.J., 2011 - *Tephrochronology and its application: A review*. *Quaternary Geochronology*, **6**: 107-153.
<http://dx.doi.org/10.1016/j.quageo.2010.08.003>
- Merdenisianos C., 2005 - *The cave of Kapsia at Mantinia and its anthropological findings*. In: *Proceedings of the 14th International Congress of Speleology, Athens-Kalamos, Greece*. Athens: Hellenic Speleological Society: 230-232.
- Palmer A.N., 1991 - *Origin and morphology of limestone caves*. *Geological Society of America Bulletin*, **103**: 1-21.
[http://dx.doi.org/10.1130/0016-7606\(1991\)103<0001:OAMOLC>2.3.CO;2](http://dx.doi.org/10.1130/0016-7606(1991)103<0001:OAMOLC>2.3.CO;2)
- Riethdorf J.-R., Nürnberg D., Max L., Tiedemann R., Gorbarenko S.A. & Malakhov M.I., 2013 - *Millennial-scale variability of marine productivity and terrigenous matter supply in the western Bering Sea over the past 180 kyr*. *Climate of the Past*, **9**: 1345-1373.
<http://dx.doi.org/10.5194/cp-9-1345-2013>
- Wu J.Y., Wang Y.J., Cheng H., Kong X.G. & Liu D.B., 2012 - *Stable isotope and trace element investigation of two contemporaneous annually-laminated stalagmites from northeastern China surrounding the 8.2 ka event*. *Climate of the Past*, **8**: 1497-1507.
<http://dx.doi.org/10.5194/cp-8-1497-2012>



Available online at scholarcommons.usf.edu/ijis

International Journal of Speleology

Official Journal of Union Internationale de Spéléologie



High-resolution digital 3D models of Algar do Penico Chamber: limitations, challenges, and potential

Ivo Silvestre^{1*}, José I. Rodrigues^{1,2}, Mauro Figueiredo^{1,2}, and Cristina Veiga-Pires^{1,3}

¹Centro de Investigação Marinha e Ambiental (CIMA) – Universidade do Algarve, Portugal

²Instituto Superior de Engenharia (ISE) - Universidade do Algarve, Faro, Portugal

³Faculdade de Ciências e Tecnologia (FCT) - Universidade do Algarve, Faro, Portugal

Abstract: The study of karst and its geomorphological structures is important for understanding the relationships between hydrology and climate over geological time. In that context, we conducted a terrestrial laser-scan survey to map geomorphological structures in the karst cave of Algar do Penico in southern Portugal. The point cloud data set obtained was used to generate 3D meshes with different levels of detail, allowing the limitations of mapping capabilities to be explored. In addition to cave mapping, the study focuses on 3D-mesh analysis, including the development of two algorithms for determination of stalactite extremities and contour lines, and on the interactive visualization of 3D meshes on the Web. Data processing and analysis were performed using freely available open-source software. For interactive visualization, we adopted a framework based on Web standards X3D, WebGL, and X3DOM. This solution gives both the general public and researchers access to 3D models and to additional data produced from map tools analyses through a web browser, without the need for plug-ins.

Keywords: karst terrestrial laser scanning; geomorphology; 3D-mesh; Web3D; X3DOM; open-source tools

Received 24 February 2014; Revised 10 August 2014; Accepted 10 September 2014

Citation: Silvestre I., Rodrigues J.I., Figueiredo M. and Veiga-Pires C., 2014. High-resolution digital 3D models of Algar do Penico Chamber: limitations, challenges, and potential. *International Journal of Speleology*, 44 (1), 25-35. Tampa, FL (USA) ISSN 0392-6672
<http://dx.doi.org/10.5038/1827-806X.44.1.3>

INTRODUCTION

The study of karst hydrogeology and geomorphology is important for our understanding of the relationships between the availability and composition of groundwater, climate, and landform evolution (Ford & Williams, 2007). Structures such as speleothems (e.g., stalagmites, stalactites, and flowstones) found in the interiors of caves can be considered as indicators of these relationships because such structures record variation in groundwater and climate through geological time (Fairchild & Baker, 2012). However, the limited accessibility, lack of light, and complexity of caves' interiors makes it difficult to document such features with the desired accuracy and precision. To date, hand-drawn speleological sketches, which are sometimes transferred to 3D rendering software [e.g., *Therion* software; <http://therion.speleo.sk> (Budaj & Mudrák, 2008)], have formed the basis of many topographic and geomorphological studies of karst. However, other scientific domains such as topographic engineering and geomatics are already using laser-based equipment for the rapid acquisition of georeferenced data in remote

and/or complex terrains (Pucci & Marambio, 2009; Roncat et al., 2011).

Accordingly, with the objective of producing a cave map that identifies the main interior speleothem structures for the purposes of palaeoenvironmental reconstruction, we conducted a terrestrial laser-based survey in a limestone cave. However, rather than just obtaining a map, the present study also aimed to expand 3D-mesh analysis, including the development of two algorithms for determination of stalactite extremities and contour lines, and the interactive visualization of 3D meshes on the Web. The chosen cave is known by local speleologists as Algar do Penico or Algar Guedes (Cavaco, pers. comm.), and is located in the Algarve region in southern Portugal. In this paper, we generate 3D-mesh models of the cave by using surface-reconstruction algorithms. These models can be used to study geomorphological structures and are able to be visualized on graphical interfaces. Several different options are presented for rendering models with high levels of detail from the same point cloud data set. For Web visualization, the selected model is simplified using a decimation method that reduces the download time. We adopt a framework

that uses X3D, X3DOM, and WebGL, enabling users to visualize 3D models on a Web browser without plug-ins. We also present an analysis of 3D meshes using two novel map tools, one that detects the extremities of the speleothems and another that returns a collection of contour lines. The results can be visualized superimposed on 3D models on the Web.

THE STUDIED CAVE: ALGAR DO PENICO

The Algar do Penico Cave, also known as Algar Guedes Cave (Cavaco, pers. comm.), is located in a Late Jurassic limestone hill named Cerro da Varjota, to the

west of Loulé city (Algarve). This cave extends about 80 m, has an entrance measuring 14 m, and a depth of about 20 m. It consists of two main chambers connected by a vertical narrow gallery of about 5 m (Fig. 1) (Zabel, 2012). Each chamber was surveyed independently because of the narrow vertical gallery, which does not allow a visual connection to be established between them. However, the work presented in this paper deals only with the main chamber, the deeper and more complex one. The main chamber contains many geomorphological structures, including stalagmites, stalactites, flowstones, and columns (Fig. 2), favouring the quantitative approach taken in this paper.

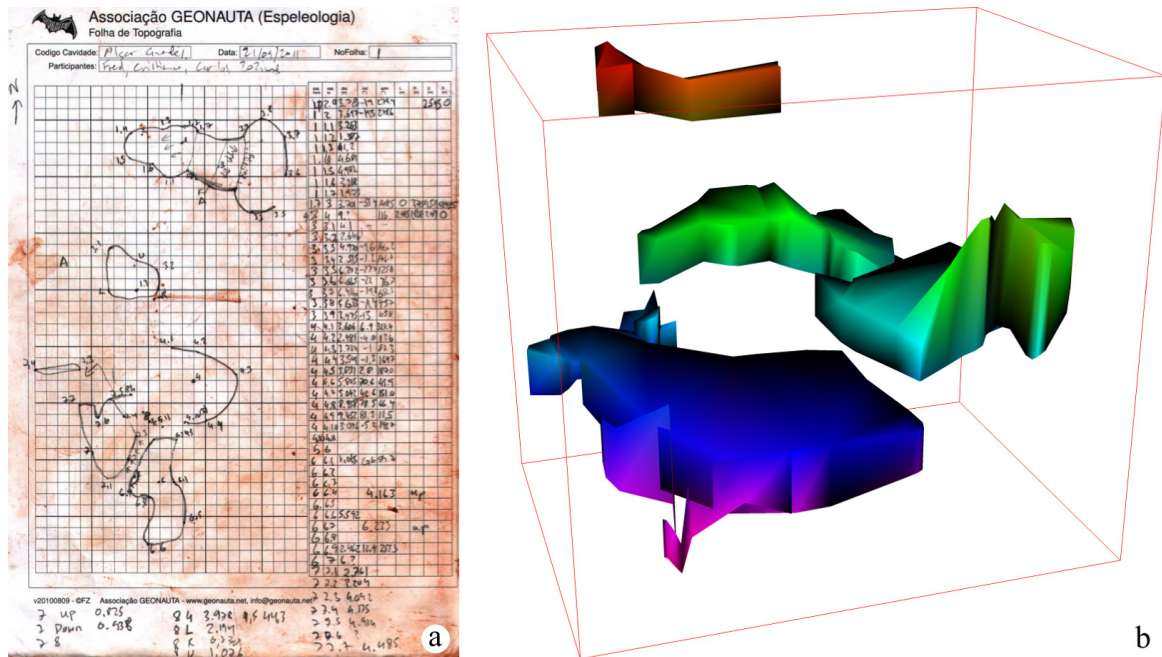


Fig. 1. Topographic information for the studied cave chamber. a) Copy of the notebook sketch based on in situ measurements; b) Digital 3D sketch based on in situ measurement data processed using Therion software (the studied chamber is the lower one) (Zabel, 2012).

DIGITAL SURVEY OF THE CAVE

The purpose of the cave survey was to measure and document the main chamber as well as to create an accurate map of its surface features. Accurate cave surveys provide the basic information to support investigations of cave geomorphology and evolution (Jaillet et al., 2011b). There are several techniques used for cave surveying, including the standard survey technique consisting of azimuth and distance measurements (e.g., Fig. 1), and relatively new techniques, such as photographic and laser-scanning tools. Photogrammetric and laser-scanning techniques markedly improve the efficiency and accuracy of surveys, and allow realistic 3D models to be generated that can better characterize the interiors of caves and their features (Grussenmeyer & Guillemin, 2011; Remondino, 2011).

However, despite the possibility of making 3D reconstructions with photogrammetry, this method is difficult to implement in karst environments due to constraints such as darkness and dampness inside a cave, or even the degree of complexity of surface irregularities. Digital photogrammetry has been successfully used in recording cave paintings rather than documenting entire caves (Tsakiri et al., 2007).

In contrast, laser scanning, and more specifically Terrestrial Laser Scanning (TLS), is a good alternative to traditional surveying approaches because the technique can measure the position and dimensions of objects in 3D space and can be manipulated in dark environments. When applied to cave surveying, laser scanning quickly acquires the shapes of cavities as point clouds (see *Point cloud data set* for definition) with high precision, even if the process of data acquisition in the interior of a cave is a complex task due to the generally difficult access and the irregular and constrained working environment (see Fig. 2a).

Terrestrial laser scanning

Terrestrial laser scanning is a relatively new technology that can be used to conduct high-resolution surveys. TLS may employ three operating measurement principles: time-of-flight, phase-shift and triangulation-based (Beraldin et al., 2011). Terrestrial laser scanners provide detailed and highly accurate 3D data rapidly and efficiently facilitates the rapid acquisition of a huge number of 3D point measurements. One of the great advantages of this surveying method is the high-resolution surface geometry (down to 1 mm) that permits accurate and detailed surface reconstruction

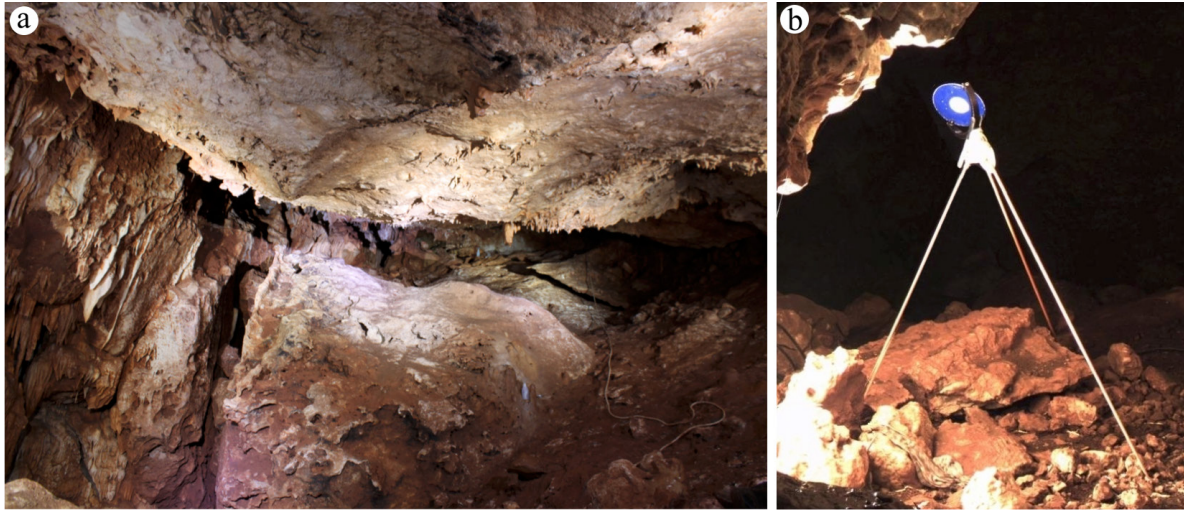


Fig. 2. a) Photographs of the Algar do Penico main cave chamber, showing the complexity and irregularity of the landscape (view towards the west); b) Photography of a target.

and modelling to be performed as well as superior visualization to that of existing measurement technologies (Roncat et al., 2011).

The main chamber of the Algar do Penico Cave was surveyed with a TLS, specifically with a Leica ScanStation C10 time-of-flight laser scanner system mounted on a tripod. The specifications of this unit include a 360° horizontal field of view and a 270° vertical field of view and a modelled surface precision of 2 mm. The scanner emits pulses of green laser light that sweep across the chambers surface and send back spot measurements that provide x , y , and z coordinates in a reference coordinate system given by the scanner, each having an associated intensity value. The output data set resulted from the survey is called point cloud and represent an underlying sampled surface. When the photography acquisition mode is used in addition to the laser beam, colour variables are also captured.

Point cloud data set

First of all, a point cloud is a set of data points in a three dimensional coordinate system that represents the external surface of an object. Accordingly, the laser scanner captures a point cloud corresponding to the true positions of points where the laser pulse hits the studied object. The point cloud represents the shape and position of scanned surfaces relative to the position of the scanner, referred to here as the station. The shape of the chamber has many irregularities and thus it requires different scanner positions to avoid gaps as far as possible. In the present study, the chamber was scanned from three different stations.

The 3D laser scanner point cloud data were collected with a point spacing of 1 cm at a distance of 10 m from the laser-scanning device. This option allowed three point cloud data sets with about 15×10^6 points each to be obtained. The coordinates of points scanned from different stations were in different local coordinate systems. Therefore, a registration process was applied to align individual point clouds into a single Cartesian reference datum. This was achieved through the use of artificial targets scanned during the survey (see Fig. 2b) (Tsakiri et al., 2007).

Six registration targets were placed inside the chamber to establish at least three tie points to register the different local scanner locations into a single point cloud representing the whole chamber (Table 1). It should be noted that only four targets were common between stations St01 and St02 (Tg01, Tg02, Tg05, and Tg06) and between stations St01 and St03 (Tg01, Tg03, Tg04, and Tg05).

Table 1. Statistics for the surveyed targets inside the main chamber, where St is station number, Tg is target number, \bar{i} is the mean intensity of the target, σ_i is the root mean square error of intensity, and # points is the number of scanned points for each target.

St	Tg	\bar{i}	σ_i	# points
01	01	1898	17	7835
	02	1880	17	8343
	03	1912	21	7067
	04	1932	19	8692
	05	1902	20	8301
	06	1913	24	8860
02	01	1917	18	9539
	02	1875	16	7222
	05	1896	19	7652
	06	1914	22	8945
03	01	1860	14	2549
	03	1852	11	1468
	04	1933	20	9591
	05	1870	16	5052

The registration process involved transformations of the original coordinates using mathematical affine transformations in 3D space. This process was performed using a *Python*; <http://www.python.org/>; routine and resulted in a root mean square error (RMSE) of about 3 mm for both pairs of scans.

The registration targets used here were 15.2 cm in diameter and flat with two concentric circles, and were designed to be easily identified (Barbarella & Fiani, 2012). Points obtained from targets present a well-differentiated intensity (i) relative to the chamber surface; a bimodal distribution of i values arises due to the existence of two distinct classes, one with a modal i value of -1298 (for the cave) and another

with a modal i value of +1925 (for the targets). Table 1 presents the average target intensity for points inside the blue disk sector (radius 5.1-15.2 cm, Fig. 2b) with values varying between 1850 and 1933 and with an RMSE σ_i of less than 21.

Targets Tg01 and Tg03 surveyed from station St03 present lower intensity values than do stations St01 and St02, as well as a lower number of collected points (# points) (Table 1). To explain these differences, we inspected the scans of the targets more closely.

Since targets are planar devices, all their scanned points lie on a single plane and the collected coordinates should satisfy the equation $Ax + By + Cz = 1$.

The system of equations for all points of each target can be expressed as a matrix equation:

$$Kw = 1 + \varepsilon \quad (1)$$

where $K_{m \times 3}$ is the matrix of x, y, z coordinates for m target points, w is the vector of plane coefficients, 1 is the m -dimension all-ones vector, and ε is the m -dimension residuals vector:

$$K = \begin{bmatrix} x_1 & y_1 & z_1 \\ x_2 & y_2 & z_2 \\ \vdots & \vdots & \vdots \\ x_m & y_m & z_m \end{bmatrix}, \quad w = \begin{bmatrix} A \\ B \\ C \end{bmatrix}$$

$$u = [1 \ 1 \ \dots \ 1]^T \text{ and } \varepsilon = [\varepsilon_1 \ \varepsilon_2 \ \dots \ \varepsilon_m]^T$$

Equation (1) can be solved using least-square adjustments to estimate w ,

$$w = (K^T K)^{-1} K^T 1$$

The residuals values ε_i correspond to the distance between each point datum and the average plane. They can thus be estimated from Equation (1). The RMSE of residuals calculated using:

$$\text{RMSE} = \sqrt{\frac{(\varepsilon^T \varepsilon)}{n}}$$

was computed and the results are presented in Table 2. Globally, RMSE is ≤ 1 mm, revealing the very high precision of coordinates even for targets Tg01 and Tg03 of station St03.

Let now n be a vector perpendicular to the plane of a target, and consider T the centre of this target, and S the centre of the station, which does not lie on the target plane. In this case, vectors n and ST are collinear when the laser beam hits the centre of the target perpendicularly to the target plane. Accordingly, the computed angle α between vector n and ST represents the angle of the target plane in relation to the laser beam and is equal to 0 when ST is orthogonal to the target plane (Table 2).

Targets Tg01 and Tg03 from station St03 show high values of α ($\approx 54^\circ$ and 65° , respectively; Table 2), which explains the low number of points collected for these targets from station 3. As expected, these high

Table 2. Measurements of target precision expressed as root mean square error (RMSE). $d(St, Tg)$ is the distance between stations and targets, and α is the angle between the laser beam and the target plane.

St	Tg	RMSE (mm)	$d(St, Tg)$ (m)	α (deg)
01	01	0.8	2.6212	34.2733
	02	0.5	4.2555	16.6815
	03	0.4	6.8277	42.5264
	04	0.3	9.2515	15.5800
	05	0.3	6.7266	20.4409
	06	0.4	5.7435	23.0697
02	01	0.5	4.5860	11.3771
	02	0.3	6.7333	28.6347
	05	0.5	4.1489	30.2960
	06	0.7	3.4935	22.6567
03	01	0.3	6.1118	54.3545
	03	0.7	2.8984	64.8606
	04	1.0	2.7055	13.2730
	05	0.2	8.8087	51.4625

values of α reduce the number of laser beam points because of an increase in the lighted area.

However, the average intensity values do not appear to be affected by the angle between laser beam and target plane except when α is greater than about 45° . Accordingly, despite intensity values having been reported to be affected by surface material as well as distance and incidence angle (Voegtler et al., 2008; Kaasalainen et al., 2011), future research is still needed to evaluate the importance of the acquisition angle in order to better understand the intensity parameter and its relationship to the scanned material (Roncat et al., 2011; Krooks et al., 2013).

CAVE CHAMBER 3D MODEL

The laser scanning produced a point cloud of about 45 million points. Point clouds can be directly rendered or inspected and there are a significant number of practical application including, tomography, contouring, data visualization or even data comparing. In general, point clouds themselves are not directly usable in most 3D applications, and therefore they are commonly converted into 3D-mesh surfaces. In the present case study, point clouds do not provide enough information for identifying geomorphological structures, thus a surface model was needed and generated. In the next subsection we present the 3D-mesh generation process.

3D-mesh generation from point cloud

The computational representation of surfaces is a widely studied problem (e.g., see the list of examples in Roncat et al., 2011). Surfaces are usually represented by a collection of vertices, edges, and faces, known as a *polygonal mesh* or *polygonal soup*, defining the shape of a polyhedral object. The faces of the mesh usually consist of triangles or quadrilaterals, where each face corresponds to a set of three vertices or four vertices, respectively (Tobler & Maierhofer, 2006). A triangular 3D-mesh could be compared locally to *Triangular Irregular Network* (TIN) in some surface interpolation.

Several commercial or open-source platforms can create surface models from point clouds. However,

in the present work, we used *MeshLab* software; <http://meshlab.sourceforge.net> (Cignoni et al., 2008), which is a free, open-source software for mesh processing and editing and which generates a triangular 3D-mesh. This software works with the most common 3D file formats, such as PLY, STL, OBJ, 3DS, COLLADA, PTX, PTS, XYZ, ASC, X3D, and VRML. Several algorithms

available in MeshLab can be used to reconstruct surfaces from point clouds. We explored two of them for possible use in this study, namely, the *Ball-Pivoting Algorithm* (BPA) and *Poisson Surface Reconstruction* (PSR) (see Fig. 3).

The BPA computes a triangular mesh to interpolate a given point cloud using a ball of fixed radius that

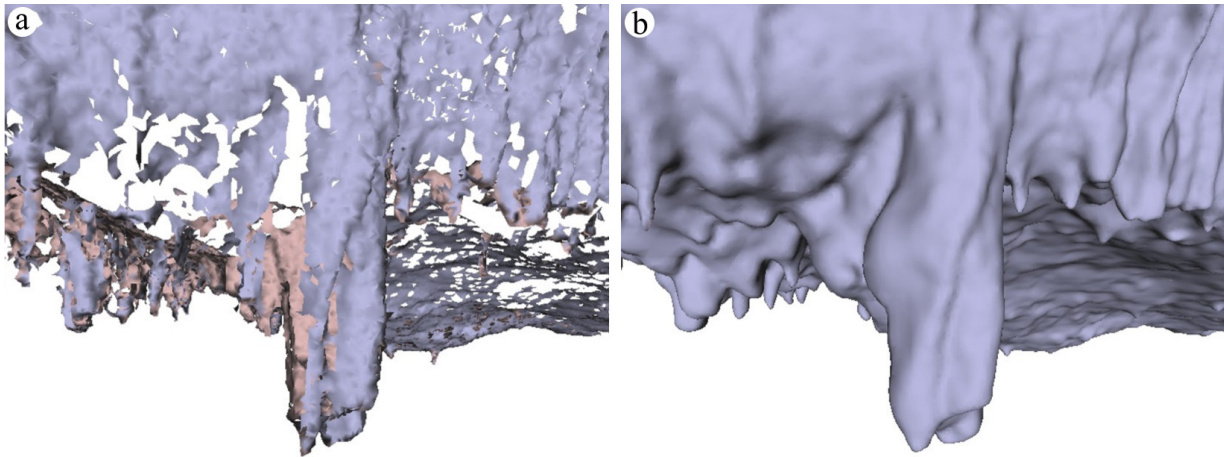


Fig. 3. Example extracted from cave 3D meshes generated with (a) the Ball - Pivoting Algorithm and (b) Poisson Surface Reconstruction.

traverses the point cloud by pivoting front edges and attaching triangles to the mesh (Bernardini et al., 1999). In the present case, this algorithm resulted in a mesh with a large number of face gaps (Fig. 3a). This problem may occur in laser scan surveys due to problems with visibility and/or complexity (Chalmovianský & Jüttler, 2003). One way to reduce the number of these holes would have been to increase the number of stations of the laser scan during the survey. However, due to the physical characteristics of the cave chamber, such a solution would have been very difficult to implement.

Unlike the BPA, PSR requires oriented vertex normals as input data. These normals can be computed as equivalent to a normalized average of the surface normals to the faces containing that vertex (Glassner, 1994). The vertex normals allow the orientations of the faces to be determined.

PSR is based on the observation that the normal field of the boundary of a solid can be interpreted as the gradient of the solid's indicator function. Therefore, given a set of oriented points sampling the boundary of a solid, a 3D-mesh can be obtained by transforming the

oriented point samples into a continuous vector field in 3D. This is performed by finding a scalar function whose gradients best match the vector field and then extracting the appropriate isosurface (Kazhdan et al., 2006). Although a thorough analysis of this algorithm is beyond the scope of this paper, it is worth noting that the vertices of the faces of these meshes do not coincide with the points of the survey.

As shown in Fig. 3, PSR (Fig. 3b) copes much better with missing data than does the BPA (Fig. 3a), and therefore we used PSR for the cave chamber model reconstruction (presented below).

3D-mesh selection

To create a 3D-mesh that best represented the input point cloud of the cave chamber, we tested different input parameters used for the PSR method. Two examples of point clouds were used (Table 3), namely, the whole cave survey, with approximately 45 million points (referenced as *Full cave* in Table 3), and a sample of it containing some interesting stalactites, with around 230 thousand points (referenced as *Stalactites* in Table 3).

Table 3. Examples of parameter variation (number of faces and PLY file size in MB) in 3D meshes generated from a point cloud containing several interesting stalactites (233940 point cloud input data) and from the whole cave survey (44399724 point cloud input data) for octree depth values ranging between 10 and 14 and samples per node (spn) of 1 and 10^3 .

3D-mesh	# faces		file size (mb)	
	Stalactites	Full cave	Stalactites	Full cave
10 depth, 1 spn	541816	2623790	26.5	132.4
10 depth, 10-3 spn	846928	2658050	41.8	134.2
11 depth, 1 spn	550168	10038522	26.9	525.4
11 depth, 10-3 spn	869730	10549762	43.0	552.5
12 depth, 1 spn	555128	31531448	27.1	1700.0
12 depth, 10-3 spn	875334	36680494	43.2	1988.1
13 depth, 1 spn	573190	58042828	28.9	3190.8
13 depth, 10-3 spn	893608	*	44.2	*
14 depth, 1 spn	637718	*	31.3	*
14 depth, 10-3 spn	960294	*	47.5	*

The surface obtained with PSR has a variable level of detail depending on the input parameters *octree depth* and *samples per node*. Accordingly, we generated 3D meshes with octree depth values varying from 10 to 14 and samples per node varying from 1 to 10^{-3} (Table 3). Samples per node is usually presented in the literature as the minimum number of sample points that should fall within an octree node as the octree construction is adapted to sampling density. For noise-free data, a value between 1.0 and 5.0 should be used and for noisy data between 15.0 and 20.0. However, this parameter is implemented in MeshLab as a floating variable, suggesting that other values than integers may be considered. In our study, due to the irregularity of the surfaces, we explored extreme values, and for this reason we used values from 1 to 10^{-3} .

The octree depth parameter is the maximum depth of the tree that is used for the surface reconstruction. An increase in the depth increases the detail of the surface. For octree depths ranging between 10 and 12, the number of faces increases by only 3% for the stalactite data set, whereas for the full point cloud it increases by 92%. It should be noted that it was not possible to generate a 3D-mesh with an octree depth of 14 for the full point cloud acquired from the TLS survey due to computational capacity. We used an Intel Core i7 processor running at 3.40 GHz with 8 GB of RAM and a NVIDIA Quadro 4000 graphics card (with 2 GB of dedicated memory), running the MeshLab software under the 64-bit Ubuntu 12.04 LTS version, a Linux-based computer operating system.

The samples per node parameter is related to the sample points that should fall within an octree node, because the octree construction is adapted to sampling density (Kazhdan et al., 2006). This value is provided by the user and depends on the noise of the samples. When the value of samples per node is decreased, the surface is represented with more detail, increasing the number of faces and the size of the file stored in PLY format (Table 3).

For the identification of small geomorphological structures, such as those presented in Fig. 4, the 3D-mesh is generated only for a specific area, thus allowing the processing of a model with an octree depth of 14 and 10^{-3} samples per node. We verified that for the mesh generated with an octree depth of 14 and 1 sample per node, only 30% of the structures appear in the 3D model. For the mesh generated with an octree depth of 14 and 10^{-3} samples per node,

more than 50% of the smaller structures appear in the 3D model. We also measured the size of several structures and concluded that the mesh generated with an octree depth of 14 and 10^{-3} samples per node was the 3D model that better represented the physical characteristics of small structures such as those shown in Fig. 4.

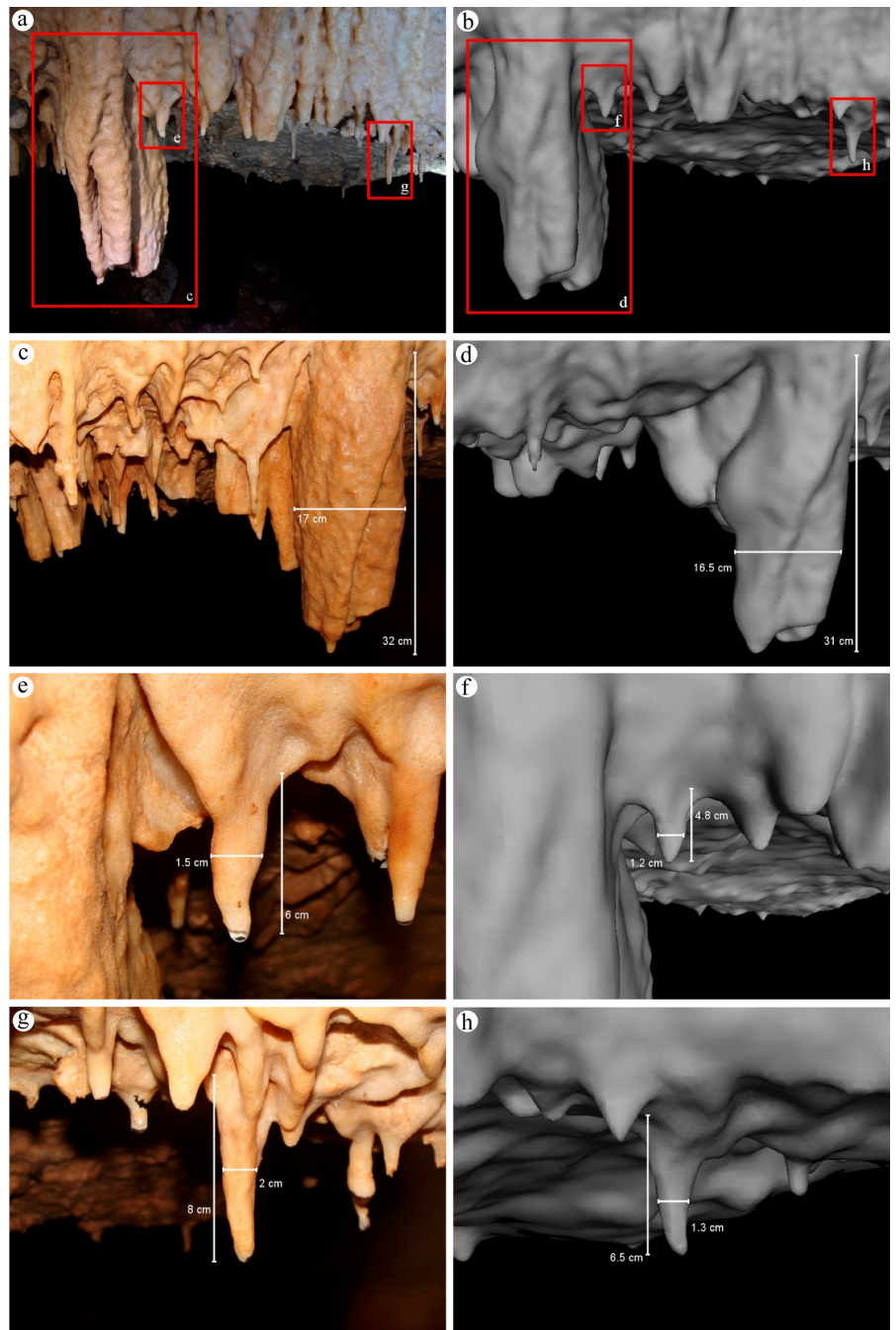


Fig. 4. Comparisons of feature measurements between photographs of actual structures (left-hand images: a, c, e, g) and the generated 3D-mesh with an octree depth of 14 and 10^{-3} samples per node (right-hand images: b, d, f, h). Note the measurements of the structures made either directly in the cave or in the 3D model.

3D data visualization on the Web

As a consequence of advances in both computer hardware and internet connection speeds, Web 3D sites that include 3D models where users navigate and interact through a 3D graphical interface are being increasingly employed in different domains. The possibility of making 3D data available on the Web is of particular interest in the geospatial field. Such availability provides researchers with the opportunity

to visualize, navigate, and interact with 3D data on a simple Web browser. Therefore, we aimed to map and visualize online geomorphological structures of the cave interior in an interactive way. It is now possible to integrate 3D content on the Web directly into the browser without plug-ins or additional components. This is the approach presented in this paper in which X3D, WebGL, and X3DOM were used to enable 3D visualization and navigation of the interior of the Algar do Penico cave in several different Web browsers. X3D is used to represent the cave chamber 3D model and is inserted on the user side for visualization in WebGL-supported browsers with the X3D document object model (X3DOM) technique. This is possible because: (i) X3D is the ISO standard XML-based file format for representing 3D computer graphics (Behr et al., 2009); (ii) WebGL is an open standard software library for a low-level 3D graphics API based on OpenGL that generates interactive 2D and 3D graphics on any browser without installing additional plug-ins (Behr et al., 2009; Prieto et al., 2012); and (iii) X3DOM is

an open-source framework that integrates HTML5 and X3D on top of WebGL (Behr et al., 2009). Thus, X3DOM manipulates X3D scenes as HTML5-DOM elements, rendered via WebGL with no plug-in required, to display the X3D content.

However, the 3D-mesh size is a problem for the efficiency and interactivity of visualization in real time on the Web. As mentioned above, the 3D-mesh generated with the PSR method with an octree depth of 11 and 1 sample per node for the entire cave chamber has about 10 million faces (Table 3 and Fig. 5a). A compromise has to be achieved between the complexity of the 3D-mesh, the realistic visualization of the chamber, and real-time interaction (Fig. 5). Accordingly, to produce a lighter model for visualization on a Web browser, we decided to simplify the cave chamber 3D-mesh by applying geometry removal operations. These operations are referred to as *mesh decimation* and consist of the iterative removal of geometrical units such as vertices, edges, and triangle faces (Heckbert & Garland, 1999; Gotsman et al., 2002).

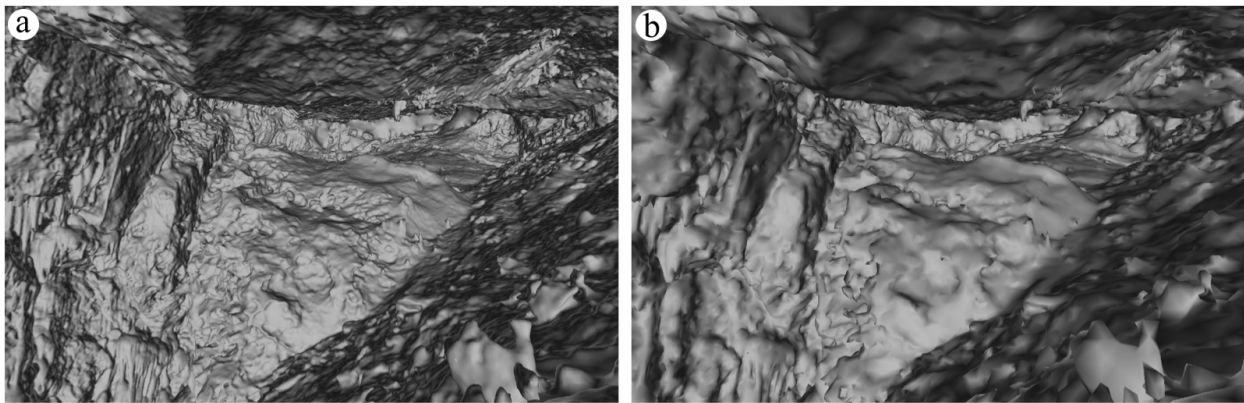


Fig. 5. Example of the cave chamber 3D-mesh obtained using Poisson Surface Reconstruction with an octree depth of 11 and 1 sample per node (a) and its simplification after the decimation process (b). Note the similarity of the 3D-mesh representations to the picture in Fig. 2a.

For the 3D-mesh simplification, we used the MeshLab multi-edge decimation function called *Quadratic Edge Collapse Decimation*. This function removed the multi-edge mesh together with the associated triangles, and then connected the adjacent vertices to the new vertex (Chen et al., 2007).

Three simplifications were generated from the 3D-mesh with an octree depth of 11. Table 4 presents the number of triangular faces and the size of each simplified 3D-mesh file in X3D format. Tests of download time were performed in a *localhost* environment. Waiting times varying between 7 and 60 s were measured.

Table 4. Tests of download speed between three mesh sizes generated after different decimations based on the original model with an octree depth of 11 and 1 sample per node, which had 10038522 faces.

decimation (%)	# faces	file size (MB)	download time (s)
90	998856	60.2	60
95	499486	29.8	19
97	249934	14.6	7

Considering the download times presented in Table 4, we selected the 3D-mesh with 249934 faces for the Web 3D visualization (see Fig. 5b). This 3D-mesh takes

about 7 s to be ready for real-time interaction in a Web browser and looks very similar to the original model and also to the real environment (see Figs. 2a and 5).

IDENTIFICATION AND RECOGNITION OF STRUCTURES FROM THE 3D-MESH

As illustrated in the Algar do Penico Cave example (Fig. 4), laser scan surveys can deal with both meso- and micromorphological features. These small features represent structures, namely stalactites and stalagmites, that are important in the study of karst hydrogeology and geomorphology (Hajri et al., 2009).

Here, we present two algorithms that allow stalactite extremities to be localized and contour lines to be sketched with a predefined equidistant between contours for a 3D model. These tools are more than just visual, as they allow users to collect additional analytical information. Both algorithms run in linear time with respect to the number of vertices and edges. They were tested with the most complex model for the specific area, which has 58042828 triangles (see Table 3).

However, triangular meshes usually consist of a collection of triangles without any associated explicit topological information. For 3D-mesh analysis, we adopted a graph

structure to disclose topological adjacency relationships between triangle vertices. Graphs are often drawn as node-link diagrams in which the nodes are represented as vertices and links as binary relations between vertices (see Silvestre et al., 2013 for more details). Several data structures are available to store graphs. We adopted the adjacency list data structure, in which there is a list of adjacent vertices for each vertex. For computational purposes, adjacency information was organized with the help of Python dictionaries, which correspond to associative arrays or hash tables in other programming languages (Beazley, 2006).

Local minima

Stalactite extremities correspond to local minima in the 3D-mesh. A local minimum in the 3D-mesh surface is a vertex v of the mesh such that its z -coordinate is smaller than the z -coordinates of all adjacent vertices of v . This local minimum is a stalactite extremity when its normal vector $\mathbf{n} = (0, 0, n_z)$ and $n_z < 0$.

For the graph $G = (V, E)$, defined from a 3D-mesh, Algorithm 1 returns a list of vertices such that its

z -coordinates are less than or equal to the z -coordinates of all adjacent vertices and the vector normal to the surface is downward oriented.

The local minima returned by Algorithm 1 for a partial view of the 3D-mesh with an octree depth of 14 and 10^{-3} samples per node (see Table 3) can be presented in a map or plane view or directly on the 3D-mesh (Figs. 6a and 6b, respectively). In the latter, it is possible to verify that local minima are indeed coincident with stalactite extremities.

With slight modifications, Algorithm 1 returns local maxima vertices corresponding to stalagmite extremities.

```

Data:  $G = (V, E)$ 
Result: Local minima array
 $L_m \leftarrow$  empty list;
for  $v \in V$  do
     $N(v) \leftarrow$  list of adjacent vertices to  $v$ ;
    if  $(z_v \leq z_{v_i}) \wedge (n_z < 0)$  for all  $v_i \in N(v)$  then
        append  $v$  to  $L_m$ ;
    end
end

```

Algorithm 1. Local minima algorithm.

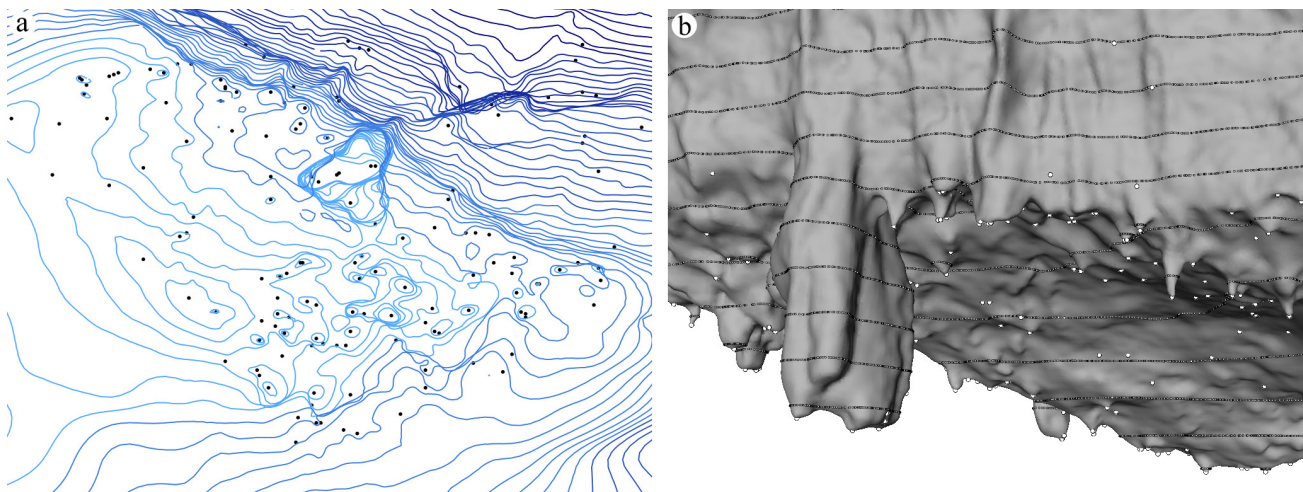


Fig. 6. Plane view with local minima representing the lower tips of stalactites and contour lines (a), and a 3D view of the same area (b). The 3D-mesh used in the diagrams was generated with an octree depth of 14 and 10^{-3} samples per node.

Contour lines

Contour lines (or contours) on nonflat surfaces are lines connecting points of the same elevation. For a 3D-mesh, if the z_0 elevation contour line intersects an edge of the model, then the contour line has two segments that lie on the triangles T_1 and T_2 incident on that edge.

Assuming the graph $G = (V, E)$ and the elevation z_0 as input, Algorithm 2 returns the collection of the segments of the polyline C_{z_0} that represent the contour of elevation z_0 .

The algorithm was used to compute a collection of contours with a predefined equidistant interval between consecutive lines.

Contours provide rich information on cave chamber morphology. They help identify smooth, flattened, or steep surfaces as well as the positioning of specific alignments. Fig. 7b shows the ceiling surface of the cave model from a top-view perspective with superimposed 15 cm equidistant contour lines, where cave relief and preferred alignments are highlighted and thus easily recognized.

```

Data:  $G = (V, E)$ ,  $z_0$  elevation
Result:  $C$  set of segments defining  $C_{z_0}$ 
 $C \leftarrow$  empty list;
for  $e \in E(G)$  do
    if  $e$  intersects  $C_{z_0}$  then
         $T_1, T_2 \leftarrow$  triangles incident on  $e$ 
         $S_i \leftarrow T_i \cap C_{z_0}$ ,  $i = 1, 2$ 
        append  $S_i$  to  $C$ 
    end
end

```

Algorithm 2. Contour lines algorithm.

DISCUSSION

TLS is an emerging technology that has been applied in various situations including the monitoring of tunnels during the construction phase, the documentation of cultural heritage, and the inspection of industrial and technical facilities. To date, there have been several case studies reporting the application of TLS to cave mapping and rock art documentation (González-Aguilera et al., 2009; Beraldin et al., 2011; Jaillet et al., 2011a; Roncat et al., 2011; Sadier et al., 2011).

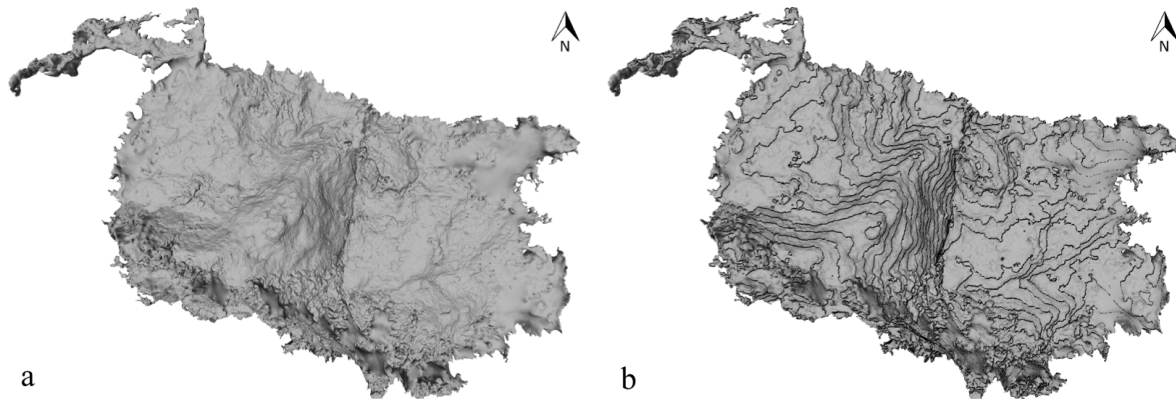


Fig. 7. Ceiling surface of the cave chamber 3D-mesh from a top-view perspective (a), and the same 3D-mesh with 15 cm equidistant contour lines (b). This 3D-mesh was generated with an octree depth of 11 and 1 sample per node.

In addition to cave mapping, the present paper has focused on 3D-mesh analysis, including the determination of local minima and contour lines from 3D-mesh (*Identification and recognition of structures from the 3D-mesh*) and on Web publishing for interactive visualization (*3D data visualization on the Web*). The entire project has been developed using only a small number of computing solutions (i.e., Python, MeshLab, X3D, WebGL, and X3DOM) for carrying out all the tasks from the TLS cave survey to the generation and analysis of the 3D-mesh (see Fig. 8 for details of the work flow). Besides their effectiveness, these computing options bear no financial cost.

There are several commercially software that offer out of the box and robust solutions for 3D-mesh generation, visualization, interpretation and analysis, such as *Leica Cyclone*, *3DReshaper* or *Geomagic Wrap* (Pucci & Marambio, 2009; Roncat et al., 2011). Nevertheless, there are open-source solutions also robust and easy to use, such as MeshLab and *CloudCompare*. In this study, we chose MeshLab, which is an open-source software able to deal with closed 3D environments, and Python programming language. The framework for 3D Web visualization is also based on open-source components, namely using X3D as the 3D data format and WebGL and

X3DOM to generate interactive 3D scenes. Accordingly, there is no need to install new software or additional plug-ins to visualize and interact with the 3D model in a Web browser. Furthermore, the possibility of visualizing 3D meshes with both contour lines and speleothem extremities (Fig. 6b) brings new application perspectives to the study of karst.

Large 3D-mesh file sizes could pose problems for visualization and interactivity on the Web. To solve this problem, Lavoué et al. (2013) proposed a method that consists of progressive 3D-content compression on the Web. In our case, we adopted a different solution whereby a 3D-mesh was simplified using a decimation process that seems quite efficient in maintaining the first-order size of the chamber and even the smaller structures (Figs. 5 and 6). This is supported by the results obtained when evaluating the differences between triangular meshes with the *Metro* tool, which allows pairs of surfaces (e.g., a triangulated mesh and its simplified representation) to be compared by adopting a surface-sampling approach (Cignoni et al., 1998). The results show that the *Hausdorff distance* (i.e., the largest distance) between the stalactite model (563405 faces) and its simplified model at 97% (with about 16902 faces) is 12 mm. The same test was

made for a partial cave chamber model with 7449484 faces and its simplification at 97% (223216 faces), which yielded a value of 25 mm. This test was made for a partial cave chamber model instead of the full model due to constraints of the *Metro* tool. The values obtained for the Hausdorff distance are both less than 0.2% of the bounding-box diagonal.

The other problem arising from the size of the point cloud data set lies in generating a 3D-mesh for the entire cave with a high octree depth parameter, as is evident in Table 3. Nevertheless, when selecting a specific region exhibiting several stalactite-type structures, the generation of a 3D-mesh with an octree depth of 14 was successful, as shown in Fig. 4. The high level of detail obtained in such a model is noticeable by the presence of small structures measuring about 1 cm. Furthermore, it is important to note that the compared dimensions of the structures obtained in the model and the actual structures in the cave

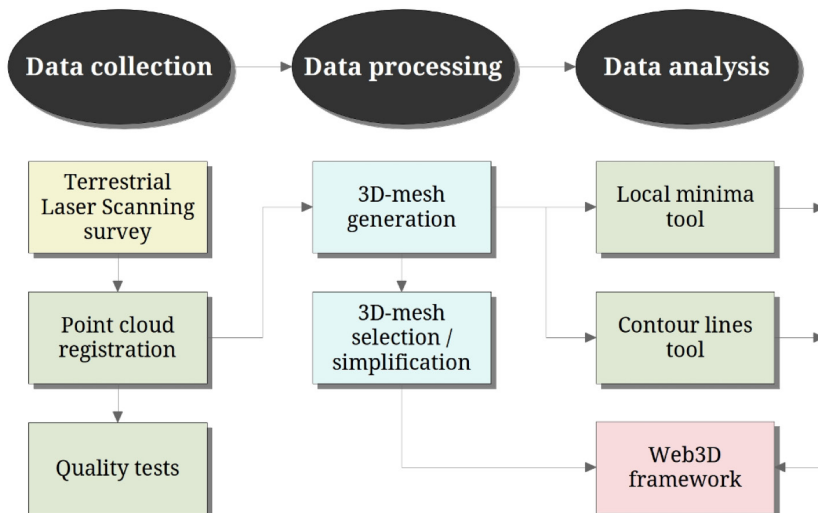


Fig. 8. Work flow showing all tasks from data collection to processing and analysis. Python programming language (green boxes) was used for the registration, quality tests, identification of local minima, and determination of contour lines. MeshLab software (blue boxes) was used to process data, namely for 3D-mesh generation and selection/simplification. The 3D-mesh and its local minima and contour lines were made available with the development of a Web3D framework.

differ by only 1 cm for the major features and by about 2 cm for the smaller ones. These smaller-scale features, which are typically not represented on standard cave maps, can thus now be well defined. The combination of TLS survey and 3D-mesh generation delivering high-resolution or very high resolution 3D models enables meso- and micromorphological features to be mapped, thereby providing a significant improvement in the level of detail available for studies of cave morphology compared with previous approaches.

CONCLUSIONS AND FUTURE WORK

This study has shown that surveying a cave using Terrestrial Laser Scanning (TLS) allows high-resolution point cloud data sets to be obtained that accurately and precisely represent the surface geometry of the studied cave. Unlike other close-range methods for cave surveying, TLS is able to be used for surveys in environments with difficult access and a lack of light. However, some problems exist regarding the massive data collection and the work environment inside the cave with respect to shadow areas and point cloud gaps. These difficulties were successfully overcome using free and open-source applications generating 3D meshes with different levels of detail, with the highest levels being used for 3D-mesh analysis and the lowest levels for 3D data on the Web, but still preserving the surface bounding and the most important geomorphological structures. The results obtained in the present work are linked to the point cloud survey resolution, i.e., 1 cm at 10 m from the laser scan. In the subsequent data-processing phase, the parameter settings for the surface reconstitution process allow developing models that have different levels of accuracy and precision. We do believe that the same type of results can be obtained in other caves as long as the parameter adjustments are adequate to the dimension and morphology of the cave.

Besides visualization platforms, researchers also need tools to map, measure, and analyse geomorphological changes through time. In this context, the development of tools for the automatic identification and characterization of speleothems and of other physical structures inside caves is one of the contributions of the present study. We built a high-precision model of a cave chamber, implemented algorithms that allowed the identification of speleothem extremities (namely, stalactites and stalagmites) and contour lines, and made the model available on a 3D Web interactive platform with no need for plug-ins. The availability of the Algar do Penico Cave 3D model in a Web3D environment is an interesting development in the geospatial field, where both researchers and the general public can navigate and interact with the cave chamber. The next steps in this continuing line of research will focus on identifying the full range of structures comprising the cave surface and on how stalactites and/or stalagmites form watersheds.

ACKNOWLEDGEMENTS

This work was supported by the Portuguese government and EU – funding, through the FCT – Fundação para a Ciência e Tecnologia funding of the SIPCLIP project

PTDC/AAC-CLI/100916/2008 and partially of the project PEst-OE/MAR/UI0350/2011 (CIMA). We are grateful to the Centre for Marine and Environmental Research (CIMA) and Geonauta's speleological association for their support. We also thank the editor and the reviewers for their support and comments, which helped us to improve the manuscript.

REFERENCES

- Barbarella M. & Fiani M., 2012 – *Landslide monitoring using Terrestrial Laser Scanner: georeferencing and canopy filtering issues in a case study*. ISPRS – International Archives of the Photogrammetry, Remote Sensing and Spatial Information Sciences, **XXXIX-B5**: 157-162. <http://dx.doi.org/10.5194/isprsarchives-XXXIX-B5-157-2012>
- Beazley D., 2009 – *Python Essential Reference*, 4th edition. Addison-Wesley Professional: 744 p.
- Behr J., Eschler P., Jung Y. & Zöllner M., 2009 – *X3DOM: a DOM-based HTML5/X3D integration model*. In: Spencer S.N. (Ed.) – *Proceedings of the 14th International Conference on 3D Web Technology (Web3D '09)*. New York, NY, USA: ACM: 127-135. <http://dx.doi.org/10.1145/1559764.1559784>
- Beraldin J.-A., Blais F. & Lohr U., 2010 – *Laser scanning technology*. In: Vosselman G. & Maas H. (Eds) – *Airborne and terrestrial laser scanning*. Whittles Publishing: 1-42.
- Beraldin J.-A., Picard M., Bandiera A., Valzano V. & Negro F., 2011 – *Best practices for the 3D documentation of the Grotta dei Cervi of Porto Badisco, Italy*. In: Beraldin J.A., Cheok G.S., McCarthy M.B., Neuschaefer-Rube U., Baskurt A.M., McDowall I.E. & Dolinsky M. (Eds) – *Three-dimensional imaging, interaction, and measurement*. Proceedings of SPIE-IS&T Electronic Imaging, SPIE Vol. **7864**: 15. <http://dx.doi.org/10.1117/12.871211>
- Bernardini F., Mittleman J., Rushmeier H., Silva C. & Taubin G., 1999 – *The Ball-Pivoting Algorithm for surface reconstruction*. IEEE Transactions on Visualization and Computer Graphics **5 (4)**: 349-359. <http://dx.doi.org/10.1109/2945.817351>
- Budaj M. & Stacho M., 2008 – *Therion – digital cave maps*. In: *Spelunca*. Spelunca Mémoires (French Federation of Speleology) **33**: 138-141.
- Chalmovianský P. & Jüttler B., 2003 – *Filling holes in point clouds*. In: Wilson M.J. & Martin R.R. (Eds.) – *Mathematics of surfaces, Proceedings of the 10th IMA International Conference*. Springer, **2768**: 196-212. http://dx.doi.org/10.1007/978-3-540-39422-8_14
- Chen H., Luo X. & Ling R., 2007 – *Surface simplification using multi-edge mesh collapse*. In: *Fourth International Conference on Image and Graphics, 2007*. ICIG 2007: 954-959. <http://dx.doi.org/10.1109/ICIG.2007.91>
- Cignoni P., Rocchini C. & Scopigno R., 1998 – *Metro: measuring error on simplified surfaces*. Computer Graphics Forum, **17 (2)**: 167-174. <http://dx.doi.org/10.1111/1467-8659.00236>
- Cignoni P., Callieri M., Corsini M., Dellepiane M., Ganovelli F. & Ranzuglia G., 2008 – *Meshlab: an open-source mesh processing tool*. In: Scarano V., De Chiara R. & Erra U. (Eds) – *Eurographics Italian Chapter Conference, 2008*: 129-136. <http://dx.doi.org/10.2312/LocalChapterEvents/ItalChap/ItalianChapConf2008/129-136>
- Fairchild I.J. & Baker A., 2012 – *Speleothem Science: From Process to Past Environments*. Wiley-Blackwell, Chichester: 432 p.

- Ford D.C. & Williams P., 2007 – Karst Hydrogeology and Geomorphology. Wiley: 576 p.
<http://dx.doi.org/10.1002/9781118684986>
- Glassner A., 1994 – *Building vertex normals from an unstructured polygon list*. In: Heckbert P.S. (Ed.) – *Graphics gems IV*. Academic Press Professional, Inc., San Diego, CA, USA: 60-73. <http://dx.doi.org/10.1016/B978-0-12-336156-1.50015-X>
- González-Aguilera D., Muñoz-Nieto A., Gómez-Lahoz J., Herrero-Pascual J. & Gutierrez-Alonso G., 2009 – *3D digital surveying and modelling of cave geometry: application to Paleolithic rock art*. *Sensors*, **9** (2): 1108-1127.
<http://dx.doi.org/10.3390/s90201108>
- Gotsman C., Gumhold S. & Kobbelt L., 2002 – *Simplification and Compression of 3D Meshes*. In: Iske A., Quak E. & Floater M.S. (Eds) – *Tutorials on multiresolution in geometric modelling*. Mathematics and visualization, 2002. Berlin Heidelberg: Springer: 319-361.
http://dx.doi.org/10.1007/978-3-662-04388-2_12
- Grussenmeyer P. & Guillemin S., 2011 – *Photogrammetry and laser scanning in cultural heritage documentation: an overview of projects from INSA Strasbourg*. In: Mohamed M. & Grussenmeyer P. (Eds.) – *Geomatics in the City, Proceedings of the GTC2011 Symposium, Jeddah, Saudia Arabia, May 10-13 2011*: 8 p.
<http://geomaticsksa.com/GTC2011/S4/PDF/21.pdf>
- Hajri S., Sadier B., Jaillet S., Ployon E., Boche E., Chakroun A., Saulnier G.-M. & Delannoy J.-J., 2009 – *Analyse spatiale et morphologique d'une forêt de stalagmites par modélisation 3D dans le réseau d'Ornac*. *Karstologia*, **53**: 1-14.
<http://hal-sde.archives-ouvertes.fr/halsde-00457291>
- Heckbert P. S. & Garland M., 1999 – *Optimal triangulation and quadric-based surface simplification*. *Journal of Computational Geometry: Theory and Applications*, **14** (1-3): 49-65.
[http://dx.doi.org/10.1016/S0925-7721\(99\)00030-9](http://dx.doi.org/10.1016/S0925-7721(99)00030-9)
- Jaillet S., Ployon E. & Villemin T. (Eds), 2011a – *Images et modèles 3D en milieux naturels*. Collection EDYTEM: 216 p.
- Jaillet S., Sadier B., Hajri S., Ployon E. & Delannoy J.-J., 2011b – *Une analyse 3D de l'endokarst: applications lasergramétriques sur l'aven d'Ornac (Ardèche, France)*. *Géomorphologie: relief, processus, environnement*, **4**: 379-394.
<http://dx.doi.org/10.4000/geomorphologie.9594>
- Kaasalainen S., Jaakkola A., Kaasalainen M., Krooks A. & Kukko A., 2011 – *Analysis of incidence angle and distance effects on terrestrial laser scanner intensity: search for correction methods*. *Remote Sensing*, **3** (10): 2207-2221.
<http://dx.doi.org/10.3390/rs3102207>
- Kazhdan M., Bolitho M. & Hoppe H., 2006 – *Poisson surface reconstruction*. In: *Proceedings of the fourth Eurographics symposium on Geometry Processing (SGP '06)*. Eurographics Association, Aire-la-Ville, Switzerland, Switzerland: 61-70.
- Krooks A., Kaasalainen S., Hakala T. & Nevalainen O., 2013 – *Correction of intensity incidence angle effect in terrestrial laser scanning*. *ISPRS Annals of the Photogrammetry, Remote Sensing and Spatial Information Sciences*, **II-5/W2**: 145-150. <http://dx.doi.org/10.5194/isprsannals-II-5-W2-145-2013>
- Lavoué G., Chevalier L. & Dupont F., 2013 – *Streaming compressed 3D data on the web using JavaScript and WebGL*. In: *Proceedings of the 18th International Conference on 3D Web Technology (Web3D '13)*. ACM, New York, NY, USA: 19-27.
<http://dx.doi.org/10.1145/2466533.2466539>
- Prieto I., Izkara J. & Delgado F., 2012 - *From point cloud to web 3D through CityGML*. In: *Proceedings of the 18th International Conference on Virtual Systems and Multimedia (VSMM)*, 2-5 Sept. 2012: 405-412.
<http://dx.doi.org/10.1109/VSM2012.6365952>
- Pucci B. & Marambio A., 2009 – *Olerdola's Cave, Catalonia: a virtual reality reconstruction from terrestrial laser scanner and GIS data*. In: *3D virtual reconstruction and visualization of complex architectures*, Proceedings of ISPRS International Workshop 3D-ARCH 2009.
- Remondino F., 2011 – *Heritage recording and 3D modeling with photogrammetry and 3D scanning*. *Remote Sensing*, **3** (6): 1104-1138.
<http://dx.doi.org/10.3390/rs3061104>
- Roncat A., Dublyansky Y., Spötl C. & Dorninger P., 2011 – *Full-3D surveying of caves: a case study of Märchenhöhle (Austria)*. In: Marschallinger R. & Zobl F., 2011 – *Mathematical geosciences at the crossroads of theory and practice, Proceedings of the IAMG2011 Conference*, September 5-9 2011, Salzburg, Austria: 1393-1403.
<http://dx.doi.org/10.5242/iamg.2011.0074>
- Sadier B., Lacave, C., Delannoy, J.-J. & Jaillet, S., 2011 – *Relevés lasergramétriques et calibration sur calcite de morphologies externes de spéléothèmes pour une étude paléo-sismologique du Liban*. In: Jaillet S., Ployon E. & Villemin T. (Eds), 2011 – *Images et modèles 3D en milieux naturels*. Collection EDYTEM, **12**: 137-144.
- Silvestre I., Rodrigues J.I., Figueiredo M. & Veiga-Pires C., 2013 – *Framework for 3D data modeling and web visualization of underground caves using open source tools*. In: *Proceedings of the 18th International Conference on 3D Web Technology (Web3D '13)*. ACM, New York, NY, USA: 121-128.
<http://dx.doi.org/10.1145/2466533.2466549>
- Tobler R. & Maierhofer S., 2006 – *A mesh data structure for rendering and subdivision*. In: Jorge J. & Skala V. (Eds.), 2006 - *The 14th International Conference in Central Europe on Computer Graphics, Visualization and Computer Vision (WSCG'2006)* Short Communication Papers Proceedings: 157-162.
- Tsakiri M., Sigizis K., Billiris H. & Dogouris S., 2007 – *3D laser scanning for the documentation of cave environments*. In: *Underground space: expanding the frontiers, Proceedings of the 11th ACUUS Conference*, September 10-13 2007, Athens, Greece: 403-408.
- Voegtle T., Schwab I. & Landes T., 2008 – *Influences of different materials on the measurements of a terrestrial laser scanner (TLS)*. In: ISPRS – International Archives of the Photogrammetry, Remote Sensing and Spatial Information Sciences, **XXXVII-B5**: 1061-1066.
- Zabel F., 2012 – *Topografia da Cavidade – Algar do Penico*. Relatório do Levantamento e Esboço: 11 p.



Available online at scholarcommons.usf.edu/ijis

International Journal of Speleology

Official Journal of Union Internationale de Spéléologie



Hairy Stalagmites, a new biogenic root speleothem from Botswana

Gerhard C. Du Preez^{1*}, Paolo Forti², Gerhard Jacobs¹, Anine Jordaan³,
and Louwrens R. Tiedt³

¹Unit for Environmental Sciences and Management, Potchefstroom Campus, North-West University, Private Bag X6001, Potchefstroom 2520, South Africa

²Italian Institute of Speleology, Via Zamboni 67, 40126 Bologna, Italy

³Laboratory for Electron Microscopy, CRB, North-West University, Potchefstroom, South Africa

Abstract: Ngamiland in northwestern Botswana hosts the Gcwihaba Caves which present unique subterranean environments and host speleothems never before recorded. Cave atmospheric conditions can be extreme with temperatures as high as 28°C and relative humidity nearing 99.9%. Within Dimapo and Diviner's Caves peculiar root speleothems that we named 'Hairy Stalagmites' were found. These stalagmites are closely associated with the roots of Namaqua fig (*Ficus cordata*) trees that enter the cave environment in search of water. Pieces of broken stalagmites were sampled from Dimapo Cave for further investigations. Stereo and electron microscopy revealed that the Hairy Stalagmites consist of multiple intertwined tubes created when thin films of CaCO₃ are deposited around fine lateral roots. The importance of the roots is substantiated with evidence of calcified epidermal cells, apical meristems and epidermal imprints. The development of these stalagmites starts when roots accumulate on the cave floor in the vicinity of a water drip and a root nest is created to capture the water. From this point the roots grow upwards (positive hydrotropism) allowing the development of the calcite structure, and as CO₂ diffusion and evaporation occurs, CaCO₃ is deposited. The environmental conditions necessary for the growth of Hairy Stalagmites, as well their developmental mechanism, are discussed and illustrated.

Keywords: Botswana; root speleothem; Hairy Stalagmites; Namaqua fig tree; developmental mechanism; scanning electron microscopy

Received 17 June 2014; Revised 14 September 2014; Accepted 7 October 2014

Citation: Du Preez G.C., Forti P., Jacobs G., Jordaan A. & Tiedt L.R., 2015. Hairy Stalagmites, a new biogenic root speleothem from Botswana. *International Journal of Speleology*, 44 (1) 37-47. Tampa, FL (USA) ISSN 0392-6672 <http://dx.doi.org/10.5038/1827-806X.44.1.4>

INTRODUCTION

The hypothesis that biological interactions may somehow play a role in the deposition of secondary chemicals in caves was first suggested by Beaumont (1676) and was later described by Tournefort (1704). Speleothems were even considered, due to the presence of inner growing layers, as true 'rock plants'. At the end of the 18th and beginning of the 19th centuries, the most common speleothem types were often represented as parts of trees with stalactites as roots, stalagmites and columns as trunks, and helictites as leaves or flowers (Forti, 2001). However, at the beginning of the 20th century, any biogenic involvement in the formation of speleothems was ruled out as a better understanding of the main chemical mechanisms was achieved. Yet, in time, it became evident that micro-organisms may play some role in the formation of speleothems (Hill, 1976), while roots were reported to induce the development of peculiar speleothems such as showerheads and rootsticles

(Hill & Forti, 1997). Today, it's generally accepted that plants (mainly roots) can passively advance the development of speleothems by enhancing capillary migration of water to structures where evaporation occurs (Forti, 2001). Also, it has recently been shown that microbial communities can actively influence the genesis and development of certain subaqueous and/or vadose speleothems (Melim et al., 2001; Barton & Northup, 2007; Dodge-Wan & Deng Hui Min, 2013).

Roots are the single portion of a tree which may somehow contribute towards speleothem development, however, it is presumably rare in deeper parts of caves since roots generally do not reach depths greater than several metres. Nevertheless, the morphological effects induced by roots over speleothems are evident. The surfaces of roots that enter cave voids may serve as pathways for the flow of seeping water and, if environmental conditions are favourable, the precipitation of CaCO₃ (calcium carbonate). This mechanism causes the development of peculiar stalactites and columns with a tilted and

often anastomosed shape over which several pseudo-helictites grow. These speleothems have globally been observed with the same characteristics and are normally called 'rootsicles' (Hill & Forti, 1997). In wet tropical environments the root apparatus of large trees may become the main driving force for the development of peculiar cone-shaped stalactites known as 'Showerheads', which were first described from Brazilian caves (Lino, 1989) and later observed in many other tropical areas (Hill & Forti, 1997). Winkelhofer (1975) was the first to describe root stalagmites from sandstone caves in Germany which were later reported from the Czech Republic and other countries of Central Europe and Northern America (Bunnell, 2010; Pavuza & Cech, 2013). In all of these cases the root stalagmites either developed in the twilight zone or in total darkness. They were described as conical and/or cylindrical dense networks of several coniferous roots that may reach up to 60 cm in height. The voids that formed within the networks consisted mainly of living terminal roots often coated by symbiotic fungi, and were filled with sandy grains and organic matter; the latter being the product of mucilaginous excretion and/or decay of the roots. A smaller part of the network was formed by thicker and/or skeletal roots directly linked to the mother tree. Owing to the chemical composition of the host rock, no part of the root stalagmite was covered by a calcite crust.

The developmental mechanism of root stalagmites was initially described by Jenik & Kopecky (1992). Kopecky & Jenik (2001) recognized the dripping of water over a sand floor as the fundamental factor allowing for the development of these biogenic speleothems. In fact, only where dripping water impacts a root, do thin new roots grow upwards and towards the water drip (positive hydrotropism). This allows for the development of conical and/or cylindrical root stalagmites of which the height and diameter depends mainly on the energy of the water splashing on them, as well as on the availability of sand grains. Until recently, root stalagmites have globally been discovered in about 40 locations including from the Czech Republic, Poland, Austria, Slovakia, Hungary, Sweden, Spain, South Africa, Australia, and the United States (Mlejnek, 2010). Most of these caves were formed in sandstone or in other non-carbonate rocks (for example granite and gneisses). Root stalagmites were first discovered in a carbonate environment in 1987 during the exploration of Pofaddergat limestone cave (Namibia), of which a written report was only published nine years later by Marais et al. (1996). These root stalagmites developed below dripping points, were typically 20 cm tall, 3-4 cm wide, and consisted of densely packed thin rootlets. However, the presence of calcite incrustations was not reported. A few other limestone (or marble) caves (Bunnell, 2010) also host root stalagmites of which only one or two are partially covered by thin calcite crusts (Pavuza & Cech, 2013). Nevertheless, the organic component of the stalagmites is by far the most dominant.

Peculiar root stalagmites, called Hairy Stalagmites due to the fineness of their roots, have recently been

discovered in dolomite caves in Botswana. These root stalagmites are peculiar since they are almost entirely composed of calcite with roots only visible on top of still-active growing speleothems. In the present paper the microclimate of the relevant cave, the morphology and chemical composition of the Hairy Stalagmites, as well as the proposed mechanism responsible for the development of this new type of root stalagmite, are discussed.

GEOLOGICAL SETTING AND CHARACTERISTICS OF STUDY AREA

Ngamiland: Botswana's host of subterranean realms

The Gcwihaba Caves, first explored in 1932 by Marthinus Drotsky and initially known as Drotsky's Caverns, are located in Ngamiland in the northwestern part of Botswana (Cooke, 1975). These caverns have facilitated various scientific expeditions, including paleoclimatic (Cooke, 1975; Railsback et al., 1994), paleontological (Robbins et al., 1996) and mineralogical (Martini, 1996) studies, but have, however, only been visited by a small number of tourists. Subsequently, the government of Botswana initiated the Gcwihaba Caves Project which aims at discovering new cave systems for the purpose of establishing an economically viable tourist destination. As part of the project, ground gravimetric surveys were conducted in order to identify cavities isolated below surface. Entry into these cavities was gained by drilling 600 mm diameter vertical shafts that penetrate on average 50 m below surface (Ellis, 2011). Until the beginning of 2014, five new caves have been penetrated of which three are extensive systems. Within two of these systems, Dimapo (20°1'12.34" S, 21°21'38.41" E) and Diviner's (20°8'32.20" S, 21°12'36.60" E) caves, Hairy Stalagmites were discovered.

Diviner's and Dimapo caves are located in the Koanaka and Gcwihaba Hills respectively; both hills form part of the Koanaka Group stratigraphy (Key & Ayres, 2000; Ellis, 2011). The latter is located in the Precambrian Damara Sequence of Ngamiland (Carney et al., 1994; Williams et al., 2012) and consists of greenschist-facies marble (Singletary et al., 2003). The surface landscape forms part of the Kalahari Desert which is classified as a semi-arid region with shrub savannah vegetation. Rainfall in the desert varies from 400 mm to 450 mm per annum and temperatures from -8.5°C to 42.2°C (Kennedy et al., 2012). Namaqua fig (*Ficus cordata*) trees naturally occur in the region, however, are mainly associated with the named hills. Preliminary field investigations have revealed that the trees found on Koanaka Hill directly overlie Diviner's and Mongongo (20°8'47.05" S, 2°12'27.08" E) caves. It is perceived that the specific location of the trees holds relation to their usage of the subterranean cavities as a water source, thus, ensuring their survival in the desert. Fig tree roots have been reported at a maximum depth of 120 meters below surface in Echo Caves (Ohrigstad, South Africa) (Kutschera, 1991).

Characteristics and features of Dimapo Cave

Dimapo Cave developed along a fault line as shallow as 40 meters below surface, and represents the main system where Hairy Stalagmites were sampled and studied. As illustrated by Fig. 1, the system is characterized by vast chambers, arrays of parallel

passages, flowstone formations such as ‘Calcite Mountain’ (Fig. 2), slopes of infiltrating Kalahari sands, and extensive boulder fields. Dimapo Cave, as well as the other drilled caves, present microclimates atypical to southern Africa’s caves. Durand et al. (2012) reported average temperatures of 17°C in the Bakwena

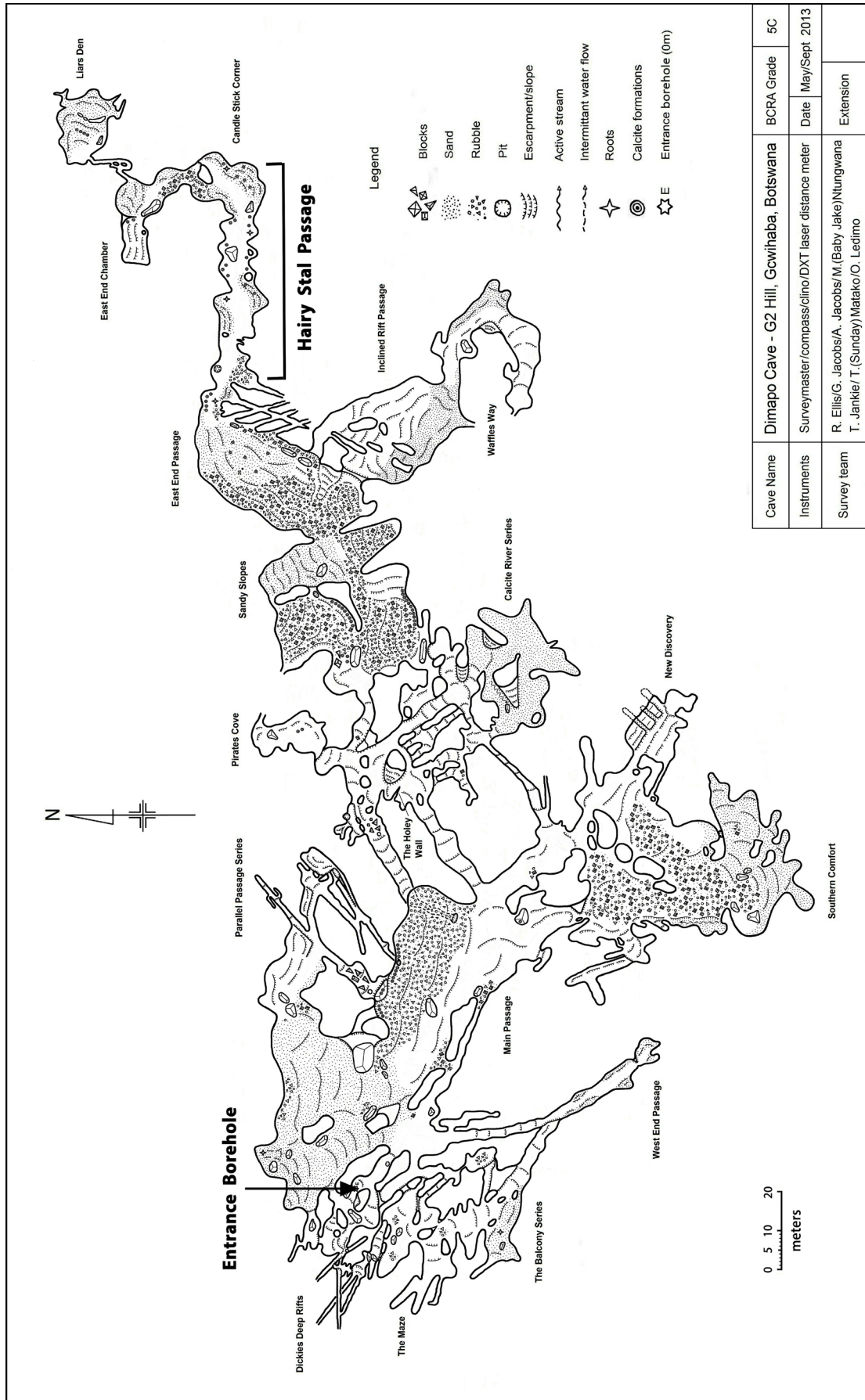


Fig. 1. Map of Dimapo Cave with the location of the Hairy Stalagmites ('Hairy Stal Passage') (Drawing provided by Roger Ellis).



Fig. 2. A flowstone formation referred to as 'Calcite Mountain' in Dimapo Cave (Photo by Anton Jacobs).

Cave (Irene, South Africa). However, temperatures within the drilled caves (Botswana) can reach as high as 28°C with 99% relative humidity, which nears 99.9% in boulder areas associated with Hairy Stalagmites. It is believed that the Namaqua fig trees utilize the subterranean environment, mainly due to the high humidity levels that result in water flowing along the roots. However, there are numerous water drips throughout Dimapo Cave, which are 'hunted' by roots extending over the cave floor. These roots, in association with the respective water drips, facilitate the development of the Hairy Stalagmites.

The Hairy Stalagmites are found within Dimapo Cave at the northeastern end of the cave system; a 10 to 15 m wide passage known as 'Hairy Stal Passage' (Fig. 1) which extends 60 m in an easterly direction, after which it continues 30 m north and ends in an alcove. On both sides of the passage are banks of infiltrating sand overlain by roots.

METHODS

Inactive and partially broken Hairy Stalagmite samples were carefully collected during September (spring) 2013 from Dimapo Cave (Botswana) by using a hand spade. Care was taken to avoid any direct skin contact. The cave atmospheric conditions were measured with a calibrated Vaisala thermo hygrometer (HMI41) which was left undisturbed for 15 minutes to ensure stable and accurate readings. The samples were stored in cushioned plastic containers, sealed, and transported to the North-West University (Potchefstroom, South Africa) and University of Bologna (Italy) for further analyses.

During all analyses, samples were handled using latex gloves and stored at room temperature in

airtight containers. In order to study the surface features of the speleothem more closely, a Nikon AZ-100 (Amsterdam, Netherlands) stereo microscope and FEI Quanta 250 FEG (Bruno, Czech Republic) scanning electron microscope (SEM) with integrated software was used. Stereo light micrographs were taken with a digital camera by making use of the Nikon NIS-Elements software package that creates multilayered-image micrographs. For SEM, smaller pieces of speleothem were sputter-coated with gold/palladium. A small piece of uncoated Hairy Stalagmite was used to analyse the chemical composition of the speleothem substrate with energy-dispersive spectroscopy (EDS) by using an Oxford X-max 20 SDD detector and INCA software.

RESULTS AND DISCUSSION

The Hairy Stalagmites

Most of the Hairy Stalagmites found in Dimapo Cave are 'dead' (Fig. 3); calcite deposition has ceased most likely due to climatic variability and is indicated by the absence of Namaqua fig tree roots associated with the structure of the speleothems. It was noted that more than 90% of the speleothems were stagnant, however, some were 'alive', as roots were directly associated and intertwined with their structure (Fig. 4). Typically, roots travel along the cave strata and where intercepted by a water drip, give rise to many smaller rootlets and root hairs; an interconnected web of roots is created which plays a vital role in the development of the speleothem. The dimensions of the different Hairy Stalagmites vary greatly; some are only a few centimetres tall, while others tower over one meter. Generally, the Hairy Stalagmites are three to five centimetres in diameter. The latter, as well as the speed of growth

of the speleothems, is most likely affected by: (1) the sustainability and volume of the water source, (2) the concentration of dissolved CaCO_3 , and (3) the kinetic energy locked within each water drop. The amount of kinetic energy, determined by the distance of travel and diameter of a water drop, affects the dispersion of

it upon impact (Salles et al., 2002) and thus possibly the initial base thickness of the speleothem.

Microscopy investigations

Multilayered-imaging micrographs revealed that the entire structure consists of multiple intertwined tubes (Fig. 5). The tubes were initially formed around a network of lateral roots that originated from several horizontally-growing roots on the cave floor. The initial Hairy Stalagmites, also referred to as nests, consist of a network of modified roots that grow upwards. Lamont & Lange (1976) referred to them as stalagmiform roots.



Fig. 3. A 'dead' Hairy Stalagmite that has collapsed and regrown over time with roots associated with the base of the speleothem.



Fig. 5. Micrograph of the external surface of a Hairy Stalagmite illustrating the intertwined calcite tubes that constitute its structure.



Fig. 4. Namaqua fig tree roots associated with an active Hairy Stalagmite. The roots create a nest at the top of the speleothem which captures the water from the drip (Photo by Anton Jacobs).

The individual tubes were studied more closely with the SEM. The inner surfaces of the calcite tubes showed the presence of both calcified epidermal cells, as well as epidermal root imprints (Fig. 6) that were sporadically found in close proximity to one another. Rarely, entire calcified root fragments (Fig. 7) were observed inside the Hairy Stalagmites. Intact calcified cells in the tubes were mostly root apical meristems (Fig. 8). Root caps appeared to be well preserved as their anatomical attributes were clearly visible as a population of thin-walled, isodiametrically-shaped cells (Fig. 8). The coarse granular texture of the root tips points to the calcification of a mucilaginous substance called mucigel that is normally secreted by root cap cells. Further back from the root tip, root imprints were predominantly observed and only occasionally intact calcified epidermal cells. In root fragments there was no evidence of calcified cortex cells, but the epidermis appeared to be multiseriate and the cell layer underneath the outermost epidermal layer was also calcified (Fig. 7). A cross section (Figs. 9; 10) revealed that no organic matter remains within the tubes because of the complete decomposition of dead roots. This process is important for nutrient recycling as it constantly makes nutrients available for new root growth and has important implications for the maintenance of the cave and above-ground ecosystem.

A possible explanation for the presence of both replicas and calcified cells is that some roots were alive when calcification occurred, while others were already dead. Calcified cells point towards rapid CaCO_3

biomineralization while the roots were still alive. Replicas are the consequence of physical precipitation of calcite around already dead roots. The dead roots subsequently disintegrate and leave epidermal imprints on the calcite. The presence of both types of rhizoliths may highlight the role of the root itself in the calcite deposition process. Living, respiring roots add CO_2 to their surroundings, which may produce H_2CO_3 in the presence of H_2O . Subsequently, higher acidity levels will produce a carbonate rich solution. This solution may penetrate intercellularly and also impregnate cell walls. As the calcite reprecipitates, it effectively preserves cell structure relatively quickly.

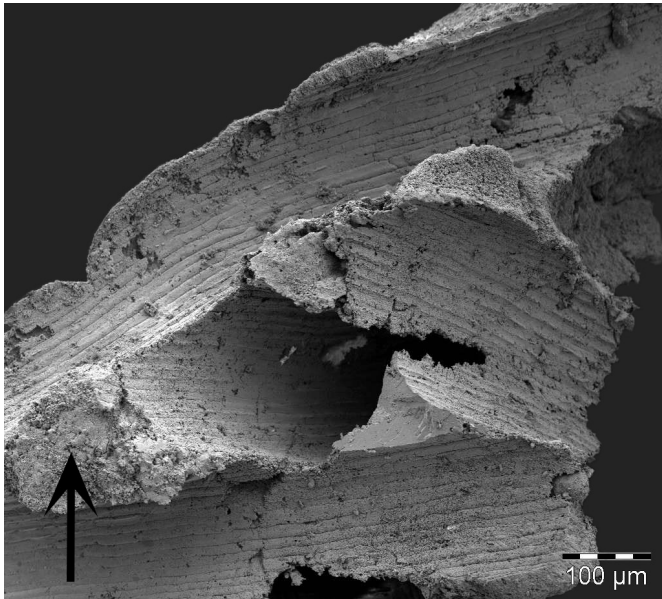


Fig. 6. Scanning electron micrograph showing root epidermal cell imprints created as CaCO_3 was deposited over the roots. Inter-tube cavities are sometimes partially filled with calcite (arrow).



Fig. 7. Scanning electron micrograph showing intact calcified root fragment with calcite partially surrounding the bottom part of it.

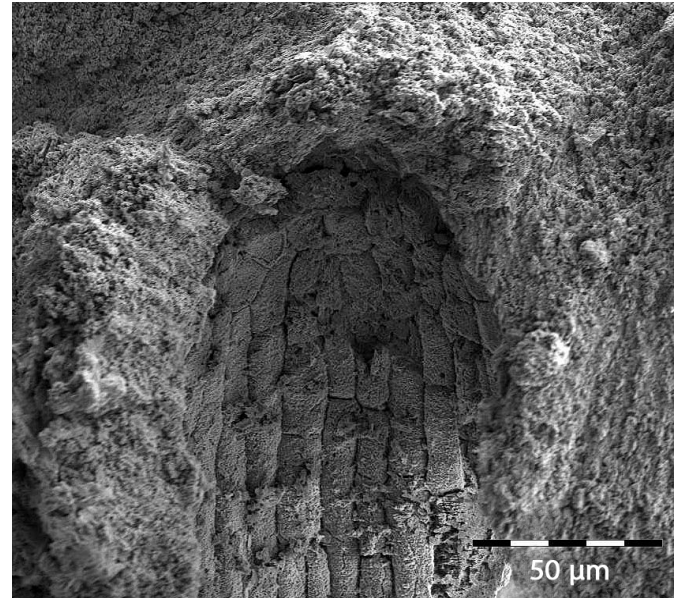


Fig. 8. Scanning electron micrograph showing root tip that contains calcified and isodiametrically-shaped thin-walled root cap cells and young epidermal cells in the zone of cell division.

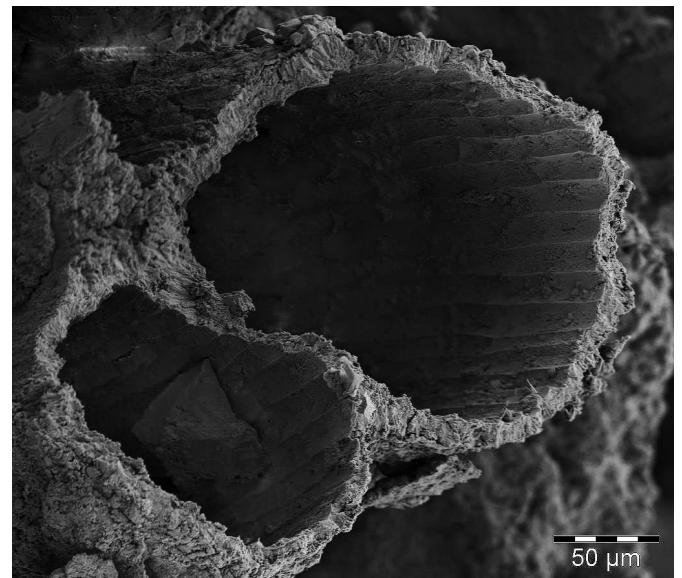


Fig. 10. Scanning electron micrograph of a cross section through calcite tubes shows that no organic matter remains within the tubes.

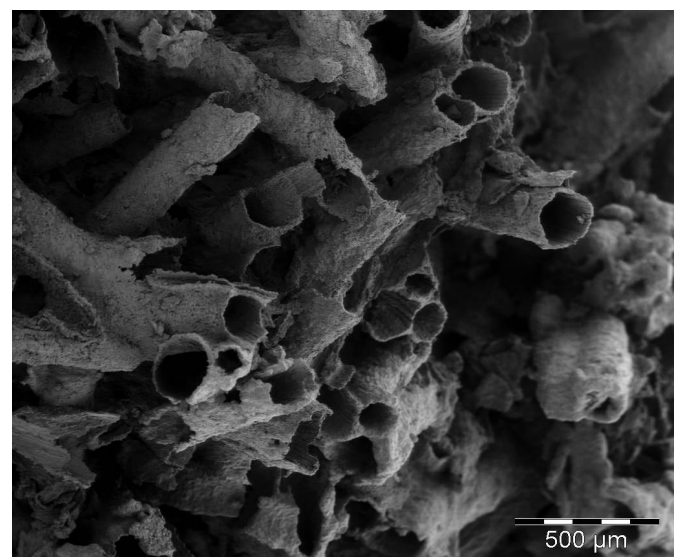


Fig. 9. Scanning electron micrograph of a cross section of multiple calcite tubes showing that all organic matter has either been decomposed or calcified.

However, water removal through absorption by mature living roots may concentrate the carbonate solution and also contribute to CaCO_3 precipitation, but mostly to the formation of calcite tubes surrounding the roots. Since there is no or limited impregnation and reprecipitation of cell walls and intercellular spaces by the carbonate solution, only epidermal imprints are left after the decomposition of organic material. The zone of cell division in the root tip consists of a population of actively dividing cells and hence high respiration rates. The more common preservation of the root cap cells in root tips, rather than older cells in mature root regions, points to the role of CO_2 from respiring roots during calcifications of cell structures. However, although biogenic processes may be involved in the calcification of some cells, it is probably a less dominant process than the physical processes involved during the precipitation of CaCO_3 around individual roots. The calcified tube walls are thin (10-20 μm) which indicates an overall slow rate of precipitation around each root. The EDS analysis (47.8% CaO , 3.8% MgO , 0.7% SiO_2 , and 47.8% CO_2) revealed that the tubes consist of more than 95% of CaCO_3 .

The developmental mechanism of a Hairy Stalagmite

When considering the development of a Hairy Stalagmite, several conditions are necessary for both the deposition of calcite, as well as the calcification of roots. The following conditions, however, are generally required for the development of any root stalagmite:

1. Trees and/or bushes of which the roots are capable of penetrating the underlying cave must cover the aboveground landscape. Thus, the depth of cave development may not exceed the limit of root penetration.
2. The cave environment must serve as a sufficient and sustainable water source.
3. Dripping water should contain dissolved CaCO_3 .
4. Dripping inside the cave must be constant and provide sufficient water to avoid the desiccation of the roots, however, the cave floor must remain dry enough to induce positive root hydrotropism.

The following additional and specific conditions are required for the development of a Hairy Stalagmite:

5. Dripping water must either be slightly undersaturated or slightly oversaturated with CaCO_3 . This is required to facilitate the development of Hairy Stalagmites and not typical speleothems (stalagmites and/or flowstones). If high supersaturation conditions were induced, it would result in rapid calcite deposition, thus burying the roots inside the formed structure.
6. Water flow, as a result of water dripping, should be minimal to allow for the deposition of calcite and to avoid the transport of deposited particles.
7. The relative humidity of the cave atmosphere must remain high in order to prevent the desiccation of the root tips, however, below 100% to avoid

condensation of CO_2 rich water over the roots, which will hinder calcite deposition.

8. Dying-off and degradation of the roots associated with the Hairy Stalagmites should be slow enough in order to facilitate adequate calcite deposition and structure forming.

The development of a Hairy Stalagmite can only occur when all of these conditions are met, explaining why these speleothems are a rare phenomenon. The developmental mechanism can be sub-divided into five stages of which a description follows:

Stage one is initiated when roots from the surface penetrate the cave and travel along the cave walls and floor until they reach a constant water dripping point (Figs. 11 A; 12). The water stimulates the growth of several small hydrophilic upwards (positive hydrotropism) growing roots, creating a rounded root nest (Figs. 11 B; 13). As root growth continues, the nest enlarges, while the impact of the droplets creates a deepening depression in the center. The concave shape of the nest and its increasing central depth progressively reduce the impact of the water drops, which subsequently prevents droplets from escaping it. The lateral expansion of the nest stops when all of the dripping water is contained within it. Furthermore, the lateral roots facilitate capillary migration of water towards the external part of the nest where calcite deposition processes are active. Nearing the end of this stage, most, if not all of the droplets, are kept within the root nest, which is substantiated by the absence of calcite deposition in the form of layered structures over the external surface or around the base of the stalagmite.

During the second stage (Fig. 11 C), the rounded root nest with a central depression captures and disperses water by capillary action throughout the nest. Supersaturation of CaCO_3 is possibly induced by several different reactions. Within this peculiar micro-environment, CO_2 diffusion and H_2O evaporation may not be the only mechanisms involved in calcite deposition, especially since the high relative humidity and CO_2 partial pressure of the cave atmosphere will inhibit these processes. Other biologically driven mechanisms, including selective water uptake by roots through a biological film (Klappa, 1980) and mineralizing microbial colonies within the biological film around the roots (Cacchio et al., 2012), may also facilitate the deposition of a thin layer of calcite around the roots, thus, creating calcite tubes (Fig. 11 D). The force of the water drops impacting the structure causes the partial detachment of some of the newly formed calcite crust. The detached calcite grains accumulate on the cave floor along the perimeter of the nest. A conical-shaped sandy deposit is formed, becomes enlarged and hardened, and ultimately serves as a protection barrier that prevents the detachment of the thin calcite layers from the individual lateral roots. Calcite deposition continues towards the core of the nest, covering new roots, thickening calcite films surrounding others, and fuses the root structures together, while also partially filling inter-tube cavities (Fig. 6). Since water is constantly introduced at the center of the nest,

supersaturation of CaCO₃ and thus calcite deposition is significantly inhibited. This, together with the impact force of the water drops, causes the core structure to be weaker than the rest of the stalagmite.

In the third stage a true Hairy Stalagmite is formed (Figs. 11 E; 4), characterized by a constant external diameter and vertically growing roots near the core. The calcite films inhibit the growth of the roots by clogging the vascular system, which prevents the roots from conducting water and food. This ultimately leads to the death of most of the roots. However, since the external diameter of the stalagmite remains relatively constant, it is evident that the roots die-off at a specific rate as root lifespan and radial growth is inhibited by the calcification process. After the organic matter has decomposed, the remaining calcite films

(10-20 μm thickness) become an intricate network of interconnected hollow tubes (Fig. 10). Some root epidermal cells and root tips are calcified (Figs. 7; 8), while other roots have died before any calcification could take place, as only root surface imprints are visible inside the calcite tubes (Fig. 6).

The described process of Hairy Stalagmite formation may last for several years, creating speleothems over 1 m tall. Discontinuities visible as indentations in the external diameter (Fig. 11 F) are most likely induced by the reduced frequency of dripping during the dry season, which will also lower the relative humidity of the cave atmosphere. Thus, H₂O uptake by roots, evaporation, and CO₂ diffusion are enhanced close to the external surface (Fig. 11 F1). These combined processes are also responsible for the deposition of

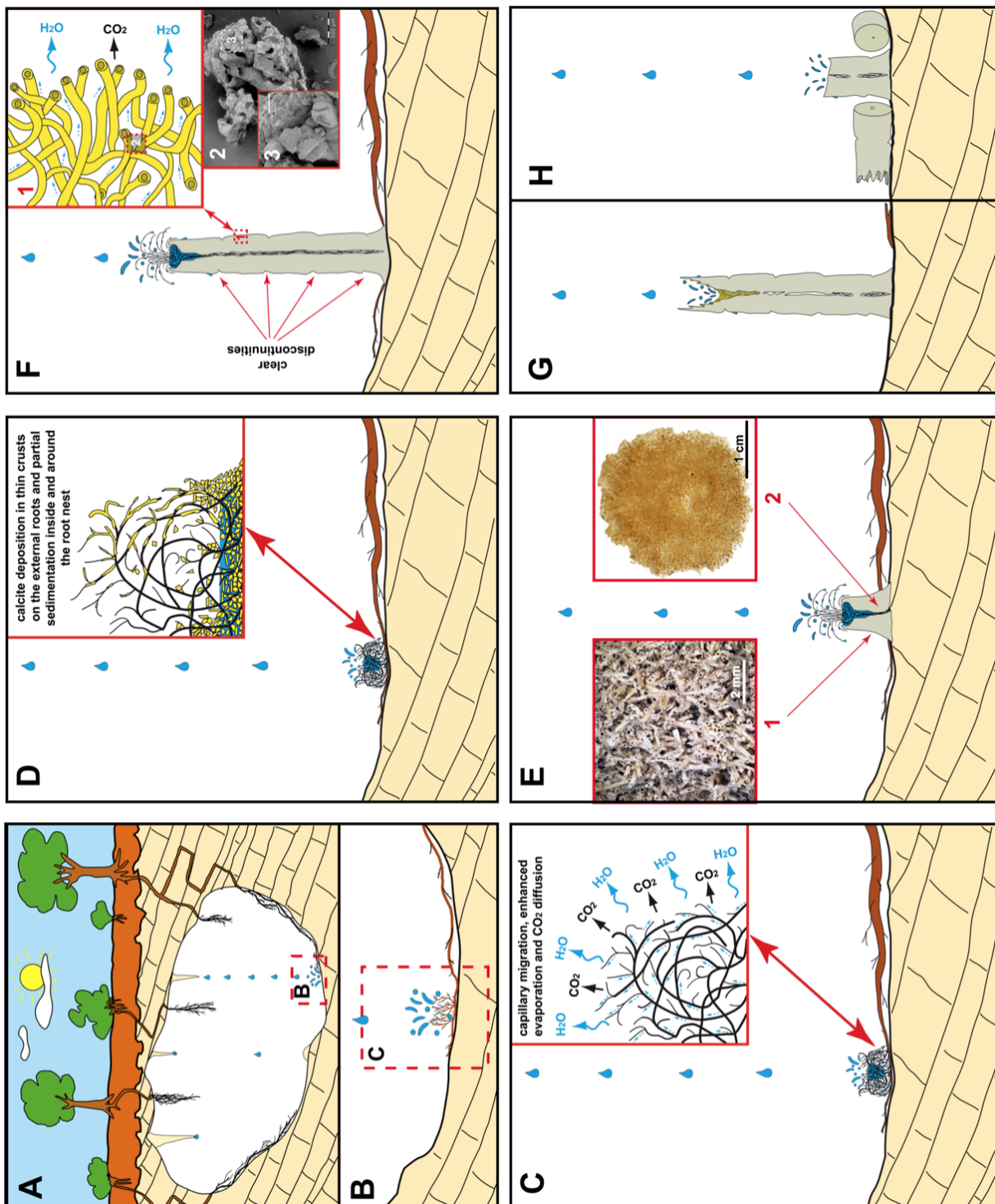


Fig. 11. The developmental stages of the Hairy Stalagmites: A) Roots of Namaqua fig trees migrate along the cave floor in search of water; B) Associated with a constant water drip, fine lateral roots grow upward creating a nest which traps the water; C, D) Evaporation and CO₂ diffusion allows for calcite precipitation within the nest; E) The process leads to the development of a Hairy Stalagmite of which the entire structure consists of calcite tubes (1), with no remaining organic material (2); F) Alternating dry and wet periods were recorded within the structure of the Hairy Stalagmite as variations in its diameter with the deposition of calcite euhedral crystals in the inter-tube cavities (1-3); G, H) After the internal roots have died, the upper nest disappears and the dripping starts eroding the inner part of the Hairy Stalagmite leading to its collapse.



Fig. 12. Dripping point on the cave floor 'hunted' by roots, which marks the start of the development of a Hairy Stalagmite.



Fig. 13. Root nest created during the first stage of development of a Hairy Stalagmite.

calcite crystals (Fig. 11 F2-3) in the voids that exist between the formed calcite tubes. While the calcite linings over the roots consist of small elongated crystals with a highly porous structure, the calcite deposited in the inter-tube cavities and on the surface of the Hairy Stalagmites has an entirely different morphology. The former is the result of alternating deposition and re-dissolution of calcite most likely controlled by biogenic processes that subsequently give rise to a high amount of CO_2 . On the contrary, the calcite in the cavities and on the surface of the Hairy Stalagmite consist of euhedral non-porous crystals (Figs. 14; 15) which suggests a slow but continuous deposition process controlled by evaporation and/or enhanced H_2O uptake by roots during the dry season. As a result, the external surface of the stalagmite is more hardened. Due to the above described process, only the roots growing vertically along the dripping line survive. However, as they reach the open space above the

partially hardened nest, they create an elaborate umbrella structure (Fig. 4) which allows the further development of the Hairy Stalagmite.

The fourth stage (Fig. 11 G) is related to the decay of the Hairy Stalagmite, which is influenced by the availability of water, the rate of calcite hardening, and the height of the structure. As the Hairy Stalagmite becomes taller, the roots within the structure may break as they become more fragile and exposed especially during the dry season. Also, if water dripping ceased for a period of time, the roots may become petrified. Consequently, the root nest at the top of the stalagmite will die and disintegrate, leaving the stalagmite exposed to the impact of dripping water. Direct contact between the water drops and the calcite structure will progressively degrade it and block the tubes with calcite fragments.

Finally, during the fifth stage (Fig. 11 H), the Hairy Stalagmites become unstable without the support of living roots. Furthermore, the impact of falling water drops is no longer cushioned by the root nest. If enough force is generated, the Hairy Stalagmite may break and collapse (Fig. 3), most likely at an area of weakness closer to the base of the speleothem. An area of weakness is probably the result of incomplete calcification and may also explain the discontinuities (Fig. 11F) that were observed in the external diameter of the stalagmite. If conditions again become favorable, the portion of the Hairy Stalagmite left standing may be recolonized by roots. This marks the start of the development of a new Hairy Stalagmite continuing from the third stage.

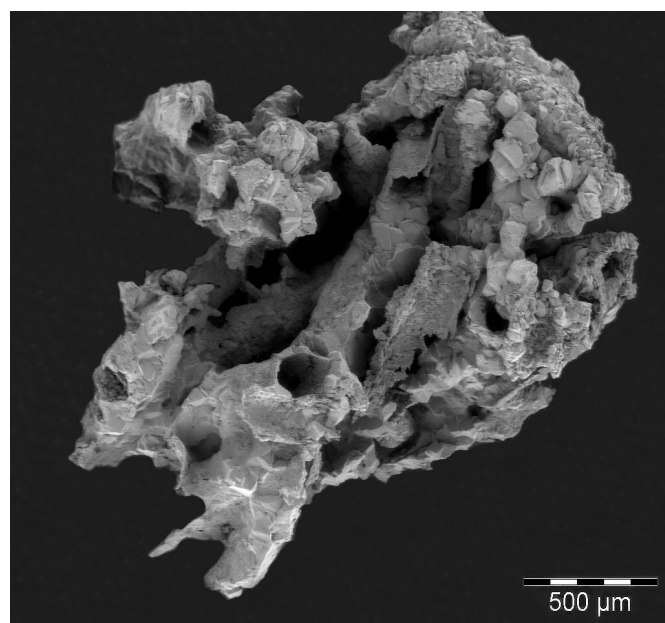


Fig. 14. Scanning electron micrograph showing euhedral calcite crystals that formed near the surface of a Hairy Stalagmite.

FINAL REMARKS

Hairy Stalagmites, a new type of biogenic speleothem, consist of both calcite tubes and calcified root cells, and are peculiar specimens representing biogenically-formed speleothems. Their development is strongly controlled by an intricate set of both atmospheric and abiotic conditions, most likely sensitive to

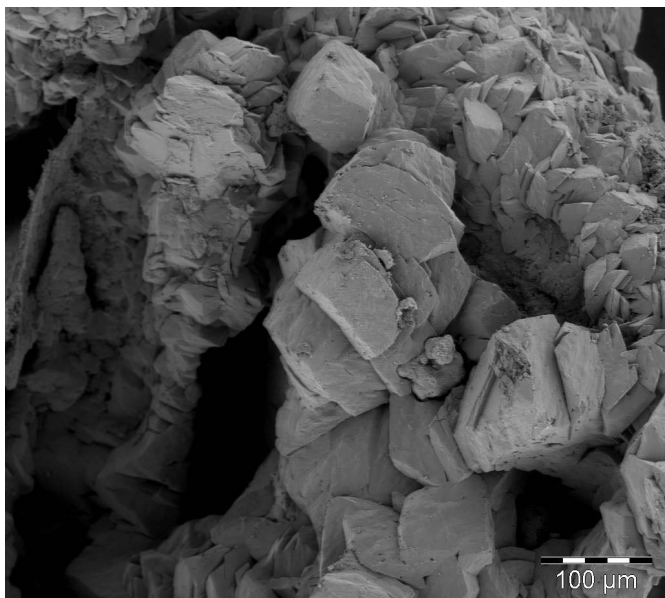


Fig. 15. Close-up view of calcite crystals formed on a Hairy Stalagmite.

climatic variations. The required conditions explain why the Hairy Stalagmites have only been observed in caves previously sealed. In order to preserve this unique environment together with this new type of speleothem, it is necessary to conserve not only the cave atmospheric conditions, but also the surface landscape that hosts the Namaqua fig trees. Therefore, with the Botswana government's efforts to create a tourist destination, adequate measures should be considered to insure the sustainability and function of the caves and surface landscape.

ACKNOWLEDGMENTS

The authors thank the government of Botswana and in particular the president, His Excellency Lieutenant General Sir Seretse Khama Ian Kama, for continuous support in exploring the wonders of the Gcwihaba Caves. We also thank the team of cavers, led by Roger Ellis, who tirelessly aided our cause, as well as Louis du Preez for insight provided. Furthermore, we thank the reviewers for their significant contribution by means of actual and relevant commentary.

REFERENCES

- Barton H.A. & Northup D. E., 2007 - *Geomicrobiology in cave environments: past, current and future perspectives*. Journal of Cave and Karst Studies, **69** (1): 163-178.
- Beaumont J., 1676 - *Two letters concerning rockplants and their growth*. Philosophical Transactions of the Royal Society, **11** (129): 732-742.
- Bunnell D., 2010 - *Root stalagmite in a carbonate cave*. NSS News July 2010: 28.
- Cacchio P., Ercole C., Contento R., Cappuccio G., Martinez M.P., Del Gallo M. & Lepidi A., 2012 - *Involvement of bacteria in the origin of a newly discovered speleothem in the gypsum cave of Grave Grubbo (Crotona, Italy)*. Journal of Cave and Karst Studies, **74** (1): 7-18. <http://dx.doi.org/10.4311/2010MB0136R>
- Carney J., Aldiss D. & Lock N.P., 1994 - *The geology of Botswana*. Geological Survey Department, Lobatse, 113 p.
- Cooke H., 1975 - *The palaeoclimatic significance of caves and adjacent landforms in western Ngamiland, Botswana*. Geographical Journal, **141** (3): 430-444. <http://dx.doi.org/10.2307/1796477>
- Dodge-Wan D. & Deng Hui Min A., 2013 - *Biologically influenced stalagmites in Niah and Mulu Caves (Sarawak, Malaysia)*. Acta Carsologica, **42** (1): 155-163. <http://dx.doi.org/10.3986/ac.v42i1.634>
- Durand F., Swart A., Marais W., Jansen van Rensburg C., Habig J., Dippenaar-Schoeman A., Ueckermann E., Jacobs R., De Wet L., Tiedt L. & Venter E., 2012 - *Die karst-ekologie van die Bakwenagrot (Gauteng)*. Suid-Afrikaanse Tydskrif vir Natuurwetenskap en Tegnologie, **31** (1): 1-17. <http://dx.doi.org/10.4102/satnt.v31i1.275>
- Ellis R., 2011 - *Report on the expedition to the Koanaka Hills, Botswana*. Cave Exploration Rescue and Adventure Club, Johannesburg, 27 p.
- Forti P., 2001 - *Biogenic speleothems: an overview*. International Journal of Speleology, **30** (1): 39-56.
- Hill C.A., 1976 - *Cave minerals*. National Speleological Society, Huntsville, 138 p.
- Hill C.A. & Forti P., 1997 - *Cave minerals of the world*. National Speleological Society, Huntsville, 464 p.
- Jenik J. & Kopecky J., 1992 - *Korenové stalagmity v piskovcovych jeskynich*. Knihovna České speleologické společnosti, **10**: 26-34.
- Kennedy A.M., Marais J., Bauer A.M., Lewis P.J. & Thies M.L., 2012 - *Effect of fire on the herpetofauna of the Koanaka Hills, Ngamiland, Botswana*. Check List, **8** (4): 666-674.
- Key R.M. & Ayres N., 2000 - *The 1998 edition of the National Geological Map of Botswana*. Journal of African Earth Sciences, **30** (3): 427-451. [http://dx.doi.org/10.1016/S0899-5362\(00\)00030-0](http://dx.doi.org/10.1016/S0899-5362(00)00030-0)
- Klappa C.F., 1980 - *Rhizoliths in terrestrial carbonates: classification, recognition, genesis and significance*. Sedimentology, **27** (6): 613-629. <http://dx.doi.org/10.1111/j.1365-3091.1980.tb01651.x>
- Kopecky J. & Jenik J., 2001 - *Root forms from pseudokarst*. In: Jubertie C. & Decu V. (Eds.) - *Encyclopaedia Biospeologica, Tome III*. Moulis - Bucharest: Sociéte de Biospéologie: 1420-1421.
- Kutschera L., 1991 - *Short review of the present state of root research*. In: McMichael B.L. & Persson H. (Eds.) - *Plant roots and their environment*. Amsterdam: Elsevier: 1-8. <http://dx.doi.org/10.1016/B978-0-444-89104-4.50005-0>
- Lamont B.B. & Lange B.J., 1976 - *'Stalagmiform' roots in limestone caves*. New Phytologist, **76**: 353-360. <http://dx.doi.org/10.1111/j.1469-8137.1976.tb01470.x>
- Lino C.F., 1989 - *Cavernas: o fascinante Brasil subterrâneo*. Editora Rios, Sao Paulo, 280 p.
- Marais J.C.E., Irish J. & Martini J.E.J., 1996 - *Cave investigation in Namibia V: 1993 SWAKNO results*. Bulletin of South African Speleological Association, **36**: 58-78.
- Martini J.E.J., 1996 - *Gwihabaite - (NH₄,K)NO₃, orthorhombic, a new mineral from Gwihaba Cave, Botswana*. South African Speleological Association Bulletin, **36**: 19-21.
- Melim L.A., Shinglman K.M., Boston P.J., Northup D.E., Spilde M.N. & Queen J.M., 2001 - *Evidence of microbial involvement in pool finger precipitation, Hidden Cave, New Mexico*. Geomicrobiology Journal, **18** (3): 311-329.
- Mlejnek R., 2010 - *America, look for root stalagmites!* NSS News April 2010: 14.

- Pavuz R. & Cech P., 2013 - *Wurzelstalagmiten in Österreich – ein Statusbericht*. *Die Höhle*, **62**: 25-31.
- Railsback L.B., Brook G.A., Chen J., Kalin R. & Fleisher C.J., 1994 - *Environmental controls on the petrology of a late Holocene speleothem from Botswana with annual layers of aragonite and calcite*. *Journal of Sedimentary Research*, **64** (1): 147-155.
- Robbins L., Murphy M.L., Stevens N.J., Brook G.A., Ivester A.H., Haberyan K.A., Klein R.G., Milo R., Stewart K.M., Matthiesen D.G. & Winkler A.J., 1996 - *Paleoenvironment and archaeology of Drotsky's Cave: Western Kalahari Desert, Botswana*. *Journal of Archaeological Science*, **23** (1): 7-22.
<http://dx.doi.org/10.1006/jasc.1996.0002>
- Salles C., Poesen J. & Sempere-Torres D., 2002 - *Kinetic energy of rain and its functional relationship with intensity*. *Journal of Hydrology*, **257** (1): 256-270.
[http://dx.doi.org/10.1016/S0022-1694\(01\)00555-8](http://dx.doi.org/10.1016/S0022-1694(01)00555-8)
- Shaw T.R., 1997 - *Historical introduction*. In: Hill C. & Forti P. (Eds.) - *Cave minerals of the world*. National Speleological Society, Huntsville, 28-43.
- Singleary S.J., Hanson R.E., Martin M.W., Crowley J.L., Bowring S.A., Key R.M., Ramokate L.V., Direng B.B. & Krol M.A., 2003 - *Geochronology of basement rocks in the Kalahari Desert, Botswana, and implications for regional Proterozoic tectonics*. *Precambrian Research*, **121** (1): 47-71.
[http://dx.doi.org/10.1016/S0301-9268\(02\)00201-2](http://dx.doi.org/10.1016/S0301-9268(02)00201-2)
- Tournefort J.P., 1704 - *Description du labyrinthe du Candie, avec quelques observations sur l'accroissement et sur la génération des pierres*. *Mémoires de l'Académie Royale des Sciences*: 406-424.
- Williams B.A., Ross C.F., Frost S.R., Waddle D.M., Gabadirwe M. & Brook G.A., 2012 - *Fossil *Papio* cranium from !Ncumtsa (Koanaka) Hills, western Ngamiland, Botswana*. *American Journal of Physical Anthropology*, **149** (1): 1-17.
<http://dx.doi.org/10.1002/ajpa.22093>
- Winkelhofer R., 1975 - *Stalagmitenförmige Wurzelbindungen in Sandsteinhöhlen*. *Der Höhlenforscher*, **7** (2): 25-26.



Available online at scholarcommons.usf.edu/ijis

International Journal of Speleology

Official Journal of Union Internationale de Spéléologie



Range of horizontal transport and residence time of nitrate in a mature karst vadose zone

Jiri Kamas¹, Jiri Bruthans^{1*}, Helena Vysoka¹, Miroslav Kovařík²

¹Faculty of Science, Charles University in Prague, Albertov 6, 128 43 Prague 2, Czech Republic

²Nature Conservation Agency of the Czech Republic, Svitavská 29, 678 01 Blansko, Czech Republic

Abstract: Nitrate concentrations in drips in Amaterska, Spolecnak, and Holstejska caves situated below a 25 to 120 m thick vadose zone in the Moravian Karst, Central Europe were studied during several periods from 1992. Each cave runs below a land-use boundary between fertilized lands and forest, which enabled study of the range of horizontal components of nitrate transport in the vadose zone. Parts of the fertilized land were turned into grassland in 1998 and 2003, and the cave drips were sampled both prior and after the changes in land use. The mean residence time of nitrate is <10 years in the 25-30 m thick vadose zone, but >16 years in the 105-120 m thick vadose zone. The maximum range of horizontal nitrate transport (H_{max}) is 18 m in the 105-120 m thick vadose zone. H_{max} was normalized by the vadose zone's thickness (T). In the Moravian Karst the H_{max}/T ratio is <0.2. A low H_{max}/T between 0.1 and 0.6 was observed in the Czech and Slovenian karst areas, unaffected by glaciations, and with an epikarst having evolved at least from the Pliocene. On the contrary, a high H_{max}/T (1.6-24) was reported from those areas affected by glaciations or mining activities, where the epikarst zone might be partly removed or sealed, and where shallow soils do not store much water after heavy rains. More data on the horizontal transport of tracers within the vadose zone are needed in order to test the potential relationship between epikarst development and H_{max}/T .

Keywords: nitrate; epikarst; vadose zone; transport; residence time

Received 17 May 2014; Revised 22 October 2014; Accepted 28 October 2014

Citation: Kamas J., Bruthans J., Vysoka H. and Kovařík M., 2014. Range of horizontal transport and residence time of nitrate in a mature karst vadose zone. *International Journal of Speleology*, 44 (1), 49-59. Tampa, FL (USA) ISSN 0392-6672
<http://dx.doi.org/10.5038/1827-806X.44.1.5>

INTRODUCTION

Double to triple porosity, typical for karst, encompasses: conduits, which are dissolution tubular openings; fracture porosity; and matrix storage (Ford & Williams, 2007). Conduits occupy only a tiny fraction of an aquifer (0.003-0.02 %) in dense well-lithified limestone (Worthington et al., 2000). As the conduits drain most of the water there, the mean residence time is extremely short, typically just hours to days. Fracture and matrix porosity occupy 1-2% in dense well-lithified limestone; in the case of diffuse recharge, the residence times are often measured in years to decades (Einsiedl, 2005). The karst vadose zone (consisting of the soil, epikarst, and a transmission zone) plays a crucial role for ground water recharge and contaminant attenuation (Pronk et al., 2009; Ravbar & Goldscheider, 2009). The residence time of water and dissolved matter in the karst vadose zone is usually studied by stable isotopes of oxygen or hydrogen, and less commonly by tritium (Perrin et al.,

2003a; Kluge et al., 2010). In the temperate climatic zone, the residence times within a karst vadose zone of several tens of meters thickness is estimated at from several months to several years (Atkinson et al., 1985; Perrin et al., 2003a; Trček, 2007; Schwartz et al., 2009; Kluge et al., 2010).

As the permeability in a karst vadose zone decreases with depth, a considerable horizontal component of the flow often occurs in the epikarst (Smart & Friederich, 1986; Motyka et al., 2001). Water flow converges towards major deep penetrating fissures (Williams, 1983; Williams, 2008; Klimchouk, 2000). Therefore, water and contaminant transport in the vadose zone always have both a vertical and horizontal component. In some areas, the horizontal component dominates (Smart & Friederich, 1986; Motyka et al., 2001); in others, the vertical component dominates (Kogovšek & Šebela, 2004). It remains unclear which factors are controlling the proportions of these horizontal and vertical components. As the permeability of vertical fractures increases over time in the vadose

zone, a decrease of the horizontal component is to be anticipated, theoretically, if sufficient time is available for epikarst evolution (Williams, 1983).

Natural sources of nitrate include wildlife waste and the degradation of organic matter in the soil. The present-day background is elevated against the former natural background due to atmospheric inputs, which include both combustion products and the evaporation of ammonia from fertilizers and livestock wastes. A present-day background of 11 mg/l (the concentration as NO₃ is used in this paper) was identified in karst springs by Panno et al. (2006). An extensive review, including data from tens of thousands wells and springs, has shown that the present-day background nitrate concentration in the USA is about 9 mg/l (USGS, 2002; Panno et al., 2006). Septic effluents, livestock wastes, and synthetic fertilizers are sources of high nitrate concentrations, exceeding present-day background levels (Kastrinos & White 1986; Panno et al., 2006). Karst aquifers often have a higher nitrate content (Boyer & Pasquarell, 1995), and nitrate is the most common contaminant (Iqbal & Krothe, 1995; Peterson et al., 2002). A strong linear relationship between the nitrate concentration in karst springs and the percentage of agricultural land was found by Kastrinos & White (1986) and Boyer & Pasquarell (1995). Movement of nitrate in the soil by matrix flow, with a rate of 65 cm/year, was described by Peterson et al. (2002). Iqbal & Krothe (1995) described the major movement of nitrate in quick pulses through the vadose zone immediately after a major storm event. The relatively long residence time (tens of years) of nitrate in a karst vadose zone was described by Katz et al. (2004).

The Moravian Karst (Czech Rep.; Fig. 1) represents an ideal area in which to study nitrate transport in the vadose zone. Extensive horizontal cave passages, mostly situated from 25 to 120 m below the ground surface, enable relatively easy access and sampling of water from the vadose zone. In some areas, the cave passages traverse below the land-use boundary between forest/grassland and fertilized land. Fertilizers have been intensively applied since 1960 (Balák et al., 1999). Maximum nitrate concentrations in cave drips, which were located below fertilized lands in the area were 115 mg/l in 1981 and 136 mg/l in 1995; while nitrate concentrations under forests was only 5-11 mg/l, on average (Balák et al., 1999; Table 1).

The intensive production of maize in the immediate surroundings of dolines caused heavy erosion of the soil cover and the transport of mud into some caves in 1980 (Balák et al., 1999). Corrosion of speleothems was observed in some of the caves and was originally ascribed to changes of water chemistry due to the intensively applied fertilizers (Balák et al., 1999). In order to protect the cave environments and its endemic biota, the fertilized lands above some of the caves and their surroundings have been turned into grasslands in several stages between 1985 and 2009 (Balák et al., 1999). This change was originally performed within the framework of a voluntary agreement between the board responsible for the protection of the area and farmers; later this was expanded with support

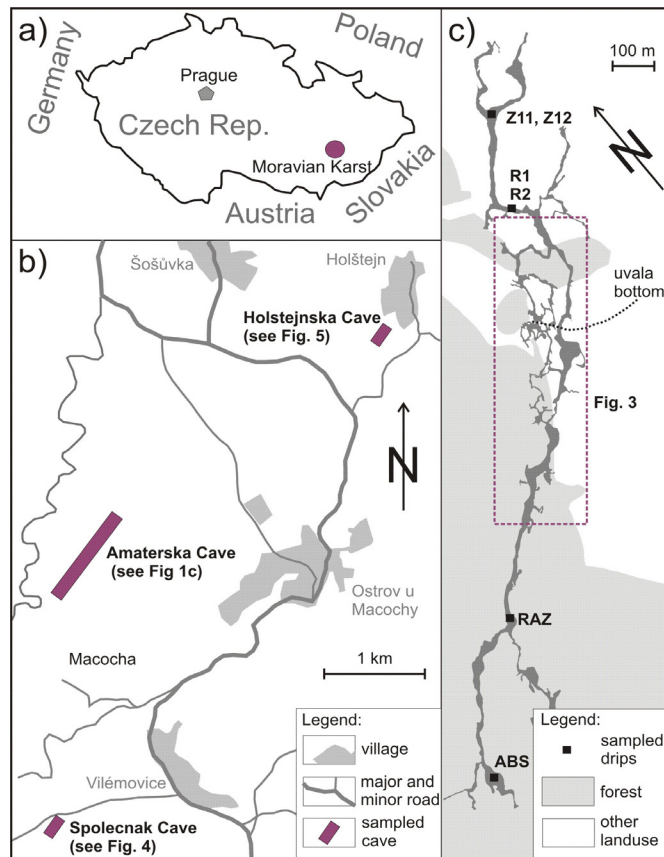


Fig. 1. a) Location of the Moravian Karst within Central Europe; b) Northeastern part of the Moravian Karst with the studied cave systems; c) Amaterska Cave with drips sampled in 1991-1994, and area selected for detailed sampling of drips (rectangular dashed-line). Drips in the dashed line rectangle are shown in Fig. 3.

Table 1. Average concentrations of nitrates below areas with different land use in 2007-2010 (mg/l). Samples taken within 18 m (H_{max}) from F/N boundary were not used for calculating the averages.

Cave	Land use	Nitrate
Amaterska	fertilized land	80
	grassland since 1998	78
	forest	10
Spolecnak	fertilized land	104
	grassland since 1850	11
Holstejska	grassland since 2003	37
	forest	5

of the EU program Sapard. Neither livestock nor the release of animal waste is allowed in grassland areas. The grass is cut and transported out of the grassland areas to decrease the nitrate content in the soil and the karst vadose zone. Based on information from employees of the Moravian Karst protected landscape area (as well as our own observations), the farmers comply with these restrictions. Presently, the planning is towards optimizing the grassland areas above the caves to a smaller extent; still ensuring the protective function, but minimizing the costs paid to farmers for restrictions on their agricultural activities.

The objective of this study is to evaluate: 1) the horizontal component of nitrate transport in the karst vadose zone, which is critical in selecting the correct width of overlap of the grass strips over the cave outlines; 2) the mean residence time of nitrate in the karst vadose zone, which is an important parameter necessary to estimate the time until the nitrate

concentrations in the drips will reach their present-day background after a change of fertilized land into grassland. The study is focused on the Moravian Karst; however, the results of the horizontal transport component are compared with similar studies from other regions in order to infer those parameters that might control the range of horizontal transport.

STUDY AREA

The study area is situated in the Moravian Karst, 200 km SE of Prague (Fig. 1). The Moravian Karst consists of a folded and faulted high-percentage limestone sequence of Devonian age, which is 25 km long, several km wide, and ~600 m thick. Well-developed karst phenomena comprise ~1,600 caves as well as hundreds of dolines and blind valleys (Bruthans & Zeman, 2003). Caves have been evolving by the activity of sinking allogenic streams. The latest phase of a continuous karstification started in the Pliocene (Kadlec et al., 2001). The Moravian Karst was subjected to periglacial and permafrost conditions during glacial periods; however, was never glaciated itself (Žák et al., 2004). All of the main caves are oriented in the direction of cleavage, faults, and calcite veins (Dvořák & Melichar, 2002). Most fractures are subvertical, striking between NNW and NNE. The bedding planes are inclined toward the NW-NE-SE, dipping 15-80°. The mean annual air temperature and precipitation totals are 7.2 °C and 616 mm, respectively. Precipitation is more abundant from May to September (rain, storms), and the snow cover occurs between December and March. Recharge dominates between December and May. The evapotranspiration to precipitation ratio is ~82% at the altitude of the Moravian Karst, based on a water budget study (Taraba, 1976).

Drips were sampled in the Amaterska, Spolecnak, and Holstejska caves. Each cave is situated below the F/N boundary, which always runs between fertilized land and that area where fertilizers have not been applied (forest or grassland; Fig. 2). The F/N boundary produces a sharp change in the nitrate concentrations in both the soil and the vadose zone. The horizontal component of nitrate transport in the vadose zone can be estimated from the width of the transition zone between those regions with low and high nitrate concentrations in their cave drips (Fig. 2). In the case of all the caves, the F/N boundary is enclosing an area that for ≥160 years has not been used for agriculture, and where fertilizers have never been applied; with the exception of the tree nurseries, which have been limited in both time and space (Figs. 3, 4, 5).

The Amaterska Cave is a large maze of passages situated 105-120 m below the surface, which enables sampling in various directions across the F/N boundary (Fig. 3). The SE part of the cave has been overlain by forest for at least 160 years (2nd Military Survey, 1852). Over a small segment of the cave there is a tree nursery in the forest where fertilizers were applied. The central part of this area was fertilized until 1998, when it was converted into grassland. Further north, there are two patches,

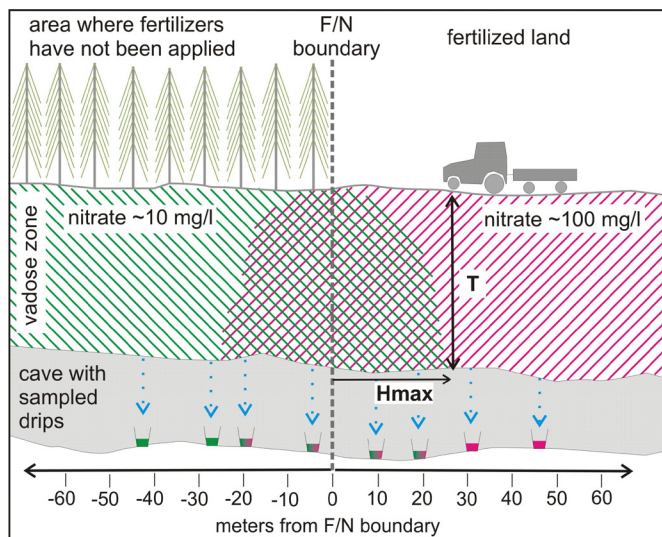


Fig. 2. Conceptual model of horizontal component of mixing on F/N boundary, and definition of the H_{max} and T parameters. The distance from the boundary towards fertilized land (at the present or in the past) is measured in positive numbers, and the distance towards forest (land never fertilized) is in negative numbers.

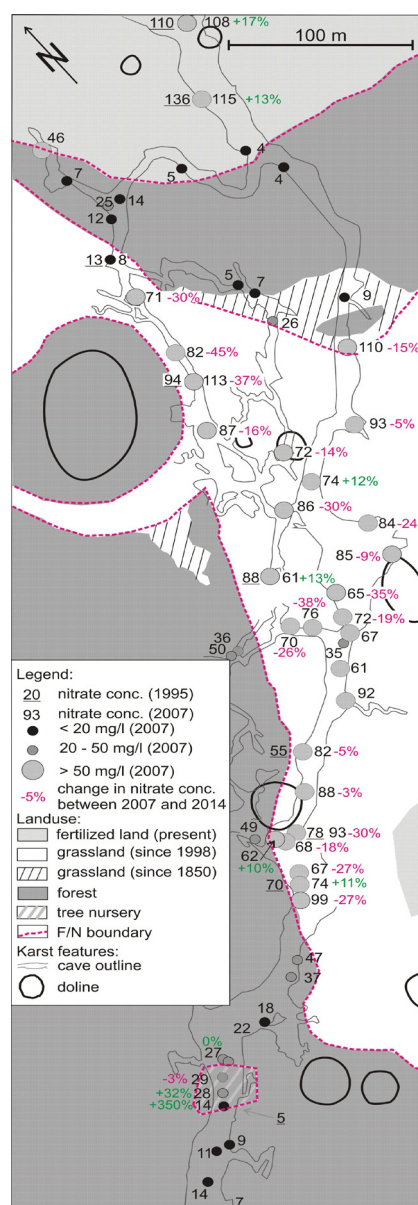


Fig. 3. Land use, cave and doline outlines, plus nitrate concentration in drips in the Amaterska Cave. Cave outline modified from Hromas et al. (2009). Land use is based on the 2nd Military Survey (1852) and current land use maps.

with trees and shrubs that have not been used for agricultural activities for at least 160 years (2nd Military Survey, 1852). Fertilized land covers the northernmost portion of study area (Fig. 3). The surface above the cave is relatively flat (gradient from 0.02-0.09). Higher surface gradients are found on the sides of the uvala depression (up to 0.24), which crosses the central part of cave (Fig. 1). The soil profile is formed by rendzina, with a thickness of 0.5-0.7 m in the forested area above the cave (Schwarcová et al., 2006). The soil thickness is higher on the fertilized land.

Spolecnak Cave is a large elongated hall situated 60-85 m below the surface (Fig. 4). Grass, shrubs, and trees cover two dolines above the cave. The remaining surface is made up of fertilized land. The F/N boundary has not changed for at least 160 years (2nd Military Survey, 1852). The surface above the

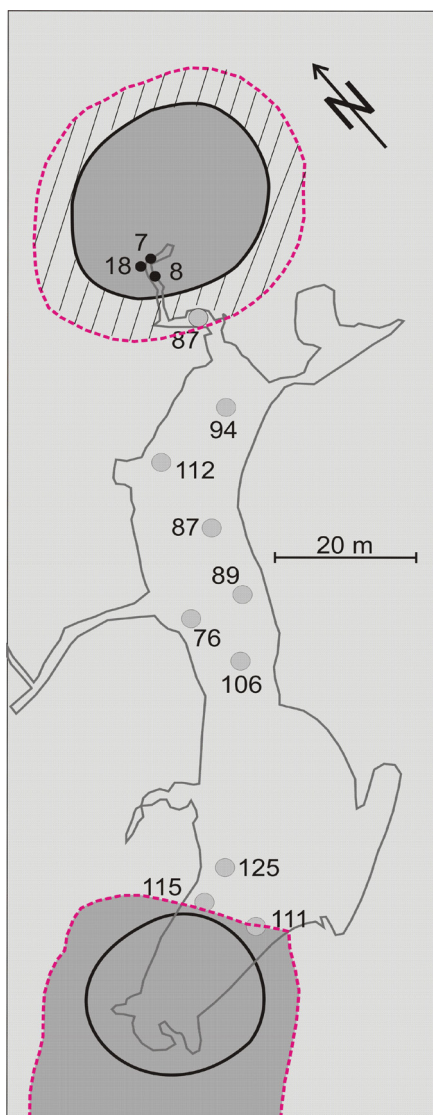


Fig. 4. Land use, cave and doline outlines, and nitrate concentration (mg/l) in drips in the Spolecnak Cave. Cave outline modified from Hromas et al. (2009). Fertilized land covers the whole area, except the dolines. Drips were sampled in June 2010. See Fig. 3 for legend.

cave is relatively flat (gradient 0.02), except for the sides of the dolines.

Holstejska Cave is a huge cave passage filled to its ceiling with gravels. It is situated 25-30 m below the surface (Fig. 5). Cavers dig small galleries crossing the

sedimentary fill in various directions. The eastern part of cave has been overlain by forest for at least 160 years. The central and western parts of the cave were once situated below fertilized land, which was converted to grassland in 2003 (Fig. 5). The surface above the cave is flat (gradients 0.05-0.08), except for the entrance portion of the cave, which is below a steep slope.

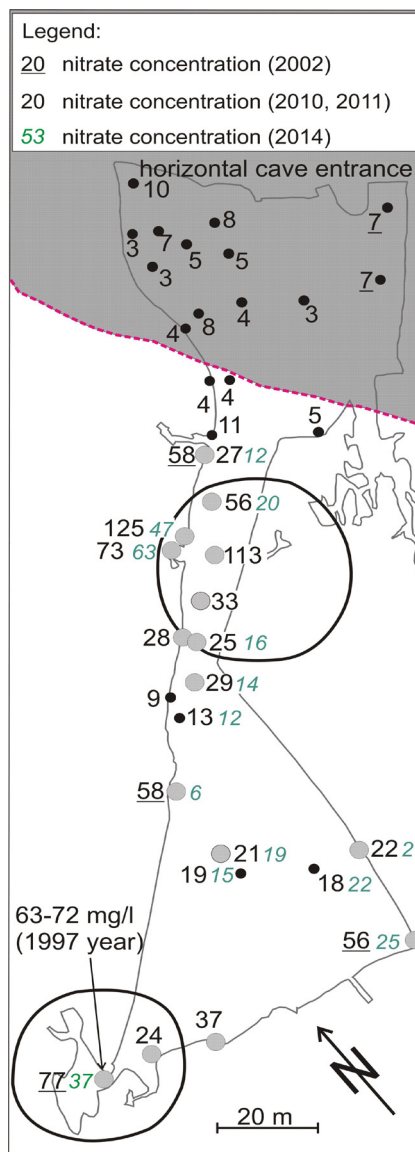


Fig. 5. Land use, cave and doline outlines, and nitrate concentration in drips in the Holstejska Cave. Cave outline modified from Hromas et al. (2009). Nitrate concentration was monitored in one drip in 1997 (Himmel, 1997) and several drips in 2002 (Jančo, 2002). See Fig. 3 for legend. White area was converted to grassland in 2003.

METHODS

Using GIS, the caves were projected onto a land use map, and those cave passages within distances up to 160 m from the F/N boundary were selected for the study. The drips were located in the caves, and the direct horizontal distance between the drips and the F/N boundary was measured in a GIS. Those distances from the F/N boundary to within fertilized lands are marked by positive numbers, and those distances from the F/N boundary to within unfertilized lands are marked by negative numbers (Fig. 2).

The sampling and analyses of these drips were done over several periods. In 1991-95 and 2002 the

drips were sampled to 1 liter PE bottles. Several tens of drips were sampled, some of them on a monthly basis. Drip intensity was measured either by the number of drips per minute or by the volume of water collected per unit time. The nitrate concentration was analyzed by photometry in the laboratory of the Nature Conservation Agency of the Czech Republic.

Drips sampled in 2007 and later were collected in PP buckets rinsed by deionized water placed below the drips for 24 hours. Sampling in the Amaterska Cave was performed in July of 2007 and March of 2014. Sampling in the Spolecnak Cave was performed in June, 2010. As there were no changes in the land-use pattern, sampling was not repeated in this cave. Sampling in the Holstejska Cave was performed in June of 2010, June of 2011, and March of 2014. All cave drips were sampled within one or two days, in order to suppress possible temporal variations. The sampled water was filtered by Nalgene vacuum filtration system (0.45 μm Millipore filter) and stored in Nalgene HDPE bottles in the cold. The nitrate, chloride, and sulfate concentrations were measured by HPLC Dionex (USA) in the Laboratories of the Geological Institutes of the Charles University in Prague. The analytical error was 1-3% RSD (depending on the concentration, calculated from 3 replicates). A blank was used during the entire analytical process, with its value subtracted from the measured values.

The nitrate concentrations in each cave were plotted against their distance from the F/N boundary. Envelope curves were constructed, which encompass maximum nitrate concentrations on the forest side of the boundary, and minimum nitrate concentrations at the fertilized side of boundary (Fig. 6a). One outlier is discussed in chapter results and discussion. The maximum range of horizontal transport of nitrate (H_{max}) was defined by the greatest distance between the F/N boundary and envelope curves (Fig. 6). To compare the horizontal transport in the various caves, which differ in the thickness of their vadose zones, the H_{max} was divided by the thickness (T) of the vadose zone above each cave (Fig. 2).

The mean residence time of nitrate in the vadose zone was determined from the time lag between the change of fertilized land to grassland, and the time when the nitrate concentration in the drip decreased to 55 mg/l, which is roughly the midpoint between the nitrate concentration in the drips below forest/grassland and fertilized land (Table 1). Such a definition of the mean residence time is the analog of tracer tests, with an instantaneous decrease of constant concentration C1 at the input point to another constant value C2 (step-injection; Käss et al., 1998). In such a case, the mean residence time is defined as the time period between the change of concentration at the input point and the time when the concentration at the sampling point reaches the midpoint between the C1 and C2 concentrations (Käss et al., 1998). This definition of mean residence time is valid for a conservative tracer in various environments, including the karst vadose zone. Nitrate is commonly considered a conservative tracer in a karst vadose zone (Jeannin et al., 2007).

C1 is the average concentration in drips below fertilized lands, while C2 is the average concentration of nitrates in drips below forests. As there are only minor temporal variations of C1 and C2 concentrations (*Temporal variation of nitrate concentration and nitrate mean residence time in the vadose zone*), and the change in landuse was abrupt, this approach should be applicable for selected areas.

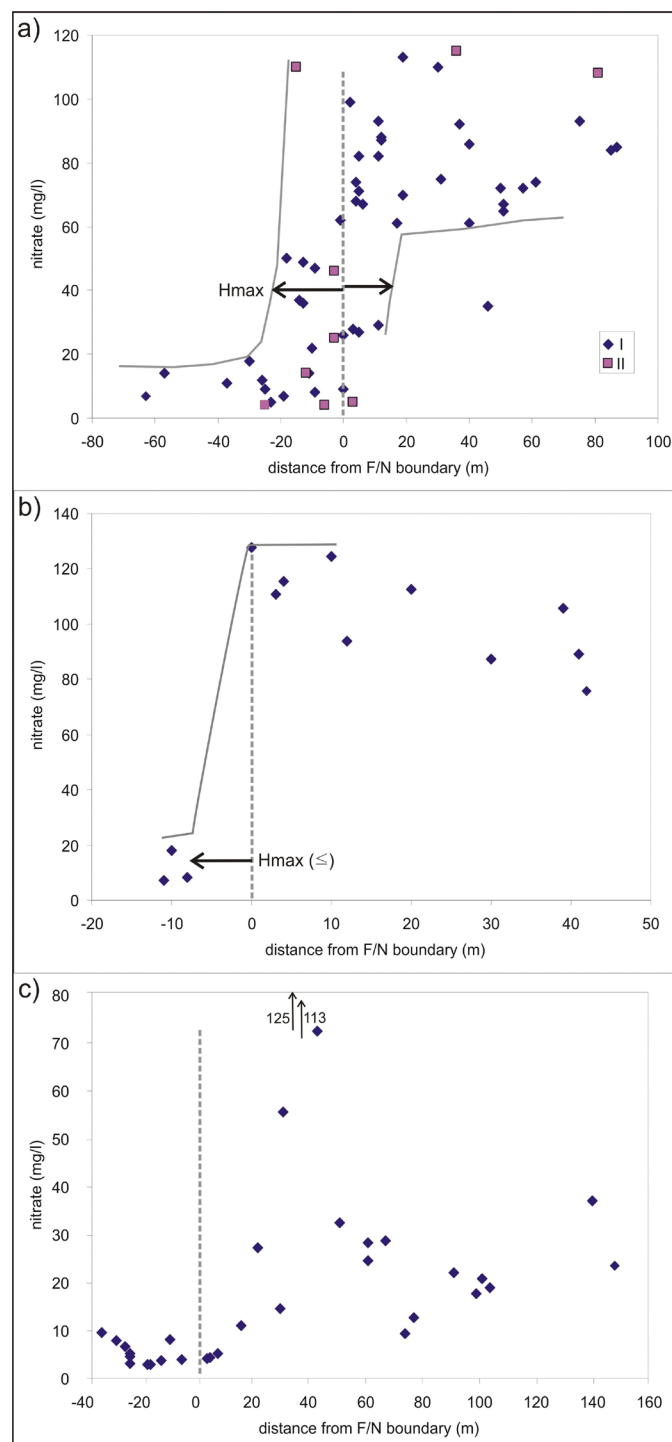


Fig. 6. Nitrate concentration in drips plotted over the distance from the F/N boundary. a) Amaterska Cave; b) Spolecnak Cave; c) Holstejska Cave; I) Drips sampled on the boundary between fertilized land converted into grassland in 1998 and forest; II) Drips sampled on the boundary between presently fertilized land and forest. The distance from the boundary towards fertilized land (at the present or in the past) is measured in positive numbers, and the distance towards forest (never fertilized land) is in negative numbers. Dashed line shows the position of the F/N boundary. Grey continuous lines show the data envelope. Arrows in diagram c show nitrate concentrations exceeding diagram range.

RESULTS AND DISCUSSION

Horizontal component of nitrate transport in the vadose zone

Nitrate concentrations were analyzed from 60 drips in the Amaterska Cave, sampled in June, 2007. The mean nitrate concentration in the drips in the areas never fertilized was 10 mg/l; in the area originally fertilized but converted to grassland in 1998 it was 78 mg/l; and in presently-fertilized land it was 80 mg/l (Table 1). The differences in nitrate concentrations between the two latter land-use categories are negligible (Fig. 6a). Therefore, the F/N boundary is enclosing the land never fertilized (Fig. 4). A abrupt change in the nitrate concentration exists at the F/N boundary (Fig. 3). Concentrations typical for forest change into concentrations typical for fertilized land within a few tens of meters (Fig. 6a). H_{max} is 18 m, and H_{max}/T is 0.15-0.17 in the 105-120 m thick vadose zone. One outlier in Fig 6a indicates that either ~5% of the flow has a higher horizontal component or water in the drip has lower residence time so that nitrates were already leached from vadose zone. The spatial distribution of the nitrate concentrations does not suggest that horizontal transport is higher in some directions (Fig. 3). The existence of dolines had no observable effect on the horizontal nitrate transport or on concentration.

The nitrate concentration was analyzed in 13 drips in the Spolecnak Cave, sampled in June of 2010. Abrupt changes in the nitrate concentration exist at the F/N boundary (Fig. 6b). Low concentrations below the doline change into concentrations typical for fertilized lands within less than 10 meters (Fig. 6b). H_{max} is <10 m, and H_{max}/T is <0.17 in the 60-85 m thick vadose zone. The mean nitrate concentration in the area never fertilized is 11 mg/l, in the fertilized land used through the present time it is 104 mg/l (Table 1).

The nitrate concentration was analyzed in 33 drips in the Holstejska Cave, sampled in June of 2010, 2011, and March of 2014. Changes in the nitrate concentration at the F/N boundary is not pronounced. After the conversion of fertilized land to grassland in 2003, the nitrate concentration dropped to values close to those typical for forested areas in some drips prior to 2010. Therefore, the H_{max} cannot be determined (Fig. 6c). The mean nitrate concentration in those areas which were never fertilized was 5 mg/l; with the case of fertilized lands converted into grassland it was 37 mg/l (Table 1).

The nitrate concentrations found in drips below forests mostly fall within the range of present-day background concentrations summarized by Panno et al. (2006). Slightly increased nitrate concentrations were detected in drips below a former tree nursery, due to occasional fertilizing (Fig. 3). The low horizontal component of nitrate transport in the caves indicates that the grass strip above the cave spaces need only overlap the cave by 20 m on both sides to ensure that

the vadose zone in a cave will not be affected by nitrate from the fertilized land adjacent to the grass strip.

Temporal variation of nitrate concentration and nitrate mean residence time in the vadose zone

Nitrate concentrations were measured on a monthly basis at several drips in the Amaterska Cave below fertilized land, forest, as well as a tree nursery during the hydrologic years 1992-94 (Fig. 7; drip position Fig. 1). The mean concentrations in the drips below fertilized lands were 61-105 mg/l (drips R1, R2, Z12, and Z13; Fig. 7). Variability of the nitrate concentrations in the drips was low (coefficient of variation, CV, 5-9%); on the other hand, the variation of the drips' flow rates was considerable (CV 39-94%). No relationship was observed between the nitrate concentration and drip flow rates. Nitrate concentrations steadily increased in the case of one drip; in the case of three other drips, no trend in nitrate concentration was observable over a three year period. Nitrate concentration below forest was 3 ± 1 mg/l (drip RAZ). The mean nitrate concentration below the tree nursery was 13 mg/l and the CV was 13% (drip ABS). Nitrate concentration below the tree nursery was probably elevated, when compared to a grown forest, due to the fertilizers applied. The absence of annual cycling of nitrate concentrations in the case of all drips indicates that the dominant flow component containing nitrate has a residence time of several years (or more). The high variability of drip rates demonstrates the fast propagation of hydraulic responses via the vadose zone. The hydraulic response often propagates much faster than water particles. Situation where the flow rate varies, but the chemical signal is stable is very common (Perrin et al., 2003b).

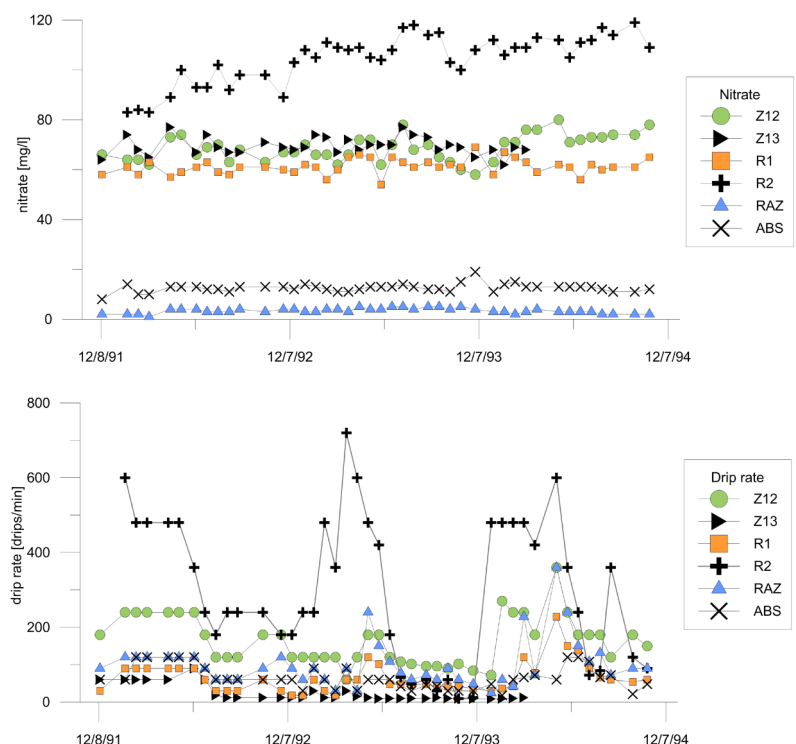


Fig. 7. Nitrate concentration in drips sampled at monthly periods in the Amaterska Cave during hydrologic years 1992-94 (upper panel); Drip flow rate. Drips: Z12, Z13, R1, and R2 - fertilized land, RAZ - forest, ABS - tree nursery (lower panel).

The nitrate concentrations, occasionally measured in the Amaterska Cave drips in 1995, are shown in Fig. 3. Nitrate concentrations in the drips measured in 1995 and 2007 are similar, even below those areas converted to grassland in 1998. Surprisingly, the nitrate concentration did not significantly decrease within the 9 year period after conversion of the fertilized land to grassland. Twenty three drips sampled in March of 2014 below the area converted to grassland in 1998, showed only a 17% decrease (on average) in nitrate concentration, compared to 2007 (Fig. 3). The maximum decrease of nitrate concentration was 45%. In 76% of the drips, the nitrate concentrations were still above 55 mg/l in 2014. This shows that the mean residence time of nitrate in the 105-120 m thick vadose zone above the Amaterska Cave generally exceeds 16 years.

In case of the Holstejska Cave, the drips sampled in 2010 below land originally fertilized but converted to grassland in 2003, generally showed nitrate concentrations at only 20-30 mg/l; significantly less than the concentration measured in 2002, prior to the conversion to grassland (Fig. 5). A different situation was found below the doline, in the central part of the cave, where a nitrate concentration up to 125 mg/l was observed. However, nitrate concentrations measured in March of 2014 were significantly decreased, even below the doline mentioned above. This demonstrates that the mean residence time of nitrate in the vadose zone in most places above the Holstejska Cave is shorter than 7 years; except in the area below the central doline, where the residence time of the nitrate is closer to 10 years. The difference in the residence times of nitrate between the Amaterska and Holstejska caves can be explained by the difference in the thicknesses of the vadose zone. The vadose zone in the case of the Amaterska Cave is ~4 times thicker than in the Holstejska Cave; and thus theoretically can take four times longer to leach nitrate. For the Amaterska Cave, this means a theoretical nitrate residence time of 28-40 years. In reality, the residence time in the Amaterska Cave's vadose zone will probably be smaller, as larger porosity is to be expected in the epikarst and upper region of the vadose zone, than in the lower portion (Williams, 2008).

Horizontal transport data derived from tracer tests

To identify those factors potentially affecting the horizontal transport of a dissolved tracer in the karst vadose zone, the data from available artificial tracer tests from the vadose zone of the Moravian Karst, as well as several other areas in temperate climates, were analyzed (Table 2). Before discussing the results of the artificial tracer tests, it is important to mention the most significant differences between the use of environmental and artificial tracers. Nitrate as a typical environmental tracer enters the vadose zone with natural diffuse recharge over the entire area anywhere nitrate is intensively applied (non-point source) for a period of many decades. Thus, the nitrate had enough time to arrive at all places where water from fertilized land flows. This is different from artificial tracers, applied to one or a few tens

of discrete points (point source), and sampled over a limited time period. An artificial tracer is often injected with an amount of water, which exceeds many times the natural recharge. This excess water may significantly increase the horizontal spread of the tracer. The much smaller concentration contrast in the case of nitrate, compared to an artificial tracer, means that an admixture <10% will probably be undetectable in drips in the case of nitrate; while in the case of artificial tracers, much smaller admixtures can be detected (Käss et al., 1998).

Himmel (2009) performed Tracer test A1 in the vadose zone above the Ochoz Cave, which is in southern part of the Moravian Karst (Table 2). KBr was injected into 33 holes situated in a 30 by 30 m square array. Injection holes were dug below the base of the soil and in the karren field. Only 0.3 l of water was used for each injection point, which does not exceed natural recharge. The H_{max}/T was 0.17 in the 60 m thick vadose zone, with a bedding plane dip of 10-20° (Table 2). Other tracer experiments (A2a and A2b) were performed above the Pekárna Cave (0.5 km SSE of the Ochoz Cave) within a 10 m thick vadose zone, using KBr injected at the natural recharge rate (5 l). The H_{max}/T was 0.2 (Himmel, 2009); the previous year the H_{max}/T was 0.4 at the same site, when an excess recharge rate was used (750 l at a single injection point). In the case of an excess recharge rate, the tracer was probably transported via additional pathways in the vadose zone, which would have stayed dry under a natural recharge rate, and thus displaying a higher H_{max}/T .

Tracer test A3 disclosed a H_{max}/T of ~0.5 in the 10 m thick fractured overburden at Sinji Vrh, Slovenia (Veselic & Čenčur Curk, 2001). The bedding plane's dip was 5-30°. Kogovšek & Šebela (2004) described two tracer tests in the 100 m thick vadose zone above the Postojna Cave in Slovenia (tracer test A4). During the first tracing, 5 m³ of water was injected with uranine (excess recharge rate); while in the second case, uranine was transported with rain alone (natural recharge rate). The H_{max}/T was 0.33 for both experiments. In this case, the large amount of water injected artificially did not increase the horizontal spreading of the tracer, but instead increased the tracer concentration (by 10,000 ×) in one drip.

Tracer test A6 reached a H_{max}/T ~0.7 at the Gännsbrunnen test site in the Swiss Jura Mountains (Flynn & Sinreich, 2010; Sinreich & Flynn, 2011) in an artificial gallery located 10 m below the ground surface, with a shallow soil and fissured Jurassic limestone dipping 0-45° (Flynn & Sinreich, 2010). The injection of tracers (fluorescent dye, Br⁻, I⁻, microorganisms, etc.) was performed on the surface via a sprinkler with short pulse tests, as well as a prolonged injection test (flow rate 55 mm/hour for up to 6 hours, excess recharge rate).

A different type of flow pattern, with a high H_{max}/T , was described by Bottrell & Atkinson (1992) in the White Scar Cave (Great Britain), as well as by Motyka et al. (2001) in the Zakrzówek horst (Poland), in horizontally bedded Carboniferous and Jurassic limestones, respectively. In both cases, the tracer

Table 2. H_{max}/T in studied tracer tests. E - environmental tracer; A - artificial tracer test.

No.	Locality	Tracer	T (vadose zone thickness)	H_{max} (m)	H_{max}/T	Recharge rate	Reference
E1	Amaterska Cave, CR	nitrate	105-120	18	0.17	natural	this paper
E2	Spolecnak Cave, CR	nitrate	60-85	<10	<0.17	natural	this paper
A1	Ochoz Cave, CR	bromide	60	10	0.17	natural	Himmel (2009)
A2a	Pekárna Cave, CR	bromide	10	2	0.2	natural	Himmel (2009)
A2b	Pekárna Cave, CR	bromide	10	4	0.4	excess	Himmel (2009)
A3	Sinji Vrh, Slovenia	uranine	10	5	0.5	natural	Veselic & Čenčur Curk (2001)
A4	Postojna Cave, Slovenia	uranine	100	33	0.33	natural	Kogovšek & Šebela (2004)
A5	Pivka Jama, Slovenia	uranine	40	20	0.5	excess	Kogovšek (1997)
A6	Gännsbbrunnen, Switzerland	bacteriophages	10	7	0.7	excess	Flynn & Sinreich (2010)
A7	White Scar Cave, Yorkshire, GB	fluorescent tracers	45-90	140	1.6-3.1	excess	Bottrell & Atkinson (1992)
A8	Zakrzówek horst, Poland	chloride, uranine	5-15	120	8-24	natural	Motyka et al. (2001)
A9	GB Cave, Mendip Hills, GB	fluorescent tracers	<10	80	8	excess	Smart & Friederich (1986)

apparently moved via discrete paths to several distant drips, while it did not arrive at many drips in between. In both cases, the largest H_{max}/T was noted in tracer tests performed after heavy rains, which could supply large amounts of recharge to the epikarst below the thin soil. In the Zakrzówek horst, the H_{max}/T was between 8-24. H_{max} was 120 m in the 5-15 m thick cave overburden. H_{max}/T reached 1.6-3.1 in the 45-90 m thick overburden above the White Scar Cave. Only 5 l of water was used at the injection point in the tracer tests in Poland. Thus, at least in Poland, the effect of artificial injection clearly did not cause a very high H_{max}/T .

A large horizontal spreading of the tracer at shallow depths (less than 10 m), in a wide front with a $H_{max}/T > 8$, described by Smart & Friederich (1986) was based on 6 tracer experiments in the Mendip Hills, Great Britain, in an area with disturbed and mined ground (tracer A9). The tracer was injected into dolines. Part of the tracing was artificially supplied by up to 4 m³ of water, but the authors reported a similar horizontal spreading of the tracer under a natural recharge rate from other tracer experiments.

Possible factors affecting horizontal transport

A low H_{max}/T of between 0.1 and 0.6 was observed in the Czech and Slovenian areas (E1-2, A1-A5; Fig. 8, Table 2), even for injections greatly in excess of the natural recharge rate (tracer tests A2b, A4). In both karst areas, the latest phase of continuous karstification has lasted at least since the Pliocene

(Kadlec et al., 2001; Pruner et al., 2010). Neither area was ever glaciated. A low H_{max}/T might be the result of both long-term epikarst development and an increase of the capacity of vertical drains, resulting in predominantly vertical transport within the vadose zone.

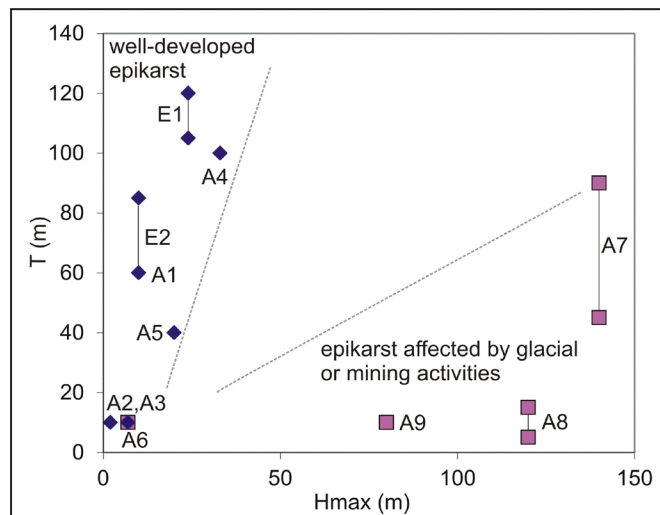


Fig. 8. Comparison of H_{max} and T (maximum) from different areas. Blue diamonds - well-developed epikarst (Moravian and Slovenian karsts); red squares - areas where epikarst was affected by glacial and mining activity.

Tracer tests A7 and A8 were performed in areas that were glaciated in the past (Clark et al., 2003), so that the epikarst zone might have been partly removed or sealed by glacier activity. In both areas, the shallow

soil does not store much water after heavy rains, and large amounts of water are recharged into the limestone environment, which does not effectively drain downward, and thus the H_{\max}/T is high (1.6-24). Tracer test A9 was performed in area affected by mining activities, which might also have negatively affected the epikarst. These observations indicate that the long-term evolution of the epikarst results in a smaller horizontal component of tracer transport in the karst vadose zone as suggested by Williams (2008). The effects of other factors (surface inclination, lithology, fracturing style, dipping of bedding, land-use type, etc.) cannot be assessed due to a dearth of information.

CONCLUSION

Nitrate concentrations in drips were studied in three caves with a 25-120 m thick vadose zone in the Moravian Karst, Central Europe during several periods since 1992. Each cave runs below the land-use boundary between fertilized land and forest/grassland, enabling the study of the horizontal component of nitrate transport in the vadose zone. While drips below forested and other never-fertilized land-use categories showed average nitrate concentrations of 5-11 mg/l, those drips below presently-fertilized land showed a mean nitrate concentration of 104 mg/l. Slightly increased nitrate concentrations were detected in drips below a former tree nursery. Portions of the fertilized land were turned into grassland in 1998 and 2003 in order to improve the drip water chemistry. Cave drips were sampled prior to and after the land use change. A considerable residence time of nitrate was observed in the vadose zone. In the case of the 25-30 m thick vadose zone, the mean residence time of nitrate was between <7 and 10 years. In the case of the 105-120 m thick vadose zone, the mean nitrate residence time exceeded 16 years at 76% of the drips. Temporal variability of the nitrate concentration in the drips was low (coefficient of variation, CV = 5-9%), while variation of the drip's flow rates was considerable (CV = 39-94%). The maximum range of the horizontal component of nitrate transport (H_{\max}) reaches 18 m in the 105-120 m thick vadose zone. In order to compare the horizontal components of tracer transport in various caves with different thicknesses of their vadose zones, H_{\max} was normalized by the vadose zone thickness (T). In the Moravian Karst, the H_{\max}/T of nitrate does not exceed 0.17.

To identify the possible factors affecting horizontal transport in the karst vadose zone, the data from available artificial tracer tests from the vadose zone of the Moravian Karst and several other areas in temperate climates were analyzed. A low H_{\max}/T of between 0.1 and 0.6 is typical for the Czech and Slovenian karst areas, which were unaffected by glaciations, and with an epikarst evolving since at least the Pliocene. On the contrary, a high H_{\max}/T (1.6-24) was observed in areas affected by glaciations or mining activities, where the epikarst zone might be partly removed or sealed, and where shallow soils do not store much water after heavy rains. These limited observations indicate that the long-term evolution of epikarst

may result in a smaller horizontal component of transport in the karst vadose zone. More data on the horizontal transport of tracers within the vadose zone are needed in order to test this potential relationship. The low horizontal component of nitrate transport in caves indicates that the grass strip above cave spaces in the Moravian Karst only needs to have an overlap of 20 m to ensure that the vadose zone in the cave will not be affected by nitrate from fertilized land adjacent to the grass strip. After turning the fertilized land into grass strips, it may take up to 20-40 years to decrease the nitrate concentration in the drips to close to present-day background concentrations in the ~100 m thick vadose zone. As karst settings are highly variable, the low horizontal transport and high residence time of nitrates in the vadose zone should not be applied to other areas until properly tested in the area of interest.

ACKNOWLEDGEMENTS:

The authors are indebted to I. Balák, L. Štefka, A. Tůma, and K. Šebková from the **Nature Conservation Agency** for their long-term support of the cave drip research; and to E. W. Peterson and two anonymous reviewers for their valuable comments on the manuscript. The research was supported by Project No. 80509 of the Grant Agency of Charles University, along with research project MSM00216220855, and also by Ceskomoravsky Cement a.s.

REFERENCES:

- Atkinson T.C., Hess J.W. & Harmon R.S., 1985 – *Stable isotope variations in recharge to a karst aquifer, Yorkshire dales, England*. Annales de la Société Géologique de Belgique, **108**: 225.
- Balák I., Jančo J., Štefka L. & Bosák P., 1999 – *Agriculture and nature conservation in the Moravian Karst (Czech Republic)*. International Journal of Speleology, **28B**: 71-88. <http://dx.doi.org/10.5038/1827-806X.28.1.5>
- Bottrel H.A. & Atkinson T.C., 1992 – *Tracer study of flow and storage on the unsaturated zone of a karstic limestone aquifer*. In: Hötzl, H., Werner, A. (Eds.) - *Proceedings of the 6th international symposium on water tracing*. Balkema. Rotterdam: 207-211.
- Boyer D.G. & Pasquarell G.C., 1995 – *Nitrate concentrations in karst springs in an extensively grazed area*. Water Resources Bulletin, **31**: 729-736. <http://dx.doi.org/10.1111/j.1752-1688.1995.tb03397.x>
- Bruthans J. & Zeman O., 2003 – *Factors controlling exokarst morphology and sediment transport through caves: comparison of carbonate and salt karst*. Acta Carsologica, **32**: 83-99.
- Clark C.D., Evans D.J.A., Khatwa A., Bradwell T., Jordan C.J., Marsh S.H., Mitchell W.A. & Bateman M.D., 2003 – *Map and GIS database of glacial landforms and features related to the last British Ice Sheet*. Boreas, **33**: 359-375. <http://dx.doi.org/10.1111/j.1502-3885.2004.tb01246.x>
- Dvořák V. & Melichar R., 2002 – *The outline of tectonic structure of the northern part of The Moravian Karst*. Geological research in Moravia and Silesia in 2001: 51-54 (in Czech).
- Einsiedl F., 2005 – *Flow system dynamics and water storage of a fissured-porous karst aquifer characterized by artificial and environmental tracers*. Journal of Hydrology, **312**: 312-321. <http://dx.doi.org/10.1016/j.jhydrol.2005.03.031>

- Ford D. & Williams P., 2007 – Karst hydrogeology and geomorphology. John Wiley & Sons, Chichester, 562 p. <http://dx.doi.org/10.1002/9781118684986>
- Flynn R.M. & Sinreich M., 2010 – *Characterization of virus transport and attenuation in epikarst using short pulse and prolonged injection multi-tracer testing*. Water Research, **44**: 1138-1149. <http://dx.doi.org/10.1016/j.watres.2009.11.032>
- Himmel J., 1997 – *Contribution for understanding the flux of nitrate in karst catchment*. Czech Speleological Society, Speleoforum, **14**: 18-20 (in Czech).
- Himmel J., 2009 – *Research of water movement through vadose zone by tracer tests in the Ochozská and Pekárna caves in the the Moravian Karst*. Czech Speleological Society, Speleoforum, **28**: 131-135 (in Czech).
- Hromas J., 2009 – *Jeskyne*. Agentura ochrany přírody a krajiny CR and EkoCentrum, Praha, 608 p. (in Czech).
- Igbal M.Z. & Krothe N.C., 1995 - *Infiltration mechanism related to agricultural waste transport through the soil mantle to karst aquifer of southern Indiana, USA*. Journal of Hydrology, **164**: 171-172. [http://dx.doi.org/10.1016/0022-1694\(94\)02573-T](http://dx.doi.org/10.1016/0022-1694(94)02573-T)
- Jančo I., 2002 - *Base line monitoring of dissolved solids in drips of Holstejn Cave prior turning the agricultural land to grassland*. Cortusa, Blansko: 12 p. (in Czech).
- Jeannin P.Y., Groves C. & Häuselmann P., 2007 - *Speleological investigations*. In: Goldscheider N. & Drew D. (Eds.) - *Methods in Karst Hydrogeology*. International Contributions to Hydrogeology. Taylor & Francis, London: 25-44.
- Kadlec J., Hercman H., Beneš V., Šroubek P., Diehl J.F. & Granger D., 2001 – *Cenozoic history of the The Moravian Karst (Northern segment): Cave sediments and karst morphology*. Acta Musei Moraviae, Scientiae Geologicae, **84**: 111-160.
- Käss W., Behrens H., Himmelsbach T., Hötzl H., Hunkeler D., Leibundgut C.H., Moser H., Rossi P., Schultz H.D., Stober I. & Werner A., 1998 – *Tracer technique in geohydrology*. Balkema, Rotterdam, 581 p.
- Kastrinos J.R. & White W.B., 1986 – *Seasonal, Hydrogeologic, and Land-Use Controls on Nitrate Contamination of Carbonate Ground Waters*. In: *Proceedings of the Environmental Problems in Karst Water*. National Well Association: 88-114.
- Katz B.G., Chelette A.R. & Pratt T.R., 2004 – *Use of chemical and isotopic tracers to assess nitrate contamination and ground-water age, Woodville Karst Plain, USA*. Journal of Hydrology, **289**: 36-61. <http://dx.doi.org/10.1016/j.jhydrol.2003.11.001>
- Klimchouk A.B., 2000 – *The formation of epikarst and its role in vadose speleogenesis*, In: Klimchouk A.B., Ford D.C., Palmer A.N. & Dreybrodt W. (Eds.), *Speleogenesis. Evolution of Karst Aquifers*. Huntsville: National Speleological Society: 91-99.
- Kluge T., Riechelmann D.F.C., Wieser M., Spötl C., Sültenfuß J., Schröder-Ritzrau A., Niggemann, S. & Aeschbach-Hertig W., 2010 – *Dating cave drip water by tritium*. Journal of Hydrology, **394**: 396-406. <http://dx.doi.org/10.1016/j.jhydrol.2010.09.015>
- Kogovšek J., 1997 – *Water tracing tests in vadose zone*. In: Kranjc A., (Ed.) - *Tracer Hydrology*. Balkema, Rotterdam: 167-173.
- Kogovšek J. & Šebela S., 2004 – *Water tracing through the vadose zone above Postojnska Jama, Slovenia*. Environmental Geology, **45**: 992-1001. <http://dx.doi.org/10.1007/s00254-003-0958-z>
- Motyka J., Rózkowski K. & Górny A., 2001 – *Results of tracer experiments in the zone of aeration on limestones of Zakrzówek horst (Cracow, S Poland)*. In: *7th conference on Limestone Hydrology and Fissured Media*. Besancon: 257-260.
- Panno S.V., Kelly W.R., Martinsek A.T. & Hackley K.C., 2006 – *Estimating background and threshold nitrate concentrations using probability graphs*. Ground Water, **44**: 697-709. <http://dx.doi.org/10.1111/j.1745-6584.2006.00240.x>
- Perrin J., Jeannin P.Y. & Zwahlen F., 2003a – *Epikarst storage in a karst aquifer: a conceptual model based on isotopic data, Milandre test site, Switzerland*. Journal of Hydrology, **279**: 106-124. [http://dx.doi.org/10.1016/S0022-1694\(03\)00171-9](http://dx.doi.org/10.1016/S0022-1694(03)00171-9)
- Perrin J., Jeannin P.Y. & Zwahlen F., 2003b – *Implications of the spatial variability of infiltration-water chemistry for the investigation of a karst aquifer: a field study at Milandre test site, Swiss Jura*. Hydrogeology Journal, **11**: 673-686.
- Peterson E.W., Davis R.K., Brahana J.V. & Orndorff H.A., 2002 – *Movement of nitrate through regolith covered karst terrain, northwest Arkansas*. Journal of Hydrology, **256**: 35-47. [http://dx.doi.org/10.1016/S0022-1694\(01\)00525-X](http://dx.doi.org/10.1016/S0022-1694(01)00525-X)
- Pronk M., Goldscheider N., Zopfi J. & Zwahlen, F., 2009 – *Percolation and particle transport in the unsaturated zone of a karst aquifer*. Ground Water, **47**: 361-369. <http://dx.doi.org/10.1111/j.1745-6584.2008.00509.x>
- Pruner P., Zupan-Hajna N., Mihevc A., Bosák P., Venhodová D. & Schnabl P., 2010 – *Paleomagnetic and rockmagnetic studies of cave deposits from Račiška pečina and Pečina v Borštu caves (Classical Karst, Slovenia)*. Studia Geophysica Geodaetica, **54**: 28-48. <http://dx.doi.org/10.1007/s11200-010-0002-1>
- Ravbar N. & Goldscheider N., 2009 – *Comparative application of four methods of groundwater vulnerability mapping in a Slovene karst catchment*. Hydrogeology Journal, **17**: 725-733. <http://dx.doi.org/10.1007/s10040-008-0368-0>
- Sinreich M. & Flynn R.M., 2011 – *Comparative tracing experiments to investigate epikarst structural and compositional heterogeneity*. Speleogenesis and evolution of karst aquifers, **10**: 60-67.
- Swarzova M., Zatloukalova I., Štelcl J. & Faimon J., 2006 – *Sedimentárně petrografická charakteristika půdních profilů na vybraných lokalitách Moravského krasu*. Geological research in Moravia and Silesia in 2005: 25-28 (in Czech).
- Schwartz K., Barth J.A.C., Postigo-Rebollo C. & Grathwohl P., 2009 – *Mixing and transport of water in a karst catchment: a case study from precipitation via seepage to spring*. Hydrology and Earth System Sciences, **13**: 285-292. <http://dx.doi.org/10.5194/hess-13-285-2009>
- Smart P.L. & Friederich H., 1986 – *Water movement and storage in the unsaturated zone of a maturely karstified carbonate aquifer, Mendip Hills, England*. In: *Proceedings of the Environmental Problems in Karst Terrains and their Solutions Conference*, Bowling Green, Kentucky: 59-87.
- Taraba J., 1976 – *Final report on regional hydrogeology study*. – Geotest, Brno, 257 p. (in Czech).
- Trček B., 2007 – *How can the epikarst zone influence the karst aquifer behavior?* Environmental Geology, **51**: 761-765. <http://dx.doi.org/10.1007/s00254-006-0387-x>
- USGS, 2002 - *The quality of our nation's waters – Nutrients and pesticides*. USGS Circular 1225. Washington, D.C.: U.S. Government Printing Office.

- Veselič M. & Čenčur Curk B., 2001 – *Test studies of flow and solute transport in the unsaturated fractured and karstified rock on the experimental field site Sinji Vrh, Slovenia*. In: Seiler K.P. & Wohnlich S. (Eds.), *Proceedings of the 31st Congress of International Association of Hydrogeologists*, Balkema, Lisse: 211-214.
- Williams P.W., 1983 – *The role of the subcutaneous zone in karst hydrology*. *Journal of Hydrology*, **61**: 45-67.
[http://dx.doi.org/10.1016/0022-1694\(83\)90234-2](http://dx.doi.org/10.1016/0022-1694(83)90234-2)
- Williams P. W., 2008 – *The role of the epikarst in karst and cave hydrogeology: a review*. *International Journal of Speleology*, **37**: 1-10.
<http://dx.doi.org/10.5038/1827-806X.37.1.1>
- Worthington R.H., Ford D.C. & Beddows P.A., 2000 – *Porosity and permeability enhancement in Unconfined carbonate aquifers as a result of solution*. In: Klimchouk A.B., Ford D.C., Palmer A.N. & Dreybrodt W. (Eds.) - *Speleogenesis: Evolution of Karst Aquifers*. Huntsville: National Speleological Society: 77-90.
- Žák K., Urban J., Čilek V. & Hercman H., 2004 – *Cryogenic cave calcite from several Central European caves; age, carbon and oxygen isotopes and a genetic model*. *Chemical Geology*, **206**: 119-136.
<http://dx.doi.org/10.1016/j.chemgeo.2004.01.012>
- 2nd Military Survey, 1836-1852, Austrian State Archive/Military Archive, Vienna, Austria.



Available online at scholarcommons.usf.edu/ijis

International Journal of Speleology

Official Journal of Union Internationale de Spéléologie



Speleoclimate dynamics in Santana Cave (PETAR, São Paulo State, Brazil): general characterization and implications for tourist management

Heros A. S. Lobo^{1*}, Paulo C. Boggiani², José A. J. Perinotto³

¹Department of Geography, Tourism and Humanities, Campus Sorocaba - UFSCar, Sorocaba, Brazil

²Departamento de Geologia Sedimentar e Ambiental, Instituto de Geociências - USP, São Paulo, Brazil

³Instituto de Geociências e Ciências Exatas, Universidade Estadual Paulista - Unesp, Rio Claro, Brazil

Abstract: Show caves provide tourists with the opportunity to have close contact with natural underground spaces. However, visitation to these places also creates a need for management measures, mainly the definition of tourist carrying capacity. The present work describes the results of climate monitoring and atmospheric profiling performed in Santana Cave (Alto Ribeira State and Tourist Park – PETAR, Brazil) between 2008 and 2011. Based on the results, distinct preliminary zones with different levels of thermal variation were identified, which classify Santana Cave as a warm trap. Two critical points along the tourist route (Cristo and Encontro Halls) were identified where the temperature of the locality increased by 1.3°C when tourists were present. Air flow from the inner cave to the outside occurs during the austral summer, and the opposite flow occurs when the outside environment is colder than the air inside the cave during the austral winter. The temperature was used to establish thresholds to the tourist carrying capacity by computing the recovery time of the atmospheric conditions after the changes caused by the presence of tourists. This method suggests a maximum limit of approximately 350 visits per day to Santana Cave. The conclusion of the study is that Santana Cave has an atmosphere that is highly connected with the outside; daily variations in temperature and, to a lesser extent, in the relative humidity occur throughout the entire studied area of the cave. Therefore, the tourist carrying capacity in Santana Cave can be flexible and can be implemented based on the climate seasonality, the tourism demand and other management strategies.

Keywords: show caves, cave management, tourism impacts, microclimate, tourist carrying capacity

Received 4 July 2014; Revised 17 October 2014; Accepted 21 November 2014

Citation: Lobo H.A.S., Boggiani P.C. and Perinotto J.A.J., 2014. Speleoclimate dynamics in Santana Cave (PETAR, São Paulo State, Brazil): general characterization and implications for tourist management. *International Journal of Speleology*, 44 (1), 61-73. Tampa, FL (USA) ISSN 0392-6672

<http://dx.doi.org/10.5038/1827-806X.44.1.6>

INTRODUCTION

Caves are the most attractive natural features of geotourism (Cigna & Forti, 2013) and speleotourism. Some caves receive up to 1,000,000 annual visitors, including for example show caves in Asia, Europe and North America (Cigna & Burri, 2000). In Brazil, the number of visitors in some famous show caves, such as Maquiné, Diabo, and Lago Azul, is comparatively small, i.e., between 30,000 and 70,000 visitors per year.

Research on cave tourism is required to prevent deterioration and aid in cave management. Previous studies have been conducted to identify the natural dynamic patterns that define the limits of human activities (Graefe et al., 1990; Calaforra et al., 2003). Among other needed investigations, such as those

concerning the biology of caves, the study of atmospheric dynamics provides the most useful information for use in setting limits on visitation (Calaforra et al., 2003; Cigna, 2004; de Freitas, 2010; Lobo et al., 2010). One way to understand the dynamics of the atmosphere is to measure and record air temperature and relative humidity at different points in the cave (Cigna, 2004; Luetscher & Jeannin, 2004), specifically in areas with and without tourists (Lobo et al., 2010; Šebela & Turk, 2014). This procedure identifies natural patterns of variation and human-induced changes (Hoyos et al., 1998; de Freitas, 2010). In some cases, more complex monitoring networks have been used that consider CO₂ variations, airflow, and atmospheric pressure (e.g., Hoyos et al., 1998; Pflitsch & Piasecki, 2003; Luetscher & Jeannin, 2004).

Although cave atmosphere studies provide scientific standards for the management of show caves, they do not prevent disagreements between scientists, preservationists and tourism stakeholders with purely commercial interests regarding the limits of tourist use. These conflicts are common, and management is one way to harmonize the diverse interests in caves (Lobo et al., 2013), including both tourism and conservation. Moreover, the findings of environmental studies (Cigna, 2002) and ongoing tourist demand (Šebela & Turk, 2014) are crucial to the logical and technical basis of tourism cave management.

Based on atmospheric monitoring conducted in Santana Cave (southeastern Brazil) over three years (2009, 2010 and 2011), this study investigates the associated human impacts and shows the definition of tourist carrying capacity of this cave.

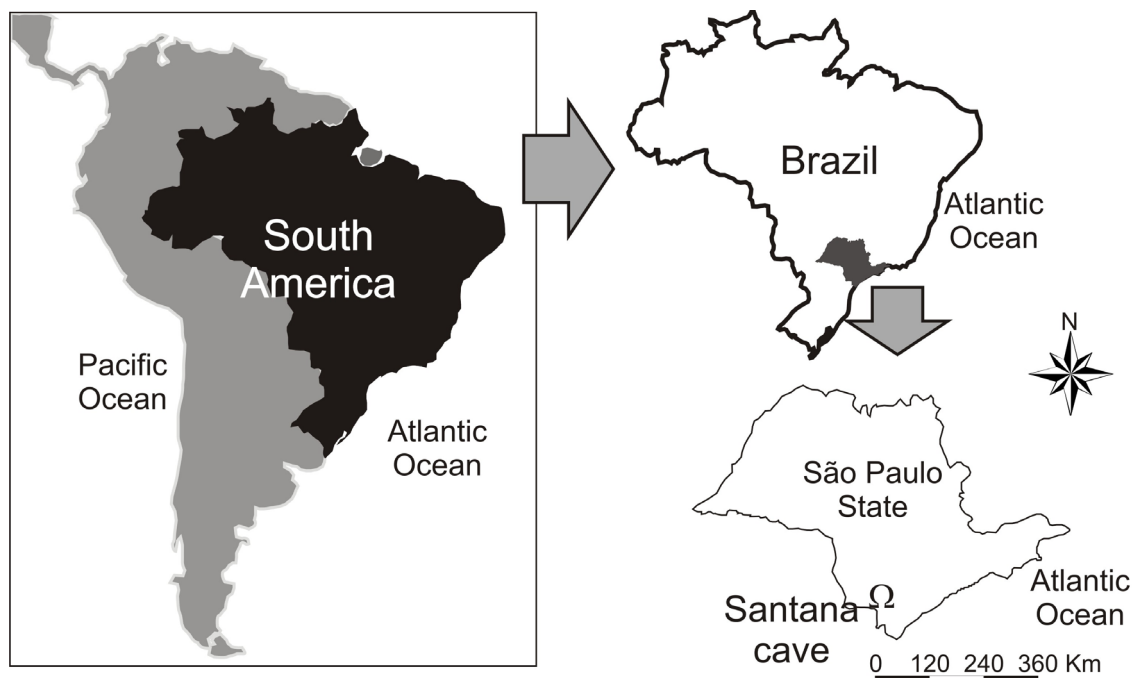


Fig. 1. Localization of Santana Cave.

is influenced by tropical and polar air masses. The relative humidity is approximately 100% throughout the year, but daily fluctuations may occur due to the local incidence of sunlight; the relative humidity can drop to 60% and then return to total saturation in the evening (Cruz Jr. et al., 2005a).

The annual average rainfall is close to 1,500 mm (Gutjahr & Tarifa, 1993; Cruz Jr. et al., 2005b). The distribution of the rain is not homogeneous; approximately 33% of the annual rain occurs in the austral summer (December to February), whereas 18% of the annual rain occurs during the austral winter (June to August) (Gutjahr & Tarifa, 1993). The long-term regional average temperature is 19°C to 21°C (Gutjahr & Tarifa, 1993) and previous studies in Santana cave measured an average of 18.6°C outside the cave (Cruz Jr. et al., 2005b).

METHODS

The research consisted of monitoring the air temperature and humidity inside and outside the

STUDY AREA

Santana Cave is located within a natural protected area (PETAR – State Tourist Park of Alto Ribeira) that is known for many caves and area of Atlantic rainforest. This location in southern São Paulo State, Iporanga Municipality, which is 340 km from São Paulo City (Fig. 1), has been promoted as a crescent tourist area with approximately 25,000 visitors per year.

The cave, which developed in Neoproterozoic carbonatic rocks of the Açungui Group (Faleiros & Campanha, 2004), presents 8,373 m of known passages and galleries (Gpme, 2012), of which only approximately 480 m are used for tourism due to environmental restrictions.

The cave is located in the Ribeira hydrographic basin, which is characterized by a humid climate that

cave using 9 thermohygrometers with data logger Testo 175-H2 (resolution: 0.1°C for temperature and 0.1% for relative humidity; accuracy: 0.1°C for temperature and 0.3% for relative humidity) and 2 thermohygrometers with data logger and external probes Testo 177-H1 (resolution: 0.1°C for temperature and 0.1% for relative humidity; accuracy: 0.2°C for temperature and 0.5% for relative humidity).

The measurements were conducted at intervals of 20 or 30 minutes depending on the situation. The monitoring was conducted in different phases over three years (2009, 2010 and 2011); thus, the distributions and positions of the monitoring stations varied, and the number of instruments (stations) used varied from 6 to 11 (Fig. 2). This temporal resolution was considered satisfactory to determine the seasonality of patterns and the changes generated by visitors. Similar studies, including those by Hoyos et al. (1998), Sánchez-Moral et al. (1999), Calaforra et al. (2003), and Fernández-Cortés et al. (2006a, b), were based on less complex networks in which the number of monitoring stations varied between 2 and 6. To complement the relatively low spatial density of the data

collection, an atmospheric profile was developed to allow for a more complete geospatialization of the data through interpolation by following the examples of Fernández-

Cortés et al. (2006b) and Milanolo & Gabrovšek (2009). For the atmospheric profiling of Santana Cave, 75 sampling points were used (Fig. 2).

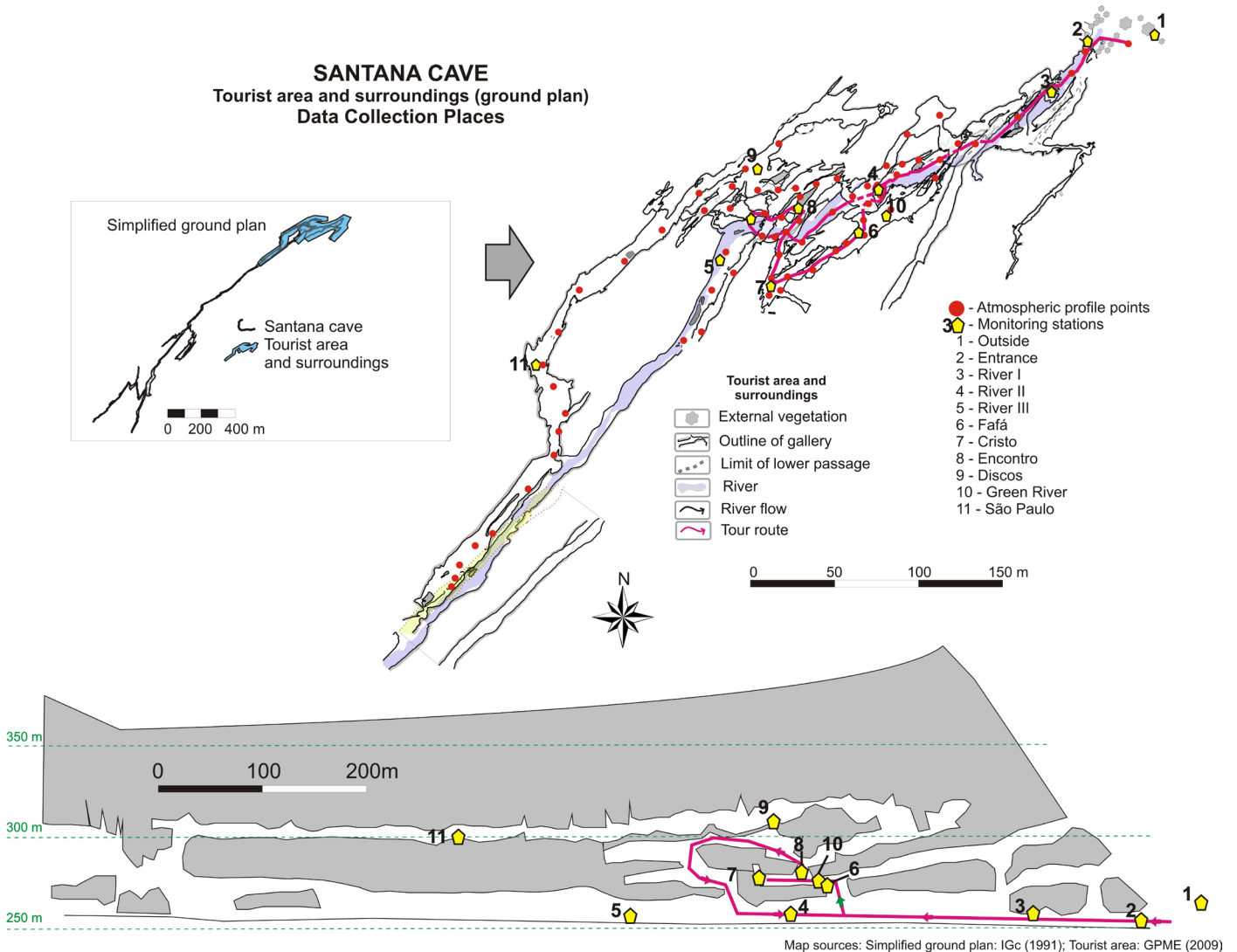


Fig. 2. Profile points and monitoring stations in Santana Cave.

The collected data were analyzed by descriptive statistics and statistical procedures for time series analysis that are widely used in hydrogeology (e.g., Mangin et al., 1999) and climatology (e.g., Calaforra et al., 2003; Fernández-Cortés et al., 2006a, b). The data on the atmospheric profiles were analyzed using geostatistical procedures and were interpolated according to three algorithms: linear triangulation, trend surface (2nd to 5th order), and ordinary kriging. The analysis was applied to the temperature and relative humidity data, but only the temperature results are presented in this article; the relative humidity had a low variability after the initial 100 m of the cave in which all of the obtained values were constant and approximately 99.9%. In the case of air temperature, the second order of the trend offered the best adjustment of the results.

After data collection and analysis, the second phase consisted of establishing the tourist carrying capacity of Santana Cave based on the atmospheric studies. To this end, a new method was developed by Lobo (2011, 2014) based on the recovery time of an atmospheric variable. Similar methods were being used in Spanish

show caves (Calaforra et al., 2011; Guirado et al., 2014). In Santana Cave, the air temperature was selected as atmospheric variable. This parameter, along with CO_2 , provides the best evidence of human presence in Santana Cave (Lobo, 2013).

The CCSC (Carrying Capacity of Santana Cave) method is based on fundamental climatic data to provide specific answers regarding the daily limits of cave usage. Basically, the maximum accepted recovery time of a specific parameter must be shorter than the interval between the end of the visitation one day and the beginning of the visitation the next day. Although there is no defined limit for acceptable impacts on Santana Cave, a cautious position was assumed to ensure that thermal accumulation would be avoided, as reported by Song et al. (2000) in a Chinese show cave. The recovery time limit is the conceptual baseline for the CCSC and is supported by public policies of natural protected areas of Brazil. The developed equations are based on simple management requirements, such as the times of tour routes, the maximum number of people in each group, the interval between groups of visitors, and the maximum acceptable duration of visits

at critical points in Santana Cave, which is likely the most important variable to avoid generating a negative impact that exceeds the maximum recovery time.

RESULTS AND DISCUSSION

Speleoclimate dynamics

The longest continuous data series (annual) of temperature is shown in Fig. 3, and the relative humidity of three monitoring stations (Outside, Entrance and

River I) is shown in Fig. 4. The relative humidity at the various stations inside the cave was constant and approximately 99.9%; the only exceptions were values between 96% and 99.9% (average of 99.8%) recorded at the River I station during the relatively drier months from June to August 2010.

Outside the cave, the maximum temperature was 32.9°C (February 2010) in the rainy season (summer), and the minimum temperature was 13.8°C (September 2009) in the dry months (winter). In the less rainy

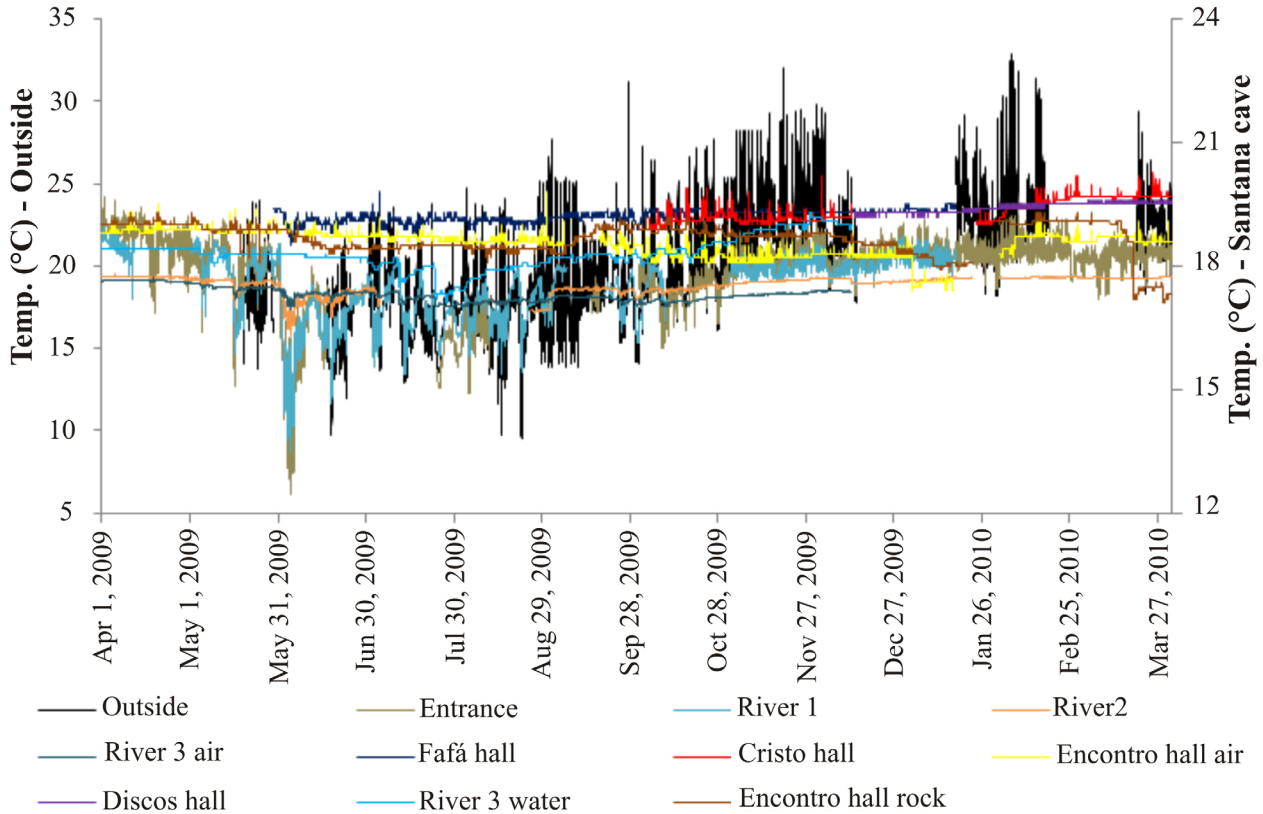


Fig. 3. Annual results of temperature monitoring of Santana Cave (2009-2010).

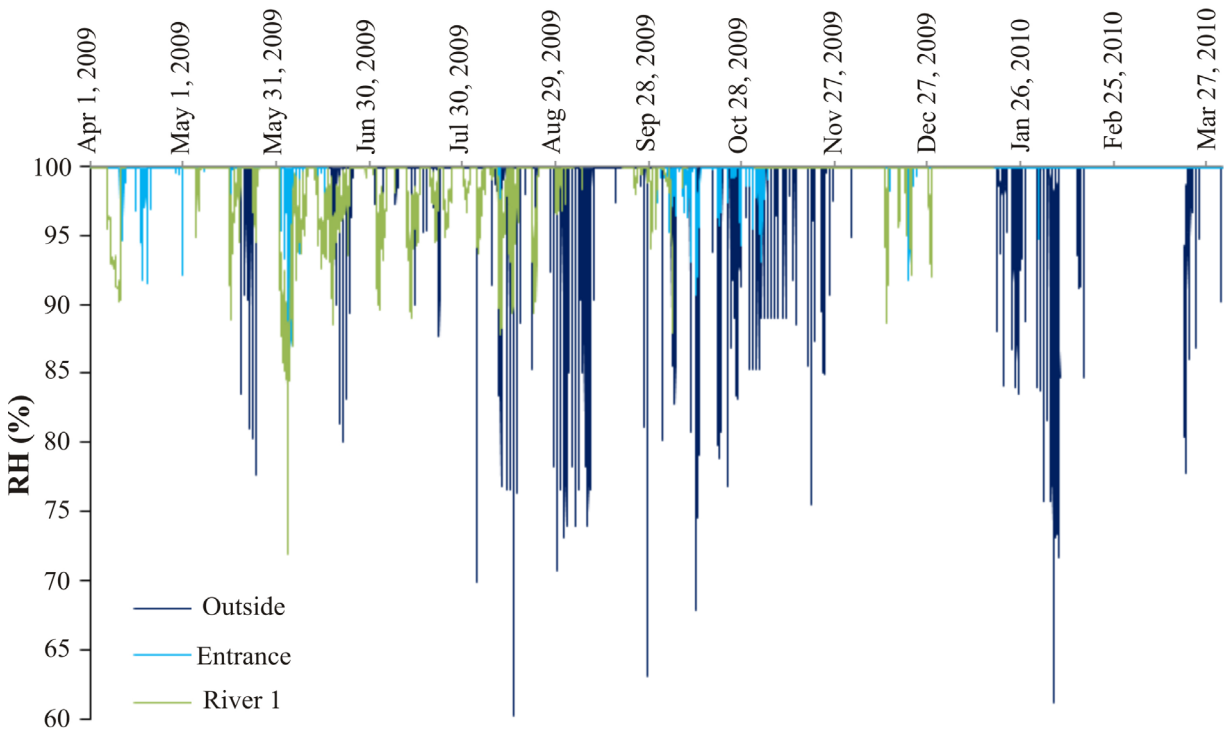


Fig. 4. Annual period of relative humidity monitoring at three stations (Outside, Entrance and River I) of Santana Cave (2009-2010).

season, the maximum temperature was 29.4°C (March 2010) and the minimum temperature was 6.1°C (June/2009). Therefore, a major difference was observed in the average temperature: 21.3°C in the rainy season and 18.0°C in the relatively drier season. The average relative humidity was 98.9%, the maximum was 99.9%, and the minimum was 60.2%.

The minimum temperature recorded in the cave was 17.3°C at the River III station, which did not experience visitor interference. The maximum temperature was 19.3°C, and the annual average was 18.2°C at the same station. The average difference found between the

rainy and relatively drier periods was less than 0.5°C. The relative humidity in the interior of the cave near the River II station was 99.9% over the entire research period. The general patterns for each data sequence of the temperature are shown in the histograms of Fig. 5. The histograms provide a visual representation of the similarity among the Entrance, River I, River II, and Fafá stations; to a lesser extent, Encontro (air) and Encontro (rock) are similar to each other. However, the Outside and River III (air and water) stations are also similar. The Cristo and Discos stations present irregular patterns compared with the other stations.

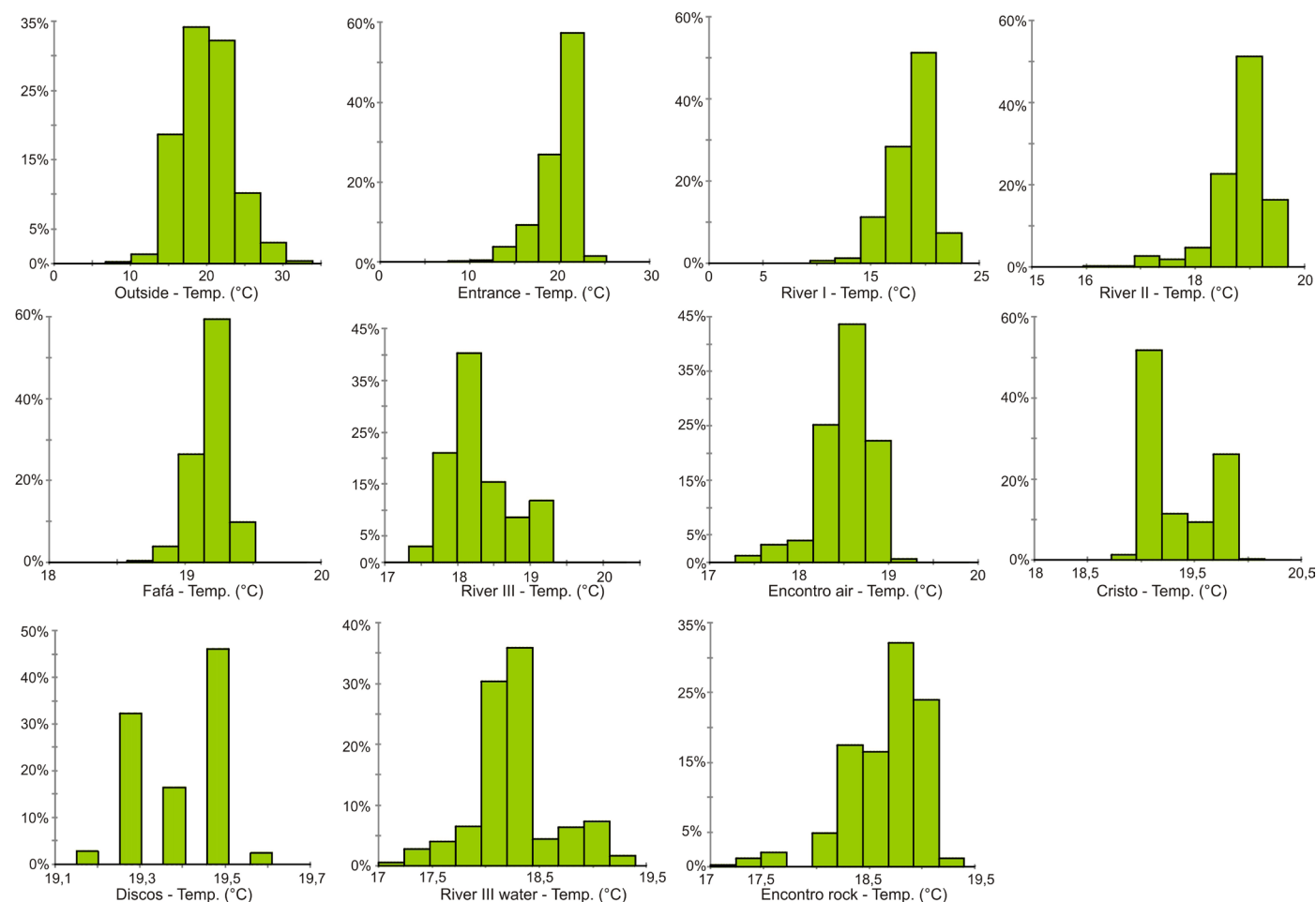


Fig. 5. Histograms of the relative frequencies of air temperature sequences at different stations (2009-2010).

To verify the visual differences and similarities, correlation tests between the variables were performed. The Cross-correlation coefficients (Tab. 1) confirm the strong connections between the temperature series. The influence of the external microclimate is greater at the Entrance (0.835), River I (0.589), River II (0.534), Fafá (0.504) and River III_{air} (0.504) stations. The Encontro station did not present a great correlation with the external environment (0.320).

The majority of the analyzed stations reflect the variations of the outside climate within a matter of hours. The autocorrelation patterns (Fig. 6) demonstrate the differences in the datasets and help determine preliminary zones based on temperature variability patterns.

Although the series of temperature correlograms (Fig. 6) present different time extensions, it is possible to compare their variations. The Outside

station presents the fastest decay, followed by the correlograms of the Entrance, Green River, and River III air stations. The diurnal variability is apparent in the four correlograms, especially at the Outside and Entrance stations. However, the Green River station has a small intensity. The Outside and Entrance stations are very similar in terms of their variability range and velocity of decline.

Based on the collected information, Santana Cave was qualitatively classified as a warm trap (Lobo, 2011; Lobo et al., 2014). The physical structure of the cave, which includes an extensive network of galleries above the base level, forces the coldest air masses found in the interior of the cave to flow toward the outside during the warmest periods (cf. Cigna, 2004). This phenomenon occurs on a diurnal cycle and seasonally due to thermodynamic equilibrium. The flow reverses when the air outside is colder than

Table 1. Cross-correlation coefficients, time lags, and index correlations between the external and internal stations (2009-2010).

Outside Station x	Variable	Value
Entrance	Correlation (zero interval)	0.835
	Lag (hours)	(0.835) 0 h
River I	Correlation (zero interval)	0.589
	Lag (hours)	(0.597) 2 h
River II	Correlation (zero interval)	0.534
	Lag (hours)	(0.536) 1 h
River III air	Correlation (zero interval)	0.504
	Lag (hours)	(0.545) 435 h
Fafá	Correlation (zero interval)	0.504
	Lag (hours)	(0.510) 4 h
Cristo	Correlation (zero interval)	0.033
	Lag (hours)	(0.285) 533 h
Encontro air	Correlation (zero interval)	0.320
	Lag (hours)	(0.510) 1872 h

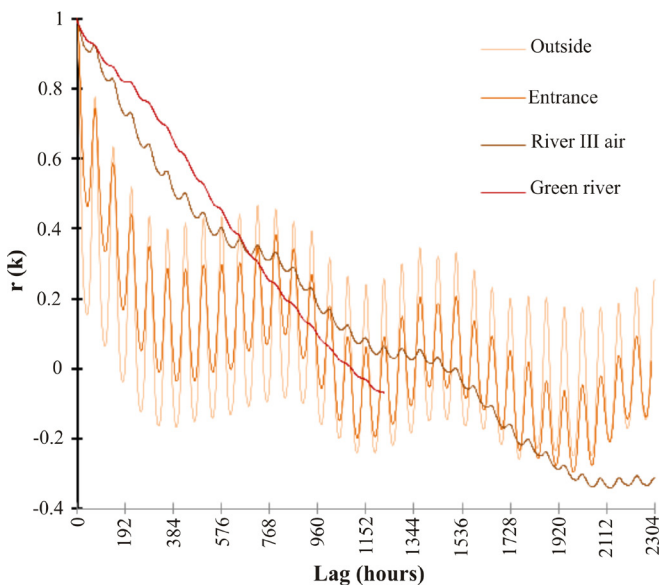


Fig. 6. Comparative correlogram of air temperature at four monitoring stations in Santana Cave.

the air inside the cave. Thus, the air moves to the interior of the cave, where the circulation is limited by a hot air pocket in the upper and most confined galleries of the system. Due to small passages (see details in Fig. 9) and the paleo-resurgence near the present resurgence area of the Roncador River, a small peripheral air circulation is generated in accordance with the principles of thermoregulation.

The hot air masses confined in the upper galleries also exhibit dynamic behavior in terms of atmospheric exchanges. These exchanges can occur due to thermal conductivity, this direct air flow is not detected by the monitoring instruments. This condition emphasizes the speleoclimatologic research conducted by Cigna &

Forti (1986), Pflitsch & Piasecki (2003) and Luetscher & Jeannin (2004); specifically, due to various factors, the speleoclimate in the inner part of a cave is not constant or static. Although the modifications occur at a small scale, in galleries and chambers, they always occur and are critical to comprehending speleoclimate dynamics, accumulation mechanisms, and “cave breathing”, at a large scale (cave systems). To thoroughly investigate this dynamic, two other data periods were selected. One period was in the cold season, and the other period was in the warm season; the data from the stations of the river gallery and the upper galleries were compared with the data from the Outside station (Tab. 2).

The coefficients shown in Tab. 2 for the cold season reveal two major correlations in the data: Outside x River I (0.638) and Encontro x River III air (0.939).

The selected period in the warm season included the days between 10 and 18 February, 2010. The coefficients of correlation among the stations in this period are shown in Tab. 3.

Pearson's r confirms a major positive correlation between the Outside station and the Entrance (0.885), Encontro (0.663) and Cristo stations (0.611) and a low correlation between the Outside station and the River II (0.188) and Discos stations (0.172). Moreover, the Encontro and Cristo stations are highly correlated (0.738).

The interpretation of the seasonal data in the cold and warm periods of the year highlighted the airflow in Santana Cave. Thus, the complete series were divided into the coldest and warmest months so that descriptive statistical analysis could be used. The maximum and minimum for every month are relevant to the present analysis (Fig. 7).

Table 2. Matrix of proximity (Pearson's r) between the selected monitoring stations – July 2009.

	Outside	River I	Fafá	Encontro	River III air
Outside	1	0.638	0.302	0.358	0.308
River I		1	0.142	0.446	0.433
Fafá			1	0.006	-0.094
Encontro				1	0.939
River III air					1

Table 3. Proximity matrix (Pearson's r) among the selected monitoring stations – February 2010.

	Outside	Entrance	River II	Encontro	Cristo	Discos
Outside	1	0.885	0.188	0.663	0.611	0.172
Entrance		1	0.111	0.562	0.538	0.122
River II			1	0.289	0.429	0.334
Encontro				1	0.738	0.232
Cristo					1	0.252
Discos						1

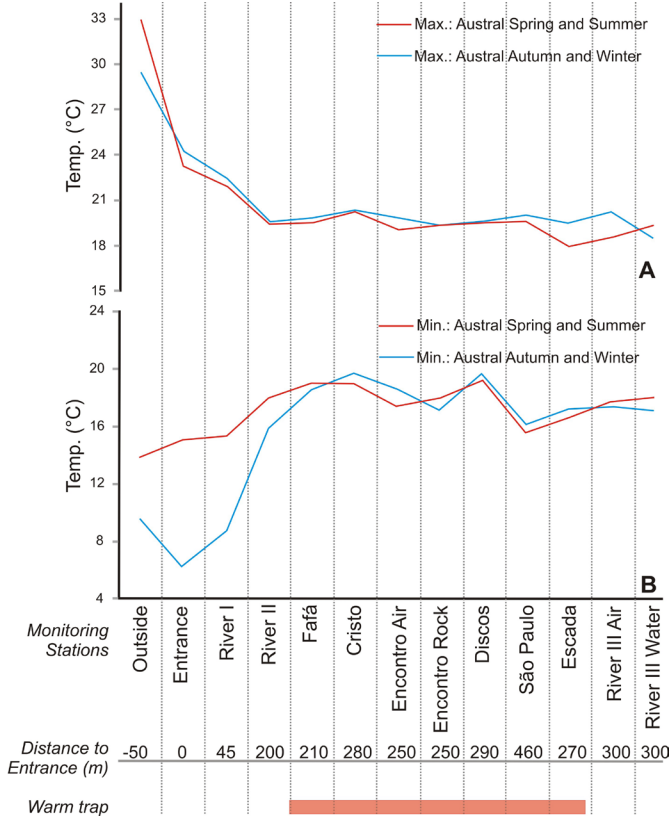


Fig. 7. Maximum (A) and minimum (B) temperature at each monitoring station during the cold and warm seasons (2009-2010). Modified from Lobo et al. (2014).

The data shown in Fig. 7 demonstrate the difference of temperature in Santana Cave during the warm and cold periods of the year and are consistent with the previous interpretation of the cave as a warm trap. In the coldest period (March – August), the maximum temperature recorded at each station in the interior of the cave is higher than the maximum recorded in the warm period (September – February); the minimum temperatures are lower in the warm period (September – February) at the stations inside the cave. Furthermore, regarding the minimum temperatures, the external climate impacts the temperatures at the Entrance, River I, River II, Fafá, and River III (air) stations. Thus, preliminary limits for the higher intensity of direct atmospheric exchange between the external and internal environments are determined.

Considering the warmest period, the correlation coefficient and supporting material can be used as time-space profiles for air temperature. In Santana Cave, the air temperature exhibits a cumulative potential toward the interior of the cave and in the upper galleries. This pattern is more evident in the temperature profile of April 2010 (Fig. 7A) and usually occurs in austral

autumn (march – may), but the lowest temperature, approximately 18°C, had already occurred in the year 2010. Notably, the thermal accumulation in the Green River station and surroundings occurred in a confined and upper gallery that is close to the external environment. The profile of January/2011 (Fig. 7B), i.e., austral summer, also exhibited thermal accumulation in the upper galleries – Cristo, Discos, Aranhas, São Paulo, and São Jorge Halls.

Moreover, the interpretation of the obtained data, together with the air flow measurements, is displayed in Fig. 8. This interpretation is based on the patterns of temperature presented in the histograms (Fig. 5), the cross-correlation coefficients (Tab. 1), the correlograms at four monitoring stations (Fig. 6) and the correlation coefficient *r* (Tab. 3).

Based on Fig. 8, a model of the atmospheric circulation proposed for the research area of Santana Cave is summarized in Fig. 9. The model focused not only on the warm trap but also on the approximate limits of the possible climate zones of the cave. Santana Cave presents various levels related to the air temperature variation. Thus, the thermal speleoclimate zones are confirmed by the previous analysis of Lobo et al. (2009), in which the air temperature was determined in a small-scale study. The transitional zone varies simultaneously with the temperature variation of the external environment. This variation becomes less intense in the internal typical zone and in the low thermal amplitude zones; thus, a more stable area is apparent. This phenomenon is observed in Flores Hall, where minimum variations occur on a weekly basis. Fig. 9 also highlights the existence of physical barriers in the environment, which were interpreted as key factors to establishing limits for these zones. However, other aspects, such as the distance to the external access, the physical formation of the environment, the presence of water and the dimensions of the galleries are also important in the thermal stratification of the cave's atmosphere (cf. Poulson & White, 1969; Luetscher & Jeannin, 2004).

A physical barrier may cause the variations of air humidity in Santana Cave in the distinct zones; the transitional zone presented a large humidity variation from ~71% to 99.9%. The interpretation is that the restricted gallery of the Roncador River and the juxtaposition of a huge conjunct of speleothems (stalactites and flowstones) may be the main factors that limit the influence of the outside microclimate on the inner parts of Santana Cave. After this point, only at River II (the beginning of the Internal-Typical zone), low variations of relative humidity were registered.

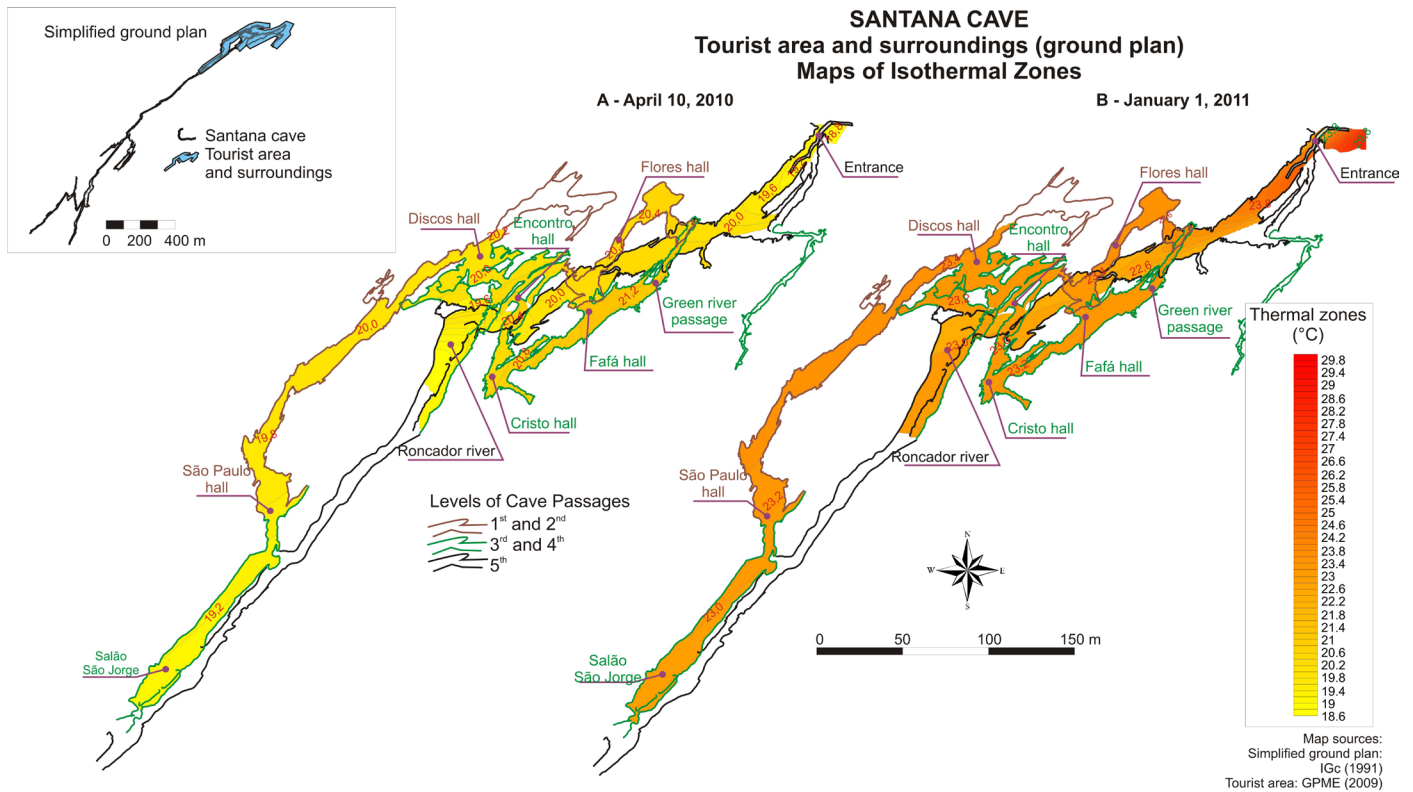
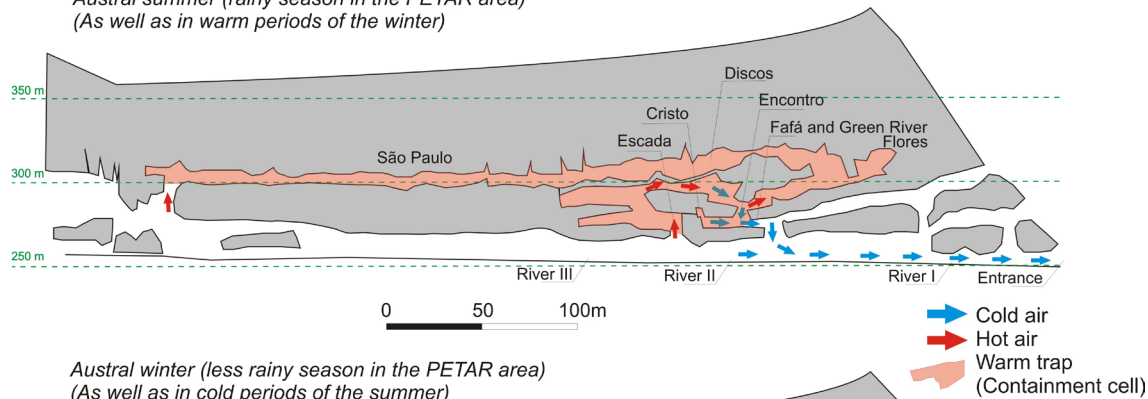


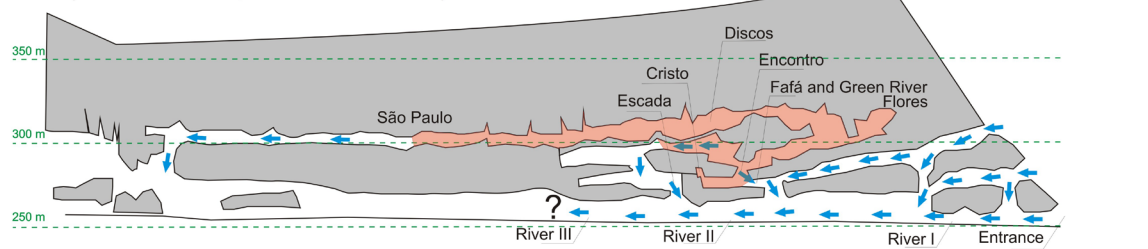
Fig. 8. Trend surface (second order) of thermal profiles of Santana Cave. Modified from Lobo (2013).

Conceptual qualitative model of air flow of the final part of Santana Cave (profile view)

*Austral summer (rainy season in the PETAR area)
(As well as in warm periods of the winter)*



*Austral winter (less rainy season in the PETAR area)
(As well as in cold periods of the summer)*



First approach for speleoclimate zones (thermal) of the final part of Santana Cave (Profile view)

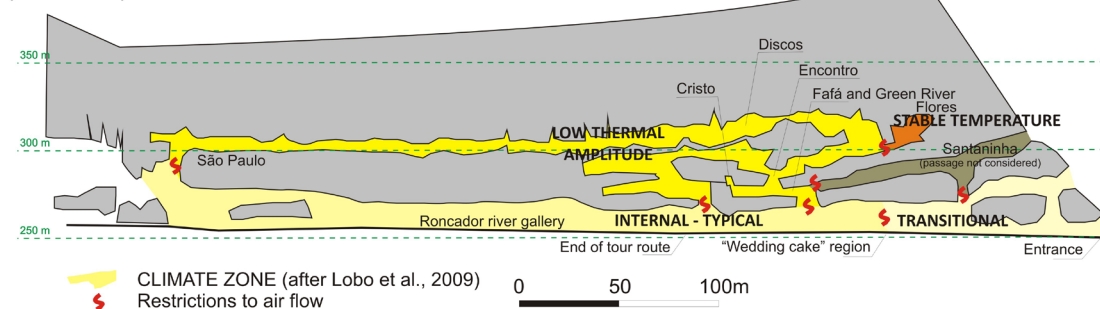


Fig. 9. Conceptual model of air circulation in a partial longitudinal section of Santana Cave, which is characterized as a warm trap (Lobo et al., 2014), and the climate zones according to Lobo et al. (2009).

Impacts on speleoclimate and tourist carrying capacity

The main problem of tourism in a cave is the alteration of the physical-chemical conditions of the inner atmosphere. In some fragile caves, such as Lascaux Cave in France (Bastian & Alabouvette, 2009) and the geode of Pulpí, Spain (Fernández-Cortés et al., 2006a), tourist activity is completely prohibited. At Lascaux Cave, tourism is prohibited to protect the rock paintings, whereas at the geode of Pulpí, tourism is banned to avoid the deterioration of the unstable minerals in this very small cave.

All environmental parameters are important to understand to protect a cave and alleviate the effects of tourism, but there are limitations to complete analyses, and investigations must prioritize the speleoclimate data (Hoyos et al., 1998, Sánchez-Moral et al., 1999, Calaforra et al., 2003, Fernández-Cortés et al., 2006a).

In the present study of Santana Cave, the analysis of the impact on the speleoclimate was concentrated on the air temperature because the relative humidity was

not influenced by tourist groups. A direct correlation with visits was conducted, and a daily visitor limit was established. However, this approach to evaluate the tourist carrying capacity of an environment provides restricted results because the dynamics of high-level energy environments, such as those in Santana Cave, were neglected. In the case presented here, extreme environmental fragilities, such as rock paintings and rare and unstable minerals, are absent.

Thus, the daily thermal amplitudes at the Cristo and Encontro stations (in the halls where the tourist groups spend more time) were calculated for the period from 23 August 2009, to 1 January 2010. Additionally, the available daily visits (tourist and tour guides) data were considered (Fig. 10).

Two monitoring stations were located in relatively small galleries where the visitors spend more time – the Cristo and Encontro stations. The comparison between the thermal amplitudes (highest temperature – lowest temperature) and the number of visits per day is shown in Fig. 10.

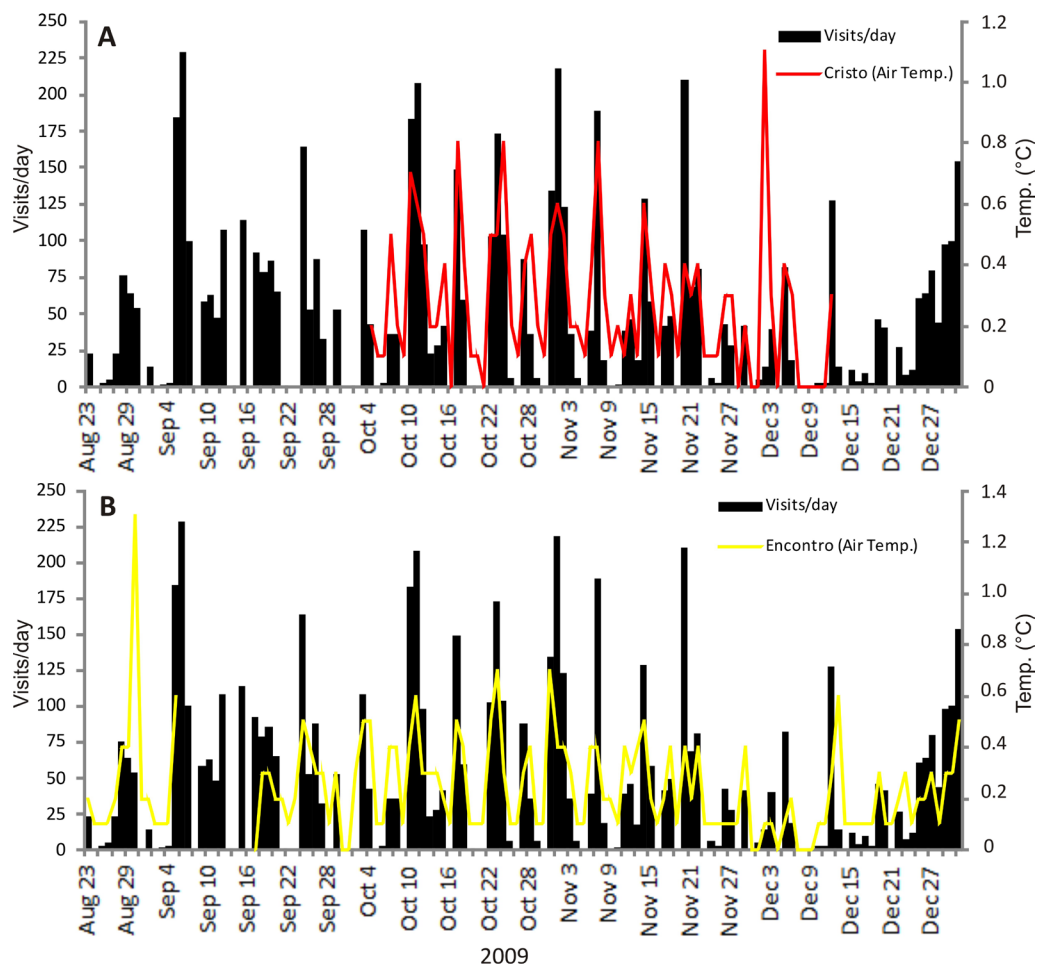


Fig. 10. Daily air temperature amplitude at the Cristo station (A) and Encontro station (B).

The predominant daily amplitude without visits in Cristo and Encontro halls was 0.1°C. The tourist groups generated maximum daily amplitudes of 1.1°C (Cristo) and 1.3°C (Encontro), although most of the variations were 0.1 – 0.5°C (Cristo) and 0.1 – 0.4°C (Encontro). These values were generated by groups with variable numbers of visitors, using just flashlights as light sources. The most of flashlights used in Santana Cave were of LED technology, which waste

less energy as heat (Cigna, 2011). Thus, the main heat source was the human body, which releases between 82 W and 160 W, according to Villar et al. (1984). In Cristo hall, for example, 2 visitors increased the daily temperature amplitude to 0.2°C, the presence of 12 visitors caused an increase of 0.3°C, and 8 visitors caused an increase of 0.4°C. In Encontro hall, the presence of 2 visitors generated a thermal amplitude of 0.1°C, and 18 visitors increased this value to 0.4°C.

In this case, two approaches could be considered to define the carrying capacity. The first approach is related to the anthropogenic variation, which should not exceed the natural variations.

Considering that tourism visits must be conducted without modifying the natural dynamics (Hoyos et al., 1998; Calaforra et al., 2003), the temperature may be a critical factor with which to measure human modifications of speleoclimate. In Santana Cave, in an extreme case, the visits to Cristo Hall would be limited to only 1 person considering that the presence of 2 visitors generates a 0.2°C temperature increase. However, the limit in Encontro Hall was 13 visitors because 14 visitors caused an increase greater than 0.1°C, which is the typical increase.

However, 92 visitors on the same day (16 September 2009) did not alter the air temperature in Encontro Hall (Fig. 10B). Thus, this assumption cannot be applied to Santana Cave, where the dynamics of the atmosphere did not respond as expected due to the nonlinear data. In another example, a group of 14 visitors generated a daily amplitude of 1.1°C in Cristo Hall (2 December 2009 - Fig. 10A). Meanwhile, 210 visitors divided into various groups generated an amplitude of 0.4°C. After many tests, it was determined that the increase in temperature was directly connected to the length of time tourists spent in the halls and not to the number of visitors in each group. This situation was observed at the Cristo and Encontro stations, where the guides spend more time during the visit and, consequently, the temperature increases.

A second approach to define the carrying capacity is to consider modern management principles, such as those presented by Graefe et al. (1990) in his framework entitled "Visitor Impact Management," which was developed for trails and used in cave management in Australia (Hamilton-Smith, 1997) and New Zealand (de Freitas, 2010). This research is based on the understanding that anthropogenic activity cannot occur without altering the environment. Based on this assumption, the study aimed to find alterations due to human presence that do not persist in the environment over long time intervals. Time-extensive impacts are not acceptable because all the consequences of alterations of a specific environmental parameter are not known.

A new methodology that is based on the data presented in this article is proposed for determining the carrying capacity of Santana Cave (CCSC - Lobo, 2011, 2014); the method is divided into three steps: I) identify and list the tourist and educational attractions and access points to delimit the walking trail and interpretative program; II) design the ideal tourist scenario; III) Obtaining a time limit based on environmental critical factors as a threshold for CCSC.

The proposed method to identify the carrying capacity (Lobo, 2014) depends on the specific characteristics of each cave, and similar procedures were carried out by Pulido-Bosch et al. (1997) at cave of the Marvels, Spain. In the case of Santana Cave, the durations for which the tourist groups remain at the two identified points inside the cave, i.e., Cristo and Encontro stations, are important. The main factor that determined the carrying

capacity of Santana Cave was the time that the tourist groups remained in the Cristo and Encontro Halls. Based on this finding, it was not relevant to determine an exact number of persons/groups that affected the atmospheric parameters. Cristo and Encontro Halls are the main bottlenecks of the walking trail of Santana Cave, and the time spent at these locations during the guided tour was identified as the principal factor of the air temperature changes. This time interval was related to the time the atmosphere needed to return to its steady state on a daily basis, following the Brazilian principles of precaution (Conama, 2004) and also considering the number of visitors per group and the time between groups without extrapolating the recovery limits of the critical factor, the air temperature (Lobo, 2011). This limit is considered a function of the recovery time and the time available to recover. In this case, the limit was considered as the time interval between the end of the visits one day and the start of the visits the next day to avoid the impacts described by Song et al. (2000). The application of the method in Santana Cave resulted in a CCSC of 378 visits per day (Lobo, 2014).

Recommendations for management issues of Santana Cave

Defining the number of visits per day is necessary for the public managers of Santana Cave to improve the tourist flow and, consequently, PETAR and the surrounding communities. Many local people economically depend on cave tourism in the park, where Santana Cave is the main attraction. Currently, the proposed maximum limit of visits to Santana Cave is 117 visits/day, including the guides. This limit was suggested in the study by Lobo (2008), which is based on the Cifuentes (1992) method of carrying capacity. This method was previously used in cave management in Brazil (e.g., Boggiani et al., 2007) and other countries (e.g., Nghi et al., 2007). The use of this method was criticized by Delgado (2007) and Lobo et al. (2010) due to two problems: the overlap of restrictions that are derived from environmental and social studies and the excessive limitation of tourist use without a proven cause and effect relationship.

The relatively low number of visits generates many problems in the region considering that the tourist influx is concentrated on weekends and holidays. To help mitigate this problem, the size of tourist groups determined in the management plan of Santana Cave (Fundação Florestal & Ekos Brasil, 2010), which has not yet been implemented, was combined with the carrying capacity obtained herein. In the management plan, the tourist groups include 24 people on business days (i.e., to accommodate school groups) and 18 people on the weekends and holidays. Thus, the carrying capacity corresponds to a maximum of 378 visits per day on weekends and holidays (21 groups). The entrance interval between these groups can be as short as 20 minutes. During weekdays, the carrying capacity can be 336 visits per day (14 groups), and the entrance interval between the groups is approximately 30 minutes (Lobo, 2014).

The proposed numbers need to be tested and monitored to prove their efficacy so that adjustments

can be made according to the options identified by the cave managers. One fundamental aspect that can be considered is the present annual average number of visits to Santana Cave, which is close to 80 tourists per day (except on Mondays, when PETAR is closed), and fewer than 35,000 visits/year. Obviously, there is an enormous discrepancy between the actual visitation and the possible visitation in this case. However, this difference can be attenuated if the carrying capacity on weekends and holidays is increased from 117 to approximately 350 visits/day. Considering that most of the visitors travel to the region on these days, modifying the limits is fundamental to improving the use of Santana Cave and would benefit the local inhabitants.

Finally, it is important to note that the atmosphere of Santana Cave is highly related to the outside conditions according to the daily variations of temperature and relative humidity in the part of the cave studied. This finding must be considered in the establishment of future methodologies, results, and conclusions for comparisons with those of this research. Likewise, it is important to remember that the external microclimate presents special features that should be taken into account. The atmosphere in the area surrounding the cave is influenced by the presence of steep hollows in the bottom of the valley (cockpit karst) and the thick vegetation of the Atlantic rainforest. Additional factors, such as the existence of an active watercourse - the Roncador River, for example - or even the thickness of rock cover, are relevant to future studies. Therefore, the tourist carrying capacity in caves with these conditions should be flexible and can be improved for the professional management of cave tourism.

CONCLUSIONS

The investigated atmospheric parameters demonstrated the importance of the temporal extension and density of the sample points not only in hygrothermal monitoring but also in determining atmospheric profiles. The atmospheric profiles can possibly identify the critical zones in the current tourist route. The identified environmental zones have a strong spatial component in all levels of the galleries; the zones are influenced by the Roncador River, the thickness of the rock layer and the horizontal stratification corresponding to the external and vertical environments. The environmental monitoring data contributed to the development of a general model of the atmospheric circulation in Santana Cave; the model demonstrated the thermal cumulative pattern in relation to the upper galleries (hot trap model). The air-trapping cell has a variable size that is more extensive in austral summer (December to February) and on warm days and smaller in austral winter (June to August) and on cold days; thus, air cycling by degasification occurs in the cave. The thermal profile calls special attention to the galleries of the Green River, Discos-São Paulo, and Flores Hall, and the monitoring highlights the importance of Cristo and Encontro Halls. Future studies must concentrate on measurements of wind velocity and direction and monitoring atmospheric pressure to test the model of airflow and speleoclimate zones of Santana Cave.

In Cristo Hall, the thermal amplitude was up to 1.1°C when tourists were present. In Encontro Hall, this value reached 1.3°C. At other points in the cave, all meaningful thermal variations were attributed to anthropogenic origins. Human impacts on the air temperature dissipate quickly; thus, the possibility of anthropogenically damaging the environment directly via the speleoclimate or indirectly throughout the entire cave decreases. Therefore, the management of cave tourism based on temporal factors and on the resilience of the environment was the main focus of this research. Hence, the total daily visits are no longer the basis for the carrying capacity. Instead, the time spent by visitors at critical points in the cave where cumulative impacts occur are more important.

The findings of this research showed the importance of using the tourist carrying capacity as a management tool in which the results should be flexible in order to identify the most appropriate limits. Hence, the methodology does not refer to a set volume limit for visitation but, rather, to dynamic intervals based on field test solutions. These solutions can differ depending on the seasonality of the tourism (and the associated climate), with distinct levels of tourist carrying capacities in caves according to the tourist season or to unique management goals.

Finally, from a philosophical perspective of environmental management, the results reaffirmed that managers and scientists are responsible for finding solutions to the carrying capacity issue. These results must be studied from different points of view without expecting mathematically exact answers to tourism management in most cases. The goal of allowing the maximum possible number of visitors to a cave reinforces the need for scientific practices and long-term measures that consider the responses of measurable environmental parameters to visitation as strategic thresholds to inform rational and responsible cave tourism management.

REFERENCES

- Bastian F. & Alabouvette C., 2009 – *Lights and shadows on the conservation of a rock art cave: the case of Lascaux cave*. International Journal of Speleology, **38**: 55-60. <http://dx.doi.org/10.5038/1827-806X.38.1.6>
- Boggiani P.C., Silva O.J., Gesicki A.L.D., Galati E., Salles L.O. & Lima M.M.E.R., 2007 – *Definição de capacidade de carga turística das cavernas do Monumento Natural Gruta do Lago Azul (Bonito, MS)*. Geociências, **26**: 333-348.
- Calaforra J.M., Fernández-Cortés A., Sánchez-Martos F., Gisbert J. & Pulido-Bosch A., 2003 – *Environmental control for determining human impact and permanent visitor capacity in a potential show cave before tourist use*. Environmental Conservation, **30**: 160-167. <http://dx.doi.org/10.1017/S0376892903000146>
- Calaforra J.M., Fernández-Cortés A., Gázquez-Parra J.A. & Novas N., 2011 – *Conservando la cueva de El Soplao para El futuro: control de parámetros ambientales*. In: Valsero J.J.D. (Ed.), *El Soplao: Una ventana a la ciencia subterránea*. El Soplao S.L., Celis: 40-43.
- Cifuentes M., 1992 – *Determinación de capacidad de carga turística en áreas protegidas*. CATIE, Turrialba, 28 p.
- Cigna A.A., 2002 – *Modern trend in cave monitoring*. Acta Carsologica, **31**: 35-54.
- Cigna A.A., 2004 – *Climate of caves*. In: Gunn J. (Ed.), *Encyclopedia of caves and karst science*. London: Taylor & Francis, 467-475.

- Cigna A.A., 2011 – *Show cave development with special references to active caves*. *Tourism and Karst Areas*, **4**: 7-16.
- Cigna A.A. & Burri E., 2000 – *Development, management and economy of show caves*. *International Journal of Speleology*, **29**: 1-27.
<http://dx.doi.org/10.5038/1827-806X.29.1.1>
- Cigna A.A. & Forti P., 1986 – *The speleogenetic role of air flow caused by convection. 1st. contribution*. *International Journal of Speleology*, **15**: 41-52.
<http://dx.doi.org/10.5038/1827-806X.15.1.3>
- Cigna A.A. & Forti P., 2013 – *Caves: the most important geotouristic feature in the world*. *Tourism and Karst Areas*, **6**: 9-26.
- Conama – Conselho Nacional do Meio Ambiente, 2004 – *Resolução CONAMA n° 347 de 10 de setembro de 2004*. *Diário Oficial da União*, **176**: 54.
- Cruz Jr F.W., Burns S.J., Karmann I., Sharp W.D., Vuille M., Cardoso A.O., Ferrari J.A., Dias P.L.S. & Viana Júnior O., 2005a – *Insolation-driven changes in atmospheric circulation over the past 116,000 years in subtropical Brazil*. *Nature*, **434**: 63-66.
<http://dx.doi.org/10.1038/nature03365>
- Cruz Jr F.W., Karmann I., Viana Júnior O., Burns S.J., Ferrari J.A., Vuille M., Sial A.N. & Moreira M.Z., 2005b – *Stable isotope study of cave percolation waters in subtropical Brazil: Implications for paleoclimate inferences from speleothems*. *Chemical Geology*, **220**: 245-262.
<http://dx.doi.org/10.1016/j.chemgeo.2005.04.001>
- De Freitas C.R., 2010 – *The role and the importance of cave microclimate in the sustainable use and management of show caves*. *Acta Carsologica*, **39**: 477-489.
- Delgado M., 2007 – *Análise da metodologia criada por Miguel Cifuentes referente à capacidade de carga turística*. *Turismo em Análise*, **18**: 73-93.
<http://dx.doi.org/10.11606/issn.1984-4867.v18i1p73-93>
- Faleiros F.M. & Campanha G.A.da C., 2004 – *Petrografia e microestruturas de tectonitos da zona de cisalhamento Ribeira, Vale do Ribeira, SP e PR: implicações no zoneamento metamórfico e estrutural do Supergrupo Açungui e unidades correlatas*. *Revista Brasileira de Geociências*, **34**: 419-430.
- Fernández-Cortés A., Calaforra J.M., Sánchez-Martos F. & Gisbert J., 2006a – *Microclimate processes characterization of the giant geode of Pulpi (Almería, Spain): technical criteria for conservation*. *International Journal of Climatology*, **26**: 691-706. <http://dx.doi.org/10.1002/joc.1269>
- Fernández-Cortés A., Calaforra J.M., Jiménez-Espinosa R. & Sánchez-Martos F., 2006b – *Geostatistical spatiotemporal analysis of air temperature as an aid to delineating thermal stability zones in a potential show cave: implications for environmental management*. *Journal of Environmental Management*, **81**: 371-383.
<http://dx.doi.org/10.1016/j.jenvman.2005.11.011>
- Fundação Florestal & Ekos Brasil, 2010 – *Plano de manejo espeleológico das cavernas do Parque Estadual Turístico do Alto Ribeira*. Secretaria do Meio Ambiente, São Paulo, 460 p.
- Graefe A.R., Kuss F.R. & Vaske J.J., 1990 – *Visitor impact management: the planning framework*. National Parks and Conservation Association, Washington, 105 p.
- Guirado E., Gázquez F., Fernández-Cortés Á., Argumosa A. & Calaforra J.M., 2014 – *Cálculo de la visitabilidad máxima en cavidades turísticas mediante el método Cavix: El Soplao (Cantabria)*. In: Calaforra J.M. & Durán J.J. (Eds.), *I Congreso Iberoamericano y V Congreso Español sobre Cuevas Turísticas*. ACTE, Aracena, **1**: 199-204.
- Gpme – Grupo Pierre Martin de Espeleologia., 2009 – *Mapa da caverna de Santana*. GPME, São Paulo.
- Gpme – Grupo Pierre Martin de Espeleologia., 2012 – *Caverna de Santana*. GPME, São Paulo.
- Gutjahr M.R. & Tarifa J.R., 1993 – *Crêterios relacionados a compartimentação climática de bacias hidrográficas: a bacia do rio Ribeira de Iguape-SP*. In: USP (Ed.), *5th Simpósio Brasileiro de Geografia Física Aplicada*. São Paulo: USP, **1**: 447-449.
- Hamilton-Smith E., 1997 – *Monitoring visitor experience and environmental conditions at Jenolan caves, New South Wales, Austrália*. In: Stitt R.R. (ed.), *13th Cave And Karst Management Symposium*. NSS, Bellingham, **1**: 87-91.
- Hoyos M., Soler V., Cañaveras J.C., Sánchez-Moral S. & Sanz-Rubio E., 1998 – *Microclimatic characterization of a karstic cave: human impact on microenvironmental parameters of a prehistoric rock art cave (Candamo cave, Northern Spain)*. *Environmental Geology*, **33**: 231-242.
<http://dx.doi.org/10.1007/s002540050242>
- IGc – Instituto de Geociências da USP, 1991 – *Mapa da caverna de Santana*. IGc/USP, São Paulo.
- Lobo H.A.S., 2008 – *Capacidade de carga real (CCR) da caverna de Santana, PETAR-SP e indicações para o seu manejo turístico*. *Geociências*, **27**: 369-385.
- Lobo H.A.S., 2011 – *Estudo da dinâmica atmosférica subterrânea na determinação da capacidade de carga turística da caverna de Santana (PETAR, Iporanga-SP)*. Unesp, Rio Claro, 392 p.
- Lobo H.A.S., 2013 – *Perfis atmosféricos da caverna Santana (PETAR, Iporanga-SP): contribuições à classificação espeleoclimática e ao manejo espeleoturístico*. *Revista Brasileira de Climatologia*, **12**: 136-154.
- Lobo H.A.S., 2014 – *Tourist carrying capacity of Santana cave (PETAR-SP, Brazil): a new method based on a critical atmospheric parameter*. UFSCar, Sorocaba, 21 p.
- Lobo H.A.S., Perinotto J.A.J. & Poudou S., 2009 – *Análise de agrupamentos aplicada à variabilidade térmica da atmosfera subterrânea: contribuição ao zoneamento ambiental microclimático de cavernas*. *Revista de Estudos Ambientais*, **11**: 22-35.
- Lobo H.A.S., Perinotto J.A. de J. & Boggiani P.C., 2010 – *Tourist carrying capacity in caves: main trends and new methods in Brazil*. In: Bella P. & Gazik P. (Ed.), *6th International Congress of International Show Caves Association*. Liptovsky Mikulas: Slovak Caves Administration, **1**: 108-115.
- Lobo H.A.S., Trajano E., Marinho M.deA., Bichuette M.E., Scaleante J.A.B., Scaleante O.A.F., Rocha B.N. & Laterza F.V., 2013 – *Projection of tourist scenarios onto fragility maps: Framework for determination of provisional tourist carrying capacity in a Brazilian show cave*. *Tourism Management*, **35**: 234-243.
<http://dx.doi.org/10.1016/j.tourman.2012.07.008>
- Lobo H.A.S., Perinotto J.A. de J. & Boggiani P.C., 2014 – *Monitoramento espeleoclimático do trecho turístico da caverna Santana (PETAR, SP)*. *Mercator*, **13**: 227-241.
- Luetscher M. & Jeannin P.Y., 2004 – *Temperature distribution in karst systems: the role of air and water fluxes*. *Terra Nova*, **16**: 344-350.
<http://dx.doi.org/10.1111/j.1365-3121.2004.00572.x>
- Mangin A., Bourges F. & D'Hulst D., 1999 – *La conservation des grottes ornées: un problème de stabilité d'un système naturel (l'exemple de la grotte préhistorique de Gargas, Pyrénées françaises)*. *Sciences de la Terre et des Planètes*, **328**: 295-301.
- Milanolo S. & Gabrovšek F., 2009 – *Analysis of carbon dioxide variations in the atmosphere of Srednja Bijambarska cave, Bosnia and Herzegovina*. *Boundary-Layer Meteorology*, **131**: 479-493.
<http://dx.doi.org/10.1007/s10546-009-9375-5>
- Nghi T., Lan N.T., Thai N.D., Mai D. & Thanh D.X., 2007 – *Tourism carrying capacity assessment for Phong Nha – Ke Bang and Dong Hoi, Quang Binh province*. *VNU Journal of Science, Earth Sciences*, **23**: 80-87.
- Pflitsch A. & Piasecki J., 2003 – *Detection of an airflow system in Niedzwiedzia (Bear) cave, Kletno, Poland*. *Journal of Cave and Karst Studies*, **65**: 160-173.

- Poulson T.L. & White W.B., 1969 – *The cave environment*. Science, **165**: 971-981. <http://dx.doi.org/10.1126/science.165.3897.971>
- Pulido-Bosch A., Martín-Rosales W., López-Chicano M., Rodríguez-Navarro C.M. & Vallejos A., 1997 – *Human impact in a tourist karstic cave (Aracena, Spain)*. Environmental Geology, **31**: 142-149.
- Sánchez-Moral S., Soler V., Cañaveras J.C., Sanz-Rubio E., Van Grieken R. & Gysels K., 1999 – *Inorganic deterioration affecting Altamira cave, N Spain: quantitative approach to wall-corrosion (solutional etching) processes induced by visitors*. The Science of the Total Environment, **243/244**: 67-84. [http://dx.doi.org/10.1016/S0048-9697\(99\)00348-4](http://dx.doi.org/10.1016/S0048-9697(99)00348-4)
- Šebela S. & Turk J., 2014 – *Natural and anthropogenic influences on the year-round temperature dynamics of air and water in Postojna show cave, Slovenia*. Tourism Management, **40**: 233-243. <http://dx.doi.org/10.1016/j.tourman.2013.06.011>
- Song L., Wei X. & Liang F., 2000 – *The influences of cave tourism on CO₂ and temperature in Bayun cave, Hebei, China*. International Journal of Speleology, **29**: 77-87. <http://dx.doi.org/10.5038/1827-806X.29.1.4>
- Villar E., Bonet A., Diaz-Caneja B., Fernandez P.L., Gutierrez I., Quindos L.S., Solana J.R. & Soto J., 1984 – *Ambient temperature variations in the hall of paintings of Altamira cave due to the presence of visitors*. Cave Science, **11**: 99-104.



Available online at scholarcommons.usf.edu/ijis

International Journal of Speleology

Official Journal of Union Internationale de Spéléologie



Structural and hydrological controls on the development of a river cave in marble (Tapagem Cave, SE Brazil)

William Sallun Filho^{1,2*}, Bruna Medeiros Cordeiro², and Ivo Karmann²

¹Geological Institute, State of São Paulo Environment Department, Rua Joaquim Távora, 822, 04015-011, São Paulo, SP, Brazil

²Geosciences Institute, University of São Paulo, Rua do Lago, 562, 05508-080, São Paulo, SP, Brazil

Abstract: Tapagem Cave (or Devil's Cave) is a river cave developed in the dolomite marble karst of the Serra do André Lopes (State of São Paulo, southeastern Brazil). Although this region is a plateau with significant variation in elevation and a humid subtropical climate, the cave is an anomalous feature in the André Lopes karst because there are few other caves. The marble, which is in a synclinal structure with subjacent phyllites, is a karst aquifer perched above the regional base level (Ribeira River) and has little allogenic recharge. The cave developed on a secondary anticline on the northwest flank of the marble synform forming a blind valley, the Tapagem River sink, that is an underground tributary of Ostras River. Development of the cave is due to the entrenchment of the Ostras through-valley and the large allogenic catchment area of the sink. In plan view, the morphology of the cave can be divided into three different sectors. The first sector, known as the Tourist Sector, has extensive collapse rooms, fossil passages and a variety of speleothems of notable dimensions. The second and most extensive sector is the river passage, which is a sinuous gallery controlled by marble banding with NE-SW cleavage and NW-SE fractures. In cross-section, the passages are vadose canyons up to 70 m in height, controlled by the marble banding. Four NW-SE diabase dykes in this passage do not affect its direction in plan view. The third sector is an extensive network of passages and collapse rooms, which are interlaced in plan view and on different levels, forming a maze pattern. Initially, the Tapagem and Ostras Rivers developed on a gentle surface and flowed into the Ribeira River. With the entrenchment of the Ostras through-valley, the Tapagem River partially infiltrated via a paleosink into the upper passage of the "Erectus Room," remaining a half-blind valley. Following a series of collapses and obstructions, the River next infiltrated via the current sink, creating a fully blind valley. Currently, the cave has a difference in elevation of 120 m between the sink and the resurgence, which corresponds to the difference in entrenchment between the two valleys.

Keywords: marble, through valley, river cave, cave morphology, Tapagem Cave, Brazil

Received ; Revised ; Accepted 10 August 2014

Citation: Filho W.S., Cordeiro B.M. and Karmann I., 2014. Structural and hydrological controls on the development of a river cave in marble (Tapagem Cave - southeastern Brazil). *International Journal of Speleology*, 44 (1), 75-90. Tampa, FL (USA) ISSN 0392-6672
<http://dx.doi.org/10.5038/1827-806X.44.1.7>

INTRODUCTION

Tapagem Cave is one of the most famous and most visited show caves in Brazil and is known for its scenic beauty and the size of its speleothems. It is the 24th longest and the 15th deepest cave in Brazil (out of 5,875 caves, according to the SBE). This cave is situated in the Serra do André Lopes, an isolated body of dolomitic marbles in the Ribeira River Valley in the south of the State of São Paulo in southeastern Brazil (Fig. 1). It is a region with several narrow bands of metamorphic carbonate rocks (mainly metalimestones) of middle to upper Proterozoic age with significant karst systems. There are approximately 400 caves registered in the Ribeira Valley karst terrains. However, caves are rare

in the Tapagem Marble, with only 25 caves registered, of which 6 are longer than 100 m in length and only the Tapagem Cave more than 1 km in length.

In Brazil, there are approximately 10,000 registered caves, 44% of which are in carbonate rocks, only 1% in marble and the remainder in other lithologies (CECAV, 2012).

The geologic and geomorphologic situation of the Tapagem Marble differs from the other karst areas in the region of Ribeira Valley. The Tapagem Marble has a dolomitic composition, which is less soluble than limestones (Rauch & White, 1970), and it is a marble, a carbonate rock with a low porosity and negligible permeability, making it difficult for karst waters to penetrate (Ford & Williams, 2007). The dolomitic

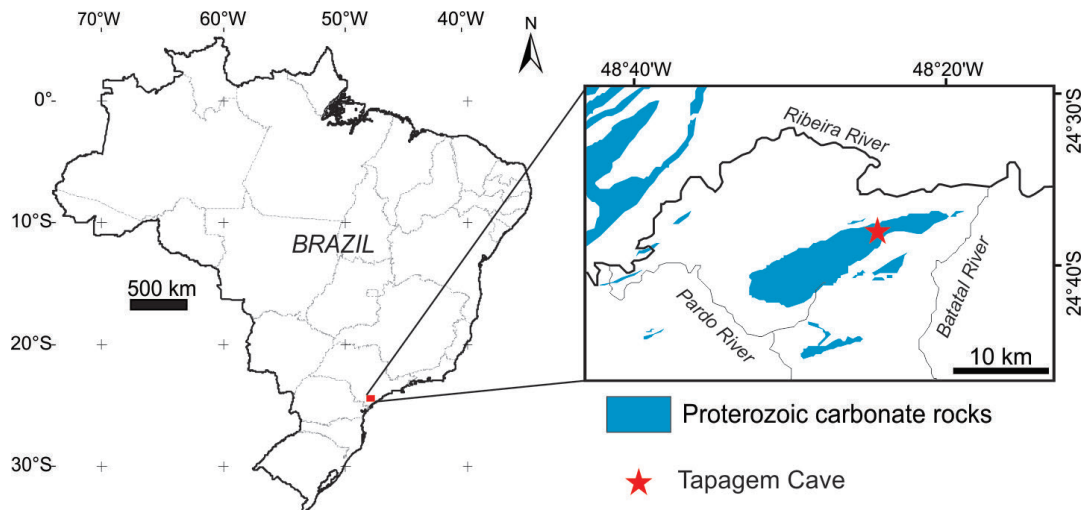


Fig. 1. Map showing the location of Tapagem Cave and carbonate rocks in the southern part of the State of São Paulo and the northern part of the State of Paraná (geology modified after Campanha, 2002).

marble forms a plateau, and mostly of the non-carbonate rocks and metalimestones of the region are at lower elevations.

Typically, narrow bands of carbonate in deformed terrains are favorable for allogenic karstification close to the contact zone (Lauritzen, 2001). The Tapagem Marble consists of a narrow, deformed carbonate band and a plateau, and even with a high perimeter/area ratio and a long allogenic contact zone perimeter, there are only a few points of effective allogenic recharge. The higher portions of the allogenic recharge areas are generally narrow.

Despite the nature of such rocks, there are several examples of cave development in marble (Karmann et al., 2001; Lauritzen, 2001; Despaigne & Stock, 2005). Caverna do Ecos (Brazil) has a simple rectilinear conduit morphology, initially developed at the intersections of fractures and bedding planes in the marble and followed by breakdown processes that opened up large vadose rooms in the overlying schist and quartzite. Crystal Cave in the Sierra Nevada (USA) is a complex, multi-level cave composed of six major levels developed in a narrow vertical band of marble (Despaigne & Stock, 2005). In Scandinavia, there are good examples of marble caves, such as Larshullet, Storsteinshola, and Horn's No. 1 (Lauritzen, 2001). Lauritzen (2001) considers these caves to be linear systems that drain between two points in the aquifer, preferably from a physical input (sink) to a physical output (spring), guided by geological structures.

In the case of Tapagem Cave, which has been known for more than one hundred years, no detailed geological study had been conducted. As a consequence, the morphology of the cave, the geomorphologic and hydrochemical characteristics of the influence basins, and the geological factors governing the cave were investigated in an attempt to interpret its origin and evolution. This study enabled an understanding of the geological and geomorphological setting of the Tapagem Cave and the processes involved in its evolution; moreover, the study demonstrates the importance of the allogenic waters in marble karst. However, future studies using sediment and speleothem dating will be required to establish the chronology of the events.

REGIONAL SETTING

The Tapagem Cave, also known as “Caverna do Diabo,” or Devil’s Cave (commercial name), receives approximately 30,000 visitors/year (Lobo et al., 2013) and is within the Devil’s Cave State Park. Tapagem Cave was first described in the literature by Krone (1904) and was the second cave recorded in the state of São Paulo. Krone (1898, 1904, 1909) was the first to explore the Ribeira Valley region at the end of the 19th Century, recording various caves and emphasizing their scientific relevance and need for conservation. Subsequently, in 1901, Lourenço Granato conducted a survey of land destined to be purchased by the government when the initial exploration and registration of Tapagem Cave occurred, and in 1910, the cave was recognized as a heritage site, remaining under the management of the São Paulo state government since that time (Brandi, 2007).

In 1961, partial exploration was performed by the *Centro Excursionista de Itatins* (CEI), led by Coronel Petenã, who encouraged descriptions of the cave in the press (Zilio, 2003) and was among those responsible for making the cave a growing attraction for tourist activity. In 1967, the cave became known as Devil’s Cave for publicity purposes through State of São Paulo Decree No. 48,818. In 1964, Michel Le Bret initiated renewed exploration and mapping of caves in the Ribeira Valley using the information gathered by Krone. The first map was prepared of Tapagem Cave along with the first interpretation of how the cave had formed via unrestricted runoff and rock joints (Le Bret, 1966). Tapagem Cave and its resurgence, Ostras Cave, had been separated due to their inaccessibility, but a route connecting them was discovered by Le Bret in the 1960s (Le Bret, 1975). In addition, in the mid- to late 1960s, the *Sociedade Excursionista e Espeleológica* (SEE) mapped the cave and conducted biological and meteorological surveys (Matos, 1966; Krüger, 1967). It was only in the 1990s that the *Sociedade Brasileira de Espeleologia* (SBE), through Project PROCAD, initiated further mapping that resulted in the current plan of the Tapagem cave system (Figueiredo et al., 2007; Rodrigues, 2002).

The Ribeira Valley karst terrains are found in narrow bands of carbonate rocks (Karmann & Sanchez, 1986; Fig. 1) lying within the “Ribeira Fold Belt,” an orogenic belt of Neo- to Mesoproterozoic age on the east coast of Brazil (Almeida, 1977). Supracrustal rocks of a low to medium degree of metamorphism, known as the Açungui Supergroup, are predominant in this area (Campanha, 1991; Campanha & Sadowski, 1999).

Tapagem Cave lies in one of these bands, termed the Tapagem Marble, an elliptical body with a major axis of 22.7 km oriented in a NE-SW direction, and a width of between 1.7 and 5.2 km. It is composed of fine-grained, white, homogeneous metadolomites (Campanha et al., 1985) (Fig. 2) with an apparent thickness of up to 500 m. Along with underlying phyllites, schists and quartzites (Metapelitic Unit), the marble composes the Serra das Andorinhas Sequence (Faleiros et al., 2012), forming a large synformal structure delimited by transcurrent faults (Neoproterozoic-Eopaleozoic) (Campanha, 1991, 2002).

The Tapagem Marble forms the Serra do André Lopes Plateau, a carbonate plateau with narrow rims of phyllites and schists (Serra das Andorinhas Sequence), with an elevation ranging from 330 to 1010 m (Fig. 2).

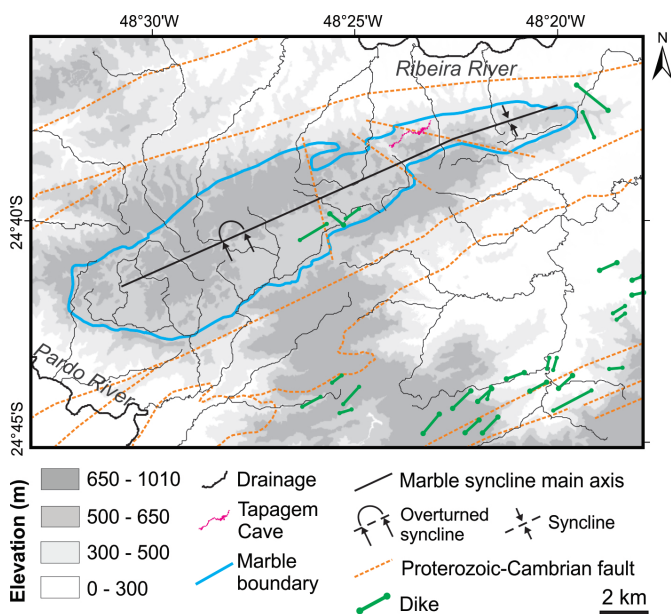


Fig. 2. Geology and hypsometry of Serra do André Lopes and the region (geology modified after Campanha, 2002, and Faleiros et al., 2012, 2013).

The geomorphological evolution of the region is the result of regressive differential erosion and the evolution of the Brazilian continental margin (Almeida, 1964; Almeida & Carneiro, 1998) related to the origin and evolution of the Serra do Mar range. Mesozoic intrusions occurred in the region during continental fragmentation, forming a NW-SE dyke swarm with a predominance of tholeiitic diabases in the failed arm of a triple junction (Almeida, 1998; Coutinho, 2008) with the injection phase occurring between 131.4 and 129.2 Ma, respectively (Renne et al., 1996; Ernesto et al., 1999).

The origin of the Serra do Mar dates from approximately 25 million years after the completion of the continental rifting process (134–114 Ma), when regional uplift was initiated in response to the passage of the South American Plate over the Trindade

hotspot (Riccomini, 1995; Zalan & Oliveira, 2005). It is believed that this uplift ended at the Cretaceous-Paleocene boundary and gave rise to a regional doming, creating a water divide between the Atlantic Ocean and the continent to the west (Riccomini et al., 2004). The erosional advance of the Ribeira basin into the interior of the continent exposed carbonate rocks of the Açungui Group. Based on a study of karst evolution in the Betari River Valley, Karmann (1994) determined that the entrenchment of the surface in the Upper Ribeira Valley occurred, at a minimum, between the Lower and Middle Miocene.

The region has a humid subtropical climate without a dry season (Alvares et al., 2013), an average annual rainfall of 1600 mm and an average annual temperature of 18°C, with a dense Atlantic Rainforest. The base level of erosion in the Serra do André Lopes is the channels of the Pardo and Ribeira rivers, which in this sector are at altitudes of 30 to 150 m (Fig. 2). Significant deposition of tufas occurs along the local drainage channels due to the essentially autogenic nature of their recharge waters (Sallun Filho et al., 2012).

MATERIALS AND METHODS

Geomorphological mapping was performed on the surface, demarcating the karst features and the drainage network using a stereoscope and panchromatic aerial photographs on a scale of 1:25,000; contours were generated using Shuttle Radar Topographic Mission (SRTM) and field survey data until the final mapping was obtained and united in an ARCGIS 10 (ESRI) environment. Topographic cross-sections of the surface relief and longitudinal profiles of the river were prepared from the SRTM base data using Global Mapper 15 (Blue Marble Geographics) software to gain a better understanding of the setting of the cave relative to the plateau and the hydrographic basins. The longitudinal profile of the river was constructed from its source to its mouth. The hydraulic gradient was calculated based on this profile, using the difference in elevation divided by the horizontal distance.

The autogenic and allogenic recharge areas were calculated based on the area of all of the drainage basins over the marble and the non-carbonate rocks, respectively, using a 1:100,000 geological map from Faleiros et al. (2012, 2013).

The pH and temperature were measured using a multiparameter instrument (Hanna HI 98129). For the saturation index (SI), two water samples recovered during the rainy (summer) and dry (winter) seasons were collected from two sites (the Tapagem and Ostras Rivers). The SI calculation was based on the Langmuir (1971) equation and was processed using *AquaChem 5.1* software.

The marble structure was delineated from structural data taken during hikes on the surface, resulting in geological cross-sections. A lithologic analysis in the cave was performed using thin sections of the marble and diabase dykes, and chemical analyses using X-ray fluorescence were performed on two samples of marbles to determine the major element contents (presented as % of oxides). The oxides was converted

into quantities of dolomite, calcite and impurities, as determined by Martinet & Sougy (1961), and classified according to Leighton and Pendexter (1962). The sample collection in the cave was performed in accordance with Brazilian legislation and authorized by CECAV-ICMBIO (No. 30591-1). For structural geology, the fractures, banding and dykes were measured in the cave and on the surface, and then merged in stereograms, plan views and cross-sections.

The study of the morphology of the cave was based on previously topographic mapping performed by PROCAD (Devil's Cave Project - SBE, 2008) and several surveys of Tapagem Cave. During the surveys, thirty transverse cross-sections and one longitudinal cross-section were generated using a laser distance meter to measure the width and height of the passages. The altimetric elevation of the initial topographic base of the cave of 460 m at the sink was based on GPS location on the 1:10,000 topographic base map (IGC, 1988). From the sink, it was possible to establish a correspondence between relative elevations derived from cave mapping and altimetric elevations used in the sections and cave levels. The morphometry of the cave is based on the

cave map. The cave river gradient was calculated using the elevation (the difference in elevation divided by the horizontal distance) and slope (measuring of the inclination in degrees of the longitudinal profile of the river). The sinuosity index of the river cave is the ratio of the length measured between two points along the river to the straight line between two points.

The transverse cross-sections and photographs of the cave are displayed in the sink-to-resurgence direction.

RESULTS

Ostras - Tapagem Basin

The Tapagem cave has developed from the Tapagem River sink at an elevation of 460 m asl, with the Ostras River as its discharge area (resurgence) at 340 m asl (Fig. 3A). The Ostras and Tapagem River valleys lie nearly parallel to one another in a NW-SE direction and are the basins that receive most of the allogenic recharge and have the largest area of non-carbonate rocks in the Tapagem Marble karst (Fig. 3A, 4). Other large areas of non-carbonate rocks have rivers that flow to points outside the karst (Fig. 2).

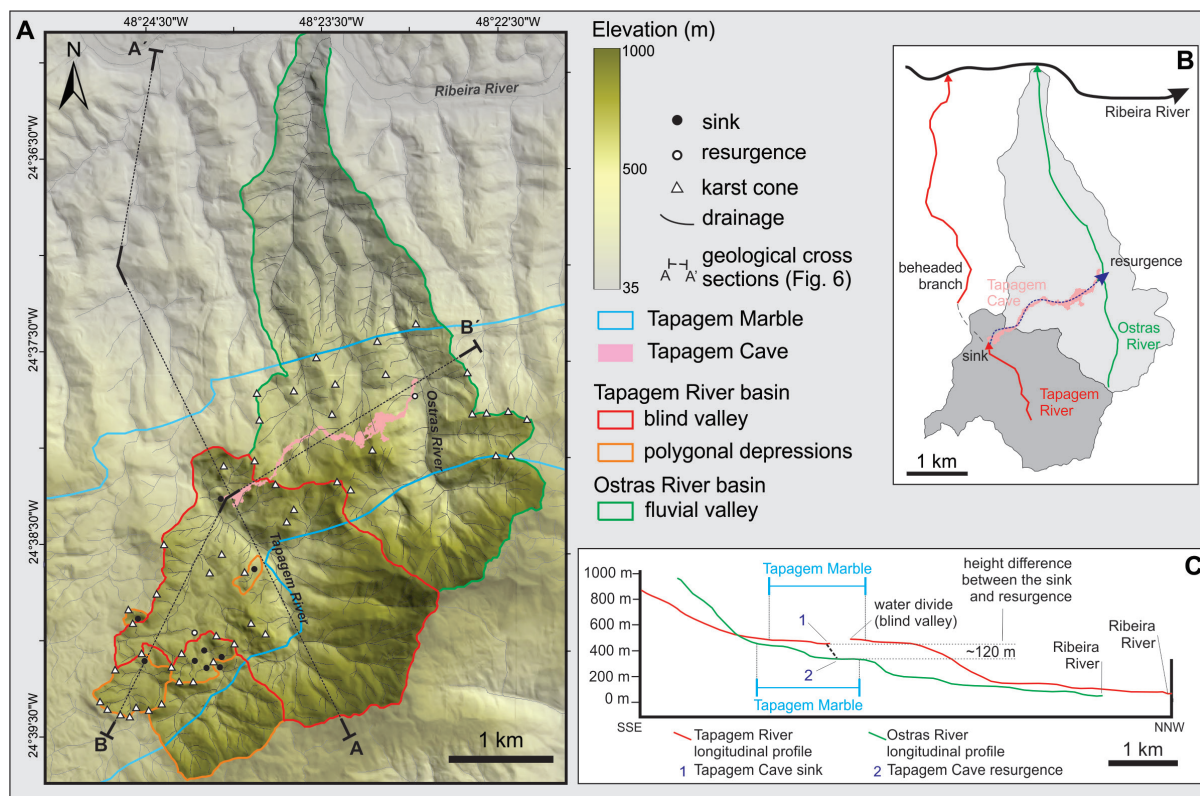


Fig. 3. The Ostras - Tapagem basin. A) DEM of the Tapagem River basin with the location of the marble and karst features and projection of Tapagem Cave; B) Diagrammatic drawing of the Tapagem River catchment area; C) Longitudinal profile of the Tapagem and Ostras rivers.

The Tapagem Valley is in the narrowest portion of the entire band of marble, with allogenic recharge from elevated borders to the southeast (600 to 924 m) composed of weathered phyllites and micaschists. The overall hydraulic gradient is 0.157, ranging from 0.3 at its headwaters to 0.068 in the marble down to the sink.

In its upper-middle course (580 m), the river flows in a narrow channel in a deeply entrenched valley at the contact between the metapelites and marbles. In the marble, the valley becomes more open with an extensive alluvial plain (488 m asl) and, about 700 m

from the contact, makes an abrupt change to the NE to enter the cave sink (blind valley). At a distance of 450 m NW of this abrupt change in direction there is a smooth topographic divide 16 m higher in elevation that separates the blind valley from the remainder of the Tapagem River Valley, providing evidence of its former continuation to the Ribeira River.

The Tapagem River basin is now a blind valley with surface runoff discharged into Tapagem Cave and the Ostras River as the local base level 120 m below it (Fig. 3B, C). The underground route followed by Tapagem

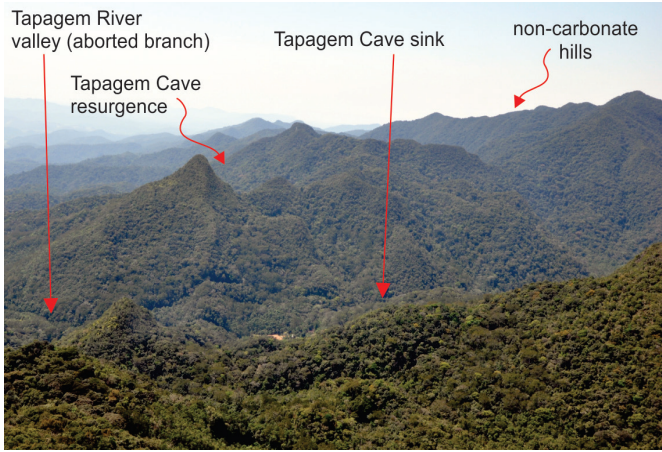


Fig. 4. Oblique aerial photograph of the Tapagem River Valley, the ridge over the cave and the Ostras River Valley in the background (view to the NE).

Cave developed perpendicular to the trend of the surface runoff (Fig. 3A, B). The blind valley captures all of the water at the Cave sink, a surface catchment basin of approximately 6 km² with an autogenic recharge area of 3.7 km² (61.72%) and allogenic recharge of 2.3 km² (38.28%) forming a mixed system.

Although the Tapagem and Ostras rivers have high pH values (8.31 and 8.63 in the summer and 8.37 and 8.53 in the winter, respectively), the saturation index for calcite is low in the Tapagem River (+0.11 in the summer and +0.38 in the winter) and high in the Ostras River (+0.67 in the summer and +0.73 in the

winter), indicating less saturated waters with a certain amount of dissolution capacity at the sink, especially during the rainy season (summer).

The Ostras River cuts deeper into the rock and reaches lower elevations in the marbles (Fig. 3C); the mean channel gradient is 0.163, ranging from 0.5 in the up-gradient phyllites to 0.095 in the marbles and 0.084 in the down-gradient phyllites.

Lithology and structural geology

The most prominent feature of the marble structure is the compositional banding (Fig. 5A). The initiation of the cave is likely related to the intersection of this banding with axial plane cleavage, as observed in certain protoconduits (Fig. 5A). The banding consists of S₁ foliation, a relic of S₀, folded in the form of recumbent, isoclinal intrafolial folds. Microscopically, it is possible to observe a granoblastic texture and fine granulation oriented in accord with S₁ (Fig. 5B, C). Chemically, the marble can be classified as dolomitic and calcareous dolomite (dolomite: 98.44 and 90.16%; calcite: 0.00 and 12.25%; impurities: 1.85 to 0.00%) with little or no impurity (terrigenous sediments).

On a larger scale, the Tapagem Marble is in a syncline with smaller secondary folds, forming the complex folding patterns typical of marbles. Tapagem Cave is located on the NW flank of the principal syncline (Fig. 6) and, more specifically, on a secondary anticline with a 246/35 axis (Fig. 6, 7). Marble banding in the cave is oriented NE-SW, with dip angles of 65° and 90° to the NW in

Fig. 5. A) Protoconduit in the river passage controlled by marble banding / cleavage with high dip angles to the NW (left); B), C). Photomicrograph of the dolomitic marble with a granoblastic texture and fine granulation (uncrossed polarizers - B, and crossed polarizers - C).

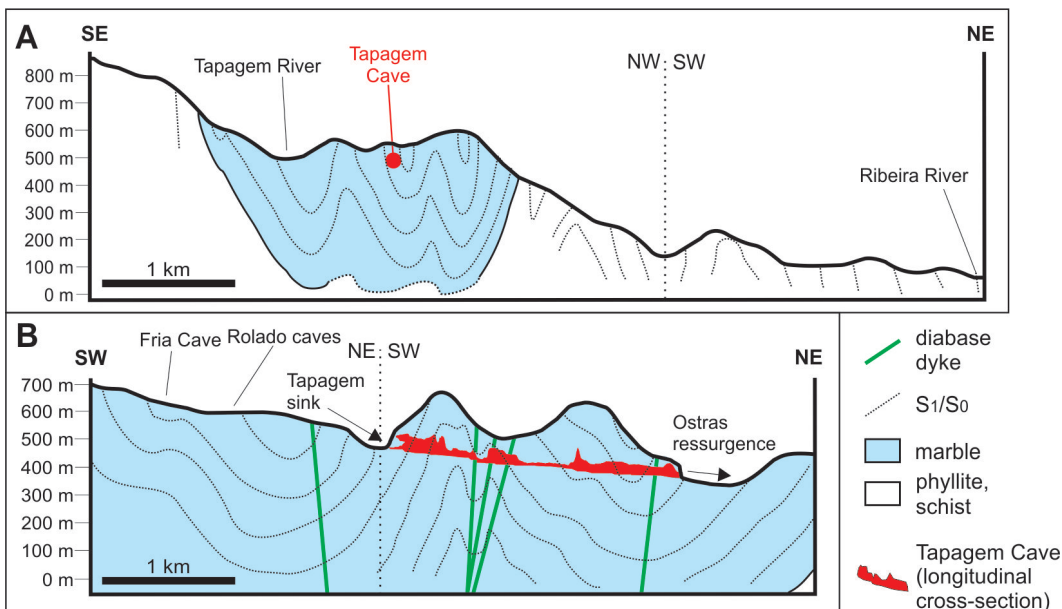
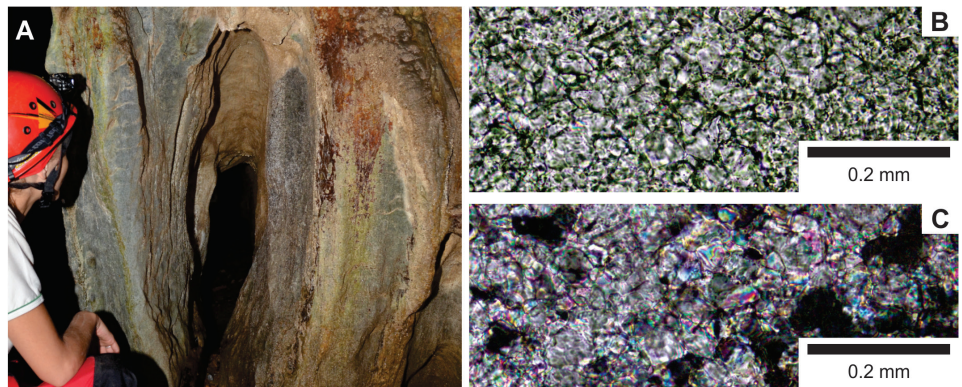


Fig. 6. Topographic-geological cross-sections of the Tapagem Marble, including the Tapagem Cave. A) Transverse section; B) Longitudinal section. The boundaries of the marble are according to Faleiros et al. (2013). Topography: SRTM; vertical exaggeration: x2. The locations of the cross-sections are shown in Fig. 3.

certain places and to the SE in others characterizing the anticline (Fig. 6-8).

Four diabase dykes were identified in the cave (dykes 1 to 4; Fig. 8A, B; Table 1) perpendicular to the overall orientation of the marble banding, with a NW-SE orientation, a dip to the SW (Fig. 7) and widths between 0.4 and 3.0 m (Fig. 9A, B). The dykes are massive tholeiitic basalts of fine granulation and a glomeroporphyritic texture. The dykes have cooling fractures; only dyke 4 has columnar joints perpendicular to the walls. Because they are less soluble rocks, the dykes stand out from the marbles on the cave walls (Fig. 8) and determine the sectors with a higher river gradient (Fig. 8C, D).

Dykes have not played a part in controlling the evolution of the cave, although certain conduits developed along the plane of the associated NW-SE fracturing. These fractures cause abrupt changes in the NE-SW pattern of the river passage and stretches of higher sinuosity index (Fig. 8E), and they control the maze sectors of the cave (Fig. 8A).

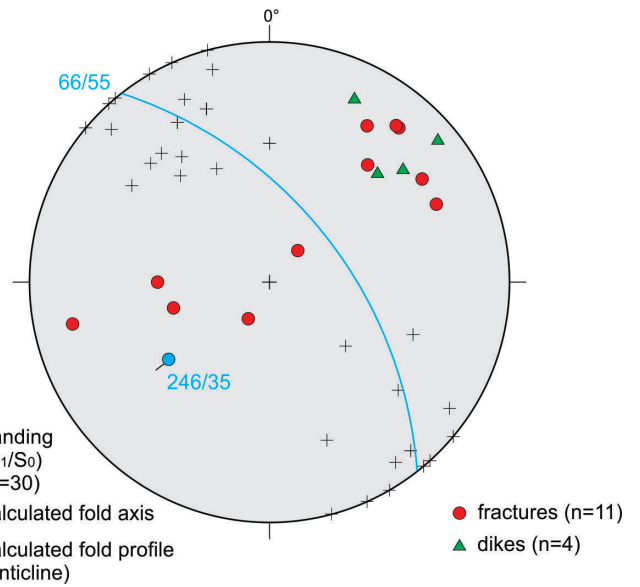


Fig. 7. Stereogram from Tapagem Cave showing the poles of the planes of the marble banding, dykes and fractures and the great circle of the fold profile and the pole of the calculated fold axis.

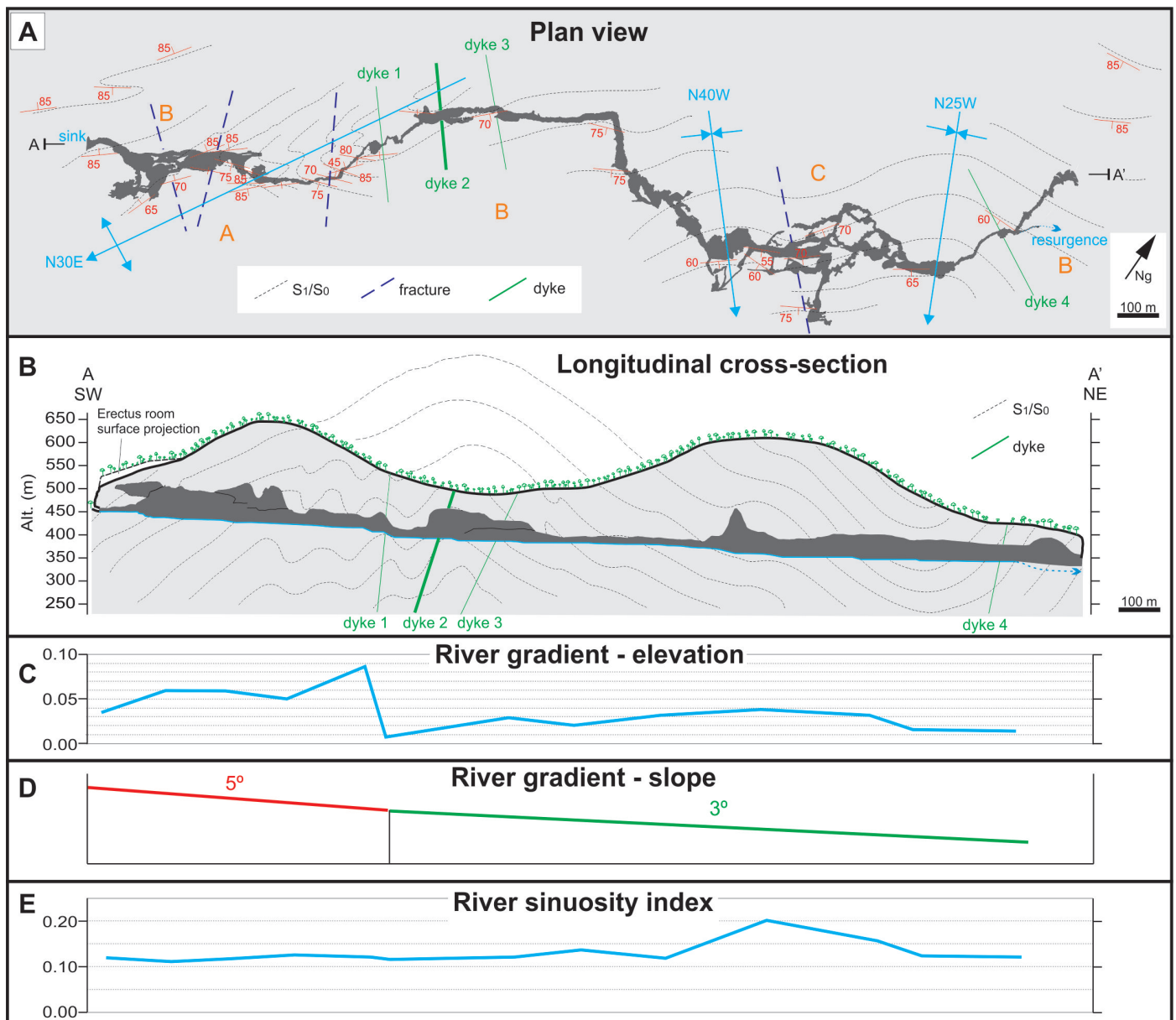


Fig. 8. Structural and morphological features of Tapagem Cave. A) Plan view of the cave with the geological structures and morphological sectors; B) Longitudinal section (projected) with the geological structures; C) River gradient (based on elevation); D) River gradient (slope); E) Sinuosity index of the river.

Table 1. Characteristics of the diabase dykes found in Tapagem Cave.

	Strike	Dip	Thickness (m)
Dyke 1	N40W	85SW	0.8
Dyke 2	N40W	72SW	3.0
Dyke 3	N45W	65SW	0.45
Dyke 4	N65W	80SW	0.4

Morphology

The cave developed over a horizontal distance of approximately 6,237 m, with a total difference in elevation of 175 m and of 120 m between the sink point and the resurgence (SBE, 2008). On the surface, there are ridges, valleys and hills (Fig. 4) resulting in a bedrock thickness over the cave that ranges from 32 to 240 m (average of 103 m).



Fig. 9. Diabase dykes encountered in Tapagem Cave. A) Dyke 2; B) Dyke 4.

In plan view, the cave's morphology is predominantly that of an active river cave that has developed in a sinuous manner (Fig. 8). In its cross-section form, the principal passage is generally an underground canyon with upper passages that are occasionally interrupted by large collapse rooms. The plan view morphology of the cave is principally controlled by the NE-SW compositional banding and cleavage and, locally, by the NW-SE fractures (Fig. 8). According to its morphological characteristics in plan view and cross-sections, it was possible to identify distinct sectors of the cave with different morphology and structural controls.

The Tourist Sector and Gava Passage (A)

This portion begins below the sink and is the initial segment of the cave, with extensive intermediate and upper rooms and passages. The passages and rooms develop in a NE-SW direction and are vertical or inclined to the NW in accordance with the marble banding in the northwest flank of the anticline (Fig. 7, 8).

The Tourist Sector is at an intermediate level and is composed of large rooms in which concrete gangways and stairs have been installed for visiting tourists along a route of approximately 800 m (Fig. 10A).

The morphology of the "Tourist Sector" consists of smooth walls inclined in accordance with the banding of the marble and altered by collapse processes (Fig. 11-2).

The richness, size, and beauty of the speleothems in this sector are noteworthy and make Tapagem Cave the tourist cave of greatest scenic beauty in the state of São Paulo, and one of the most remarkable in Brazil. Columns with a height of more than 20 m and a diameter of 6 m and stalagmites with heights more than 15 m are deposited upon an immense pile of collapsed blocks of rocks and earlier speleothems. Various fallen speleothems show the growth of new flowstones, stalagmites and columns, which are also of a large size (Fig. 10B). A large colluvial-eluvial deposit with blocks of the marble with large stalagmites upon them, the "Cathedral Room," fills a portion of one of the rooms (Fig. 10C, 11-2). This sediment was injected by a vadose invasion originating from a collapse depression (doline) above the cave.

The "Erectus Room" is the highest in the cave, at a level 50-60 m above the current river (Fig. 11-1). This room is highly decorated by various types of speleothems, especially stalagmites and fluvial deposits with the associated allochthonous material. The direction of the passage and its elliptical shape in cross-section are controlled by the dip of banding. The location and orientation of this passage, as a branch of the principal passage, suggests that it was the paleosink of the Tapagem River.

The “Rede Gava” is an upper level of the current river canyon that is partially isolated from it by speleothems and sediment levels (Fig. 11-3, 11-4). The difference in elevation between the “Rede Gava”

and the current water level is up to 50 m. The cross-sections are elongated, following the vertical structure of the banding in the rock, and are remnants of the river passage canyon.



Fig. 10. Tourist Sector. A) Room formed by collapse events and filled with speleothems; B) Large fallen stalagmite with the subsequent growth of other stalagmites upon it; C) “Cathedral Room” with a cone of colluvial-eluvial sediment injected from the surface and the subsequent growth of large stalagmites (Photos: Adriano Gambarini).

River Passage (B)

The river passage begins shortly after the cave sink (460 m asl) and continues in a sinuous manner although it is entrenched into the left side (NW) of the passage. In plan view, the passage is narrow, elongated (2.84 km in length) and sinuous (sinuosity index of 1.3).

Most of the river passage has the form of an underground canyon, with certain sections showing more circular shape and rooms with a concave ceiling and collapse blocks on the ground. Generally, the canyons show rectilinear, vertical or inclined walls (Fig. 12) with their direction alternating with the dip direction in accordance with the attitude of the marble structure; however, in certain cases, the dip direction is in accordance with the hydraulic gradient rather than the structural features. The width of the canyon ranges from 2 to 15 m, in proportion to the height of the passage which varies from 20 to 70 m throughout the cave (Fig. 12). In the sectors in which the passage has been partially filled by speleothems or the ceiling is inaccessible, it is difficult to visualize and interpret its original morphology.

In the first half of the cave, the river passage trends NE-SW, with a cross-section that is vertical or inclined to the NW following the banding in the marble (Fig. 12-5) in the NW part of the anticline (Fig. 7, 8). In the other half of the cave, the passage still follows the NE-SW banding but is inclined to the SE following the dip

of the banding in this direction (Fig. 12-8) in the SE part of the anticline (Fig. 7, 8).

In the central portion of the cave, there is a 90-degree change in the direction of the passage where the cave follows a NE direction before continuing to the SE perpendicular to the bedding. At this point there is fracture or fault control related to the dykes, and the dip of the banding changes direction from NW to SE. In cross-section the passage morphology becomes circular to elliptic, as in the case of phreatic features.

Several smaller collapse rooms interrupt the river passage canyons. A large room opens up that is influenced by dyke 1 (“Dyke Room”), with a collapse of the marble and dyke rock (Fig. 9A). In the sector near dykes 1, 2 and 3, the river has more waterfalls (i.e., a higher gradient; Fig. 8C).

Slightly more than 200 m from the cave exit (which is a fossil resurgence), the channel enters a siphon descending approximately 60 m beneath the water table before its resurgence between rock blocks in the Ostras River valley at an elevation of 340 m.

Generally, the underground river is flowing over deposits of pebble- to boulder-sized clasts of marble, phyllite, quartzite, quartz and diabase (rounded or columnar joints) along with speleothems, originating from the collapse of the upper passages. Less often, there are deposits of sand or mud or the stream flows on bedrock where erosive features of the pothole type are very common in the riverbed.

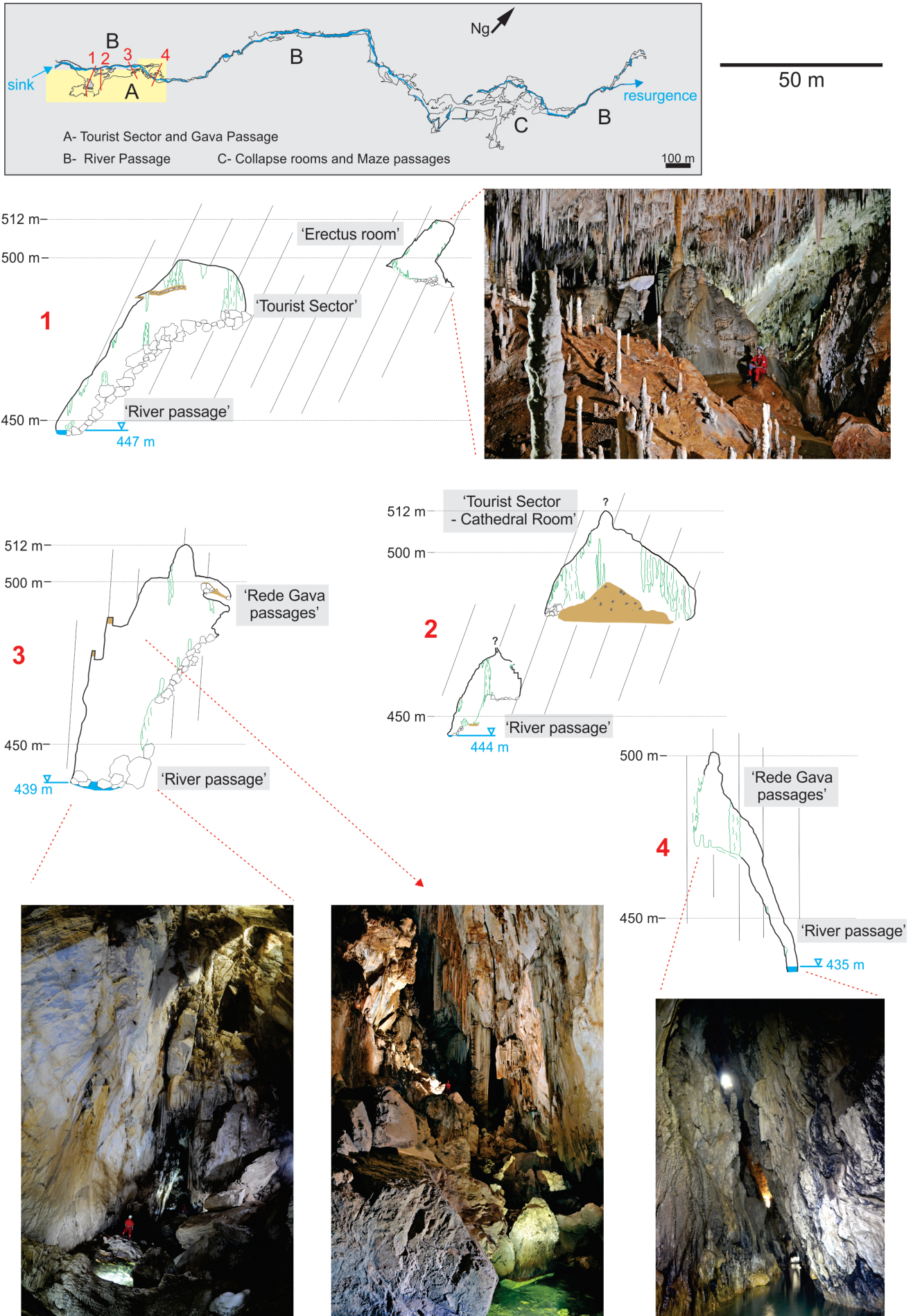


Fig. 11. Cross-sections of Sector A. 1) Morphology controlled by the banding in the river passage and the upper room of the "Erectus Room"; 2) Morphology controlled by the banding in the river passage and the intermediate level of the "Tourist Sector"; 3) Canyon controlled by the banding and the upper level of the "Rede Gava" (second photo looking toward the sink); 4) Vertical canyon and the upper level of the "Rede Gava" (Photos 1, 2, 3: Adriano Gambarini).

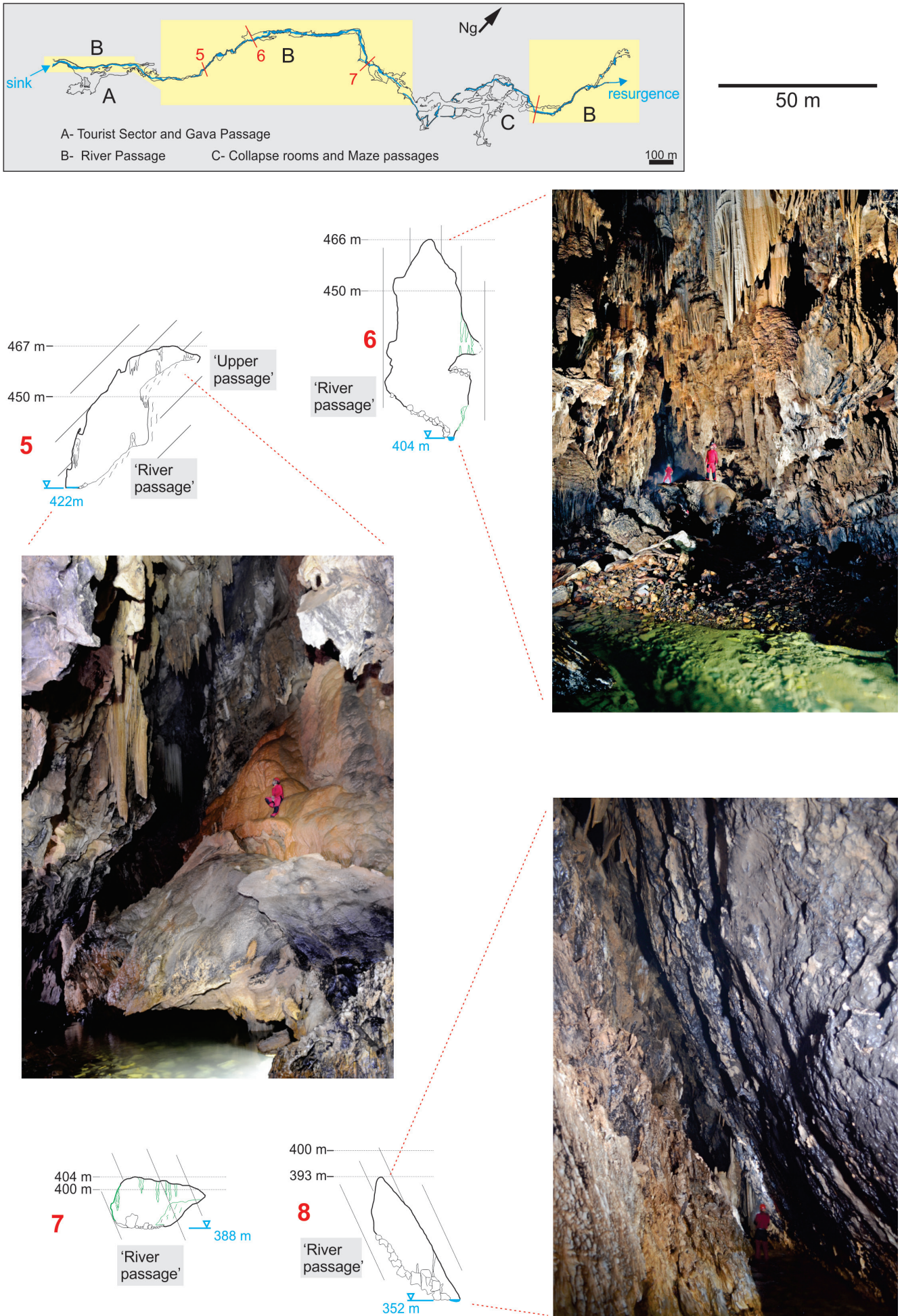


Fig. 12. Cross-sections of Sector B. 5) Canyon and upper passages; 6) Vertical canyon; 7) Elliptical morphology; 8) Canyon inclined to the SE (Photos 5, 6: Adriano Gambarini).

Collapse Rooms and Maze Passages (C)

Section C differs from the other sections in that a series of rooms and abandoned stream passages interrupt the homogeneous sinuous pattern of the modern river passage. These passages are oriented in NE-SW and NW-SE directions, accordant with banding

in the marble in the SE flank of the anticline and fracturing associated with the dykes. The predominant morphology of the large rooms is that of bedrock collapse, as in the “Fallen Giants Room,” the “White Room” the “Philippe Room,” and particularly the “Michel Room” which has a height of 80 m (Fig. 13-9).

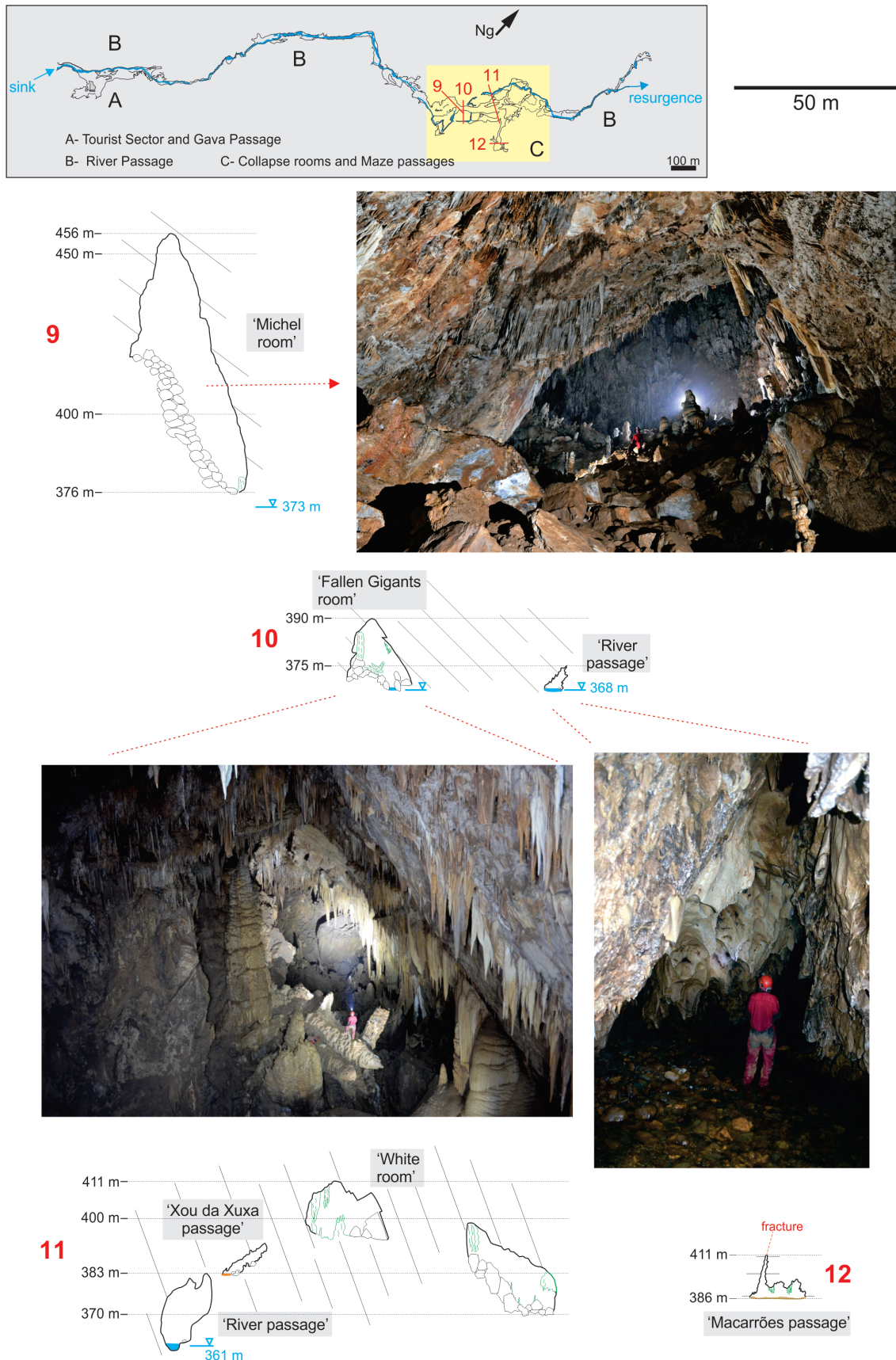


Fig. 13. Cross-sections of Sector C. 9) Large collapse room (the “Michel Room,” 80 m high; photo looking upward); 10) Collapse room with fallen stalagmites (the “Fallen Giants Room”) and the “River Passage”; 11) Four passages, the upper “White Room” and diversions to the SE and NW (the “Xou da Xuxa” and “River Passages”); 12) The Macarrões Passage (Photos 9, 10: Adriano Gambarini).

These passages are located at various levels (Fig. 13-11) that are masked by collapse events, forming several rooms and comprising a complex network that, in plan view, is a maze. The “Philippe Room”, up to 10 m above the current river, is connected to the river passage (B) by the downgradient “Barro Passage”. The original morphology of the “Xou da Xuxa” (NE-SW) and “Macarrões Avenue” (NW-SE) passages remains well preserved, the former corresponding to an entrenchment and the latter showing phreatic features, both forming a second level 20 m above the current river. The morphology of the phreatic passage in the “Macarrões Avenue” passage is interpreted as a fracture-controlled phreatic initiation succeeded by bedding-controlled vadose widening. The central passage extends from the “Fallen Giants Room” and the “White Room,” which is connected to the “Black Room” via the “Alto do T.” This is the highest level in Sector C, 40 m above the river.

The rooms have irregular ceilings, and floors filled with large fallen blocks that obstruct the river, making its progress difficult and forcing it to penetrate between the blocks and abandon its principal course for routes at lower elevations. There are large fallen speleothems, including two stalagmites known as the “Fallen Giants” (Fig. 13-10). In cross-section, the river channel morphology becomes triangular passages of smaller dimensions than the underground canyon elsewhere.

After the change in direction of the river, the channel adopts a highly structured form (Fig. 8). At this point, passages trending SE diverge (braid) in various directions, determined by the foliation in some places and by the NW-SE fractures in others. Considering the route followed by the river alone, its sinuosity index is higher in Sector C, between 1.5 and 2.0 (Fig. 8E).

Cave levels

By observing elements that record the phases in the fluvial entrenchment and depositional processes, four levels of evolution of the cavity were identified, which were parallel to the overall trend of the cave and river. Palmer (1987) has proposed that cave levels (passages) are controlled by a fluvial base level which, in the case of Tapagem Cave, is the through valley of the Ostras River.

The 1st level corresponds to the course of the current river, which begins at the Tapagem River sink and extends up to 10 m above the river. The 2nd level is found at 10 to 20 m above the 1st level, characterized by erosional features such as the undermining of the base of speleothems, light sediment deposition and fluvial terraces along the river passage. In the Tourist Sector near the sink, it is possible to clearly

observe its record on the walls of the passage and through the light sediments. The 3rd level is found at a height of 30 to 40 m above the river, with fluvial terraces being encountered in the Tourist Sector and the “Rede Gava”, sediments cemented in the form of pendants that indicate this level of erosion and by the “Macarrões Avenue” at this level in Sector C. The 4th level, the highest, is found at a height of more than 40 m, for example, in the passages of the “Erectus Room.” Parts of the “Michel,” “White” and “Alto do T” Rooms are also at this level.

Along the active river course, the cave levels are generally represented as ghost passages or in the form of erosion levels, overlapping with several fossil passages in the canyon. In sectors A and B, the levels are distributed laterally in a northwesterly direction (Fig. 14A) due to canyon entrenchment and channel migration. In Sector C, the passages indicate the migration of the principal drainage channel and its junction with several tributaries, which results in a maze pattern (Palmer, 1975) with a high degree of structural control by the fractures (NW-SE) and foliation in the marble (Fig. 14B). In this sector, the morphology of the cave changes from a sinuous river passage to a labyrinthine pattern when all of the passages and levels are considered together in plan view. However, analysis of the river passage in Sector C alone reveals that it remains a sinuous river passage. In this sector, the large-scale collapses that have occurred in the upper passages (the Michel and White rooms) might have been responsible for the migration and diversion of the drainage channel.

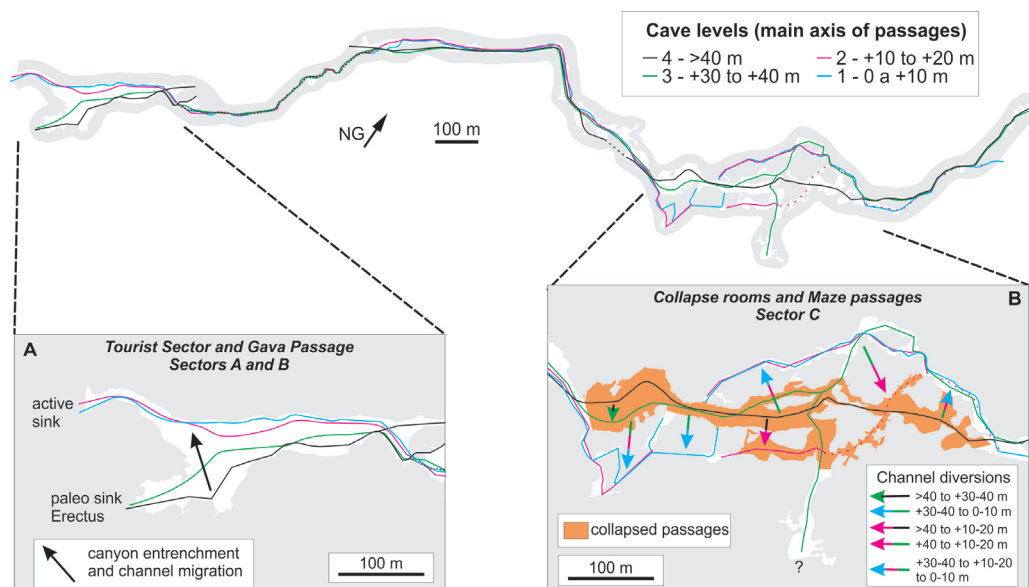


Fig. 14. Cave levels in plan view. The colored lines represent the main axis of the passages in each level. A) Detail of Sectors A and B; B) Detail of Sector C.

DISCUSSION

The Tapagem Marble is a long and narrow carbonate band, causing the marble to be an isolated, separate and confined aquifer. The synclinal structure with subjacent phyllites and the topographic situation of the carbonate plateau makes the karst a perched aquifer above the regional base level (the Ribeira River), with little allogenic recharge. The entire Tapagem Marble

band has a combination of dolomitic composition, low degree of primary porosity and predominantly autogenic recharge (86%), which results in a situation where there can be little development of caves. Caves are rare in the Tapagem Marble, so that Tapagem Cave is an anomaly. Its origin was possible due to the development of the Ostras River as a through valley and the allogenic recharge at the sink. Although the saturation index for calcite is positive, we believe that during flooding events, it can be negative. The cave originated in the narrowest portion of the marble band, a site favoring the injection of allogenic waters. The Tapagem River upstream of the cave has a very high hydraulic gradient over weathered non-carbonate rocks. Inside the cave, the river and the hydraulic gradient are also high. In addition to chemical corrosion, the river can transport clastic sediments, thus the effect of mechanical erosion on the enlargement of the conduits cannot be ignored.

The Tapagem and Ostras Rivers developed on a gentle surface draining to the Ribeira River: both cross the boundary of the marble at right angles. Progressively, the Ostras River formed a through valley at the surface because the allogenic surface runoff exceeded the capacity of the karst to absorb it (Ford & Williams, 2007). With the entrenchment of the Ostras River, there was an accelerated decrease in the water table in this sector of the karst that was allowed for a higher amount of water infiltration. The Tapagem River was swallowed via the Erectus paleosink and formed an underground flow path (initiation phase) aided by the action of allogenic waters (Palmer, 2001).

In the initial stage, the Tapagem River remained in a half-blind valley (Monroe, 1970), a blind valley with a proportion overflowing seasonally into the Ribeira River, which marks the beginning of the drainage reorganization process via karstification (Williams, 1982). Increase in the efficiency of the underground drainage channel resulted in capture of more of the Tapagem River into the cave and its becoming a tributary of the Ostras River, the local base level of the karst aquifer in the northeastern sector of the plateau. Therefore, the Tapagem River lost volume at the surface, and the rate of entrenchment of the valley decreased. At this stage, the volume of water in the cave remained low, with a slow rate of erosion.

Following further enlargement of the conduits, the water absorption capacity increased in the cave and the entire drainage of the Tapagem River went underground. Significant collapses occurred in Sectors A and C, however, because the action of the vadose water forming highly entrenched canyons induced extensive breakdown in the upper levels (White, 2005). The infiltration capacity decreased due to this obstruction of the passages by the collapse of the upper levels, and the drainage began to infiltrate at a new, lower sink (current) and develop new pathways.

Surface drainage once again reached higher volumes, favoring some surface overflow of the Tapagem River into the Ribeira River. In this stage, there was a long period of deposition of speleothems upon the collapsed blocks in the upper rooms.

When the drainage was able to infiltrate once again at the current sink in a more effective manner, the entire

flow of the Tapagem River went underground with a permanent capture (beheading) of the drainage and the formation of the current blind valley. With increased flow underground, the rate of entrenchment of the vadose canyon was very high, causing lateral erosion of the passages and the collapse of a portion of the upper rooms and their speleothems. Flooding events, along with the predominance of coarse sediments on the riverbed, led to erosion through abrasion, giving rise to distinctive features such as potholes in stretches of rocky riverbed (Palmer, 2007), which are also favored by the steep gradient of the river and the hardness of the rock (Ford & Williams, 2007).

The large pre-existing collapses in Sector C caused some diversions of the river, forming a maze pattern (Fig. 14B). The maze was created when the main passage was obstructed, and the stream divided into a network of bypasses that return to the main passage at several points (Palmer, 1975); collapsed blocks may obstruct the passages, breaking long, continuous conduits into various smaller, less efficient segments (White & White, 2000). In Sector C, the river flows in the NE-SW and NW-SE directions, controlled by foliation in certain places and by fractures oriented in the same direction as the dykes in other places.

Considering the cave system evolutionary development model known as the "Four-State Model" (Ford & Ewers, 1978; Ford, 2000), the Tapagem Cave is currently in the last evolutionary stage, Stage 4 (ideal water table caves). In a longitudinal section, it is possible to observe the remnants of loopings associated with the initial stages of the cave formation, currently carved by vadose entrenchment and filled with air, and low-ceiling sequences denoting the bypassing and filling of lower phreatic passages. Vadose inlet passages are infrequent, with only a few infiltration points for soil and gastropods, as in the example of the colluvial-eluvial sediment deposits found in the "Cathedral Room," which is currently inactive due to surface relief inversion. The frequency of penetrable discontinuities is low and most likely did not increase with time beyond a level sufficient to create pathways able to drain all of the runoff in the basin. Additionally, the lowering of the base level is an important factor in the cave evolution and conduit development (Worthington, 2005). In Tapagem Cave, it is generally possible to observe vadose entrenchment passages. The canyon morphology of the cave is a product of passage enlargement by base level lowering and vadose entrenchment processes through the dissolution of the floor to a lower level (Ford & Williams, 2007). In the process of opening up passages by vadose entrenchment, turbulent flow predominates, in which phreatic passages are entrenched and evolve into canyons with vertical walls (Palmer, 1991). Episodes involving a lowering of the base level of the karst are generally contemporaneous with surface geomorphological episodes (Powel, 1970). This underground morphology also occurs in the caves of other carbonate bodies in the Ribeira Valley, with canyons having entrenchments of up to 50 m because of lowering of the base level that was controlled by tectonic uplift (Karmann, 1994). With the exception of Sector C, few fossil passages are observed along the

river passage, indicating a continuous entrenchment of the Ostras River Valley (Palmer, 1987).

The canyons found in Sectors A, B, and D are influenced by metamorphic banding in the Tapagem Marble, whereas in Sector C, the gradient of the Ribeira River to the NW controls the evolution of the vadose widening of the passages and, in certain situations, flows against the direction of the local hydraulic gradient, thus interrupting the bedrock structural controls.

The dykes create sectors with waterfalls and higher river gradient with greater erosive capacity. Several small rooms interrupt canyon formation along the river passage that could have been caused by the erosional resistance of the dykes during the initial phases, inducing flooding upstream of them and enlarging the rooms there.

CONCLUSION

Tapagem Cave, or Caverna do Diabo, is one of the most famous and most visited show caves in Brazil and is known for its scenic beauty, remarkable canyons and large speleothems. This cave is situated in a narrow and isolated band of dolomitic marbles.

The cave developed in a basin with 38.28% of allogenic recharge in a mixed system and in the greatest allogenic catchment area of the André Lopes karst. The creation of the cave was possible due to the development of the Ostras River as a through valley and the allogenic recharge at the sink.

The Tapagem River sank in the Erectus paleosink in a half-blind valley at the initial stages of cave formation and the entrenchment of the Ostras River. Although there is scarcely any matrix porosity in the marble, the metamorphic banding and the axial plane cleavage in an overall NE-SW direction exert an influence on the direction of the passages in plan view and their shape in cross-section. The synclinal structure exercises hydraulic control with a regional gradient to the Ribeira River to the NW, but the cave developed SE toward the Ostras River because of proximity to phyllites to the NW that function as an impermeable barrier. The cave is mostly controlled by marble banding, cleavage (NE-SW) and fractures (NW-SE). The cave has 6.3 km of passages in plan, including 2.84 km of the River Passage, a 2.8 km narrow, elongated and sinuous passage.

The action of vadose water creating highly entrenched canyons induced breakdown in the upper levels. The collapses led to obstruction of the early passages, causing the drainage to infiltrate at a new sink and develop new pathways. In due course the entire flow of the Tapagem River went underground, with a permanent capture beheading the drainage and the river downstream of it, forming the current blind valley. With a higher flow of water underground, the rate of entrenchment of the vadose canyon was very high, causing lateral erosion of the passages and the collapse by erosion of a portion of the upper rooms and their speleothems. In the River Passage, certain vadose canyons reach a height of 70 m.

The maze pattern in the central part of the cave was created by dividing and bypassing the main passage

due to obstruction by the collapse, which was strongly controlled by NE-SW foliation and by NW-SE fractures.

Intrusive dykes have been breached during the evolution of the cave, and variations in the hardness of the rock at them have led to the formation of several waterfalls and sectors with higher river gradients.

ACKNOWLEDGEMENTS

The authors thank the São Paulo Research Foundation FAPESP (Grant #2011/10822-2) for financing the study and CNPq for the scholarships. We thank SBE and all of the PROCAD team for providing the cave map, COTEC for authorization of the activities in the park and CECAV for authorizing the rock sampling. We would like to thank Devil's Cave State Park for its support, particularly Josenei Cara and Mayra Jankowsky and all of the employees and monitors. We thank photographer Adriano Gambarini for the excellent photographs of the cave. Thanks are extended to all of the following colleagues for providing assistance in the field: Josias Moreira, Juliana Almeida, Jhonatas Moreira, Ladio Furquim, Marcos Silvério, Daniel Menin, Roberto Brandi, Valdomiro Pereira, Carlos Moraes, Luis Almeida, Rodrigo Borghezán, Tamires Zepon, Jonas Gallão, Bruno Consentino, Beatriz Boggiani and Bruna Torresi. We would also like to thank the Aristides of the Kaverna restaurant and the reviewers for their suggestions, especially Prof. Derek Ford for improving the text.

REFERENCES

- Almeida F.F.M., 1964 - *Fundamentos geológicos do relevo paulista*. Boletim do Instituto Geográfico e Geológico, **41**: 169-262.
- Almeida F.F.M., 1977 - *O Cráton de São Francisco*. Revista Brasileira de Geociências, **7**: 349-364.
- Almeida F. F. M. & Carneiro C.D.R., 1998 - *Origem e Evolução da Serra do Mar*. Revista Brasileira de Geociências, **28 (2)**: 135-150.
- Alvares C.A., Stape J.L., Sentelhas P.C., Gonçalves J.L.M. & Sparovek G., 2013 - Köppen's climate classification map for Brazil. Meteorologische Zeitschrift, **22 (6)**: 711-728.
<http://dx.doi.org/10.1127/0941-2948/2013/0507>
- Brandi R. 2007 - *Ricardo Krone e Lourenço Granato: Influências na história da espeleologia paulista no final do século XIX e início do século XX*. O Carste, **19 (2)**: 36-60.
- Campanha G.A.C., 1991 - *Tectônica Proterozóica no Alto e Médio Vale do Ribeira, Estados de São Paulo e Paraná*. Ph.D. thesis, Instituto de Geociências, Universidade de São Paulo, 296 p.
- Campanha G.A.C., 2002 - *O papel do sistema de zonas de cisalhamento transcorrente da porção meridional da Faixa Ribeira*. Habil. thesis, Instituto de Geociências, Universidade de São Paulo, 105 p.
- Campanha G.A.C. & Sadowski G.R., 1999 - *Tectonics of Southern portion of the Ribeira Belt (Apiáí Domain)*. Precambrian Research, **98**: 31-51.
[http://dx.doi.org/10.1016/S0301-9268\(99\)00027-3](http://dx.doi.org/10.1016/S0301-9268(99)00027-3)
- Campanha G.A.C., Gimenes Filho A., Caetano S.L.V., Alves Pires F., Lucas Dantas A.S., Teixeira A.L., Dehira L.K., Hachiro J. & Stefani F.L., 1985 - Geologia das folhas Iporanga (SG:22-X-B-V-2) e Gruta do Diabo (SG:22-X-B-VI-I). Estado de São Paulo, IPT/Pró-Minério. (Report n°22.352).

- CECAV, 2012 - Cavernas: Base de Dados Geoespacializados de Cavidades Naturais Subterrâneas do CECAV/ICMBIO, situação em Fevereiro de 2012.
<http://www.icmbio.gov.br/cecav/downloads/mapas.html>
- Coutinho J.M.V., 2008 - Dyke Swarms of the Paraná Triple Junction, Southern Brazil. *Revista Geologia USP, Série Científica*, **8 (2)**: 29-52.
- Despain J.D. & Stock G.M., 2005 - *Geomorphic history of Crystal Cave, Southern Sierra Nevada, California*. *Journal of Cave and Karst Studies*, **67 (2)**: 92-102.
- Ernesto M., Raposo M.I.B., Marques L.S., Renne P.R., Diogo L.A. & Min, A., 1999 - *Paleomagnetism, geochemistry and ⁴⁰Ar/³⁹Ar dating of the Northeastern Paraná magmatic province: tectonic implications*. *Journal of Geodynamics*, **28 (4-5)**: 321-340.
[http://dx.doi.org/10.1016/S0264-3707\(99\)00013-7](http://dx.doi.org/10.1016/S0264-3707(99)00013-7)
- Faleiros F.M., Morais S.M. & Costa V.S., 2012 - Unidades litoestratigráficas. In: Faleiros, F.M. & Costa, V.S. (Orgs.). *Geologia e recursos minerais da folha Apiaí, SG.22-X-B-V, estados de São Paulo e Paraná, Escala 1:100.000*. CPRM, São Paulo, 107 p.
- Faleiros F.M., Morais S.M. & Costa V.S., 2013 - Unidades litoestratigráficas. In: Faleiros, F.M., Costa, V.S. (Orgs.). 2013 - *Geologia e recursos minerais da folha Eldorado, SG.22-X-B-VI, estados de São Paulo e Paraná, Escala 1:100.000*. CPRM, São Paulo, 128 p.
- Figueiredo L.A.V., Zampaulo R.A., Geribello F.K., Pedro E.G., Dell'Antonio R. & Lobo H.A.S., 2007 - *Projeto Caverna do Diabo (PROCAD): Aspectos históricos (1990-2007) e resultados das expedições da terceira fase*. In: *Anais do XXIX Congresso Brasileiro de Espeleologia*, Ouro Preto: 113-119.
- Ford D.C., 2000 - *Speleogenesis under unconfined settings*. In: Klimchouk, A.V., Ford, D.C., Palmer A.N. & Dreybrodt W. (Eds.), *Speleogenesis: Evolution of Karst Aquifers*. Huntsville: National Speleological Society: 319-24.
- Ford D.C. & Ewers R.O., 1978 - *The development of limestone cave systems in the dimensions of length and depth*. *Journal of Speleology*, **10**: 213-244.
<http://dx.doi.org/10.5038/1827-806X.10.3.1>
- Ford D.C. & Williams P.W., 2007 - *Karst Hydrogeology and Geomorphology*. Wiley, Chichester, 561 p.
<http://dx.doi.org/10.1002/9781118684986>
- IGC 1988 - *Cartas Topográficas do Instituto Geográfico e Cartográfico do Estado de São Paulo. Folha Córrego das Ostras (SG-22-X-B-VI-1-SO-B)*.
- Karmann I., 1994 - *Evolução e dinâmica atual do sistema cárstico do Alto Vale do Rio Ribeira de Iguape, sudeste do Estado de São Paulo*. Ph.D. thesis, Instituto de Geociências, Universidade de São Paulo, 228 p.
- Karmann I. & Sanchez L.E., 1986 - *Speleological Provinces in Brazil*. In: *Proceedings of 9th International Speleological Congress*, Barcelona: 151-153.
- Karmann I., Sánchez L.E., & Fairchild T.R., 2001 - *Caverna dos Ecos (Central Brazil): Genesis and geomorphologic context of a cave developed in schist, quartzite, and marble*. *Journal of Cave and Karst Studies*, **63 (1)**: 41-47.
- Krone R., 1898 - *As grutas calcareas de Iporanga*. *Revista do Museu Paulista*, **3**: 477-500.
- Krone R., 1904 - *Grutas calcareas do Valle da Ribeira*. *Revista do Centro de Ciências, Letras e Artes de Campinas*, **2**: 90-95.
- Krone R., 1909 - *Estudo sobre as cavernas do Valle do Ribeira*. *Arquivos do Museu Nacional*, **15**: 139-166.
- Krüger M.V., 1967 - *A gruta da Tapagem: II parte*. *Revista da Escola de Minas, Ouro Preto*, **25 (4)**: 173-177.
- Langmuir D., 1971. *The Geochemistry of some Carbonate Groundwaters in Central Pennsylvania*. *Geochimica Cosmochimica Acta*, **35 (10)**: 1023-1045.
[http://dx.doi.org/10.1016/0016-7037\(71\)90019-6](http://dx.doi.org/10.1016/0016-7037(71)90019-6)
- Lauritzen S.E., 2001 - *Marble stripe karst of the scandinavian caledonides: an end-member in the contact karst spectrum*. *Acta Carsologica*, **30 (2)**: 47-79.
- Le Bret M., 1966 - *Estudos Espeleológicos no Vale do Alto da Ribeira*. *Boletim Instituto Geográfico e Geológico*, **47**: 71-123.
- Le Bret M., 1976 - *Merveilleux Brésil Souterrain*. Les Editions d'Octogone, Vestric, 235 p.
- Leighton M.W. & Pendexter C., 1962 - *Carbonate rock types, in Ham, W.E., ed., Classification of carbonate rocks: Tulsa, USA*, American Association of Petroleum Geologists, **1**:33-61.
- Lobo H.A.S., Trajano E., Marinho M.A., Bichuette M.E., Scaleante J.A.B., Scaleante O.A.F., Rocha B.N. & Laterza F.V., 2013 - *Projection of tourist scenarios onto fragility maps: Framework for determination of provisional tourist carrying capacity in a Brazilian show cave*. *Tourism Management*, **35**: 234-243.
<http://dx.doi.org/10.1016/j.tourman.2012.07.008>
- Martinet B. & Sougy J., 1961 - *Utilisation pratique des classifications chimiques des roches carbonatées*. *Annales de la faculté des sciences de l'Université de Dakar*, **6**: 81-92.
- Matos F.A., 1966 - *A Gruta da Tapagem ("Caverna do Diabo")*. *Revista da Escola de Minas*, **24 (3)**: 147-154.
- Monroe W. H. (Compiler), 1970 - *A Glossary of Karst Terminology*. Geological Survey Water-Supply Paper 1899-K. U.S. Geological Survey. U.S. Government Printing Office, Washington, D.C., 26 p.
- Palmer A.N., 1975 - *The origin of maze caves*. *Bulletin of the National Speleological Society*, **37 (3)**: 56-76.
- Palmer A.N., 1987 - *Cave levels and their interpretation*. *National Speleological Society Bulletin* **49 (2)**: 50-66.
- Palmer A.N., 1991 - *Origem and morphology of limestone caves*. *Geological society of American Bulletin*, **103**: 1-21.
[http://dx.doi.org/10.1130/0016-7606\(1991\)103<0001:OAMOLC>2.3.CO;2](http://dx.doi.org/10.1130/0016-7606(1991)103<0001:OAMOLC>2.3.CO;2)
- Palmer A.N., 2001 - *Dynamics of cave development by allogenic water*. *Acta Carsologica*, **30 (2)**: 14-32.
- Palmer A.N., 2007 - *Cave Geology*. Cave Books, Dayton, 454 p.
- Powel L.R., 1970 - *Base level, lithologic and climatic controls of karst groundwater zones in South-central Indiana*. *Proceedings of Indiana Academy of Science*, **79**: 281-291.
- Rauch H.W., White W.B., 1977 - *Dissolution kinetics of carbonate rocks. 1. Effects of lithology on dissolution rate*. *Water Resources Research*, **13 (2)**: 381-394.
<http://dx.doi.org/10.1029/WR013i002p00381>
- Renne P.R., Deckart K., Ernesto M., Feàraud G. & Piccirillo E.M., 1996 - *Age of the Ponta Grossa dike swarm (Brazil), and implications to Parana flood volcanism*. *Earth and Planetary Science Letters*, **144 (1-2)**: 199-211.
[http://dx.doi.org/10.1016/0012-821X\(96\)00155-0](http://dx.doi.org/10.1016/0012-821X(96)00155-0)
- Riccomini C., 1995 - *Tectonismo gerador e deformador dos episódios sedimentares pós-gondvânicos da porção centro-oriental do Estado de São Paulo e áreas vizinhas*. *Habil. thesis, Instituto de Geociências, Universidade de São Paulo*, 100 p.
- Riccomini C., Sant'anna L.G. & Ferrari A.L., 2004 - *Evolução geológica do rift continental do sudeste do Brasil*. In: Mantesso-Neto V., Bartorelli A., Carneiro C. D. R. & Brito-Neves B. B. (Eds.), *Geologia do Continente Sul-Americano: Evolução da Obra de Fernando Flávio de Almeida*. São Paulo: Beca: 383-405.
- Sallun Filho W., Almeida L.H.S., Boggiani P.C. & Karmann I., 2012 - *Characterization of quaternary tufas in the Serra do André Lopes karst, southeastern Brazil*. *Carbonates and Evaporites*, **27**: 357-373.
<http://dx.doi.org/10.1007/s13146-012-0118-1>

- SBE - Sociedade Brasileira de Espeleologia, 2008 - Mapa da caverna do Diabo. Campinas: SBE.
- White E.L., 2005 - *Breakdown*. In: Culver D. C & White W.B, *Encyclopedia of Caves*. Burlington: Elsevier: 56-60.
- White E.L. & White W.B., 2000 - *Breakdown Morphology*. In: Klimchouk A.V., Ford D.C., Palmer A.N. & Dreybrodt W. (Eds.), *Speleogenesis: Evolution of Karst Aquifers*. Huntsville: National Speleological Society: 427-429.
- Williams P.W., 1982 - *Karst landforms in New Zealand*. In: Soons J. & Selby M.J. (Eds.), *Landforms of New Zealand*. Auckland: Longman Paul: 105-125.
- Worthington S.R.H., 2005 - *Evolution of caves in response to base-level lowering*. *Cave and Karst Science*, **32 (1)**: 3-12.
- Zalán P.V. & Oliveira J. A. B., 2005 - *Origem e evolução estrutural do Sistema de Riftes Cenozóicos do Sudeste do Brasil*. *Boletim de Geociências Petrobrás*, **13 (2)**: 269-300.
- Zilio C., 2003 - *Nas pegadas de Krone (1861-1918) - 1ª Parte*. Informativo SBE, n° 87: 25-26.



Available online at scholarcommons.usf.edu/ijis

International Journal of Speleology

Official Journal of Union Internationale de Spéléologie



Radiaxial-fibrous and fascicular-optic Mg-calcitic cave cements: a characterization using electron backscattered diffraction (EBSD)

Detlev K. Richter¹, Adrian Immenhauser¹, Rolf D. Neuser^{1*}, and Augusto Mangini²

¹Institut für Geologie, Mineralogie und Geophysik, Ruhr-Universität-Bochum, D-44801 Bochum

²Forschungsstelle Radiometrie, Heidelberger Akademie der Wissenschaften Im Neuenheimer Feld 229, 69120 Heidelberg

Abstract: Electron backscattered diffraction (EBSD) applied to crystal fabric research in speleothems aids in our understanding of the origin of those fabrics. A significant advantage of this approach is the three dimensional data set of crystal c-axes. Here, we show a rare case of both convergent (radiaxial-fibrous) and divergent (fascicular-optic) orientations of the c-axes in pool calcites. The seemingly defective structure of the calcite lattice resulting in radiaxial-fibrous crystal orientations is probably caused by differential incorporation of Mg during crystal growth. The observation that radiaxial-fibrous and fascicular-optic fabrics co-exist in the same pool environment is remarkable and documents the complexity of the system.

Keywords: Mg-calcite; cave cements; radiaxial-fibrous; fascicular-optic; EBSD

Received 14 August 2014; Revised 27 October 2014; Accepted 3 November 2014

Citation: Richter D.K., Immenhauser A., Neuser R.D. and Mangini A., 2015. Radiaxial-fibrous and fascicular-optic Mg-calcitic cave cements: a characterization using electron backscattered diffraction (EBSD). *International Journal of Speleology*, 44 (1), 91-98. Tampa, FL (USA) ISSN 0392-6672 <http://dx.doi.org/10.5038/1827-806X.44.1.8>

INTRODUCTION

Most calcitic speleothems are characterized by a crystal structure of isometric (equicrystalline) grains or oblong crystals (columnar to fibrous) with different length in the growth direction (Frisia et al., 2000; Railsback, 2000; Self & Hill, 2003; Frisia & Borsato, 2010). According to Folk & Assereto (1976) two subtypes of calcites with oblong crystals are distinguished: Such with (i) the c-axis oriented along the longitudinal extent of the calcite (length-fast) and such with (ii) the c-axis approximately perpendicular to the longitudinal extension of the calcite (length-slow; a rare subtype). For more detail, the reader is referred to Onac (1997) for a comprehensive review on the crystal types and morphologies of carbonate and sulfate minerals.

Given that some of the calcite crystals building speleothems display a radial fibrous texture (type 2.1.1 or 2.1.2 in Self & Hill, 2003) and show strong undulatory extinction, a quantitative understanding of the spatial c-axis orientation in the crystals can be of particular importance. For an accurate characterization of the oblong calcites with different undulatory extinction the reader is referred to Kendall (1985) who established a classification for marine cements (Fig. 1). Accordingly, three cement types require attention in this context: (i) such with divergent

c-axes in growth direction ("fascicular-optic"), (ii) such with converging c axes in growth direction ("radiaxial-fibrous") and (iii) such with uniform c-axes ("radial-fibrous"). Following this classification, Neuser & Richter (2007) have presented oblong calcite crystals with converging and diverging c-axes in growth directions within stalagmites from caves located in dolostone host rock lithologies. Data obtained at these sites clearly documented that the Mg content of the drip waters is significant (Richter et al., 2011).

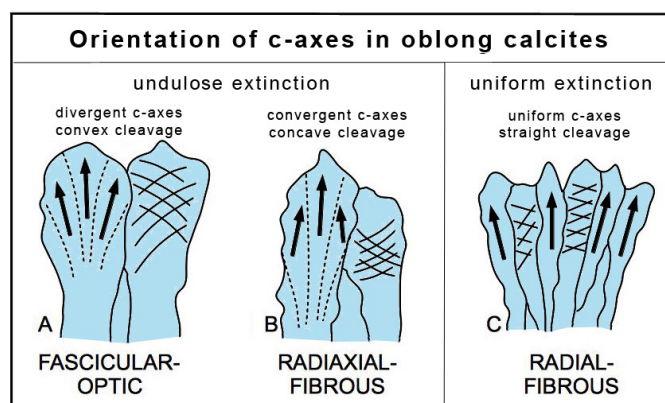


Fig. 1. Types of oblong calcite crystals according to internal orientation of the c-axis (modified after Kendall, 1985). Arrows: c-axis orientation; solid lines: cleavage cracks; dashed lines: subcrystal boundaries.

In this study, two cave cements with different c-axis orientations in calcites from subaqueous environments (pools) of Zoolithen Cave (Germany) are presented and discussed in the context of their environment and crystallography.

CAVE SETTING AND SAMPLE LOCATIONS

The calcite samples were taken from rimstone pools of Zoolithen Cave, Germany, a cave being mainly known for its fossil vertebrate remnants (Heller, 1972). We only collected 6 samples due to the protection status of the cave. The cave is located in the Upper Jurassic Franconian dolomite (Frankendolomit) at Burggailenreuth (E' Forchheim; Fig. 2A) above the Wiesent Valley, and exhibits a labyrinth shape with many liviations (most recent cave survey: Dreyer, 2000).

The entrance level of the Zoolithen Cave (Kataster-Nr. D 109) is located 455 m above sea level (the Wiesent Valley is 310 m above sea level). The mean temperature in the cave was previously documented in Tietz (1988) as 7.5°C for the 1977/78 period, and by the Bochum Geology Group as 8-9°C since 2010. The two sampled rimstone pools (Fig. 2B) are found in the central part of the cave.

Location 1 (Zaunikhalle):

In Zaunikhalle Room the largest rimstone pool extends NNE - SSW (5.3 m below the entrance level, length = 10.3 m, maximum width = 3.2 m, maximum depth = 0.88 m; Fig. 3A). The black color of the rimstone is likely due to soot from torch activities carried out during the paleontological excavations by Esper from 1770 to 1790 (see Heller, 1972). Furthermore, recent construction (wood-piles for visitor paths) has affected the natural conditions of the Zaunikhalle at least temporarily.

Location 2 (Windspalte):

In Windspalte Room, 19 m below the cave entrance next to the visitor's path, between Zaunikhalle and Löwengrube, a second rimstone pool (now dry) was sampled (10 m below the entrance level, length = 1.7 m, width = 1.4 m, maximum depth of the now empty basin = 0.35 m; Fig. 3B). This locality 2 corresponds to the extraction point of stalagmite ZOO2 studied at high-resolution by Wurth (2002).

ANALYTICAL WORK CONVENTIONAL METHODS

For documentation, the outer contours of the filigreed cements have been cleaned in an ultrasonic bath and afterwards been sputtered with gold to prevent charging in a high-resolution field emission scanning electron microscope (HR-FESEM) type LEO/ZEISS 1530 Gemini.

Polished thin sections were prepared to obtain first information concerning the internal structures of the cement crystals using a polarizing microscope.

The mineral compositions of the carbonate phases were obtained by X-ray diffraction (XRD) using a pananalytical MPD diffractometer equipped with a copper tube, 0.5° divergent and diffracted beam, 0.04 rad soller slits, and a secondary graphite monochromator as documented by Mioa et al. (2009). Methodically ground samples with quartz powder as internal standard have been measured by a diffraction angle range of 26-38° (2 θ), identifying each $d_{(104)}$ value of the rhombohedral carbonates in terms of their Ca/Mg distribution (Füchtbauer & Richter, 1988).

Carbon and oxygen isotopic compositions of the carbonates were determined with a delta S mass spectrometer (Finnigan MAT) and calibrated against V-PDB (standards: CO-1 and CO-8). The

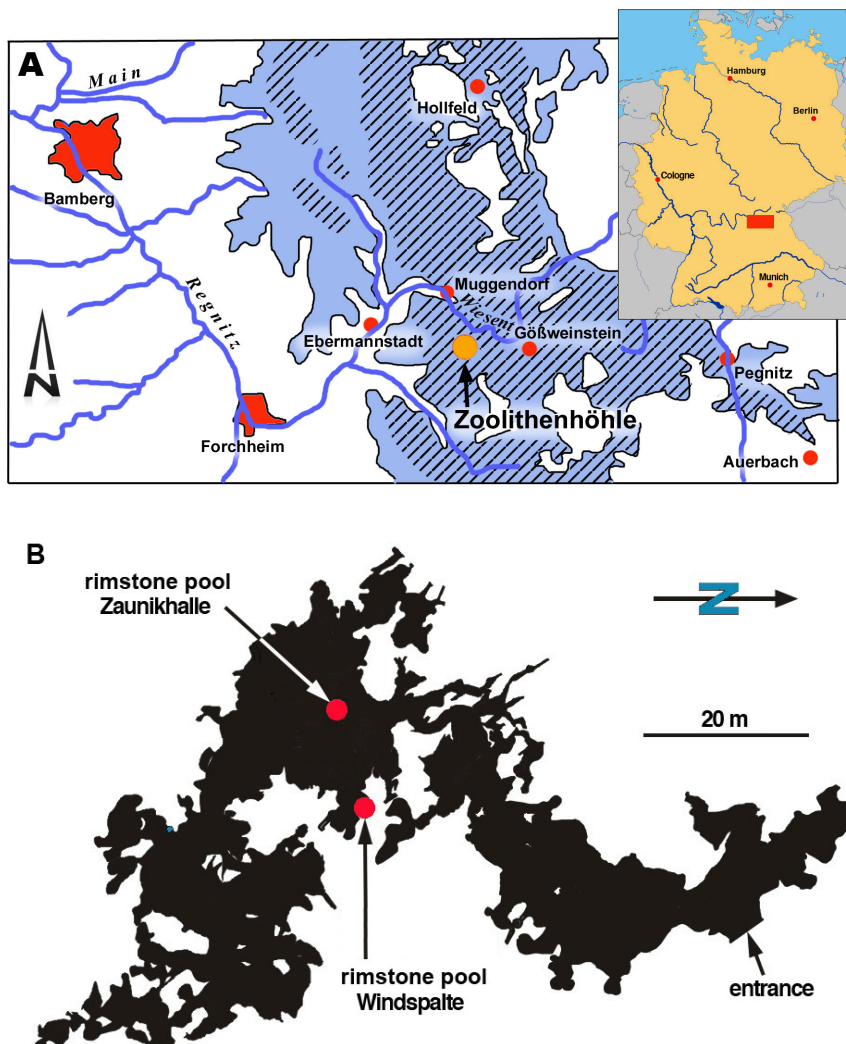


Fig. 2. Overview. A: Location of Zoolithen Cave in the Franconian dolomite (hatched area) of the Franconian Alb. B: Map of Zoolithen Cave (simplified after Dreyer, 2000) with markers for the location of the investigated rimstone pools (1: Zaunikhalle, 2: Windspalte).

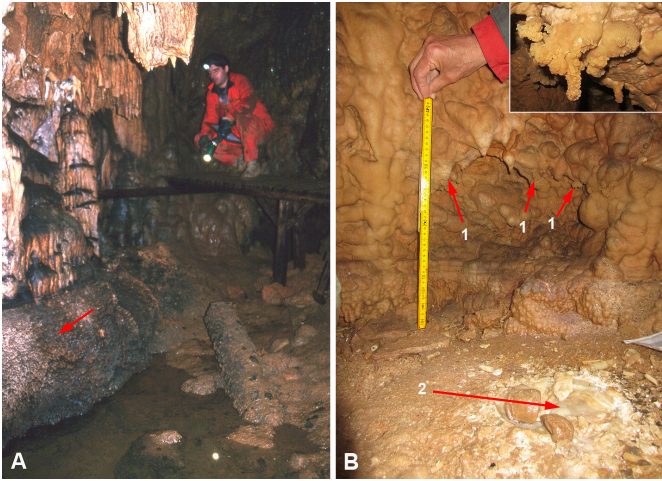


Fig. 3. Sampled rimstone pools: A: Zaunikhalle (arrow: sampled rimstone crust); B: Windspalte (arrows (1) point to mural calcite crusts of the paleobasin, detailed picture see upper right corner; arrow (2) points to sampling site of stalagmite ZOO2). Images Zaunikhalle courtesy of R. Dreyer, Windspalte courtesy of M. Harder.

1 σ -reproducibility of the measurements is 0.04‰ V-PDB for $\delta^{13}\text{C}$ and 0.08‰ V-PDB for $\delta^{18}\text{O}$, respectively.

Cation and anion concentration were measured at the University of Heidelberg at the Institute for Ecologic Geochemistry by A. Schröder-Ritzrau. For the analysis of the cations each sample was acidified with 100 μl of nitric acid. The subsequent analysis was performed using an ICP-OES Vista MPX by Varian. NIST 1643e was used as a standard providing a reproducibility between 2 and 3% for Na^+ , K^+ , Ca^{2+} , Mg^{2+} , and Sr^{2+} . An ion chromatograph type DX120 by Dionex company was employed for the anion measurements.

Age dating was performed using the Th/U-method at the Heidelberg Academy of Sciences. For each sample between 1 and 2 g were prepared at the clean laboratory and their ^{238}U , ^{234}U , ^{232}Th , and ^{230}Th contents were determined using Finnigan Thermal Ionization Mass Spectrometry (TIMS) MAT 262 RPQ (for details see Frank et al., 2000).

ELECTRON BACKSCATTERED DIFFRACTION

The SEM-based EBSD - methodology was applied using the computer program "Channel5" (Day & Trimby, 2004) in combination with the acquisition software "AZtec" by OXFORD Instruments. First, the surfaces of polished thin sections were chemo-mechanically etched for about 15 min with colloidal silica (OPS) to remove surface defects at an atomic scale (Massonne & Neuser, 2005). After coating with of a thin carbon layer the samples were examined using a SEM LEO/Zeiss Gemini 1530 with an EBSD detector (Nordlys, OXFORD Instruments). The SEM was operated at an 20 keV accelerating voltage, a 60 micron aperture, a working distance of 25 mm and a tilt angle of 70°. EBSD allows a determination of the crystallographic orientation of down to about 500 nm sized crystals, thus information on the 3D structure of the sample in a micro- or nanometer range is provided (for details see Day & Trimby, 2004). To eliminate analytical artifacts and to limit measurement errors, the crystals of the thin sections were scanned in a 1x1 μm dot matrix. Thus

the smallest calcite crystals could be measured at a resolution of at least 100 points.

The scanned crystals were color-coded to better visualize their orientations, where the colors indicate angular deviation within crystal bundles. In addition, the crystal axes were plotted in a Schmidt net (lower hemisphere).

SAMPLE MATERIAL

The sample material was taken from localities with similar cave waters. The Mg/Ca weight ratio of the recent water is nearly identical (0.88 versus 0.83), but the saturation index of the dripwater in the rimstone pool of Windspalte is significantly higher than that of Zaunikhalle (0.87 versus 0.54).

The studied rimstone pools are characterized by up to 5 cm (Loc. 2) and 50 cm (Loc. 1) thick calcitic cement crusts with a highly porous filigreed structure and small (<1 mm to 2 cm), leaf-like individual elements of calcite crystal bundles. Macroscopically, the thickest crusts of Zaunikhalle (Loc. 1) resemble subaquatic coralloids described and illustrated by Hill & Forti (1997).

The sampled pool cements of Zaunikhalle reflect a Holocene to subrecent age because in thin section only a thin layer of clear calcite crystals is observed on the black crusts. U/Th dating of the crust yielded a corrected age of 5.7 ± 4.0 ka. The imprecision was due to high proportion of ^{232}Th (1.36 ng/g) and low amounts of ^{238}U (0.03051 $\mu\text{g/g}$). The high Th concentrations are probably due to the presence of clay-sized insoluble components.

The calcitic cement crusts taken from the chamber wall of Windspalte correspond to a speleothem crust level of equal crystal formation in ZOO2 (Fig. 4), which according to U-Th datings (Fig. 4) were younger than

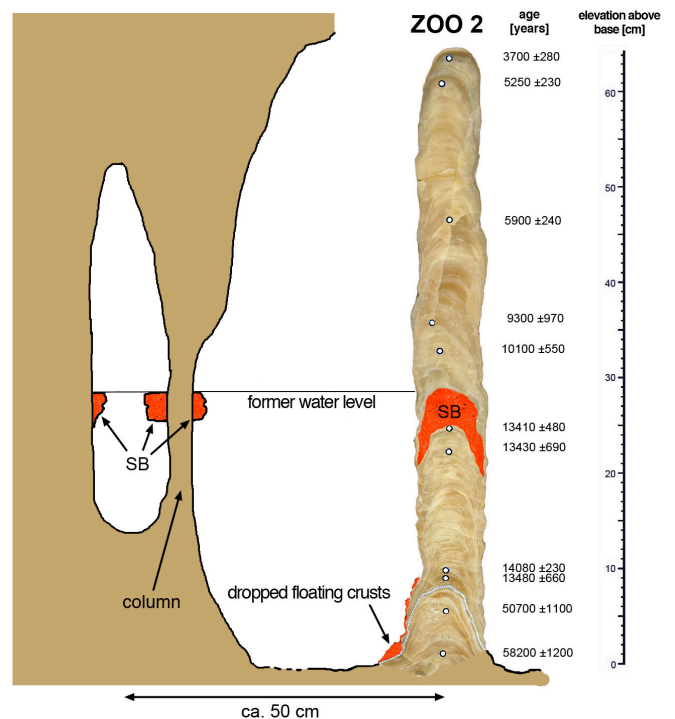


Fig. 4. Reconstruction of position of the rimstone crust areas of the fossil cave pools in relation to the palaeo-water level of Windspalte. Right image stalagmite ZOO2 with U/Th age data, left image chamber wall with a small column, SB: calcitic cement crusts of pool.

13 ka and older than 10 ka and probably correspond to the period of Younger Dryas (12.6 - 11.6 ka BP). Under a similar calcite layer at the bottom of the dry rimstone pool a <3 cm thin debris deposit is present (crusts, calcitic crystal bundles of the same type as in the rimstone pool of Zaunikhalle, fragments of flow stone, bones, and siliciclastic detritus all of which had fallen to the floor and were not collected in situ).

According to XRD-analyses the crystal crusts are composed of $Mg_{4.8-5.7}$ -calcite (Loc. 1) and $Mg_{4.7-5.3}$ -calcite (Loc. 2), respectively. These values are typical of calcite in dolomite caves (4-7 mol% $MgCO_3$ after Tietz, 1988, 1.5-6 mol% $MgCO_3$ by Neuser & Richter, 2007). Only from strongly ventilated caves (abri) in dolostone host rocks, calcitic coralloids with up to 23 mol% $MgCO_3$ have been reported (Niggemann et al., 1997).

The carbon and oxygen isotope composition of the calcitic cements of the rimstone pool of Zaunikhalle (Loc. 1) correspond to the data of the Pleistocene and Holocene stalagmites of Zoolithen Cave, while the calcites of the rimstone pool of Windspalte (Loc. 2) have relatively heavy $\delta^{13}C$ values (Fig. 5). This could be indicative of a reduced microbial soil activity during the Younger Dryas in the Franconian Alb.

Two-dimensional microscopic observations under crossed polars of calcitic cement fans from both rimstone pools reveal an overall systematic extinction with a divergent orientation of the c-axes (Fig. 6A and B). But at a higher magnification, a finer, fibrous structure becomes visible where individual fibers are less than 100 μm in width.

Judging from scanning electron microscope (SEM) analyses, the calcitic cement bundles of Loc. 1 are composed of ellipsoidal shaped crystal aggregates

(Fig. 7A) with very steep rhombohedral faces at the tip of the fibers (Fig. 7B). The corresponding crystal aggregates of Loc. 2 show a botryoidal shape (Fig. 7C), and the fibers have less steep rhombohedral faces at their tips (Fig. 7D).

The fibers from both locations exhibit undulatory extinction, a feature that is particularly pronounced in the larger fibers of rimstone pool 2. In order to quantify the systematic change in lattice orientation of the calcite fibers, electron backscatter diffraction (EBSD) was applied.

DATA PRESENTATION OF ELECTRON BACKSCATTERED DIFFRACTION

The section perpendicular to the ellipsoidal (Loc. 1) or botryoidal (Loc. 2) shape of the bundles reveals a concentric color coding, where the red color indicates the strongest deviation from the central phase (blue) of the bundle (Fig. 8A/B and D/E). The result is a circular bundle-shaped orientation of the fibers. In sections parallel to the length of the bundle (Fig. 8C/F), the EBSD analysis reveals a divergent c-axis orientation in single fibers of Zaunikhalle calcites (Loc. 1), while the individual fibers of Windspalte calcites (Loc. 2) are characterized by a converging c-axis orientation.

The measured maximum angle of convergence of a fiber is 15° while the angle of divergence of a fiber achieves a maximum of 7° . As documented in Fig. 8B and D, the internal bundle-like c-axis orientation is three-dimensional as exemplified for individual fibers.

INTERPRETATION AND DISCUSSION

The filigreed structured calcite crusts of both rimstone pools are made up of a multitude of fiber bundles, which in turn are made of sub-individual calcite fibers. In the classification scheme of Maltsev (1996, cited in Onac, 1997), this structure corresponds to the "second-order individuals." This is accomplished by splitting the end of the calcites at the end of growth (especially in the bundles of the speleothems of Loc. 1).

Considering extensive literature the descriptions and classifications by Onac (1997) primarily refer to the calcite shape and the formation of the crystal surfaces. But as the crystals of the rimstone pools of Zoolithen Cave revealed an undulatory extinction, the EBSD method was applied for accurate quantification of the crystal lattice orientation. Obviously, the different patterns - divergent c-axis in the calcite fibers of Zaunikhalle pool, versus converging c-axis in the calcite fibers of Windspalte pool - requires attention.

Following Füchtbauer & Richter (1975), an undulatory extinction in carbonate crystals is primarily due to their spatially heterogeneous chemical composition (Mg in calcite, excess Fe and Ca in dolomite) and due to the frequency distribution and type of solid and fluid inclusions (especially non-carbonatic doping) or secondarily to epitactic displacement of recent mineral phases with undulatory extinction. Given that the calcites from the rimstone pools of Zoolithen Cave are virtually free of inclusions and evidence of epitactic

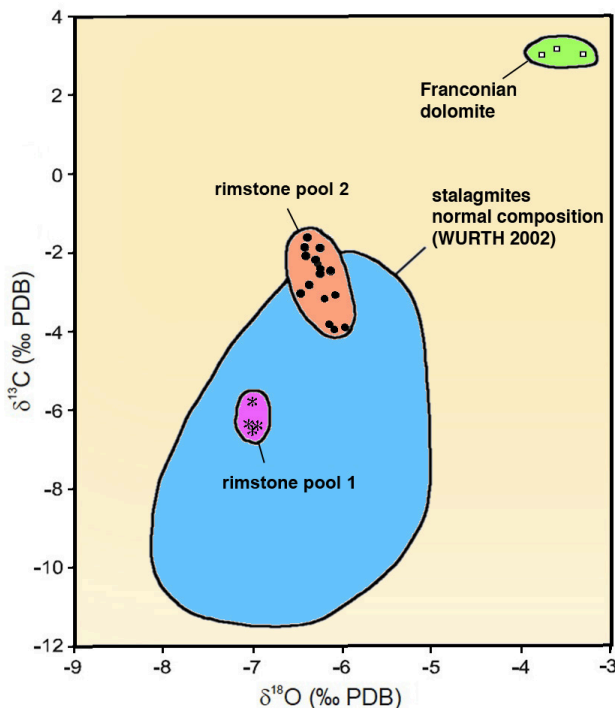


Fig. 5. Carbon and oxygen isotopic composition of calcite cements from Zaunikhalle (rimstone pool 1, *) and Windspalte (rimstone pool 2, ●) compared to the fields of columnar calcite layers of stalagmites from Zoolithen Cave after Wurth (2002, shaded blue) and the dolostone host rock (shaded green, □).

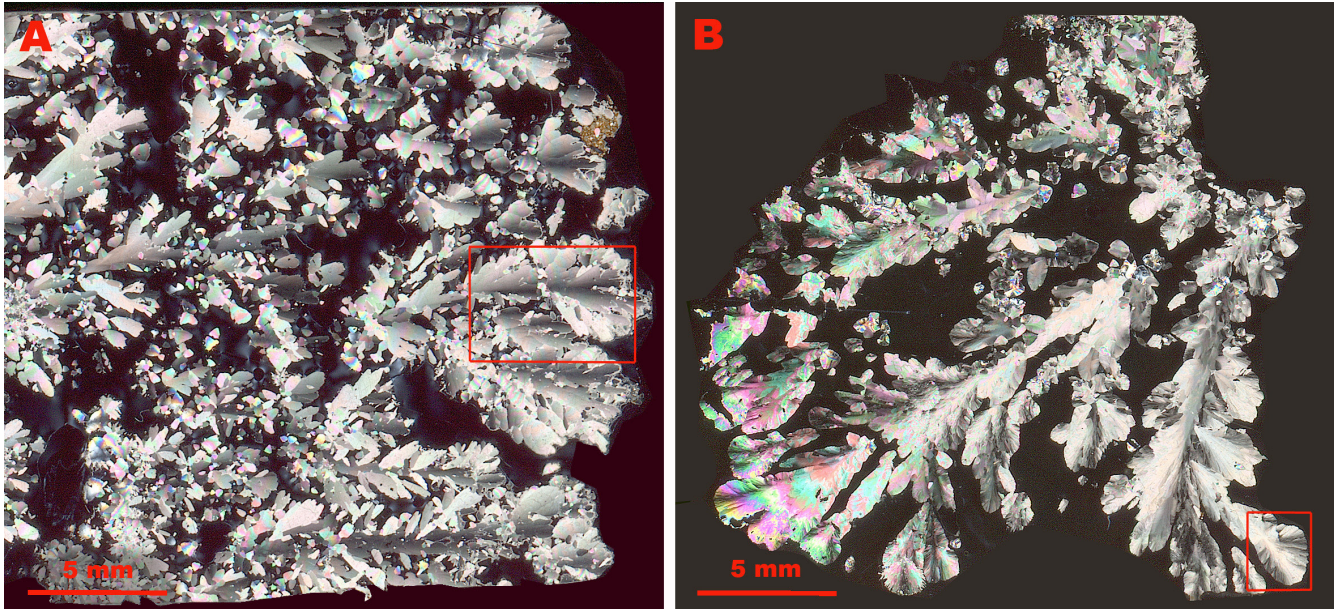


Fig. 6. Thin section images under crossed polarizers: A: calcitic cement Zaunikhalle, B: calcitic cement Windspalte.

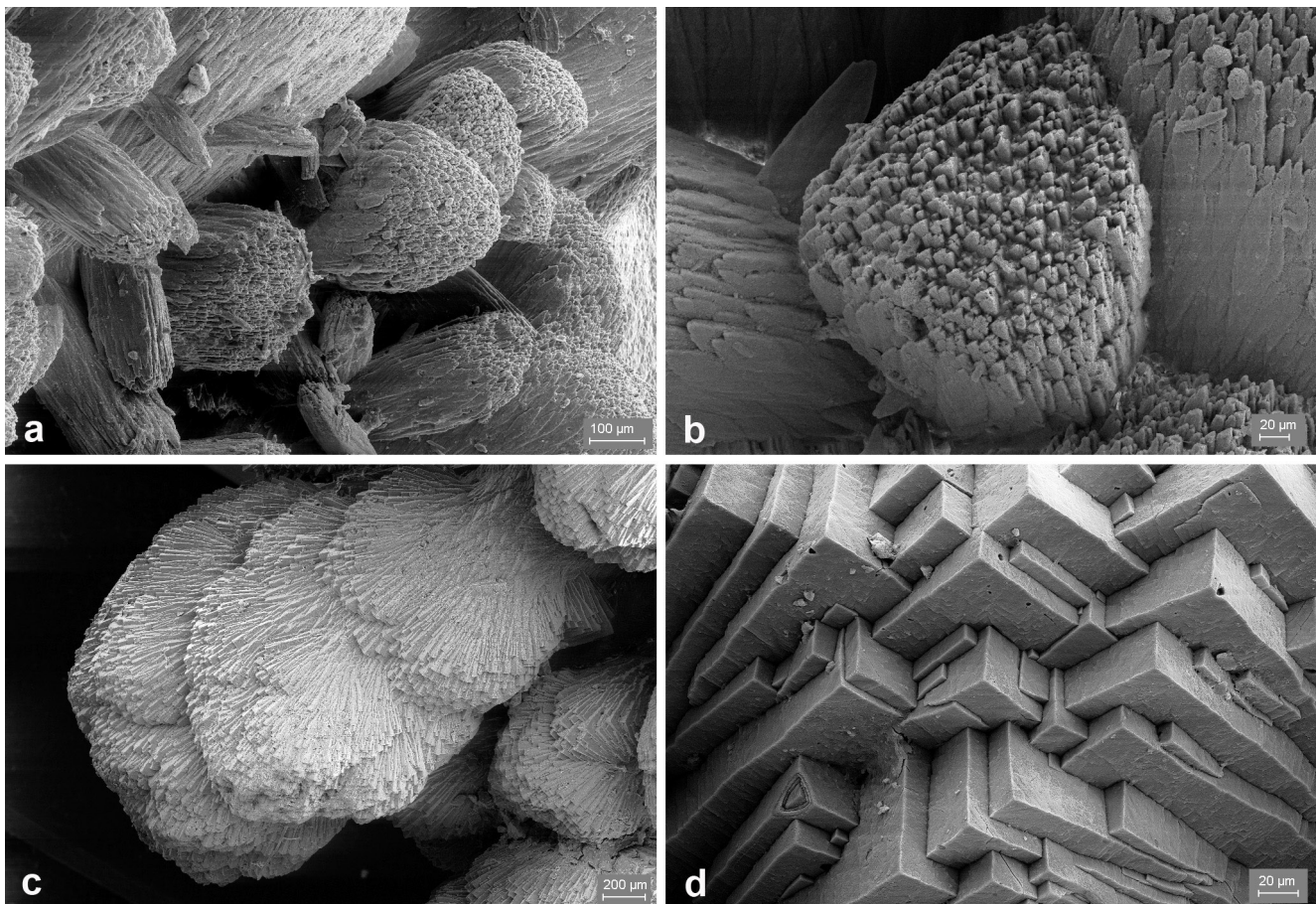


Fig. 7. Scanning electron micrographs of calcite bundles from Zaunikhalle (A: overview, B: detail of crystal tip) and from Windspalte (C: overview; D: detail of crystal tip).

recrystallization of a precursor mineral is missing, the third option, i.e. the spatially heterogeneous chemical composition offers itself as the most likely reason for the formation of undulatory extinction in calcite. This notion is consistent with the variable 4–6 mol% MgCO_3 in the calcite of the rimstone pools. The divergent c-axis orientation in the calcite fibers of Zaunikhalle, however, is in contrast to the converging c-axis orientation in the calcite fibers of Windspalte. This contrasting pattern cannot be explained by Mg incorporation as both

calcite fabrics have identical Mg contents. According to previous EBSD work by Richter & Riechelmann (2008), stoichiometrically composed calcite fibers of cryogenical precipitates of the Malachitdom near Brilon equally reveal divergent c-axis orientation. Given these contrasting observations, other potential mechanisms require attention.

An alternative mechanism leading to diverging and converging crystal c-axes in the same precipitation environment might include the molarity of the pool

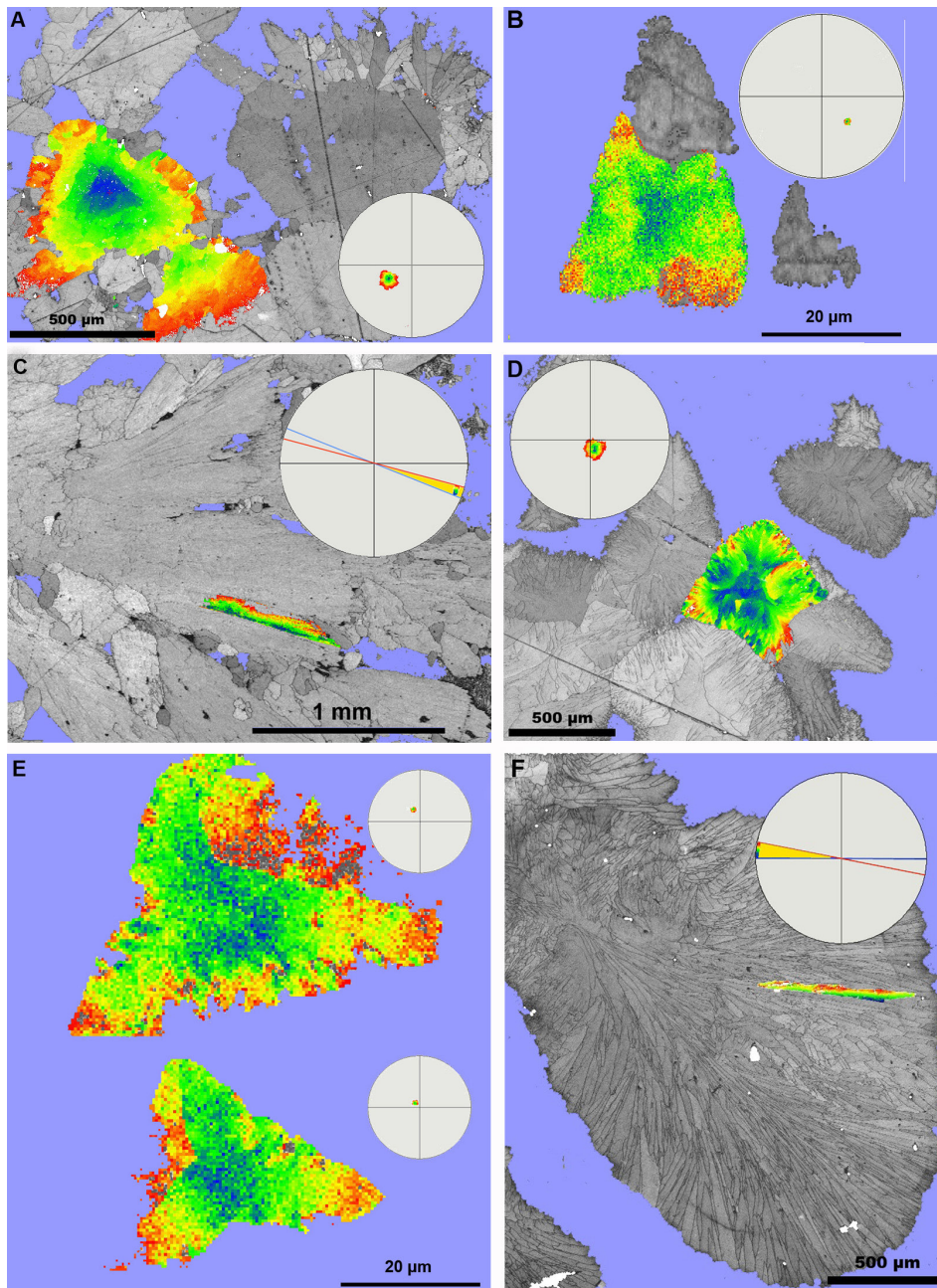


Fig. 8. Electron backscattered diffraction image with color code in sections perpendicular and parallel to the long orientation of the fiber bundle. Within the parallel sections (C + F) same colors represent identical fiber directions. Within perpendicular sections (A, B, D + E) same colors represent same angular deviations from the central axis. Angular deviation from blue to red is up to 10°. A, B + C calcites of Zaunikhalle: A: perpendicular section of fiber bundle; B: perpendicular section of single fiber; C: parallel section of single fiber. D, E + F calcites of Windspalte: D: perpendicular section of fiber bundle; E: perpendicular section across two single fibers; F: parallel section across single fibers.

waters. Evidence for this is based on ongoing cave monitoring. First data sets suggest, that the saturation index of the drip water in the rimstone pool of Windspalte is significantly higher than that of Zaunikhalle (0.87 versus 0.54 - SI calcite), a fact, that is likely to affect the growth rate. This may also explain the moderately higher carbon and oxygen isotope values of Windspalte calcites compared to Zaunikhalle calcites (see Fig. 5). Given & Wilkinson (1985) suggest a stronger saturation and/or increased fluid flow to explain oblong calcite crystals, yet this is still no explanation of divergent versus convergent c-axis orientation as observed here.

A first possible line of circumstantial evidence for the mechanisms causing undulatory extinction of carbonate crystal textures comes from plain-light microscopy.

After determination of the general c-axis orientation in a calcite fiber using a compensator tube slot, or taking into account the orientation of the curved cleavage cracks, the observed extinction under crossed polarizers shifts to the opposite direction at converging c-axes (see Richter et al., 2011) during rotation of the fiber in the clockwise direction. The limitation of this approach is that data obtained data represent two-dimensional observations only. This is where the here applied EBSD method provides three-dimensional information.

In sections perpendicular to the long fiber orientation, the color coding indicates a circular pattern in three-dimensional convergence and divergence and a more linear pattern in two-dimensional convergence and divergence. Regarding the precipitates in the rimstone pool of Zoolithen Cave, EBSD analyses of the sample from Zaunikhalle displayed a three-dimensional divergence, while the Windspalte sample exhibited a three-dimensional convergence. A filigreed structure of the calcitic cements of the rimstone pools, such as those presented here, is rather common in caves (e.g., Meyer & Dorsten, 2009; their Fig. 8; “coral-like calcite crystals growth in the large rimstone pools of the “Kindergarten” of the Riesenberg Cave”), offering the availability of a large sample base from different caves for further analysis.

The filigreed structure of the speleothems (Fig. 6) is similar to the dendritic structure of flowstones and stalagmites (Frisia et al., 2000; Railsback, 2000). According to Frisia & Borsato (2010) this is indicative of dry and instable conditions during dripstone growth. The structure of speleothems from pools of Zoolithen Cave is quite dendritic, but the crystals do not show skeletal shape in a crystallographic sense. The afore mentioned authors did not respond to a potential undulosity of the crystals in the dendritic fabric.

At present, speleogroups from Bochum and Mainz (Germany) are working together on stalagmites and pool calcites of Zoolithen Cave in combination with laboratory experiments to find more clues to convergent/divergent crystal growth. Preliminary results concerning mineralization in water films suggest a predominance of stalagmite layers with convergent crystal structure within several stalagmites of caves with dolomitic host rocks (Niggemann &

Richter, 2006, Wassenburg et al., 2012). Currently performed laboratory experiments using solutions of different Mg/Ca ratio suggest a relationship of crystal nucleation to the respective crystal faces of calcite (Schreuer, oral comm.). This corresponds to crystal formation in cave pools.

Summing up, the here presented data document the full petrographic complexity of cave carbonate fabrics. The validity of state-of-art technological approaches in the characterization of the complex three-dimensional texture of these precipitates is shown. A further understanding on the controlling reasons requires a combination of field and laboratory experiments including the strict control (laboratory) and monitoring (cave) of physico-chemical and environmental parameters.

SUMMARY

Non-ideal calcite crystals from rimstone pools in dolostone caves have been studied for their three-dimensional c-axis orientation using the electron backscatter diffraction method (ESBD). The two studied locations (cave pools, Zaunikhalle, Windspalte) from the central part of Zoolithen Cave in Germany yield filigreed speleothem structures (crusts) with different internal calcite lattice structure.

From a three-dimensional viewpoint, both of these calcitic cement crusts are composed of a texturally complex array of bundles of calcite fibers. Remarkably, the fibers of the Zaunikhalle location show a 3D diverging c-axis orientation whilst those of the Windspalte sampling location display a 3D converging c-axis orientation.

The underlying mechanism of this abnormal c-axis behavior of the fibrous calcites of pure calcite composition (similar to Iceland spar) is considered. The free Mg aquo ions are derived from the Franconian dolomite and transported in the cave setting by aquifer waters into the sinter basin where they are incorporated into calcite at 4-6 mol% MgCO₃.

The mechanistic reasons for different orientation of the c-axes in the calcite samples investigated (diverging or converging c-axes in growth direction) are at present not understood. Possible reasons might include variable degrees of Mg saturation of mother fluids promoting convergence of the calcite lattice structure. Experimental work and field monitoring campaigns are instrumental have a significant potential for the improved understanding of these enigmatic fabrics.

ACKNOWLEDGEMENTS

Sampling and testing were made possible through the courtesy of E. Ziegler (tenant of the Zoolithen Cave). For technical assistance we thank M. Conrad and M. Harder (Cave Research Group "Höhle und Karst Franken e.V."), A. Schröder-Ritzrau (University Heidelberg) and M. Born, S. Schremmer, T. Meyer and A. Niedermayr (Ruhr University Bochum). N. Look kindly improved the English. The critical reviews of A. Hood, B.P. Onac, V. Polyak, and an anonymous reviewer are greatly appreciated.

REFERENCES

- Day A. & Trimby P., 2004 - *Channel 5*, HKL-Technology, Hobro, Denmark.
- Dreyer R., 2000 - *Die Zoolithenhöhle bei Burggailenreuth (Fränkische Alb-Revisionskartierung und Ereignisabfolge)*. Bochumer geologische und geotechnische Arbeiten, **55**: 153-167.
- Folk R.L. & Assereto R., 1976 - *Comparative fabrics of length-slow and length-fast calcite and calcitized aragonite in a holocene speleothem, Carlsbad Caverns, New Mexico*. Journal of Sedimentary Petrology, **46** (3): 476-496.
- Frank N., Braum M., Hambach U., Mangini A. & Wagner G., 2000 - *Warm period growth of travertine during the last interglacial in Southern Germany*. Quaternary Research, **54**: 38-48. <http://dx.doi.org/10.1006/qres.2000.2135>
- Frisia S. & Borsato A., 2010 - *Karst*. In: Alonso-Zarza A.M. & Tanner L.H. (Eds.), *Carbonates in continental settings: Facies, environments and processes*. Developments in Sedimentology. Elsevier, Amsterdam: 269-318.
- Frisia S., Borsato A., Fairchild I.J. & McDermott F., 2000 - *Calcite fabrics, growth mechanisms and environments of formation in speleothems from the Italian Alps and Southwestern Ireland*. Journal of Sedimentary Research, **70** (5): 1183-1196.
- Füchtbauer H. & Richter D.K., 1975 - *Undulose extinction in carbonate petrography*. IXth International Congress of Sedimentology, **Theme 7**: 55-61.
- Füchtbauer H. & Richter D.K., 1988 - *Karbonatgesteine*. In: Füchtbauer H. (Ed.), *Sedimente und Sedimentgesteine*. Elsevier, Stuttgart: 233-434.
- Given R.K. & Wilkinson B.H., 1985 - *Kinetic control of morphology, composition and mineralogy, composition and mineralogy of abiogenic sedimentary carbonates*. Journal of Sedimentary Petrology, **55**: 109-119.
- Heller F., 1972 - *Die Forschungen in der Zoolithenhöhle bei Burggailenreuth/Ofr. – 200 Jahre wissenschaftliche Forschung 1771 – 1971*. Erlanger Forschungen, Reihe B (Naturwissenschaften), **5**: 7-56.
- Hill C.A. & Forti P., 1997 - *Cave minerals of the world*. 2nd Edition. National Speleological Society, Huntsville, Alabama: 463 p.
- Kendall A.C., 1985 - *Radial fibrous calcite: a reappraisal*. In: Schnerrmann N. & Harris P. M. (Eds.), *Carbonate cements*. Society of Economic Paleontology, Mineralogical Special Publication, **36**: 59-77.
- Massonne H.J. & Neuser R.D., 2005 - *Ilmenite exsolution in olivine from the serpentinite body at Zöplitz, Saxonian Erzgebirge – microstructural evidence using EBSD*. Mineralogical Magazine, **69**: 119-124. <http://dx.doi.org/10.1180/0026461056920239>
- Meyer S. & Dorsten I., 2009 - *Die Riesenberghöhle – Norddeutschlands größtes Höhlensystem in Jurakalken*. Die Höhle, **60** (1-4): 88-93.
- Miao S.J., D'Alnoncourt R.N., Reinecke T., Kasaktin I., Berens M., Schlögel R. & Muhler M., 2009 - *A study of the influence of composition on the microstructural properties of ZnO/Al₂O₃ mixed oxides*. European Journal of Inorganic Chemistry, **2009**: 910-921. <http://dx.doi.org/10.1002/ejic.200800987>
- Neuser R.D. & Richter D.K., 2007 - *Non-marine radial fibrous calcites – examples of speleothems proved by electron backscatter diffraction*. Sedimentary Geology, **194**: 149-154. <http://dx.doi.org/10.1016/j.sedgeo.2006.05.015>
- Niggemann S., Habermann D., Oelze R. & Richter D.K., 1997 - *Aragonitisch/calcitische Koralloide in Karbonathöhlen unterschiedlicher Mg-Betonung*. Speläologisches Jahrbuch – Verein für Höhlenkunde in Westfalen, **1995/96**: 151-168.
- Niggemann S. & Richter D.K., 2006 - *Ein mittelpleistozäner Aragonitstalagmit aus der B7-Höhle (NW-Sauerland, Nordrhein-Westfalen)*. Die Höhle, **57**: 47-56.

- Onac B.P., 1997 - *Crystallography of speleothems*. In: Hill C.A. & Forti P. (Eds.), *Cave minerals of the world*. National Speleological Society, Huntsville, Alabama: 230-236.
- Railsback L.B., 2000 - *An atlas of speleothem microfabrics*. <http://www.gly.uga.edu/railsback/speleoatlas/SAindex1.html>
- Richter D.K. & Riechelmann D.F.C., 2008 - *Late Pleistocene cryogenic calcite spherulites from the Malachitdom Cave (NE Rhenisch Slate Mountains, Germany): origin, unusual internal structure and stable C-O isotope composition*. *International Journal of Speleology*, **37** (2): 119-129. <http://dx.doi.org/10.5038/1827-806X.37.2.5>
- Richter D.K. Neuser R.D., Schreuer J., Gies H. & Immenhauser A., 2011 - *Radiaxial-fibrous calcites: a new look on an old problem*. *Sedimentary Geology*, **239**: 23-36. <http://dx.doi.org/10.1016/j.sedgeo.2011.06.003>
- Self C.A. & Hill C., 2003 - *How speleothems grow: a guide to the ontogeny of cave minerals*. *Journal of Cave and Karst Studies*, **65** (2): 130-151.
- Tietz G.F., 1988 - *Zur Genese rezenter Karbonatbildungen in Dolomithöhlen Frankens*. *Karst und Höhle*, **1988**: 7-79.
- Wassenburg J.A., Immenhauser A., Richter D.K., Jochum K.P., Fietzke J., Deininger M., Goos M., Scholz D. & Sabaoui A., 2013 - *Climate and cave control on Pleistocene/Holocene calcite-to-aragonite transitions in speleothems from Morocco: elemental and isotopic evidence*. *Geochimica Cosmochimica Acta*, **92**: 23-47. <http://dx.doi.org/10.1016/j.gca.2012.06.002>
- Wurth G., 2002 - *Klimagesteuerte Rhythmik in spät- bis postglazialen Stalagmiten des Sauerlandes, der Fränkischen Alb und der Bayerischen Alpen*. Dissertation Ruhr-University Bochum, 123 p + Appendix.



Available online at scholarcommons.usf.edu/ijis

International Journal of Speleology

Official Journal of Union Internationale de Spéléologie



Groundwater lowering and stream incision rates in the Central Appalachian Mountains of West Virginia, USA

Gregory S. Springer¹, Holly A. Poston¹, Ben Hardt² and Harold D. Rowe³

¹Department of Geological Sciences, Ohio University, Athens, OH 45701, USA

²12201 Sunrise Valley Dr., MS 926A, Reston, VA 20192, USA

³Bureau of Economic Geology, University Station, Box X, University of Texas at Austin, TX 78713-8924, USA

Abstract: Surface channel incision rates are of broad geomorphological interest because they set the boundary conditions for landscape change by affecting changes in local relief and hillslope angles. We report groundwater table lowering rates associated with subsurface Buckeye Creek and the surface channel of Spring Creek in southeastern West Virginia, USA. The mountainous watersheds have drainage areas of 14 km² and 171 km², respectively. The lowering rates are derived from U/Th-dating of stalagmites and the paleomagnetostratigraphy of clastic sediments in Buckeye Creek Cave. The oldest stalagmites have a minimum age of 0.54 Ma and we use a minimum age of 0.778 Ma for clastic cave sediments deposited during a period of reversed magnetic polarity. The water table at Buckeye Creek has lowered at a rate of ≤ 40 m Ma⁻¹. Based on the relative elevations of Buckeye and Spring creeks, the water table at Spring Creek has lowered at a rate of ≤ 47 m Ma⁻¹. These values are consistent with previously published rates obtained from caves in the region, although those rates were reported as surface channel incision rates, based on the assumption local groundwaters drained to the surface channel of interest. However, the rates we report are almost certainly not simple bedrock incision rates because of karst processes acting within the cave and surrounding, well-developed fluvio-karst (e.g., stream capture). Caveats aside, incision rates of ≤ 47 m Ma⁻¹ now appear typical of landscapes of the Appalachian Mountains and Plateau.

Keywords: cave, karst, river incision, incision rate, Appalachian Mountains

Received 15 September 2014; Revised 5 December 2014; Accepted 15 December 2014

Citation: Springer G.S., Poston H.A., Hardt B. and Rowe H.D., 2014. Groundwater lowering and stream incision rates in the Central Appalachian Mountains of West Virginia, USA. *International Journal of Speleology*, 44 (1), 99-105. Tampa, FL (USA) ISSN 0392-6672
<http://dx.doi.org/10.5038/1827-806X.44.1.9>

INTRODUCTION

Surface channel incision rates are of broad interest to geomorphologists because they strongly influence landscape development and denudation rates by setting the boundary conditions for hillslope angles and relief (Burbank et al., 1996). However, incision may not be continual and short- and long-term changes in incision rates may be affected by climate or other perturbations through their effects upon stream discharges, sediment supply, and regional base-level elevations. Thus, long-term histories of stream incision may offer insights into events not readily preserved in the geological record (Yang et al., 2011). Incision rates can be calculated by age-dating alluvial and bedrock (strath) terraces, but these may be too few or too difficult to date in erosional environments, which has led various workers to use cave evolution as a proxy for surface channel lowering (Granger et al., 1997; Springer et al., 1997; Granger et al., 2001; Anthony

and Granger, 2007). Caves can shield sedimentary deposits from surface processes for millions of years, while cave morphologies give context to those deposits by serving as records of past water table elevations. If one assumes water table elevations reflect local minima in surface channel elevations, a water table history can be used to reconstruct surface channel histories and incision rates (Granger et al., 2001). This assumption is inherent in the studies cited above and may not be true where the surface stream is itself subject to significant subsurface piracy. We consider just such a case and report two independently derived groundwater table lowering rates.

Cave deposit ages can be calculated using multiple techniques and here too interpretations are dependent upon key assumptions. The greatest uncertainty arises from our inability to age-date cave passages, which are erosional voids, as opposed to the deposits they contain; a deposit can be substantially younger than its host cave passage (Sasowsky, 1998; Stock et al., 2005).

Thus, deposit ages provided a minimum age for the enclosing passages and must be interpreted as such. This applies to the two dating methods we utilize, U-Th dating of stalagmites and paleomagnetostratigraphy, with the former prone to substantially underrepresenting cave ages because stalagmites may have grown long after a stream passage was abandoned (Stock et al., 2005). Nonetheless, they provide a minimum age for the enclosing passage and a maximum incision rate.

Ages are estimated using paleomagnetostratigraphy by comparing the magnetization of cave deposits to established histories of the Earth's magnetic field. This is possible because magnetic particles may align with the Earth's magnetic field as they were deposited from suspended sediments. Upon deposition, the magnetically oriented grains preserve a depositional remnant magnetization (DRM), which can be isolated and measured in samples to determine whether the sediment was deposited when the Earth possessed a normal or reversed polarity field (Schmidt, 1982). The current period of normal polarity has persisted since 0.778 Ma (Singer & Pringle, 1996), which is generally inferred to be the minimum age of detrital, reversed DRM sediments in caves. This may be a significant underestimate of the age of cave sediments and it is very difficult to determine whether sediments possessing a normal DRM are from the current normal episode (Brunhes) or some previous normal period (Stock et al., 2005). We report all reverse DRM samples as being >0.778 Ma in age and make no assumptions about the ages of samples preserving a normal DRM.

In general, cave deposits are the most practical means of estimating incision rates in the region of our study. The rugged watersheds we examine, Spring Creek and Buckeye Creek, are in southeastern West Virginia in the central Appalachians and have moderate to high relief (200-1000 m) with narrow valley floors and comparatively few terraces. Spring Creek is a tributary of the Greenbrier River for which Shank and Sasowsky (2001) report a long-term incision rate of 40 m Ma^{-1} , based on the paleomagnetostratigraphy of sediments in a cave adjacent to the Greenbrier. The Greenbrier rate broadly similar to regional studies, including a rate of $\sim 27 \text{ m Ma}^{-1}$ for the New River (Granger et al., 1997), for which the Greenbrier River is a tributary. The New River values were obtained using cosmogenic isotope dating of cave sediments and is lower than the 59 m Ma^{-1} rate reported for the Cheat River in northern West Virginia (Springer et al., 1997). The incision rates of the Cheat, Greenbrier, and New Rivers are broadly similar to those of the Cumberland and Green rivers of Kentucky and Tennessee, respectively, but the incision histories of the latter two rivers are much better understood (Granger et al., 2001; Anthony & Granger, 2007). Incision rapidly accelerated in those rivers after formation of the Ohio River at $\sim 1.5 \text{ Ma}$ (Granger et al., 2001). The periods of rapid incision occurred as knickpoints migrated upstream and lowered local and regional base levels (Anthony & Granger, 2007), a process which also may have occurred within the New River watershed, a major headwater tributary of the Ohio. The results we report do not have direct bearing on this question because

our cave deposits are comparatively young (<1 Ma). As a result, we focus our analysis on local phenomena, including processes acting only or entirely within the local karst (i.e., autogenic).

STUDY AREA

We report incision rates for Buckeye and Spring Creeks in southeastern West Virginia. Spring Creek is a large perennial stream draining the eastern margins of the Appalachian Plateau (Fig. 1). The region is tectonically inactive (Miller et al., 2013), although local relief can exceed 500 meters. Spring Creek has a total drainage area is 363 km^2 , of which 171 km^2 is upstream of the stream segment we consider (Dasher & Balfour, 1994). The creek is a major tributary of the Greenbrier River, the local base level stream. The Spring Creek watershed includes the 14-km^2 Buckeye Creek watershed, whose center is a large closed depression from which the basin's waters exit via Buckeye Creek Cave (BCC). The 1.6 km long, underground path is entirely traversable, ending at a spring on the banks of Spring Creek (Fig. 2). The active stream passage is the lowest of four tiers or passage levels, the highest of which is 30 m above the modern cave stream. The abandoned tiers contain clastic stream sediments and stalagmites, some of which were sampled for this study. Dasher and Balfour (1994) described the 7-km long cave system in detail and modern channel hydraulics are analyzed in Springer et al. (2003) and Springer (2004).

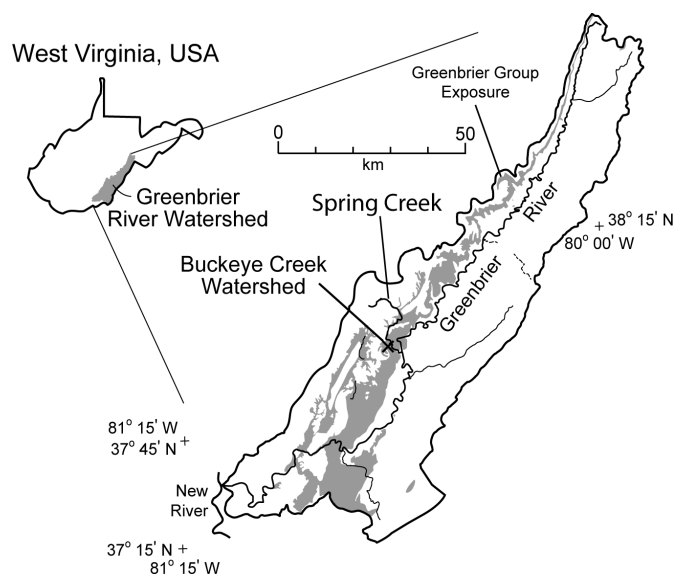


Fig. 1. Locations of Buckeye and Spring Creeks within West Virginia and the Greenbrier River watershed. The shaded portions of the watershed map represent outcrops of the Greenbrier Group (limestones), including the outcrops across which Spring Creek flows.

Spring Creek descends from the Allegheny Front where local peaks are $\sim 1250 \text{ masl}$. The stream has a bed elevation of 579 masl at Buckeye Creek. The bedrock channel is perched at BCC atop the lower Pickaway Formation of the Greenbrier Group, a mixed unit of calcareous shales, siltstones, and limestones, and the underlying, shale-dominated Taggard Formation. However, the riverbed is normally dry between 4 and 10 kilometers upstream where the

Buckeye Creek Cave, West Virginia

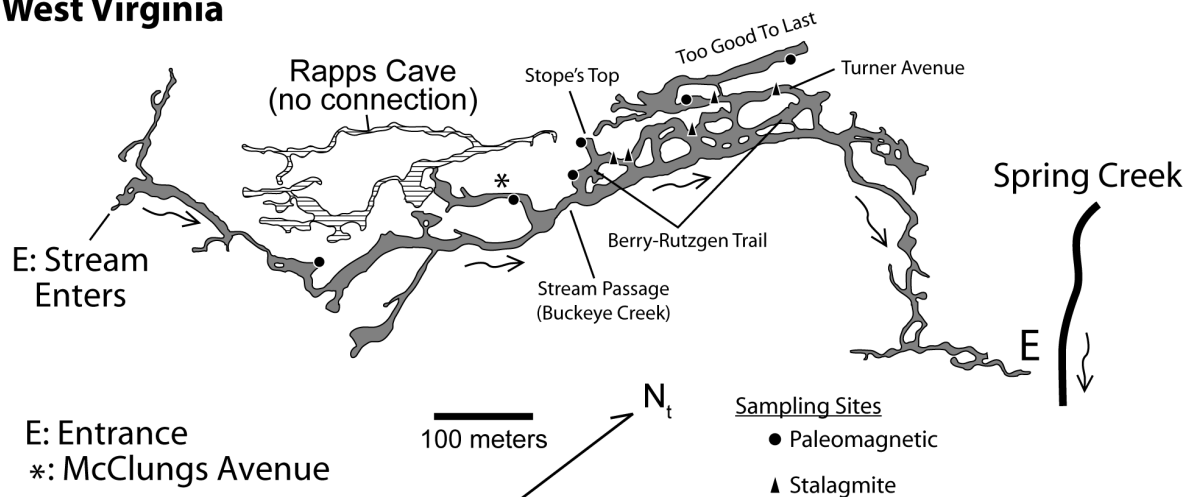


Fig. 2. A plan view of Buckeye Creek Cave. The southern most passage is the lowest tier and contains the cave stream. All other passages are abandoned upper level stream passages. Paleomagnetic sampling locations are shown as filled circles. Narrow triangles mark stalagmite collection points. The map is adapted from a cave map published in Dasher and Balfour (1994). Passage names are from the cave map.

bed is developed in cave-forming limestones of the Union Formation. The water diverted underground reappears downstream of BCC in several large springs (Dasher & Boyer, 2000), having passed through the Taggard Formation via comparatively deep phreatic flow. The perennial flow in Spring Creek adjacent to BCC is from nearby karstic tributaries, also perched on the Pickaway Formation, and not the headwaters of Spring Creek (Balfour, pers. comm. June 2013).

Along this stream segment, the surface channel is within the Union and upper Pickaway Formations, which are highly caverniferous, containing >150-km of surveyed passages in caves tributary to Spring Creek (Dasher & Boyer, 2000; Jones, 1997). The ephemeral Spring Creek segment currently found upstream of BCC is directly analogous to ancient Spring Creek at BCC before it had incised to its present position. Thus, it is possible BCC once fed a subsurface Spring Creek flowing within conduits well below the surface channel, but nonetheless at or near the water table.

METHODS

Elevation data

Incision rates are calculated using relative elevations of sample locations, the active bed of Buckeye Creek in the cave, and the bed of Spring Creek. In-cave distances and inclinations were measured simultaneously using a tripod-mounted laser device. A 450 m long loop yielded a vertical closure error of 1.2 cm. Compass bearings was not measured. The elevation of the Spring Creek bed was determined by tying into a cave and surface survey conducted in the 1980s by George Dasher and the West Virginia Association for Cave studies (Dasher & Balfour, 1994). Their surface survey was tied directly to the cave survey and included the channel of Spring Creek. Their in-cave loops yielded vertical closures of less than 10 cm, which translates to $\leq 1\%$ uncertainty in the relative elevations of sample locations and stream beds.

U/Th samples and ages

Stalagmites were collected between 2003 and 2012. Individual stalagmites were collected whole from the three lowest cave levels: active stream passage (SP), Berry-Rutzgen Trail (BRT), and Turner Avenue (TA) (Fig. 2). The latter two names follow Dasher and Balfour (1994). The stalagmites were collected in conjunction with a paleoclimate study and, except for sample BCC-027, dates were obtained to establish age chronologies for stable isotope transects ($\delta^{13}\text{C}$ and $\delta^{18}\text{O}$). Herein, we report basal ages for individual stalagmites and the age of the top of BCC-027. Where multiple ages were obtained, dates are in stratigraphic order, once again excepting BCC-027 (discussed below). Individual stalagmites were sliced along their growth axis into halves for sub-sampling. Ages are not reported from stalagmites whose interior calcite lacks growth laminations, probably due to post-depositional recrystallization.

Radiometric age constraints were provided by U/Th dating techniques developed for carbonates (Broecker, 1963) and adapted for measurement on an inductively coupled plasma mass spectrometer (Edwards et al., 1987; Shen et al., 2002) at the University of Minnesota. Calcite powder was sampled using a dental drill with a 0.9-mm diameter tungsten-carbide drill bit. Chemical procedures for isolation of uranium and thorium were run along with a chemical blank, which was used to correct the final measurements. Age determinations were made using U/Th disequilibrium measurements conducted on a Finnegan Neptune inductively coupled plasma mass spectrometer with a single MasCom multiplier using the decay constants of Cheng et al. (2009).

Paleomagnetic ages

Samples were collected in 8-cm³, demagnetized plastic cubes (boxes) from unconsolidated, laminated sediments in abandoned stream passages (*c.f.*, Sasowsky et al., 1995). The sampled silts are all interpreted to be former "mud banks" and slackwater sediments deposited by

Buckeye Creek during floods. The sediments were firm and horizontal projections were carved using plastic knives from cleaned, freshly created exposures. Boxes were placed on the projections and the three-dimensional orientation of the end face was measured using a Brunton by measuring the strike direction of the face, its left-right tilt, and its forward-backward tilt. These values were recorded before samples were severed from their exposure. An end cap was inserted on each box to completely and permanently enclose the samples in plastic.

The samples were collected and analyzed in 1993 during a pilot study, but were not reported until their use here. The samples were analyzed in a magnetically shielded room in the University of Pittsburgh Paleomagnetic Laboratory using a rock magnetometer. The process was automated with individual samples being mechanically inserted into the 3-axis, superconducting magnetometer, sequentially rotated, and demagnetized on a step-wise basis. Demagnetization removes secondary magnetic imprints arising from post-depositional, magnetically-driven reorientation of grains, typically by the Earth's field (Schmidt, 1982; Sasowsky et al., 1995). The alternating field demagnetization was performed with field strengths of 0 to 120 mT. Among our samples, several yielded reverse polarity DRMs after demagnetization removed overprinted normal signals, as can be seen in orthogonal vector plots of sample field orientations in Fig. 3. It was sufficient for our purposes to determine whether the DRMs possessed normal, reverse, or indeterminate field orientations because our samples were collected from multiple sedimentary deposits.

RESULTS

U/Th samples

We report U/Th ages from eight BCC stalagmites and paleomagnetic data from 16 clastic sediment samples (8 pairs). The U/Th ages span the modern to >540,000 years before the present, where present is defined as 1950 AD. In general, young BCC stalagmites contain comparatively high concentrations of uranium and thorium (Hardt et al., 2010), probably because a 10-m thick shale caps the overlying hillside. U/Th ratios in older stalagmites are consistent with similarly high initial U concentrations. Reliable maximum ages could not be obtained from five stalagmites. The five stalagmites have growth-laminated calcite encased within a cm-scale weathering rind whose calcite has a chalk-like texture easily scraped off. These stalagmites were collected in their growth positions, suggesting the weathering rind is due to interactions with the cave atmosphere and, perhaps, recrystallization. Inactive stalagmites from which reliable ages were obtained often lack weathering rinds, but others possess mm-scale rinds of similar texture to the undatable stalagmites. Active stalagmites entirely lack weathering rinds. The smallest specimen, BCC-027, yielded a questionable basal age of 539 ka, but an age of infinity closer to its tip remnant. The other four stalagmites also yielded extreme ages, so based on the sensitivity of the Neptune mass-spectrometer; we assign a minimum, rounded age of 0.540 Ma to the five stalagmites.

Table 1. Paleomagnetism results for clastic sediments collected in Buckeye Creek Cave. Locations refer to cave passages discussed in the text and shown in Fig. 2.

Location	Paleomag. sample	P.R.M.*	Average primary		Initial intensity (J/m)
			Inclination (°)	Declination (°)	
Active Stream Passage	007	N (normal)	44.6	340	9.32×10^{-6}
Active Stream Passage	008	N	41.6	359	8.74×10^{-6}
Active Stream Passage	009	N	23.5	3	7.45×10^{-5}
Active Stream Passage	010	N	36.2	8	5.8×10^{-5}
McClungs Avenue	011	N	59.6	350	2.57×10^{-5}
McClungs Avenue	012	N	55.9	355	2.55×10^{-5}
BRT	015	N	54.3	352	3.85×10^{-5}
BRT	016	N	25.2	10	2.4×10^{-5}
Stope's Top	017	R (reversed)	-48.9	185	9.93×10^{-6}
Stope's Top	018	R	-2.4	198	3.47×10^{-5}
TGTL	019	R	-34.1	185	1.39×10^{-6}
TGTL	020	R	-43.6	203	4.41×10^{-6}
TGTL	021	R	-45.9	191	1.61×10^{-5}
TGTL	022	R	-45.1	224	2.29×10^{-5}
Prism Canyon	023	N	49.6	354	3.08×10^{-5}
Prism Canyon	024	N	25	353	2.46×10^{-5}

* Primary remnant magnetization.

Paleomagnetic samples

Six of 16 paleomagnetic samples displayed reversed primary remnant magnetizations after normal polarity overprints were removed (Table 1, Fig. 3). The three sample pairs were collected from the highest known cave level and all six samples display reversed primary magnetism. Two sample pairs were obtained from silt banks in the Too Good To Last Passage (TGTL) and the remaining

pairs were obtained from Stope's Top, a fragment of the same passage exposed by collapse of underlying passages (Fig. 2). At Stope's Top, sediments had filled the river-right (south) side of the passage to its ceiling. A subsequent collapse exposed cut-and-fill gravels overlain by cross-bedded sands, and capped by ~2 meters of laminated silt. The samples were collected from the silt, which is superficially similar that observed in TGTL.

Table 2. Groundwater lowering and incision rates calculated for Buckeye Creek. All rates are maximum values. The real incision rates are equal to or less than the numbers given.

Location	Height above stream (m)	Minimum age (years)	Max. incision rate (m/Ma)	Age control
TGTL	26.8	778,000	34	Paleomag Samples 019-022
Stope's Top	29.9	778,000	38	Paleomag Samples 017/018
Prism Canyon	24.4	540,000	45	Stalagmite BCC-022
Prism Canyon	24.4	581,000	42	Stalagmite BCC-024
Prism Canyon	24.4	628,000	39	Stalagmite BCC-025
Turner Avenue	21.0	308,000	68	Stalagmite BCC-011
Turner Avenue	21.0	298,000	71	Stalagmite BCC-012
BRT	18.3	294,000	62	Stalagmite BCC-013
BRT	18.3	108,700	168	Stalagmite BCC-026
BRT	18.3	540,000	34	Stalagmite BCC-027

Ten of 16 paleomagnetic samples displayed normal primary remnant magnetizations (Table 1, Fig. 3). These samples include all those collected from below TGTL. The lowest samples were collected from a completely silt-filled, 5-meter high passage exposed in cross-section where it has been bisected by the active stream passage. The other normal polarity samples were collected from ancient silt banks in the upper level passages labeled in Fig. 2. These deposits are assumed to represent stream marginal deposition analogous to silt banks currently forming alongside subterranean Buckeye Creek.

Incision or groundwater table lowering rates

The sampled stalagmites grew above the water table and point bar sedimentary structures suggest the sampled clastic cave sediments were deposited in a vadose or epiphreatic setting. Hence, sample ages and elevations constrain evolution of the local water table. The minimum stalagmite and paleomagnetic ages were converted to maximum possible groundwater table lowering rates using relative elevations. The latter were divided by the minimum ages and are reported in m Ma^{-1} in Table 2. The table is arranged by relative elevations above the

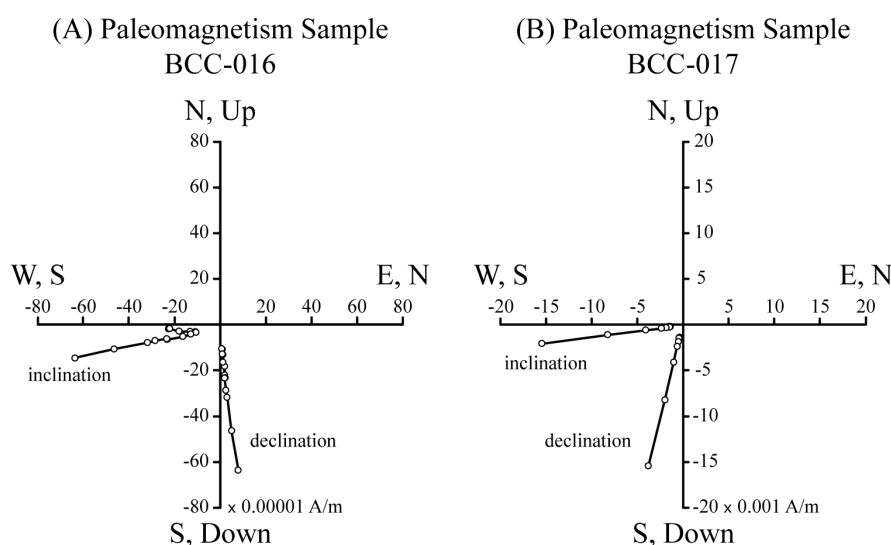


Fig. 3. Vector plots of paleomagnetism samples pBCC-016 and pBCC-017 as samples were demagnetized. Declinations and inclinations changed as samples were progressively demagnetized. The negative inclinations and southerly declinations are both consistent with the sampled cave sediments having been deposited during a period of reversed geomagnetism.

present cave stream with the highest samples at the top and lowest at the bottom. As calculated, the lowering rates are all $\leq 168 \text{ m Ma}^{-1}$. The latter value is of comparatively little value because it makes possible a wide range of incision rates. However, four rates are below 40 m Ma^{-1} , which narrows the range of possible rates to 0 to 40 m Ma^{-1} . The four rates are drawn from 3 of the 4 upper level tiers in BCC and were obtained using both of our methods: stalagmitic and paleomagnetic age dating. Agreement among these samples leads us to report a conservative incision rate estimate of $\leq 40 \text{ m Ma}^{-1}$ for Buckeye Creek. We note the real long-term lowering rate may be $\leq 35 \text{ m Ma}^{-1}$ (Table 2) and any periods of rapid lowering were of insufficient durations to be detectable by our methods.

We assume Spring Creek has served as local base level during development of BCC and, as such, the BCC data records groundwater table lowering induced by Spring Creek. As such, the BCC data places constraints on the Spring Creek incision rates. Vadose deposition of the clastic sediments and stalagmites sets minimum elevations for Spring Creek at the times of deposition. Using the elevation differences between samples and the modern channel, the long-term Spring Creek incision rate must be $\leq 46 \text{ m Ma}^{-1}$ and $\leq 47 \text{ m Ma}^{-1}$, for the paleomagnetic and stalagmitic data, respectively. The very similar values may be a coincidence, but the similar results from paleomagnetostragraphy and stalagmite ages strengthen our confidence in the overall results.

DISCUSSION

Changes in the elevation of Buckeye Creek are the result of channel bed incision and capture of the cave stream by lower passages without complete incision of intervening rocks. These episodic piracys presumably arose as Spring Creek incision increased local hydraulic gradients and lowered the local water table. However, lowering of the water table and steepening of local hydraulic gradients could have been accomplished in two ways: (i) vertical incision of the Spring Creek surface channel with corresponding decreases in water table elevations; and (ii) lowering of local water tables as subsurface conduits developed below the Spring Creek streambed and fed down-gradient springs. There is reason to suspect both have been important controls on BCC development; groundwater table lowering rates are unlikely to be interchangeable with Spring Creek channel bed incision rates.

As described above, present day Spring Creek is perched upon interbedded limestones, siltstones, and shales in the vicinity of BCC and the stream is perennial with the groundwater table and streambed having the same elevation. Elsewhere along Spring Creek, the surface channel is still within the cave-forming limestones of the Union Formation and an extensive vadose zone separates the surface channel from epiphreatic caves below. These caves include the Boartal Cave System whose normally air-filled passages are as much as 30 meters below the surface channel. The Buckeye and Spring creek incision rates we report are probably composites of surface channel incision and subsurface piracy if Spring Creek at BCC was partially or wholly diverted underground while the surface channel was within the Union Formation.

Conceptually, long-term incision rates in similarly well-developed fluviokarst may represent regional incision rates if the elevations of local base level springs are responding to regional downcutting. Here too, any calculated or observed rates will be affected by karst process, but if the time spans examined are sufficiently long they may extend beyond the onset of subsurface piracy and decoupling the water table from surface channel bed. Our record extends to $\geq 0.778 \text{ Ma}$ and may "average across" any such decoupling because BCC currently drains to the Spring Creek surface channel, as it would have before breaching the Union limestones

near the elevation of the TGTL passage. Nonetheless, at present, we can only conclude the long-term incision rate of Spring Creek is $\leq 47 \text{ m Ma}^{-1}$ and acknowledge the rate is probably a composite effect of subsurface piracy and surface channel incision. We can state more confidently that subsurface Buckeye Creek has incised at a rate $\leq 40 \text{ m Ma}^{-1}$ over the last $\sim 1 \text{ Ma}$.

The degree to which incision rates reported from elsewhere in the Appalachian Mountains and Plateau are influenced by autogenic karst processes is unclear, as the possibility is not often discussed. However, episodic changes in base level caused by stream capture are common in many karst settings and long-term karst evolution is more complex than the evolution of a downcutting surface stream. But published cave-based studies have utilized deposits whose ages are in excess of 0.5 Ma and, presumably, the reported incision rates average across internal karst processes (e.g., Granger et al., 1997; Springer et al., 1997; Granger et al., 2001; Anthony & Granger, 2007). The previously reported rates are below 60 m Ma^{-1} and our rates of $\leq 47 \text{ m Ma}^{-1}$ highlight the slow pace of incision in the region at million-year time scales. For comparison, Stock et al. (2005) used multiple dating methods to estimate incision rates within karstic canyons of the Sierra Nevada Mountains of California and report similarly low incision rates of ~ 30 to 50 m Ma^{-1} despite active uplift. The similar incision rates despite such dissimilar geologies are not easily explained, although incision in the Sierra streams may be limited by the wearing away of highly resistant igneous and metamorphic rocks exposed downstream of the examined caves. In contrast, climatically driven changes in karst landscape processes have resulted in incision rates approaching $\sim 1200 \text{ m Ma}^{-1}$ in the European Alps where carbonates dominate the landscape and channel beds amid ongoing uplift and high local relief (Haeuselmann et al., 2007). A comparative lack of relief and uplift in the Appalachians must necessarily decrease the energy available for incision and transport of sediment, thereby yielded low incision rates.

Bedrock streams predominate in southeastern West Virginia and many Appalachian rivers have comparatively steep gradients (Springer et al., 2003; Dortch et al., 2011). We suggest future work be focused on the mechanisms that preclude higher long-term incision rates, such as climate-driven aggradation/degradation cycles (c.f., Springer et al., 2009). Incision rates are useful for interpreting erosion histories, but studying cyclic changes in fluvial and karst systems would improve our understanding of the fundamental processes at work during landscape evolution; we should examine both sides of the coin.

ACKNOWLEDGMENTS

The authors thank the late Gene Turner for access to Buckeye Creek Cave and permission to sample its stalagmites and cave sediments. We acknowledge the West Virginia Association for Cave Studies (<http://www.wvacs.org>) for providing material support, including

lodging, during our research. We thank three anonymous reviewers and the editor, B.P. Onac, for comments and guidance that improved the manuscript.

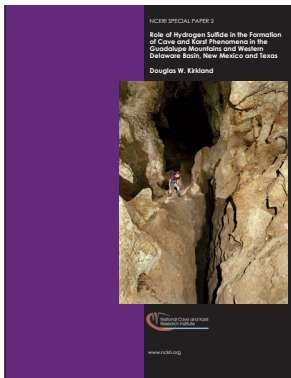
REFERENCES

- Anthony D.M. & Granger D.E., 2007 – *A new chronology for the age of Appalachian erosional surfaces determined by cosmogenic nuclides in cave sediments*. *Earth Surface Processes and Landforms*, **32**: 874–887. <http://dx.doi.org/10.1002/esp.1446>
- Broecker W.S., 1963 – *A preliminary evaluation of uranium series inequilibrium as a tool for absolute age measurement on marine carbonates*. *Journal of Geophysical Research*, **68**: 2817–2834. <http://dx.doi.org/10.1029/JZ068i009p02817>
- Burbank D.W., Leland J., Fielding E., Anderson R.S., Brozovic N., Reid M.R. & Duncan C., 1996 – *Bedrock incision, rock uplift and threshold hillslopes in the northwestern Himalayas*. *Nature*, **379**: 505–510. <http://dx.doi.org/10.1038/379505a0>
- Dasher G. & Balfour W. (Eds.), 1994 – *The caves and karst of the Buckeye Creek Basin*. *West Virginia Speleological Survey Bulletin* **12**, Barracksville, West Virginia, 236 pp.
- Dasher G. & Boyer D.G., 2001 – *Recent Spring Creek area dye tracings, Greenbrier County, West Virginia*. *West Virginia Speleological Survey Monograph* **2**, 28 pp.
- Dortch J.M., Dietsch C., Owen L.A., Caffee M.W. & Ruppert K., 2011 – *Episodic fluvial incision of rivers and rock uplift in the Himalaya and Transhimalaya*. *Journal of the Geological Society*, **168**: 783–804. <http://dx.doi.org/10.1144/0016-76492009-158>
- Granger D.E., Fabel D. & Palmer A.N., 2001 – *Pliocene–Pleistocene incision of the Green River, Kentucky, determined from radioactive decay of cosmogenic ^{26}Al and ^{10}Be in Mammoth Cave sediments*. *Geological Society of America Bulletin*, **113**: 825–836. [http://dx.doi.org/10.1130/0016-7606\(2001\)113<0825:PPIOTG>2.0.CO;2](http://dx.doi.org/10.1130/0016-7606(2001)113<0825:PPIOTG>2.0.CO;2)
- Granger D.E., Kirchner J.W. & Finkel R.C., 1997 – *Quaternary downcutting rate of the New River, Virginia, measured from differential decay of cosmogenic ^{26}Al and ^{10}Be in cave-deposited alluvium*. *Geology*, **25**: 107–110. [http://dx.doi.org/10.1130/0091-7613\(1997\)025<0107:QDROTN>2.3.CO;2](http://dx.doi.org/10.1130/0091-7613(1997)025<0107:QDROTN>2.3.CO;2)
- Haeuselmann P., Granger D.E., Jeannin P.-Y., Lauritzen S.-E., 2007 – *Abrupt glacial valley incision at 0.8 Ma dated from cave deposits in Switzerland*. *Geology* **35**: 143–146. <http://dx.doi.org/10.1130/G23094A>
- Hardt B., Rowe H.D., Springer G.S., Cheng H. & Edwards R.L., 2010 – *The seasonality of east central North American precipitation based on three coeval Holocene speleothems from southern West Virginia*. *Earth and Planetary Science Letters*, **295**: 342–348. <http://dx.doi.org/10.1016/j.epsl.2010.04.002>
- Jones W., 1997 – *Karst hydrology atlas of West Virginia*. *Karst Waters Institute Special Publication* **4**, 124 pp.
- Edwards R.L., Chen H. & Wasserburg G.J., 1987 – ^{238}U – ^{234}U – ^{230}Th – ^{232}Th systematics and the precise measurement of time over the past 500,000 years. *Earth and Planetary Science Letters*, **81**: 175–192. [http://dx.doi.org/10.1016/0012-821X\(87\)90154-3](http://dx.doi.org/10.1016/0012-821X(87)90154-3)
- Miller S.R., Sak P.B., Kirby E. & Bierman P.R., 2013 – *Neogene rejuvenation of central Appalachian topography: Evidence for differential rock uplift from stream profiles and erosion rates*. *Earth and Planetary Science Letters*, **369–370**: 1–12. <http://dx.doi.org/10.1016/j.epsl.2013.04.007>
- Sasowsky I.D., 1998 – *Determining the age of what is not there*. *Science*, **279**: 1874–1874. <http://dx.doi.org/10.1126/science.279.5358.1874>
- Sasowsky I.D., White W.B. & Schmidt V.A., 1995 – *Determination of stream-incision rate in the Appalachian plateaus by using cave-sediment magnetostratigraphy*. *Geology*, **23**: 415–418. [http://dx.doi.org/10.1130/0091-7613\(1995\)023<0415:DOSIRI>2.3.CO;2](http://dx.doi.org/10.1130/0091-7613(1995)023<0415:DOSIRI>2.3.CO;2)
- Schmidt V.A., 1982 – *Magnetostratigraphy of Sediments in Mammoth Cave, Kentucky*. *Science*, **217**: 827–829. <http://dx.doi.org/10.1126/science.217.4562.827>
- Shen C.-C., Edwards L.R., Cheng H., Dorale J.A., Thomas R.B., Moran B.S., Weinstein S.E. & Edmonds H.N., 2002 – *Uranium and thorium isotopic and concentration measurements by magnetic sector inductively coupled plasma mass spectrometry*. *Chemical Geology*, **185**: 165–178. [http://dx.doi.org/10.1016/S0009-2541\(01\)00404-1](http://dx.doi.org/10.1016/S0009-2541(01)00404-1)
- Singer B.S. & Pringle M.S., 1996 – *Age and duration of the Matuyama-Brunhes geomagnetic polarity reversal from $^{40}\text{Ar}/^{39}\text{Ar}$ incremental heating analyses of lavas*. *Earth and Planetary Science Letters*, **139**: 47–61. [http://dx.doi.org/10.1016/0012-821X\(96\)00003-9](http://dx.doi.org/10.1016/0012-821X(96)00003-9)
- Springer G.S., 2004 – *A pipe-based, first approach to modeling closed conduit flow in caves*. *Journal of Hydrology*, **289**: 178–189. <http://dx.doi.org/10.1016/j.jhydrol.2003.11.020>
- Springer G.S., Rowe H.D., Hardt B., Cocina F.G., Edwards R.L. & Cheng H., 2009 – *Climate driven changes in river channel morphology and base level during the Holocene and Late Pleistocene of Southeastern West Virginia*. *Journal of Cave and Karst Studies*, **71**: 121–129.
- Springer G.S., Kite J.S., & Schmidt V.A., 1997 – *Cave sedimentation, genesis, and erosional history in the Cheat River Canyon, West Virginia*. *Geological Society of America Bulletin*, **109**: 524–532. [http://dx.doi.org/10.1130/0016-7606\(1997\)109<0524:CSGAEH>2.3.CO;2](http://dx.doi.org/10.1130/0016-7606(1997)109<0524:CSGAEH>2.3.CO;2)
- Springer G.S., Wohl E.E., Foster J.A. & Boyer D.G., 2003 – *Testing for reach-scale adjustments of hydraulic variables to soluble and insoluble strata: Buckeye Creek and Greenbrier River, West Virginia*. *Geomorphology* **56**: 201–217. [http://dx.doi.org/10.1016/S0169-555X\(03\)00079-5](http://dx.doi.org/10.1016/S0169-555X(03)00079-5)
- Stock G.M., Granger D.E., Sasowsky I.D., Anderson R.S. & Finkel R.C., 2005 – *Comparison of U-Th, paleomagnetism, and cosmogenic burial methods for dating caves: Implications for landscape evolution studies*. *Earth and Planetary Science Letters*, **236**: 388–403. <http://dx.doi.org/10.1016/j.epsl.2005.04.024>
- Yang G., Zhang X., Tian M., Ping Y., Chen A., Ge Z., Ni Z. & Yang Z., 2011 – *Geomorphological and sedimentological comparison of fluvial terraces and karst caves in Zhangjiajie, northwest Hunan, China: an archive of sandstone landform development*. *Environment and Earth Sciences*, **64**: 671–683. <http://dx.doi.org/10.1007/s12665-010-0887-6>

Douglas W. Kirkland

Role of hydrogen sulfide in the formation of cave and karst phenomena in the Guadalupe Mountains and western Delaware Basin, New Mexico and Texas.

2014, National Cave and Karst Research Institute Special Paper 2, 77 p., ISBN 978-0-9910009-1-3 color and b/w photos and illustrations, \$25.



The caves of the Guadalupe Mountains are among the most spectacular in the world. Carlsbad Cavern, with the immense Big Room, and Lechuguilla Cave, the deepest cave in the U.S., are rightfully the most famous, but the area is riddled with hundreds of smaller caves distributed in a relatively narrow band (the 'cave belt') parallel to the Permian reef escarpment formed by the Capitan Limestone. Despite their iconic fame, a complete model for the speleogenesis of the Guadalupe caves has eluded researchers... until now.

The newest offering from the National Cave and Karst Research Institute, "*Role of Hydrogen Sulfide in the Formation of Cave and Karst Phenomena in the Guadalupe Mountains and Western Delaware Basin, New Mexico and Texas*" proposes a new model for speleogenesis and associated features. The author, Doug Kirkland, is not well known in the karst community, but has a long and distinguished record of studying evaporites, including the Permian evaporite deposits of the Delaware Basin. Accessing this broad background, this work also addresses the related topics of the origin of the native sulfur deposits in the basin and evidence for the anaerobic reaction of methane and sulfate as the primary driver of speleogenesis. The result is a complete and coherent model for the evolution of the karst features of the Guadalupe Mountains and surrounding area, which ties together a wide variety of data.

Leaning heavily on Palmer (2006, 2009), Kirkland starts by outlining the current speleogenesis model for the Guadalupe caves. Most workers agree these spectacular caves formed from the reaction of H_2S with O_2 above the water table, within the Capitan Formation and associated outer shelf facies. This reaction produced H_2SO_4 , a very strong acid, either through an intermediate S phase or more directly utilizing a biocatalyst. Sulfuric acid explains most of the unusual features of the Guadalupe Caves, including the unusually large rooms, the pattern of cave passages, and the presence of an assortment of minerals, including most notably gypsum, native sulfur, endellite, and alunite. In addition, the variable and negative isotopic values of the gypsum, first reported by Hill (1981) and Kirkland (1982), support a microbial origin for the H_2S precursor of that gypsum.

The primary controversy still surrounding Guadalupe speleogenesis is the origin of the H_2S . The two currently competing models, the *Basinal Model* of Hill (1987) and the *Shelfal Model* of DuChene and Cunningham (2006), differ in their source for the needed H_2S . The Basinal Model proposed a source in the basin to the east, where abundant castiles, discrete masses of diagenetic limestone, within the evaporites of the Castile Formation suggest H_2S generation via reaction with sulfate. Hill (1987) proposed migration of this H_2S through the Bell Canyon Formation, which interfingers with the Capitan foreereef. However, this model fails because it requires flow against the hydraulic gradient from the Castile Formation down into the underlying Bell Canyon. In addition, the Bell Canyon sands trend sub-parallel to the reef and would not channel flow to the cave belt. The Shelfal Model proposed instead that the H_2S originated in the shelf evaporites to the northwest and migrated downdip to the cave belt, consistent with the hydraulic gradient. According to Kirkland, the primary problem with this model is the absence of a sufficiently large source of H_2S for the quantity required for the amount of speleogenesis observed. The shelf sediments lack evidence, such as the castiles, of substantial H_2S generation.

To solve this controversy, Kirkland proposes a **Modified Basinal Model** where late Tertiary structural and thermal events triggered a series of relatively short-lived events in the adjacent basin that resulted in speleogenesis, castile formation, and the deposition of sulfur deposits. Kirkland then walks the reader through this series of events, carefully documenting each step. Kirkland's presentation provides enough background that the more casual reader should be able to follow the story. At the same time, a more advanced reader will be satisfied with the rigor of his arguments and thorough citation of relevant literature, both older and current.

Kirkland first summarizes the origin and stratigraphy of the Castile Formation and the overlying Salado, Rustler, and Dewey Lake formations. The interbedded anhydrite and halite of the Castile Formation and the way these beds terminate against the steep front of the Capitan reef are key to the model that follows. Kirkland proposes that aggressive artesian waters from the underlying Bell Canyon Formation entered the Castile during Late Tertiary uplift and propagated upward through free convective dissolution of the halite members. The slight structural dip of 1-2° to the east, and the relative insolubility of the anhydrite members (as compared to halite), produced channels that delivered these fluids to the Capitan. These fluids initially contained abundant methane derived from alteration of earlier formed oil during a Late Tertiary high heat flow event. Within the Castile Formation, a microbially mediated reaction of methane with sulfate resulted in the calcitization of the Castile sulfates. This reaction produced the large 'castile' masses of diagenetic limestone, and also generated large amounts of H₂S. The H₂S was then carried up dip along conduits at the base of anhydrite layers into the Capitan and shelf edge facies. There speleogenesis occurred at the water table when the H₂S reacted with atmosphere O₂ to produce H₂SO₄. Thus, Kirkland's model supports the existing model of speleogenesis by providing a large source of H₂S and documenting a viable pathway for its delivery to the cave belt in the Capitan and shelf edge facies.

Kirkland then turns his attention briefly to two related topics: the origin of native sulfur deposits to the east of the cave belt and a more detailed argument for methane, not oil, as the primary hydrocarbon source for the H₂S generated by microbes. The native sulfur deposits form in areas where the ascending methane-rich fluids followed fault-derived fractures through the Castile into the overlying Salado evaporites. There, according to Kirkland, H₂S was again generated, but reacted with O₂ in the phreatic zone to produce native sulfur within the diagenetic limestone instead of migrating into the more distant reef.

Although complex, the new modified basinal model proposed by Kirkland is coherent and compatible with the existing data, both from the caves and from the larger Delaware Basin region. The reader must be patient, as the careful explanations sometimes seem to wander off-topic. This patience will be rewarded, as each apparent digression eventually reveals more details on the way to a complete model. Although the larger stratigraphic picture is based on the classic early literature, the referencing and discussion are fully up-to-date in the more relevant sections related to speleogenesis. The figures are unsophisticated, with minimal color, so readers used to high-tech modern graphics may be tempted to discount them. However, each illustrates nicely the point being made and their simplicity often aids in understanding the complex ideas being presented.

Kirkland presents his model to "stimulate debating, challenging, and reasoning that results in improved knowledge of these extraordinary cave and karst features" (p. 4). In this, he has set the standard of discussion very high. His elegant model integrates the available data on tectonics, sedimentology, basin history, regional fluid flow, and speleogenesis into a satisfyingly complete narrative that is highly recommended for all interested readers.

References cited:

- DuChene H.R. & Cunningham K.I., 2006 - *Tectonic influences on speleogenesis in the Guadalupe Mountains, New Mexico and Texas*. In: Land L., Lueth V.W., Raatz W., Boston P. & Love D.L. (Eds.) - *Caves and Karst of Southeastern New Mexico*, New Mexico Geological Society Guidebook 57th Field Conference, p. 195-202.
- Hill C.A., 1981 - *Speleogenesis of Carlsbad Caverns and other caves in the Guadalupe Mountains*. In: Beck B.F. (Ed.) - *Proceedings of Eight International Congress of Speleology*, Bowling Green, Kentucky, **1**: 143-144.
- Hill C.A., 1987 - *Geology of Carlsbad Caverns and Other Caves in the Guadalupe Mountains, New Mexico and Texas*, New Mexico Bureau of Mines and Mineral Resources Bulletin **117**, 150 p.
- Kirkland D.W., 1982 - *Origin of gypsum deposits in Carlsbad Caverns, New Mexico*. *New Mexico Geology*, **4 (2)**: 20-21.
- Palmer A.N., 2006 - *Support for a sulfuric acid origin for caves in the Guadalupe Mountains, New Mexico*. In: Land L., Lueth V.W., Raatz W., Boston P. & Love D.L. (Eds.) - *Caves and Karst of Southeastern New Mexico*, New Mexico Geological Society Guidebook 57th Field Conference, p. 195-202.
- Palmer A.N., 2009 - *Cave Geology*. Cave Books, Dayton, 454 p.

Leslie A. Melim